UNIVERSITY OF TEXAS AT ARLINGTON

DOCTORAL THESIS

# Electroluminescent Signals and Cosmogenic Backgrounds in High Pressure Xenon Gas Time Projection Detectors

*Author:*
Leslie ROGERS

*Supervisor:*
Dr. Benjamin J.P. JONES

*A thesis submitted in fulfillment of the requirements for the degree of Doctor of Philosophy*

*in the*

College of Science
Physics

December 2021

# Declaration of Authorship

I, Leslie ROGERS, declare that this thesis titled, "Electroluminescent Signals and Cosmogenic Backgrounds in High Pressure Xenon Gas Time Projection Detectors" and the work presented in it are my own. I confirm that:

- This work was done wholly or mainly while in candidature for a research degree at this University.
- Where any part of this thesis has previously been submitted for a degree or any other qualification at this University or any other institution, this has been clearly stated.
- Where I have consulted the published work of others, this is always clearly attributed.
- Where I have quoted from the work of others, the source is always given. With the exception of such quotations, this thesis is entirely my own work.
- I have acknowledged all main sources of help.
- Where the thesis is based on work done by myself jointly with others, I have made clear exactly what was done by others and what I have contributed myself.

Signed: _____

Date: _____

Dedicated to all the ladies who came before me who laid the foundations making my education and work possible.

*"If they don't give you a seat at the table, bring a folding chair."*

- Shirley Chisholm

UNIVERSITY OF TEXAS AT ARLINGTON

# *Abstract*

College of Science
Physics

Doctor of Philosophy

**Electroluminescent Signals and Cosmogenic Backgrounds in High Pressure Xenon Gas Time Projection Detectors**

by Leslie ROGERS

The NEXT collaboration is developing a sequence of high pressure xenon gas time projection chambers with the aim of creating a ton-scale, very low background neutrinoless double beta decay search. Finding evidence of neutrinoless double beta decay would give insight into the origins of the matter-antimatter asymmetry in the universe, the smallness of neutrino mass, and the symmetry structure of the Standard Model. My research involves addressing critical challenges on the path to realization of high pressure xenon gas detectors for ton-scale, very low background neutrinoless double beta decay searches. While most aspects of this technology are easily scalable, some detector elements require R&D in order to be realized on a large scale. These challenges include creating electroluminescent regions and high voltage systems capable of holding high and well controlled electric fields as well as reducing and understanding backgrounds.

$^{136}$Xe is used as the target medium for many experiments searching for $0\nu\beta\beta$ decay. Despite underground operation, cosmic muons that reach the laboratory can produce spallation neutrons causing activation of detector materials. A potential background that is difficult to veto comes in the form of $^{137}$Xe created by the capture of neutrons on $^{136}$Xe. These spallation neutrons are directly proportional to the muon rate and therefore the cosmogenic background rate can be predicted once the muon flux is known. This work developed an analysis that was able to predict and measure the muon rate through NEXT-White.

This work also proposes and explores the concept of adding a small percentage of $^{3}$He to xenon as a means to capture thermal neutrons and reduce the number of activations in the detector volume. When using this technique we find the contamination from $^{137}$Xe activation can be reduced to negligible levels in tonne and multi-tonne scale high pressure gas xenon neutrinoless double beta decay experiments running at any depth in an underground laboratory. With the cosmogenic backgrounds well understood the realization of very low background, tonne-scale comes closer to reality.

# *Acknowledgements*

I would like to thank many of the individuals who have helped me through the completion of this dissertation. First and foremost I am grateful to my advisor Dr. Ben Jones for taking me in as his student and guiding me throughout my graduate studies. He has been a true mentor and friend and I have been very lucky to watch the field of high energy physics progress through numerous students under his guidance.

I am grateful to Dr. Austin McDonald who convinced me to see Dr. Ben Jones and Dr. David Nygren's lab and introduced me to their research topics. He taught me the specifics of the lab and has shared any knowledge he finds that he thinks could potentially improve the efficiency of my work.

Thank you Ryan Clark, Zane Miller, and Fahad Karim for providing invaluable help in the lab. Ryan stayed late many days helping support the work included in Chapter 4. Zane Miller ran the simulations and tests in Appendix E to help us design the Cathode and EL planes and contributed to the entire assembly process of the initial cathode design. Jackie Baeza-Rubio and Fahad Karim helped with tests for determining options of various geometries of cathode and anode designs to be used within NEXT.

I also want to thank our undergraduate engineers Logan Norman and Sanmitra Pingulkar who provided numerous hours making many of the final designs discussed throughout this thesis. Most notably Logan Norman designed, built, and coded the robot that is discussed in Section 3.5. Sanmitra Pingulkar showed immense patience designing and redesigning uncountable iterations of the EL rings and support brackets.

Coming into physics I did not having much coding experience and Benjamin Smithers helped out more than I'd even expect from a postdoc; filling in gaps of missing knowledge, looking into source code, and helping teach me best practices. When we submitted the paper in Chapter 5 an editor wanted a Fluka comparison so the appendix there was done largely by Ben who stepped in and ran the Fluka simulations himself. Also thanks to Dr. Justo Martin-Albo, Dr. Andrew Laing, Dr. Pau Novella, Dr. Gonzalo Martínez Lema, Gonzalo Diaz, and Alberto Uson Andres for spending untold hours getting me on the right track for understanding all the internal components of NEXT software.

Of course many thanks to my committee members; Dr. David Nygren, Dr. Amir Farbin, Dr. Jonathan Asaadi, and Dr. Roxanne Guenette who gave invaluable feedback numerous times and introduced me to people throughout the physics society.

If I continued to thank everyone who helped me get to where I am today this page would be as long as the entire thesis so sadly I cannot. For all my friends, coworkers, and peers unmentioned, thank you as well, you are appreciated and will not be forgotten.

# Contents

# Chapter 1

# Introduction

One of the most important physics questions being explored today is why the visible universe is made predominantly of matter rather than antimatter. One possible mechanism that can explain the generation of matter is leptogenisis. Experimentally, one of the most promising avenues for probing this question is to learn if neutrinos are their own antiparticles. This would be beyond all standard, known physics and would be a Nobel prize level discovery. The most sensitive known way to observe this is through a very rare theoretical process called neutrinoless double beta decay ($0\nu\beta\beta$ ). Neutrinoless double beta decay would imply lepton number violation and existence of massive fermions that are neither matter nor antimatter. We would then know that there are other mass generating mechanisms in nature beyond the Higgs mechanism, and on top of that we could potentially set constraints on the mass of the neutrino. If neutrinoless double beta decay is ruled out rather than discovered, then the scientific community will require a new theory to explain the origin of mass. Therefore experiments probing this interaction are of fundamental importance to science.

## 1.1 Baryon Asymmetry

Assuming the universe started with both matter/antimatter symmetry and in thermal equilibrium, something happened to force an imbalance of matter which is why we exist today. At the beginning of the universe there was a dense, hot primordial plasma where pair production and annihilation could take place. As the universe started expanding the plasma starts cooling, which provides photons with less energy, eventually not having enough energy to cause pair production of heavy particles. The expanding universe also decreased the density of baryons and antibaryons until they became separated enough that pair annihilation cannot occur, termed the "freeze out" and these particles are still traveling through the universe today[1].

Baryon asymmetry, $\eta$, is defined as the difference between baryons and antibaryons over the number of photons in the universe and has been measured through big bang nucleosynthesis and the cosmic microwave background.

$$\eta = \frac{n_B - n_{\bar{B}}}{n_\gamma} = 6.2 \times 10^{-10} \tag{1.1}$$

Explaining this residual asymmetry is a major challenge. One option would be to assume the universe did not start in equilibrium or that this asymmetry existed from the beginning, however any prebaked asymmetry would be expected to be removed during inflation[2], so it appears the baryon density is dynamically generated somehow.

### 1.1.1 Sakharov Conditions

Sakharov developed what are now known as the Sakharov conditions that constrain what must have happened earlier in the universe in order to generate a baryon asymmetry where the Standard Model is no longer applicable. He listed the physical conditions under which matter can emerge in an initially symmetric Universe. Three things are required for baryogenesis to be the mechanism behind matter-antimatter asymmetry starting from symmetric conditions:

- Departure from thermal equilibrium
- Baryon number violation
- Violation of both C symmetry and CP symmetry

Thermal equilibrium requires that all quantum numbers are conserved, so in order for the baryon number to remain unconserved once broken there must be a freeze out that removes the system from equilibrium. An example of a freeze out process is decoupling of the cosmic microwave background. When the universe cooled enough that pair production could no longer occur the photons were left behind, traveling through the universe unabsorbed. This meets the first condition.

In condition two, baryon number must be violated for the number of matter to antimatter particles to go from $n_B - n_{\bar{B}} = 0$ to $n_B - n_{\bar{B}} \neq 0$. Baryon number cannot be the only symmetry violated because if charge conjugation is conserved then the rate at which matter is being produced in one process, antimatter will be produced at the same rate as the opposite process. One process theorized by Grand Unified Theories is proton decay which would look like:

$$\Gamma(p^+ \to e^+ + \gamma) =_C \Gamma(p^- \to e^- + \gamma) \tag{1.2}$$

If baryon number plus charge conservation is violated then the rates above could be different. However, if charge-parity is conserved, the helicities would go at the same rates, canceling the barium number violation.

$$\begin{aligned} \Gamma(p_L^+ \to e_R^+ + \gamma) &\neq_C \Gamma(p_L^- \to e_R^- + \gamma) \\ \Gamma(p_L^+ \to e_R^+ + \gamma) &=_{CP} \Gamma(p_R^- \to e_L^- + \gamma) \end{aligned} \tag{1.3}$$

The same reasoning is used for the case of CP violation with C conservation. Therefore to generate baryons dynamically, C and CP must both be violated.

$$\begin{aligned} \Gamma(p_L^+ \to e_R^+ + \Gamma) &\neq_C \Gamma(p_R^- \to e_L^- + \gamma) \\ \Gamma(p_R^+ \to e_L^+ + \Gamma) &\neq_{CP} \Gamma(p_L^- \to e_R^- + \gamma) \end{aligned} \tag{1.4}$$

While these conditions can be met through the Standard Model, proton decay has not been discovered despite decades of searching. Even if it did exist the C and CP violation in the quark sector is insufficient to meet the existing baryon asymmetry.

There are thus no processes involving Standard Model particles that can explain the asymmetry, creating a need to look for particles outside the Standard Model that can violate baryon or lepton number. Particularly notable is the fact that any asymmetry brought about through lepton numbers will be partially converted into baryon asymmetry through sphaleron processes[2] which conserve B-L but not B+L. When the Sakharov conditions are met using lepton asymmetry, it is called Leptogenesis. Leptogenesis can be realized if and only if lepton number is violated, and one of its low energy predictions is the Majorana nature of the neutrinos.

## 1.2 Majorana Fermions

Majorana fermions are theorized particles that are their own antiparticles. This means being identical under charge conjugation:

$$\psi^c = i\gamma^2\psi^* = \psi \tag{1.5}$$

to satisfy this condition a particle must have at least the following three conditions:

- carry zero gauge charges for its equation of motion to remain unchanged under charge conjugation
- have spin 1/2 to follow the Dirac equation
- be massive else it will be identical to the Dirac fermion equivalent

The only known particle that matches these conditions is the neutrino. If Majorana neutrinos exist then there will be mass terms of both the Dirac and Majorana types in the Lagrangian. The Majorana neutrino can be described by a two-component spinor while the Dirac will have four components. The Dirac spinor can be written as four components with the top two being the left chiral field and the bottom two being right. For the Majorana neutrinos the left-handed antineutrinos correspond to the CP conjugate field for the left-handed antineutrino. Noting that

$$\psi_D = \begin{pmatrix} \xi \\ \eta \end{pmatrix} \tag{1.6}$$

$$\psi_M = \begin{pmatrix} \xi \\ {}_{CP}\eta \end{pmatrix} = \begin{pmatrix} \xi \\ \xi^C \end{pmatrix} \tag{1.7}$$

The Lagrangian for the mass terms are:

$$\mathcal{L}_D = -\frac{1}{2} m_d (\bar{\xi}\eta + \bar{\eta}^C \xi^C) + h.c. \tag{1.8}$$

$$\mathcal{L}_M = -M_M (\bar{\xi}^C \xi) + h.c. \tag{1.9}$$

The two mass terms can be combined without breaking gauge invariance of the Standard Model[3].

$$\mathcal{L}_{DM} = -\frac{1}{2} \begin{pmatrix} \bar{\xi} & \bar{\eta}^C \end{pmatrix} \begin{pmatrix} 0 & m_D \\ m_D & M_M \end{pmatrix} \begin{pmatrix} \xi^C \\ \eta \end{pmatrix} + h.c. \tag{1.10}$$

The masses of the physical neutrino states are the eigenvalues of the mass matrix $\begin{pmatrix} 0 & m_D \\ m_D & M_M \end{pmatrix}$ which results in:

$$m_\pm = \frac{1}{2} M_M \pm M_M \sqrt{1 + 4m_D^2 / M_M^2} \tag{1.11}$$

Taking the Majorana mass to be much greater than the Dirac mass, this results in a heavy neutrino state, and a light neutrino state. This is called the seesaw mechanism.

$$m_{lightest} = \frac{m_D^2}{M_M}$$
$$m_{heaviest} = M_M \tag{1.12}$$

This structure is realized 3 times over for 3 massive light neutrinos, accompanied by 3 heavy partners. The mass and mixes of the 3 observed light neutrinos is discussed in the next session.

## 1.3 Neutrino Masses

In 2015 a Nobel prize was awarded for the unexpected discovery that neutrinos oscillate, determining they have mass, albeit small. Physics as described by the Standard Model indicated neutrinos would be massless. Because the masses are so small, on the order of 1 eV or less, it is often speculated that they could have a mass generating mechanism outside of the Higgs mechanism, adding plausibility to the Majorana mechanism.

Neutrinos interact weakly via flavor eigenstates, $\nu_e$,$\nu_\mu$,$\nu_\tau$ and propagate in the mass eigenstates, $\nu_1$,$\nu_2$,$\nu_3$. How the neutrinos oscillate and mix with each other is defined through the PMNS matrix.

$$\begin{pmatrix} \nu_e \\ \nu_\mu \\ \nu_\tau \end{pmatrix} = \begin{pmatrix} U_{e1} & U_{e2} & U_{e3} \\ U_{\mu 1} & U_{\mu 2} & U_{\mu 3} \\ U_{\tau 1} & U_{\tau 2} & U_{\tau 3} \end{pmatrix} \cdot \begin{pmatrix} \nu_1 \\ \nu_2 \\ \nu_3 \end{pmatrix} \tag{1.13}$$

This can further be parameterized in terms of the mixing angles $\theta_{13}$,$\theta_{12}$, and $\theta_{23}$, and phases $\alpha$, $\beta$, and $\delta_{CP}$. $\delta_{CP}$ accounts for CP violation in oscillations and is the only phase that will remain should neutrinos be solely Dirac particles and not Majorana. The full PMNS matrix in the majorana case can be written as:

$$U = \begin{pmatrix} C_{13}C_{12} & C_{13}S_{12} & S_{13}e^{-i\delta_{CP}} \\ -C_{23}S_{12} - S_{13}S_{23}C_{12}e^{i\delta_{CP}} & C_{23}C_{12} - S_{13}S_{23}S_{12}e^{i\delta_{CP}} & C_{13}S_{23} \\ S_{23}S_{12} - S_{13}C_{23}C_{12}e^{i\delta_{CP}} & -S_{23}C_{12} - S_{13}C_{23}S_{12}e^{i\delta_{CP}} & C_{13}C_{23} \end{pmatrix} \cdot \begin{pmatrix} e^{i\alpha} & 0 & 0 \\ 0 & e^{i\beta} & 0 \\ 0 & 0 & 1 \end{pmatrix} \tag{1.14}$$

where $S_{ij} = \sin\theta_{ij}$ and $C_{ij} = \cos\theta_{ij}$. The angles $\theta_{ij}$ are between 0 and $\frac{\pi}{2}$ while the phases are between 0 and $2\pi$.

Oscillations have been observed in atmospheric, solar, reactor and accelerator experiments, measuring with great accuracy the parameters needed to define the mixing matrix. The difference between the masses squared have been measured via solar and atmospheric neutrinos, however which flavor is the most massive is currently unknown. The question still exists, do neutrino masses follow normal ordering with two light and one heavy neutrino, or inverted with two heavy and one light. These ordering options are called the neutrino mass hierarchy and are shown in Fig.1.1.

## 1.4 Double beta decay

Double beta decay was first theorized by Dr. Maria Goeppert Mayer in [7] and is one of the rarest processes ever observed with half-lives on the order of $10^{21}$ years. The process occurs when two neutrons simultaneously decay to two protons as shown in Fig. 1.2 left. This process

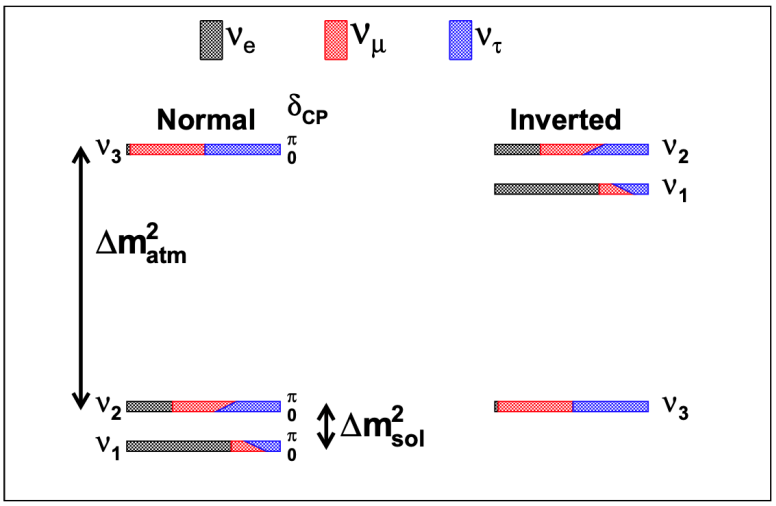


FIGURE 1.1: From [4]. Mass orderings of neutrinos where the masses are made from a mixture of neutrino flavors indicated by the black, red, and blue portions of each mass. Left: normal hierarchy with one heavy neutrino and two light. Right: inverted hierarchy with two heavy neutrinos and one light.

only occurs in nuclei with even numbers of protons and neutrons where single beta decay or electron-captures are energetically forbidden. To conserve charge and lepton number two electrons and two antineutrinos are emitted as well. However if the neutrino is a Majorana particle then that means one of the antineutrinos can annihilate with the other and only two electrons are emitted with no neutrinos, Fig. 1.2 middle, a process which would violate lepton number conservation by two units. This neutrinoless double beta decay ($0\nu\beta\beta$) process is only possible if neutrinos are majorana fermions.

The only practical way to distinguish between two and no neutrino decay mode is by

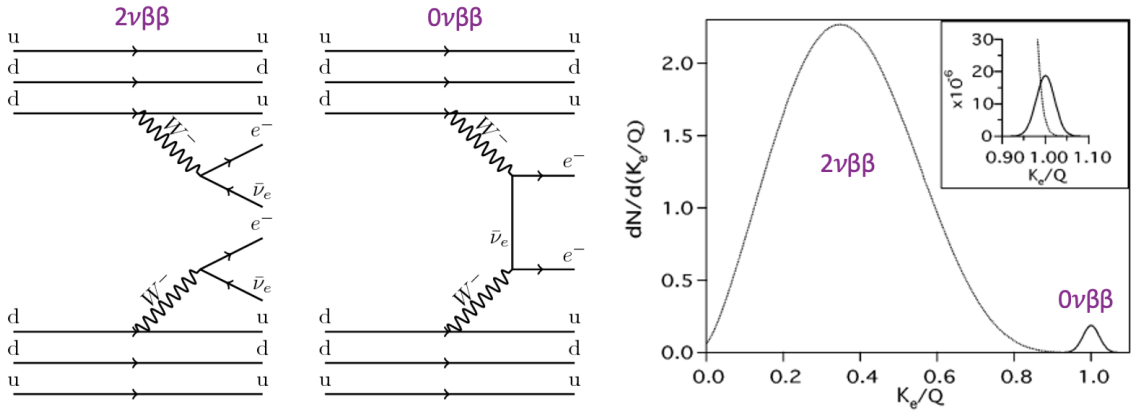


FIGURE 1.2: Left: Feynman diagram of a $2\nu\beta\beta$ decay. Middle: Feynman diagram of a $0\nu\beta\beta$ decay where neutrinos would be Majorana particles. Feynman diagrams reproduced from [5]. Right: From [6]. Energy spectrum of double beta decay. Note the peak around the Q value associated with $0\nu\beta\beta$ decay; this is the signal that would indicate discovery and requires superb energy resolution capabilities to observe it.

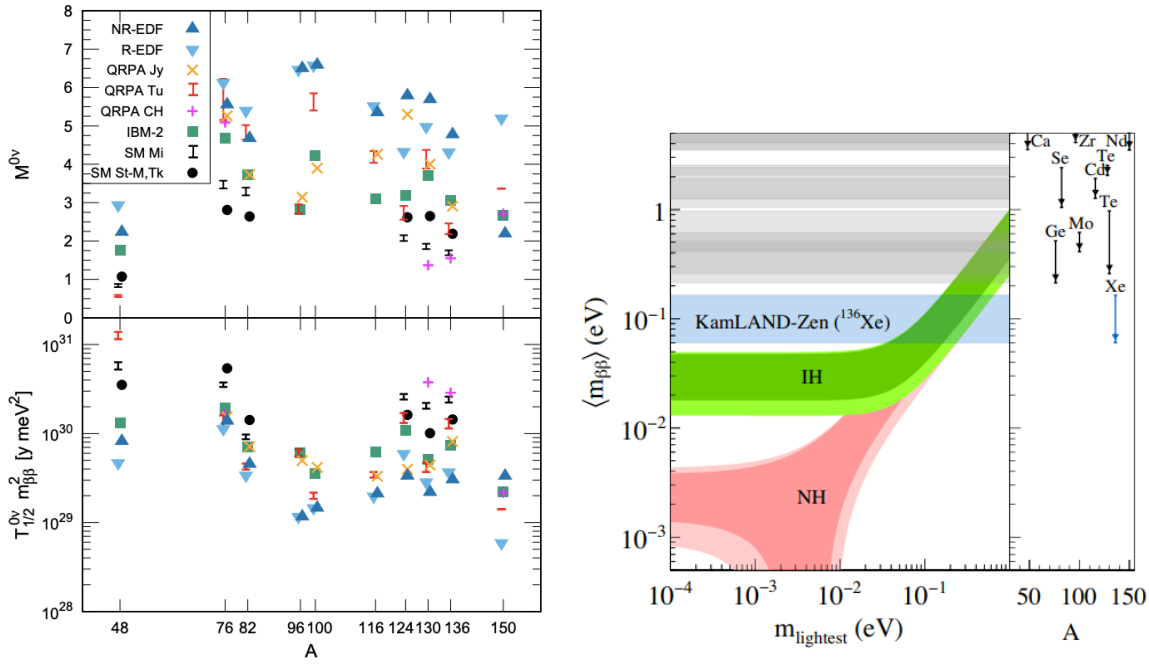


FIGURE 1.3: Left: Reproduced from [8] with top showing calculated $M'^{0\nu}$ for various isotopes capable of double beta decay and bottom giving the corresponding calculated half-lives. Right: From [9] showing the effective neutrino mass as a function of the lightest neutrino mass with the experimental limits set by KamLAND-Zen overlaid.

measurement of the energy of the two beta particles emitted. As long as the neutrinos are included in the decay they will take some of the energy of the transition whereas the recoil nucleus is heavy enough not to take any. Since neutrinos have no charge and extremely low cross sections, they cannot be observed in $0\nu\beta\beta$ detectors. However if the energy of the beta particles is measured and they emerge with exactly the energy of the decay, then no neutrinos were emitted with them. This energy distribution can be seen in Fig. 1.2, right where the peak at the end of the energy spectrum would be the signal required for a positive identification of $0\nu\beta\beta$ decay. The tail of the two neutrino mode reaches to the peak so energy resolution of better than 2.0% FWHM is required from any detectors searching for $0\nu\beta\beta$ to distinguish from $2\nu\beta\beta$ . The spread around the peak at the Q value for $0\nu\beta\beta$ is due to detector effects else it would be an exact spike.

With $2\nu\beta\beta$ decay already being a rare process, an estimate of the decay rate of $0\nu\beta\beta$ is helpful for determining the scale of detectors required for observations. The inverse half-life for $0\nu\beta\beta$ decay is, in the simplest light Majorana neutrino exchange mode:

$$\frac{1}{T^{0\nu}_{1/2}} = \left|\frac{m_{\beta\beta}}{m_e}\right|^2 |M'^{0\nu}|^2 G^{0\nu}(E_0, Z) \tag{1.15}$$

where $G^{0\nu}(E_0, Z)$ is a known integral over phase space which can be found in [10] with $E_0$ being the energy release, or $Q_{\beta\beta}$, equalling $M_i - M_f - 2m_e$. $M'^{0\nu}$ is the nuclear matrix element, $m_{\beta\beta}$ is the effective Majorana mass, and $m_e$ is the electron mass.

The nuclear matrix element depends on nuclear structure effects and therefore varies between

different isotopes and carries some uncertainties from nuclear physics. This has been calculated using several different many-body approximation methods with the various methods agreeing within a factor of 2-3 as shown in Fig. 1.3, left. As computation power becomes more available it is hoped that the calculations will converge in the future.

The effective Majorana mass depends on all of the neutrino masses and the elements of the PMNS matrix[3] from Eq. 1.14

$$m_{\beta\beta} = \sum_i U_{ei}^2 m_i \tag{1.16}$$

Expanding this gives:

$$m_{\beta\beta} = C_{12}^2 C_{13}^2 e^{2i\alpha} m_1 + C_{13}^2 S_{12}^2 e^{2i\beta} m_2 + S_{13}^2 m_3 \tag{1.17}$$

Then putting the masses in terms of the difference squared masses (the observable parameters neutrino oscillations) this becomes:

$$m_{\beta\beta} = C_{12}^2 C_{13}^2 e^{2i\alpha} m_1 + C_{13}^2 S_{12}^2 e^{2i\beta} \sqrt{m_1^2 + \Delta m_{12}^2} + S_{13}^2 \sqrt{m_1^2 \pm |\Delta m_{23}^2|} \tag{1.18}$$

where the $\pm$ encodes that we know the scale of $\Delta m_{23}^2$ but not if it is inverted or normal hierarchy. Choosing a discrete sign for $\Delta m_{23}^2$ and plotting all allowed values for $\alpha$,$\beta$, and $m_1$ gives two bands of allowed $m_{\beta\beta}$ as a function of the lightest neutrino mass as shown in Fig. 1.3, right.

The current generation of experiments are all being designed with the goal of being able to cross the inverted hierarchy band. This will require a ton or multi ton-scale detector and extremely low backgrounds to cross within a few-year time period. Figure 1.4 demonstrates the importance of reducing backgrounds to near non-existence. For a 1 ton experiment to cross and exclude the inverted heirarchy within 15 years would require less than 0.1 counts/ROI/ton/years.

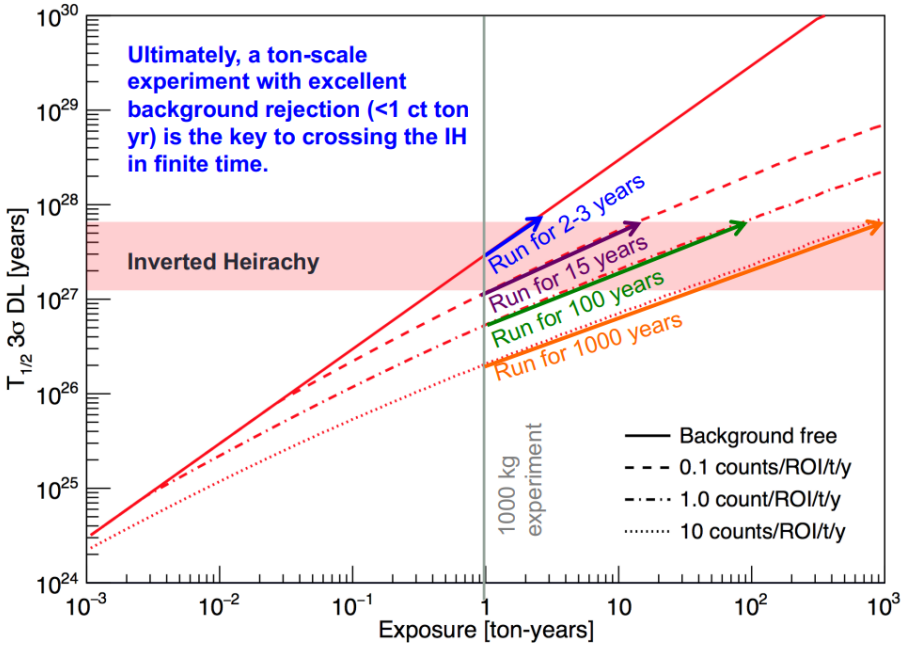


FIGURE 1.4: Sensitivity vs background index for neutrinoless double beta decay, figure from [11].

As such, experiments are working towards reducing backgrounds through selection of radiopure materials, cutting-edge technology, and advanced data analysis methods, covered with more detail in Chapter 2. My contributions are the subject of this thesis.

Up until this point it has been assumed there are only three light neutrinos that would contribute to $0\nu\beta\beta$ decay. However if sterile neutrinos exist an additional mass term would need to be added to Eq. 1.16 and those that follow. There could also be other lepton-number-violating physics involved as well within the nucleus which could mediate $0\nu\beta\beta$ . No matter how the decay occurs if $0\nu\beta\beta$ is observed it is definitively a lepton-number-violating process. The Schechter Valle theorem states no matter what lepton number violating physics causes $0\nu\beta\beta$ , a Feynman diagram can be drawn that encloses the physics as an internal component with the output being a Majorana neutrino mass[12].

## 1.5 Summary

Leptogenesis is a compelling theory which could answer the question of why there is a matter asymmetry in the universe. Discovering a Majorana neutrino through double beta decay would lend support to leptogenesis through a lepton number violating process and demonstrate the existence of fermions that are their own anti-particle.

However, the search for neutrinoless double beta decay is not an easy task. The decay is such a rare process that an extremely high precision and low background detector is required. Double beta decay with two neutrinos is already a rare process (half-life of $10^{19}$ to $10^{21}$ years) that occurs in certain isotopes where it is energetically favorable to double rather than single beta decay. Neutrinoless double beta decay is even more rare (half-life > $10^{26}$ years), requiring either waiting an extremely long time (order $10^{28}$ years) to see the decay from an atom, or have an enormous number of atoms. To see results within a finite time this would ultimately require a ton-scale experiment with excellent background rejection (<1 ct/ROI/t/y) to cross the inverted hierarchy.

# Chapter 2

# Neutrinoless Double Beta Decay Detectors

To discover neutrinoless double beta decay ($0\nu\beta\beta$ ) an isotope must be used that is energetically predisposed to double beta decay rather than single beta decay. One such example is Xenon-136 shown in Fig. 2.1 Left. As can be seen, to decay to Cesium-136 would require an increase in mass energy, whereas Barium-136 would be a decrease. There are several isotopes that do this, some which are listed in Fig. 2.1 Right. To be viable for a large-scale detector there has to be a high enough natural abundance to extract large quantities. Percentages of the double beta decaying isotope present in non-enriched quantities of the base element are listed in the right hand column. Another important requirement is that the energy that is emitted during the decay process, known as $Q_{\beta\beta}$ needs to be high enough to measure with good resolution to be above gamma-ray backgrounds and be able to distinguish $2\nu\beta\beta$ from $0\nu\beta\beta$ decays. The different isotopes that meet this criteria are highlighted in Fig. 2.1 and have different detection methods that benefit from their use rather it be ionization, scintillation, phonon collection, or a combination of two, explained in more detail throughout this chapter.

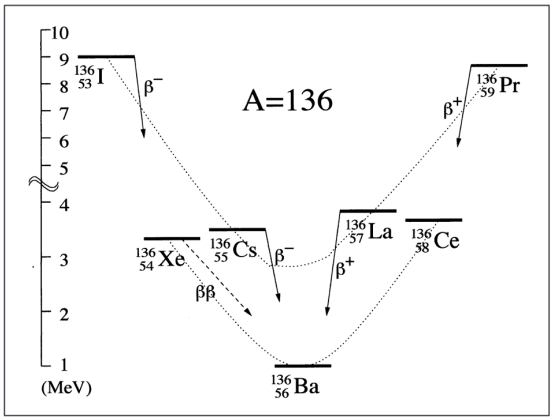


| Candidate | $Q_{\beta\beta}$ (MeV) | Abund. (%) |
|---|---|---|
| $^{48}Ca \rightarrow {}^{48}Ti$ | 4.27 | 0.19 |
| $^{76}Ge \rightarrow {}^{76}Se$ | 2.04 | 7.8 |
| $^{82}Se \rightarrow {}^{82}Kr$ | 3 | 9.2 |
| $^{96}Zr \rightarrow {}^{96}Mo$ | 3.35 | 2.8 |
| $^{100}Mo \rightarrow {}^{100}Ru$ | 3.03 | 9.6 |
| $^{110}Pd \rightarrow {}^{110}Cd$ | 2.01 | 11.8 |
| $^{116}Cd \rightarrow {}^{116}Sn$ | 2.8 | 7.5 |
| $^{124}Sn \rightarrow {}^{124}Te$ | 2.23 | 5.6 |
| $^{130}Te \rightarrow {}^{130}Xe$ | 2.53 | 34.5 |
| $^{136}Xe \rightarrow {}^{136}Ba$ | 2.48 | 8.9 |
| $^{150}Nd \rightarrow {}^{150}Sm$ | 3.37 | 5.6 |

FIGURE 2.1: Left: masses of isotopes of nucleon number 136 and their decay order. Right: Isotopes which double beta decay and their corresponding $Q_{\beta\beta}$ values and natural abundances. The colored rows are commonly used isotopes of $0\nu\beta\beta$ decay searches.

## 2.1 Xenon Based Gaseous $0\nu\beta\beta$ Detectors

Xenon-136 is used by several collaborations some in liquid phase like EXO-200 and nEXO[13], some with liquid scintillater doped with xenon like KamLAND-Zen[14], and some in gas like for NEXT[15]. This section concentrates on operational principles of xenon gas detectors, but the other phases can be found in Sec.2.2.

### 2.1.1 Time Projection Chambers

Time projection chambers (TPCs), invented by Dr. David Nygren[16], are widely used in the particle detector field whether it be to search for $0\nu\beta\beta$ decays, weakly interacting massive particles (WIMPS)[17], or neutrino oscillations[18]. WIMPs, like $0\nu\beta\beta$ decays are theorized within the particle physics field to expand outside the standard model and explain the existence of matter within the universe, though in the case for WIMPs it would give a model for dark matter rather than matter. TPCs work by having a drift field that passes charged particles from their initial position to a readout plane. The particles that reach the readout plane first were produced closer, i.e. smaller z dimension, and those further away take longer to get there; hence the name "time projection chamber"; projecting time into a z component. The NEXT line of detectors are all time projection chambers, operating at 10 to 15 bar with pure xenon gas.

### 2.1.2 Electroluminescence

Electroluminescence produces a well understood, fluctuationless gain of photons to thermal electrons. It works by an electron first gaining kinetic energy while moving through an electric field and elastically scattering off surrounding atoms. Once it has enough energy it will inelastically scatter off a xenon atom resulting in an excited xenon atom. That excited atom then combines with another xenon atom to create an excimer which then decays emitting a photon at 172 nm.

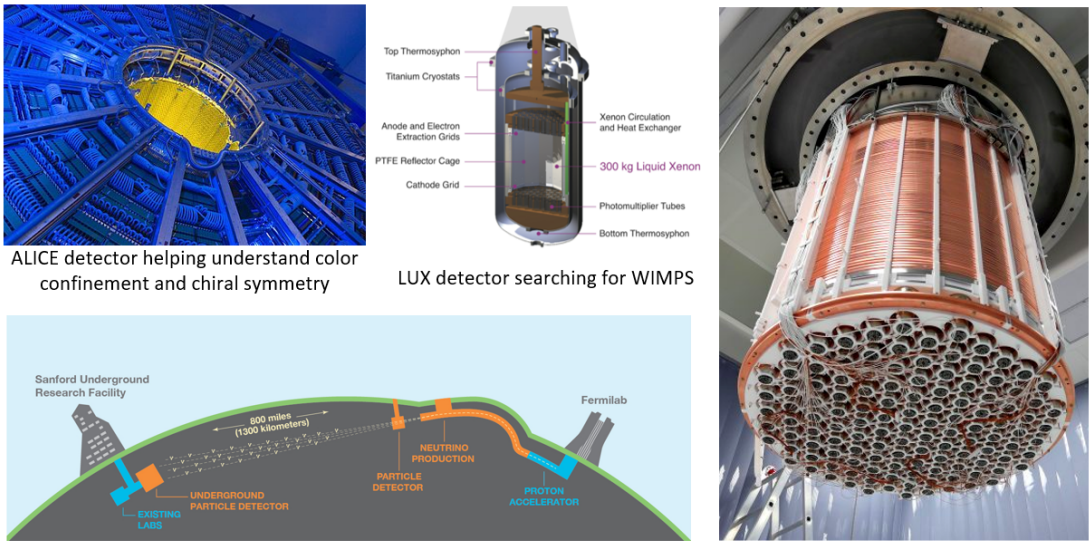


ALICE detector helping understand color confinement and chiral symmetry

LUX detector searching for WIMPS

DUNE looking into neutrino oscillations

XENON1T detector looking for WIMPS

FIGURE 2.2: Time projection chambers from around the world.

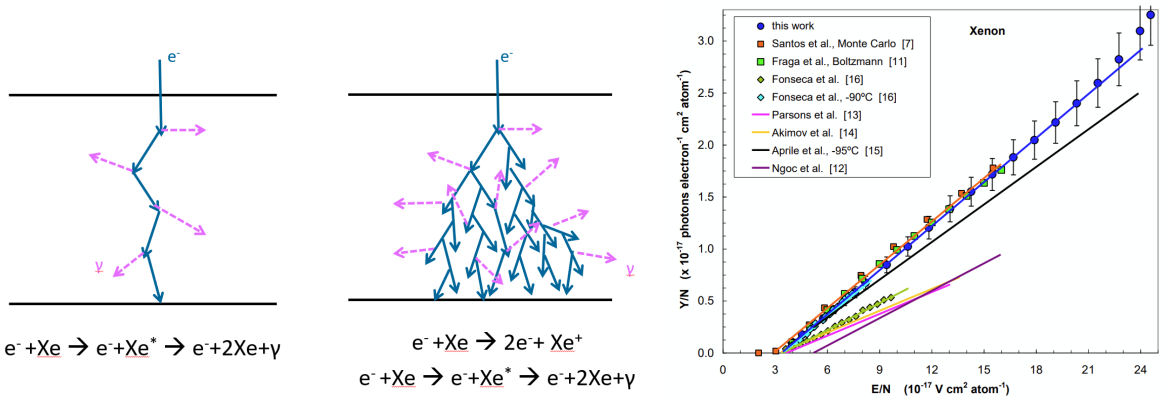


FIGURE 2.3: Electroluminescence (left) versus avalanche gain (middle). Right: Plot from [19] showing the photon yield per primary electron over different electric fields.

Between each excitation the electron will have elastically scattered off atoms at least $10^4$ times. If fewer than $10^4$ elastic collisions occur before an inelastic collision, then the result will be electron avalanches instead of excitation[19] which will give intrinsically worse energy resolution. The EL yield is sensitive to impurities and additives in the gas because an electron inelastic scattering off a molecule will transfer energy into additional thermal and rotational states before excitation can occur.

The optimal excitation efficiency is reached at a reduced electric field i.e., electric field divided by gas pressure, of 4 kV/cm/bar. Anything lower than this will have more energy lost from additional elastic collisions and anything lower than 0.8 kV/cm/bar will provide zero excitations. If E/p reaches 4.5 kV/cm/bar or higher, then ionization starts occurring which provides a nonlinear unpredictable gain because the ionized electrons can also produce electroluminescence rather than just the primary initial electrons and early fluctuations in the avalanche become amplified.

Figure 2.3, Right shows measurements of number of photons per electron versus a reduced electric field. This was experimentally determined by using a xenon gas proportional scintillation counter equipped with a large area avalanche photodiode (LAAPD) and varying the electric field in the driftless scintillation gap[19]. The LAAPD could detect both the photons from the electroluminescence and the original x-rays that created the electrons so that the EL yield could be measured. At higher E/N the light yield deviates away from a linear trend where ionization is occurring. From [19] the following equations are given for calculating the reduced electroluminescence yield:

$$Y/N\ (10^{-17}\text{photons electron}^{-1}\ \text{cm}^2\ \text{atom}^{-1}) = 0.140\ E/N - 0.4 \tag{2.1}$$

where E/N is given in $10^{-17}$ V cm$^2$ atom$^{-1}$, and

$$Y/p\ (10^{-17}\ \text{photons electron}^{-1}\ \text{cm}^{-1}\ \text{bar}^{-1}) = 140\ E/p - 116 \tag{2.2}$$

where $E/p$ is given in kV cm$^{-1}$ bar$^{-1}$. These equations can be used to convert number of photons to how many electrons were created from the initial ionizing radiation event and therefore the energy of said event.

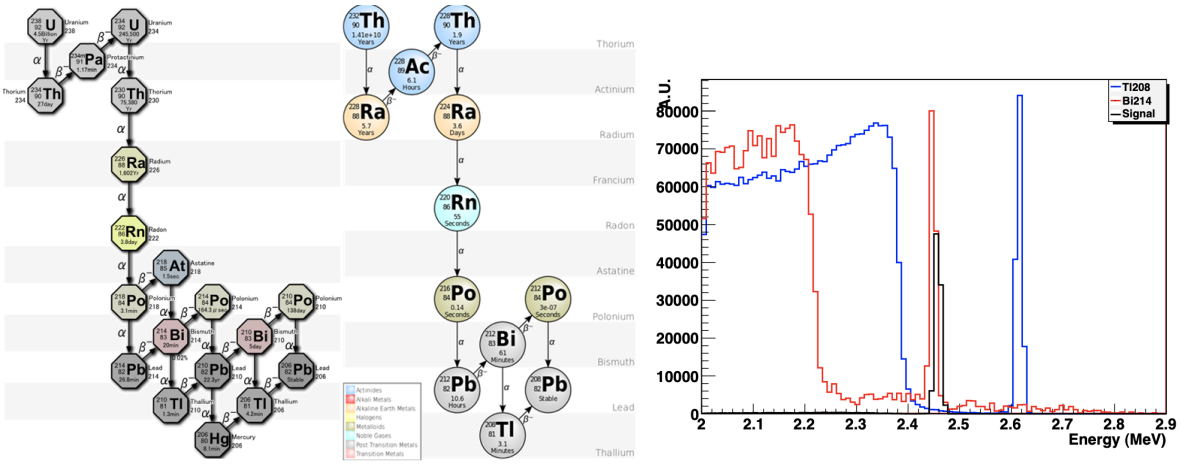


FIGURE 2.4: Decay chains of Left: Uranium-234 resulting in Bismuth-210, a main source of background and Middle: Thorium-232 to Thallium-208. Right: from [20], peaks and compton curves of $^{214}$Bi and $^{208}$Tl and the signal for $Q_{\beta\beta}$ of $^{136}$Xe. Note that the amplitudes are arbitrary and carry no physical meaning.

### 2.1.3 Backgrounds

The future of $0\nu\beta\beta$ searches involves experiments using one to several metric tons of target mass running for tens of years deep underground.

Any radioactivity that produces an event within the detector depositing energy around or above our energy of interest is a background. The main backgrounds in xenon gas TPCs are $^{214}$Bi and $^{208}$Tl from uranium and thorium chains, shown in Fig.2.4, from detector materials themselves. $^{214}$Bi and $^{208}$Tl produce gamma lines at 2.4 MeV and 2.6 MeV respectively. The photoelectric peak of the gamma at 2.4 MeV will fall into the region of interest for $Q_{\beta\beta}$ if the EL resolution is worse than 0.5%[20].

The 2.6 MeV gamma is a de-excitation photon from the daughter of $^{208}$Tl, $^{208}$Pb. The electron tracks from the photo-peak can lose energy via bremsstrahlung and fall into the region of interest. The compton edge of the gamma is at 2.38 MeV which can generate other electron tracks close enough to the original compton electron that they get reconstructed as a single track with energy in the region of interest. There are also photoelectric electrons created above $Q_{\beta\beta}$, but they lose energy via bremsstrahlung and if the photons escape the detector the collected energy will be within the region of interest as well.

Great care is taken in choosing the types of materials within detectors used to reduce uranium and thorium contamination. Even then, each specific batch of materials must have their radiopurity measured to ensure it is within the acceptable limits. There are several ways that materials can be screened for radiopurity. One non-destructive way is with germanium $\gamma$-ray spectrometry[21] which places the material or part in question inside a 5-10 cm copper vessel with a high purity germanium detector and surrounded by 20 cm of low activity lead. To keep out radon contaminants from the atmosphere, nitrogen is continuously blown over the top of the vessel.

Glow Discharge Mass Spectrometry (GDMS) is another common way to screen materials. This works by creating a plasma with a gas (typically argon) and sputtering the sample materials with the gas ions. Then transporting the sputtered species into the gas plasma they are ionized and

extracted for mass spectrometry. This technique is quicker but normally only gives concentration of elements rather than particular isotopes[21].

Inductively Coupled Plasma-Mass Spectrometry (ICP-MS) is similar to GDMS by creating a plasma with a gas, sputtering the materials, then measuring the material ions with mass spectrometry. The difference between the two is that ICP-MS can be done with the sample at atmospheric pressure, allowing for samples to be tested more frequently.

Another source of background in these experiments are from cosmogenic origins. To minimize cosmogenics passing through the detector, experiments require shielding which include being deep underground so cosmic rays are stopped in the surrounding dirt, as well as water tanks. For the cosmic rays that do make it through the detector additives can be added to absorb the neutrons in a way that does not produce a gamma ray within the region of interest. One of the projects I worked on simulated adding Helium-3 into a gaseous xenon detector which showed great reduction in backgrounds which can be seen in Chapter 5. The other option to reduce cosmic ray backgrounds detecting when a particle passes through the detector. This can be done with muon vetos that sit around the detector, or through code that recognizes distinct features of a muon. Creating a muon selection code was the data analysis portion of my thesis and can be found in Chapter 6.

### 2.1.4 Advantages of High Pressure Xenon Gas

There are several reasons to favor high pressure gas detectors. Fluctuationless EL gain and low Fano factor produces energy resolution comparable with solid-state technologies in a ton-scale TPC experiment. Lower density gas vs a liquid detector allows for powerful single-vs-multi electron topological rejection. This topological reconstruction lends itself to active background rejection rather than self shielding which uses the isotope efficiently.

#### Energy

As mentioned before, achieving a precise energy resolution is vital to distinguish between $0\nu\beta\beta$ and $2\nu\beta\beta$ . In a gaseous TPC this is done by taking the electrons produced through

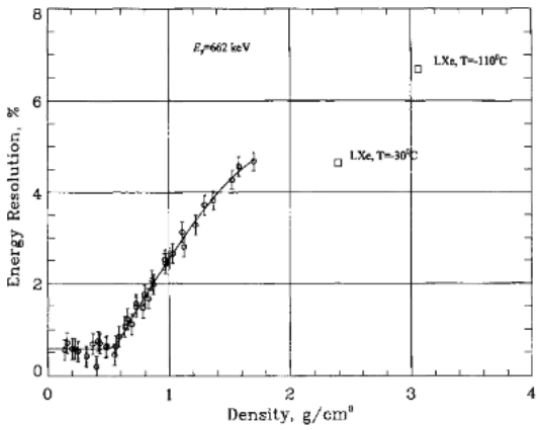


FIGURE 2.5: Left: Plot from [22] showing fluctuations of energy being collected after ionization increases, therefore worsening energy resolution the denser the material.

ionization and passing them to a high field region to induce electroluminesce. Following [23], the FWHM energy resolution is written as:

$$R_E = 2\sqrt{2ln2}\sqrt{\frac{\sigma_e^2}{\bar{N}_e^2} + \frac{1}{\bar{N}_e}\frac{\sigma_{EL}^2}{\bar{N}_{EL}^2} + \frac{\sigma_{ep}^2}{\bar{N}_{ep}^2} + \frac{1}{\bar{N}_{ep}}\frac{\sigma_q^2}{G_q^2}} \tag{2.3}$$

taking into account all the contributions of fluctuations within an EL detector.

The first term in eq. 2.3 corresponds to how many of the original primary charges of the event reach the EL region. With a drift field in gas detectors we are able to minimize loses by drifting the primary electrons away from the ionized particles before they can recombine. Figure 2.5 copied from [22], measures ionization from a 662 keV gamma-ray from $^{137}$Cs and shows how the resolution deteriorates rapidly after around 6 g/cm$^3$ when the gas is too dense to efficiently drift the electron cloud away so the electrons start recombining with ions and not making it to the measurement plane.

The second term in eq. 2.3 corresponds to the EL gain fluctuations. This is where EL is advantageous over avalanche gain. As shown in Fig. 2.3 right, while higher electric fields create more light, the fluctuations get larger as ionization starts to occur along with the electroluminescence. In the lower reduced electric region, around 4 kV/cm/bar there is very little fluctuations.

The third term corresponds to electron fluctuations at the photocathode. This means having a good means of collecting the photons produced in the EL region is important. This requires being able to cover the entire optical plane with photodetectors (like PMTs) and having optical detection at the 172 nm xenon eximer wavelength. The fourth term corresponds to the gain fluctuations within the photodetector and is generally taken to be $\frac{\sigma_q}{G_q} = 1$ because the PMT's single electron pulse height distribution has been measured as nearly exponential, giving $(1 + \frac{\sigma_q^2}{G_q^2}) \approx 2$ [24].

#### Topology

Xenon gas detectors can use topology to distinguish backgrounds versus double beta decay because the ionizing decay particles are able to travel far enough to leave behind a distinguishable track. As the beta particles move through the medium depositing their energy through ionization they get slower and slower, depositing more of their energy in a tight clump at the end, resulting in a Bragg peak for each beta particle. If there is only one ionizing particle like in the case of a background event there will be only one Bragg peak. Fig. 2.6, copied from [25], shows the signature double beta decay spectrum with two Bragg peaks vs the background event with only one. As long as the density is low enough for Bragg peaks to form then this can be used as a cut for signal vs background reduction. Fig. 2.6 shows an event display after post processing with a Richardson-Lucy deconvolution. Because of diffusion of electrons within the gas as it transverses the detector, the track is not as well defined as shown here and requires Richardson-Lucy deconvolution to iteratively recover the underlying track image. It does this by viewing the image as a point spread function and iteratively decreasing the gradient between each point[25] until the initial track appears.

### 2.1.5 NEXT

One leading experimental design, pioneered by the Neutrino Experiment with a Xenon Time Projection Chamber (NEXT) collaboration, uses the isotope $^{136}$Xe in a gas-phase time projection chamber to search for double beta decay. This is currently done with high pressure gas and an

asymmetric design as shown in Fig. 2.7. When double beta decay occurs, the gas is ionized by the beta particles emitted and the ionized electrons are subjected to a low electric field so that they are drifted over to an electroluminescence region and avoid recombination with the now ionized xenon. The initial scintillation light is the trigger S1 for the event start. The electroluminescence region has a high enough field to excite the xenon atoms which then relax, releasing a 172 nm photon providing the second scintillation called S2. The walls of the field cage are coated in Tetraphenyl Butadiene (TPB) which shifts the wavelength of the photons to 420 nm. The photons are then collected with an array of SiPMs or other tracking device for topological reconstruction and PMTs for a precise energy readout.

To distinguish between the background and signal events, we look at the shape of the tracks from the topological reconstruction. A double beta decay will produce "blobs" at both ends of the track, whereas backgrounds will have a single blob or pass directly through the detector. This is the strength of using $^{136}$Xe in its gaseous phase but at relatively high pressure. A liquid is too dense for the beta particles to move through, producing a localized spot of light rather than a track. On the other hand the gas also needs to be dense enough that the beta particles are fully contained within the detector and do not pass into the walls.

The SiPMs used for tracking have too high of a dark count rate for a high resolution energy reading thus presently a second sensitive energy plane is used. NEXT depends on electroluminescence to achieve precise energy resolution in order to distinguish the $0\nu\beta\beta$ peak in the decay spectrum for double beta decay. Note that without tracking information a gamma ray background event could happen at 2.48 MeV and we would not be able to distinguish it from our signal. Whereas without an energy plane we would not be able to distinguish between a $2\nu\beta\beta$ or $0\nu\beta\beta$ event. Unfortunately while PMTs are fantastic at energy reading, they require too

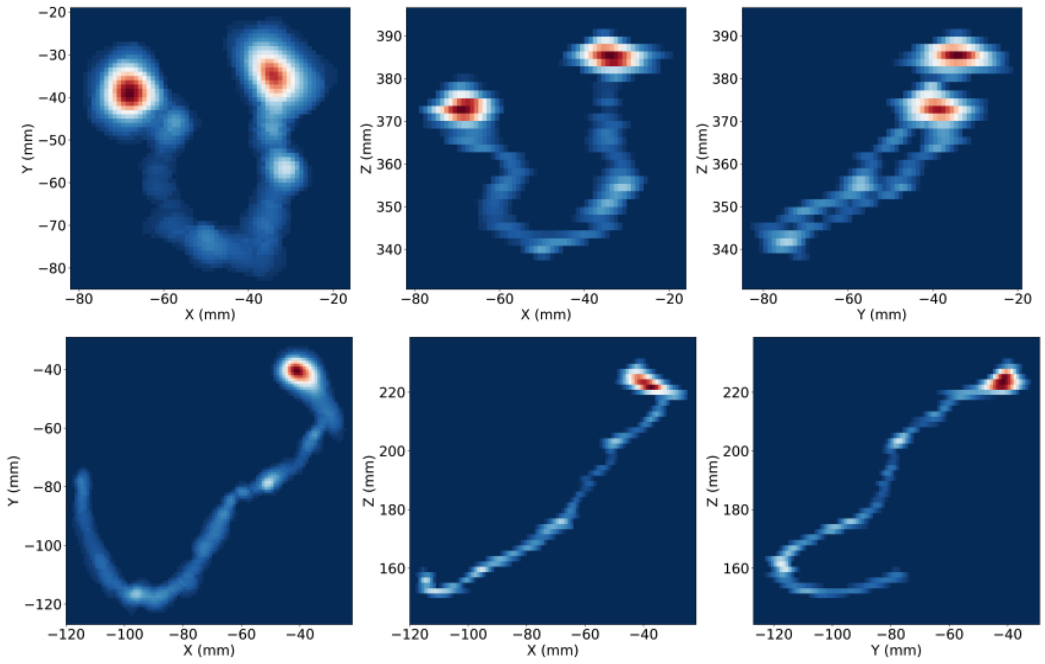


FIGURE 2.6: Plots from [25]. Top Row shows a $2\nu\beta\beta$ event found during NEXT-White data taking. Bottom Row is a background event. Each column corresponds to the XY, XZ, and YZ planes respectively, providing a full 3d reconstruction of the event.

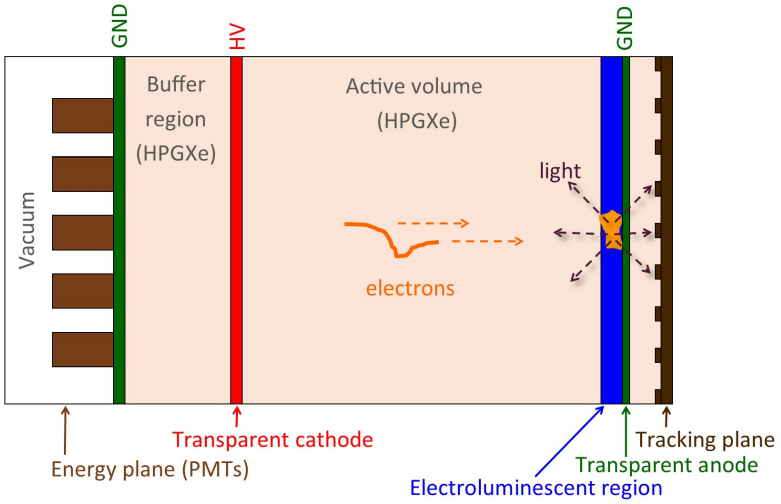


FIGURE 2.7: From [26]. Schematic of an asymmetrical NEXT detector with PMTs on the left which collect light for an energy reading. A buffer region is used for stepping voltage up to the strength needed at the cathode and the drift region then steps voltage across to the EL region. Behind the EL region is an array of SiPMs to collect light for topological reconstruction.

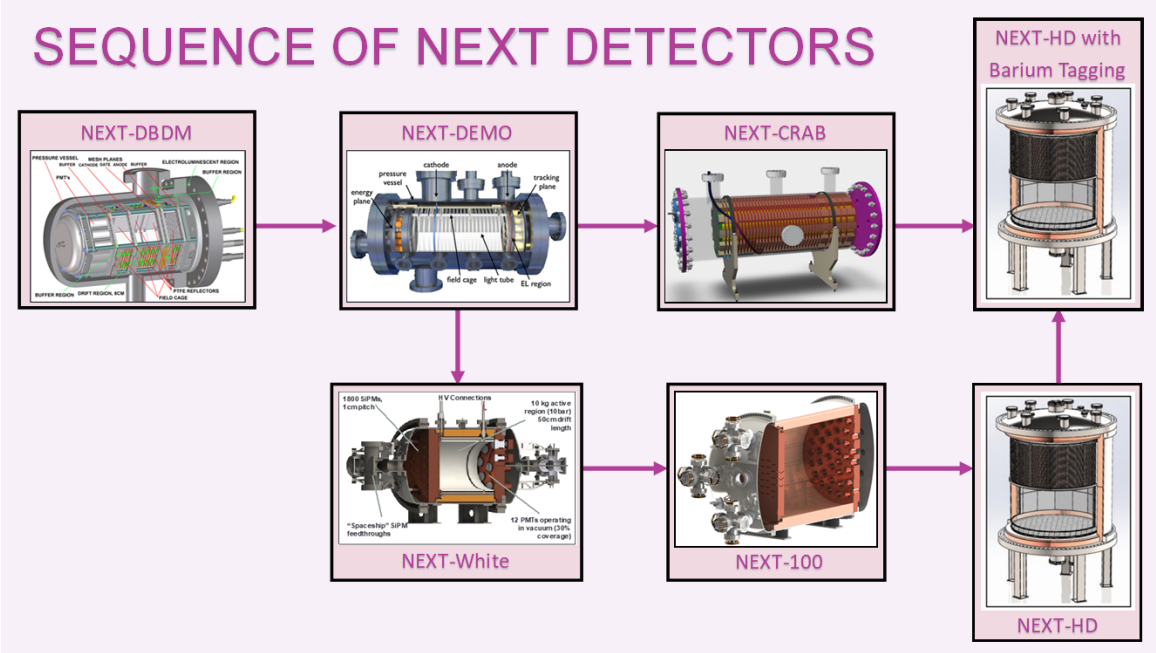


FIGURE 2.8: Sequence of NEXT detectors that have run, are currently running, or planning on being built.

much surface area and angle to be able to see a distinguishable shape of the track.

The order of demonstrators is shown in Fig. 2.8. NEXT-DBDM, NEXT-DEMO, and NEXT-White have all ran and collected data, results which will be discussed below in their respective sections. At the time of writing this NEXT-CRAB and NEXT-100 are being assembled and will

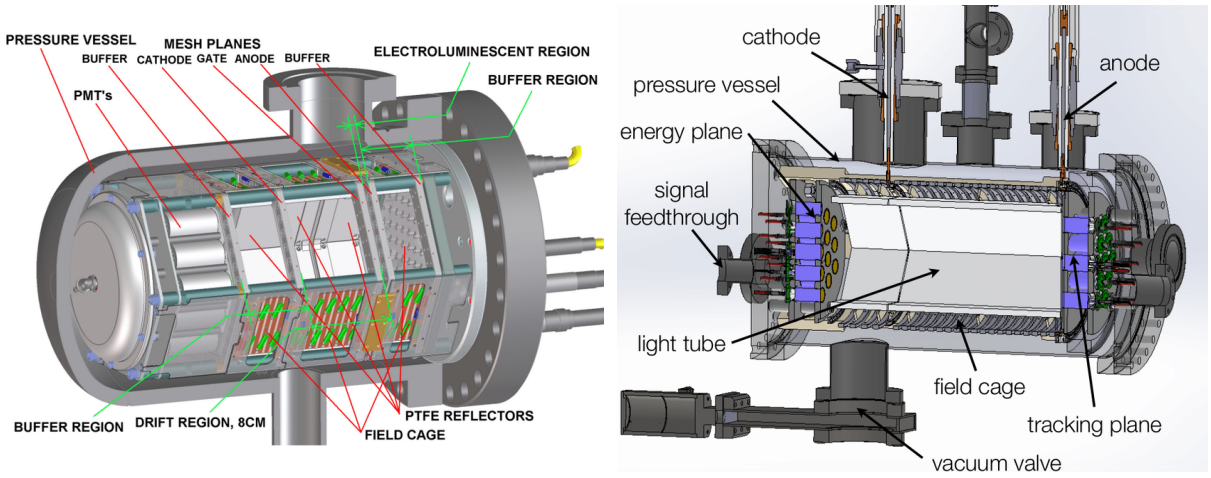


FIGURE 2.9: First prototypes of NEXT used as proof of concept. Left: NEXT-DBDM prototype, Right: NEXT-DEMO prototype. [29]

begin data taking in 2022. NEXT-HD and NEXT-HD with Barium tagging will be the subsequent stages containing a ton or more of enriched xenon.

### NEXT-DBDM and NEXT-DEMO

NEXT-DBDM was the first prototype of the NEXT series looking into the feasibility of the detector for finding double beta decays as well as dark matter searches. It tested energy resolution using an electroluminescent region with 19 Hamamatsu R7378A PMTs on the side of the detector opposite of the electroluminescent region. It was able to get an impressive energy resolution of 1% FWHM for 662 keV Gamma-rays which extrapolated to 0.52% at $Q_{\beta\beta}$[27]. The fiducial volume was fairly small; 17 cm diameter by only 8 cm long, holding 1 kg of xenon at 15 bar[28].

NEXT-DEMO was the first to implement a tracking plane with nearly 300 $\times$ 1 mm$^2$ Hamamatsu Multi-Pixel Photon Counters (MPPCs). The energy plane was identical to NEXT-DBDM with 19 Hamamatsu R7378A PMTs though the detector was larger at 30 cm diameter and 60 cm long[28]. NEXT-DEMO also compared using the wavelength shifter TPB on the walls which shifted photons into a more efficient collection range of the PMTs allowing three times as many photons to be collected [29] for the same events without the TPB coating.

NEXT-DEMO has been repurposed and is currently being run at IFIC, Valencia with SiPMs in the tracking plane and will measure energy resolution capabilities with the electroluminescence region mesh designs (description in Chapter 3) that are built for NEXT-CRAB and NEXT-100.

### NEXT-White

NEXT-White has recently been decommissioned after collecting data at Laboratorio Subterráneo de Canfranc (LSC), Spain for five years. NEXT-White was built to prove the electronics concepts, background model, and develop calibration systems for future high pressure xenon gas experiments looking for $0\nu\beta\beta$ detectors. NEXT-White had an energy plane consisting of 12 Hamamatsu R11410-10 PMTs and a tracking plane with 1792 SensL C-Series SiPMs[32]. It was able to hold 5 kg of xenon with a diameter of 522 mm and length of 664.5 mm.

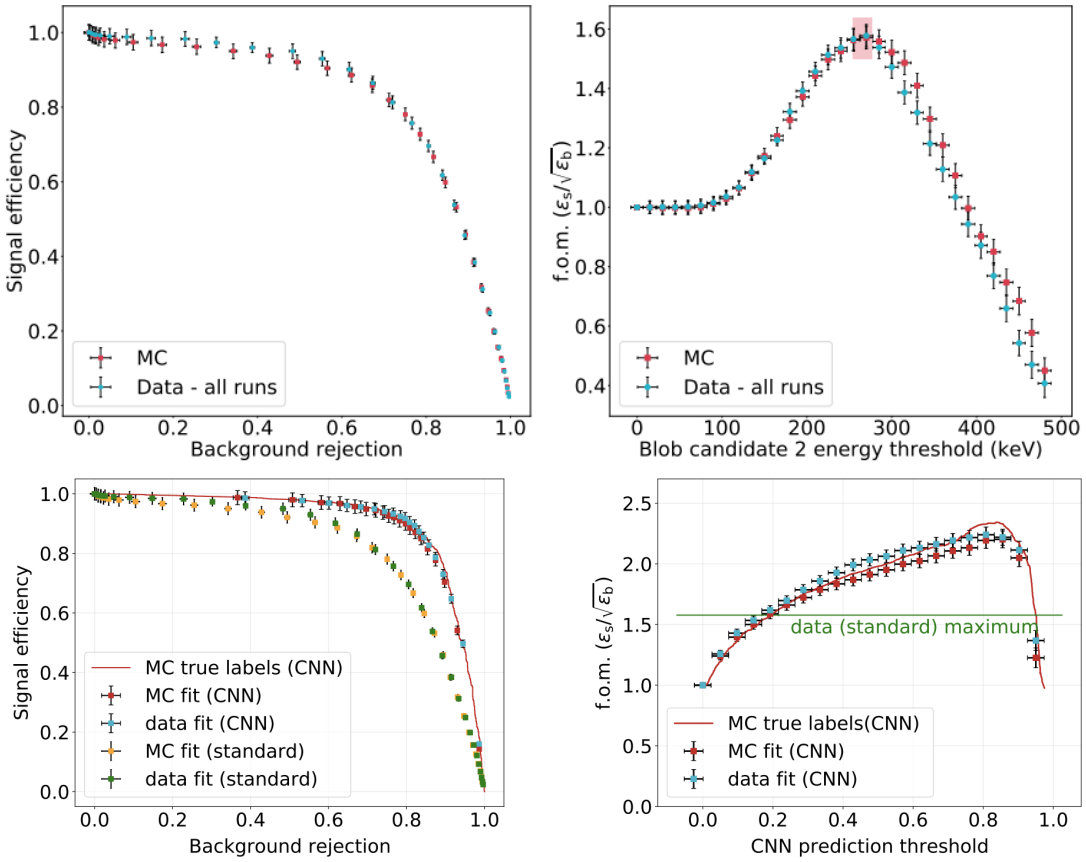


FIGURE 2.10: Top plots are from [30]. Top Left: Signal efficiency as a function of background rejection, i.e. the portion of background events removed from the sample by a blob cut, varying the minimum energy kept for both blobs. Top Right: Figure of merit as a function of the lowest energy blob. Bottom plots are from [31]. Bottom Left: signal efficiency as a function of background rejection based off neutral network classifications. Bottom Right: Figure of merit as a function of the CNN prediction threshold.

NEXT-White used the array of SiPMs to get pixelated images of particle tracks and then used a series of deconvolutions to smooth the track out to its initial form before diffusion and pixelation occurred. To calibrate the topological reconstruction capabilities a $^{228}$Th source was placed on the detector. The $^{208}$Tl daughter decayed and produced a gamma of 2.6 MeV which could enter into the active region of the detector and get converted into a positron and electron, called a double escape peak. The positron moves the same as an electron within the xenon gas until it annihilates with an electron and emits two back-to-back 511 keV gammas which escape the detector, leaving 1.593 MeV to be put into the double escape peak. These peaks look identical to a neutrinoless double beta decay, albeit at a different energy, since they originate from a single point and both the positron and electron move identically. This provides additional signals for calibration on single electron versus double electron tracks.

The first cuts to remove background events are fiducial, single track, and energy within the region of interest. The next step is a blob cut which finds the two blobs of the track and defines them by how much energy is in each. Then varying the minimum energy kept for both blobs can improve signal efficiency. It was found in [30] and shown in Fig. 2.10 that for pure signal-like

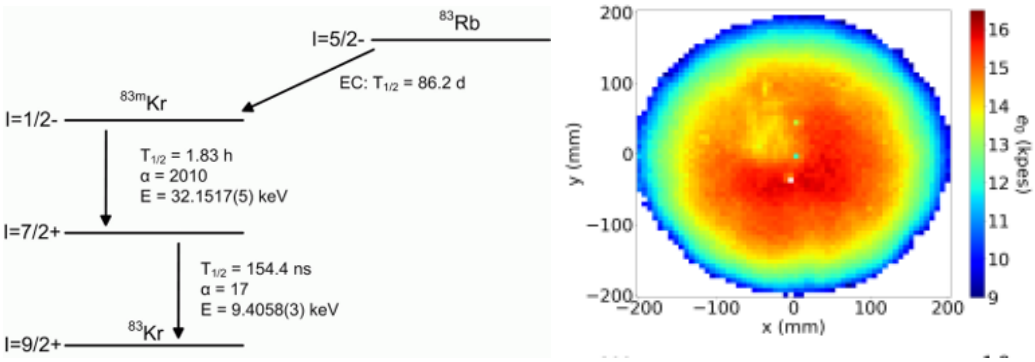


FIGURE 2.11: Left: $^{83}$Rb decay chain used for inserting krypton into the detector for calibrations. Right: energy map obtained by fitting the lifetime over x and y with a krypton source[33].

events the efficiency is 71.6±1.5% with a background acceptance of 20.6±.4%. The same cut on Monte Carlo gave a signal efficiency of 73.4±1.2% with a background acceptance of 22.3±.4% which agrees well with data and corresponds to a figure of merit of 1.578±.038%, calculated using Eq.2.3.

NEXT-White also trained CNNs to be able to classify tracks within the detector as either signal or background. Fig. 2.10 bottom shows signal acceptance over background rejection using trained CNNs, being able to reduce background contamination from data sets to 10 % while still maintaining 65 % signal efficiency[31].

The position dependent response of NEXT-White was calibrated by injecting krypton-83m into the gas [33] to get 41.5 keV point-like events uniformly distributed throughout the detector. With a half life of about 2 hours there is no long term contamination. While krypton-83m has a two step decay process as shown in Fig. 2.11 left, the second step is so quick that it is essentially instantaneous and can be used as a point source. These events can be used for measuring the finite electron lifetime which is necessary to know so that the final energy measurements can be corrected for lost electrons due to attachment on $O_2$ and $H_2O$ impurities. The lifetime of

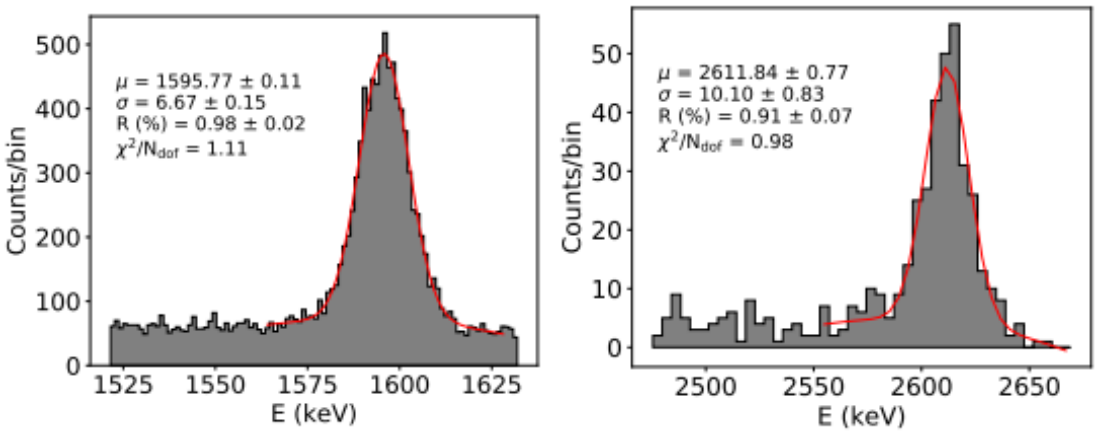


FIGURE 2.12: Energy peaks and their resolution at FWHM at Left: 1592 keV from $^{208}Tl$ double escape peaks and Right: 2615 keV from $^{208}Tl$ photopeaks.[34]

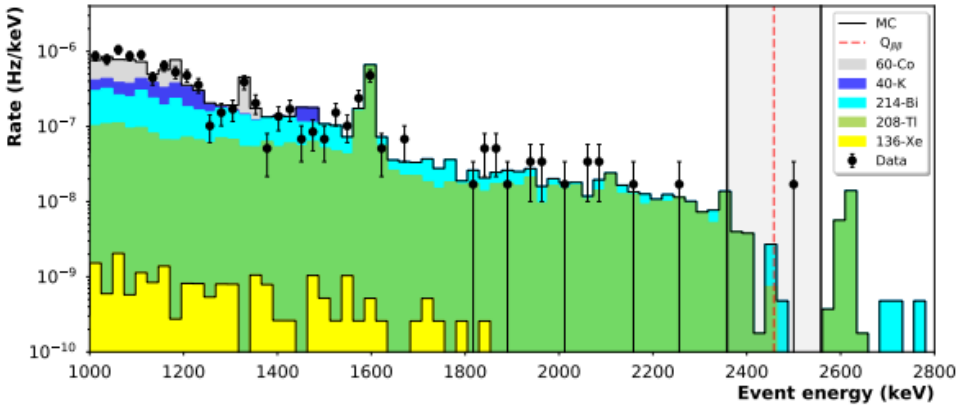


FIGURE 2.13: Plot from [32] after removing single blob events, showing good agreement between data and the monte carlo background model.

electrons can vary depending on nonhomogeneous recirculation of gas and concentration of impurities due to virtual leaks and outgassing but was found to be consistent along z. However the lifetime dependence on the xy position changes depending on how long the gas has been circulated and cleaned.

Krypton calibration is vital to achieve good energy resolution. The longer the drift times the less electrons that made it to the EL region which results in lower resolution at higher z. The light collected for events at each xy location is mostly uniform in the center with the energy collected tapering at the edges as the solid angle collected by the PMTs goes to zero. The less PMT coverage at the edges means lower energy resolution at larger radii.

Figure 2.12 shows the latest published results on energy resolution, already better than 1% FWHM for Q values on either side of $Q_{\beta\beta}$ and is expected to get even better with more calibration and understanding of detector effects.[32]

Detailed GEANT-4 based monte carlo models were made taking into account isotopes and detector materials affecting background rates[32]. To check the background predictions, data was taken with depleted xenon. Figure 2.13 shows the results of 37.9 days of data taking with good agreement to the model.

### NEXT-100

NEXT-100 is under construction now and will collect data at the LSC. NEXT-100, named as such because of the 100kg of xenon it will house, is similar to NEXT-White in the overall design description being an asymmetric TPC with PMTs for the energy plane and SiPMs for the tracking directly behind the EL region. The difference for this detector is proving the concept of scaling up this detector. Many of the manufacturing concepts like a large scale mesh and quartz plate for the EL region and a solid light tube in the center could not be copied at this larger detector scale. Details on many of the specific design choices are covered in Chapter 3 and 4. Currently NEXT-100 is estimated to have a background level of $4\times10^{4}$ counts$^{-1}$keV$^{-1}$yr$^{-1}$ or less[35].

### NEXT-CRAB

NEXT-CRAB or Camera Readout And Barium tagging is a demonstrator that will focus on implementing new designs to enable scaling NEXT up to the ton scale. For large, ton-scale

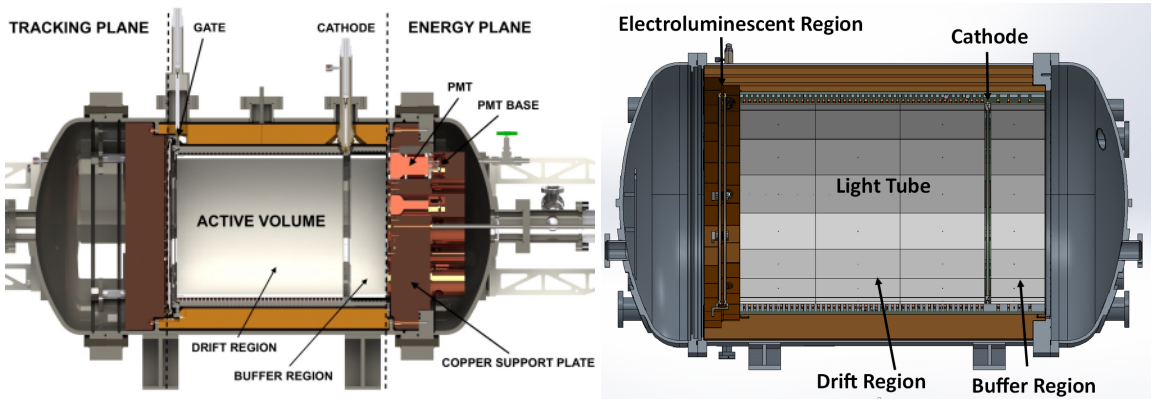


FIGURE 2.14: Left: Image from [36] of NEXT-White detector layout. Right: NEXT-100 layout with more in depth details available in 3

proportions it is very difficult to read out the required number of SiPMs for accurate topological characterization and carries challenges including radiopurity, heat load, system complexity, and cost. A full array of SiPMs would be expensive and each SiPM would require a wire from inside to outside the vessel. The tracking plane may end up with low resolution to compensate; either using as large of SiPMs as possible or spacing them out from each other resulting in a degradation of topological sensitivity. Rather than using SiPMs to get the tracking information, we could use a fast optical camera to quickly snap pictures of the entire electroluminescence region. Co-developed by UTA and ANL, NEXT-CRAB will use a TimePix camera instead of SiPMs which couple to an image intensifier and takes pictures via time-over-threshold and time of arrival readout. This would provide several advantages. The TimePix camera does not need to be directly behind the EL region to collect light so the detector can be made symmetric with the cathode at ground on either side and the EL region in the middle as shown in Figure 2.16.

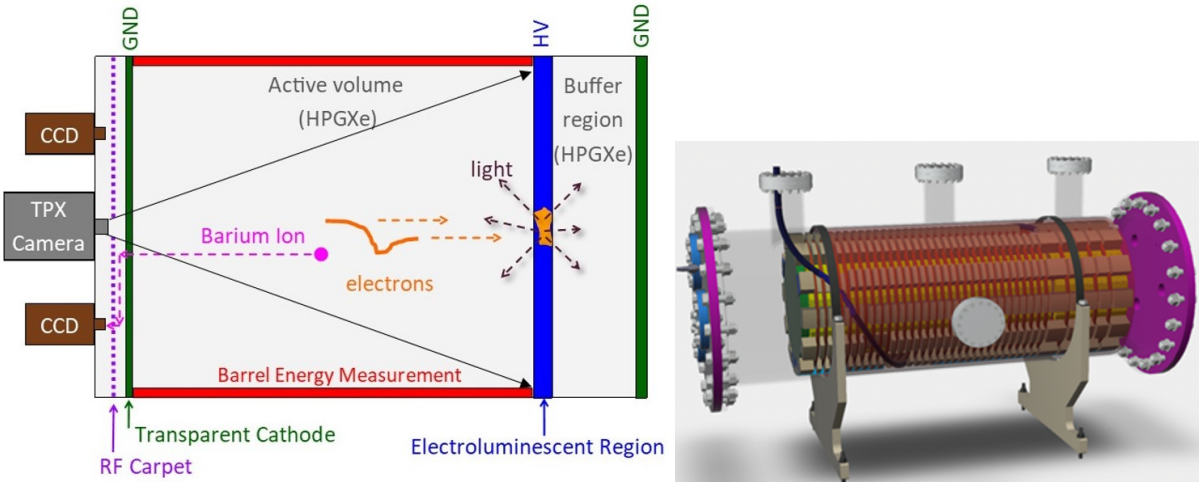


FIGURE 2.15: Left: Asymmetric TPC with Timepix camera rather than SiPMs for topological imaging and energy reading done around the barrel. Barium ions would drift opposite of the electrons, be swept over by an RF carpet, and then light up a fluorescent dye so it can be captured by the CCD. Right: Internal components of the NEXT-CRAB TPC being built at Argonne National Lab.

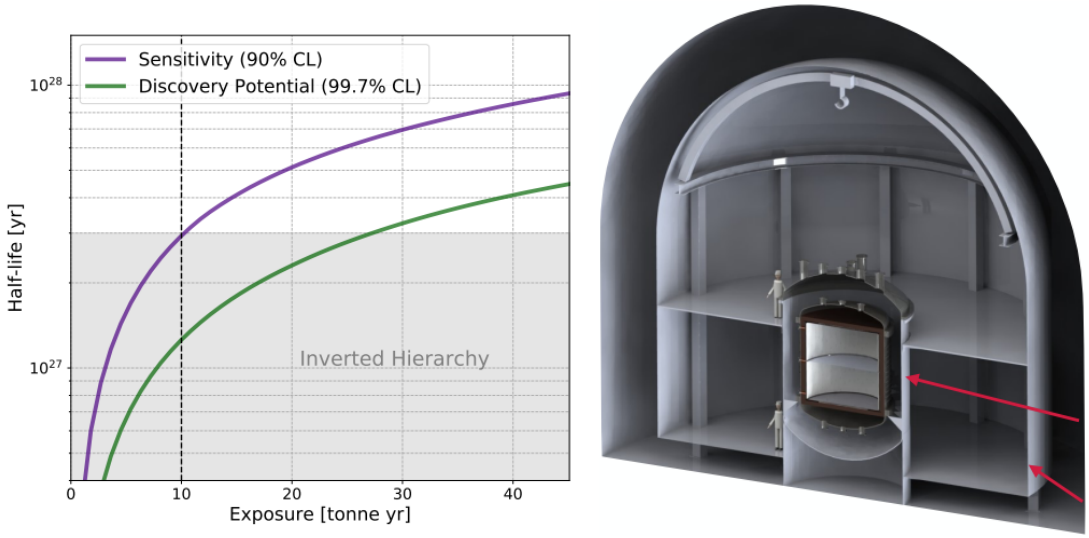


FIGURE 2.16: Left: Projected sensitivity to the half life and discovery potential for a NEXT-style ton-scale experiment located at Laboratori Nazionali del Gran Sasso[37]. Right: NEXT-HD concept design with the pressure vessel housing the TPC being inside a cryogenic facility, all within a water vessel.

This reduces the distance the electrons have to drift, reducing diffusion and therefore providing a more accurate energy measurement.

A barium tagging apparatus and optical cameras are expected to utilize all surface area of the TPC at the endcap. As energy resolution is a critical component of neutrinoless double beta decay, we will require a novel energy readout method around the barrel of the TPC. The leading technology for this is MCP-PMTs, already in the R&D stage at Argonne. For more information on barium tagging refer to Sec. 2.1.5.

### NEXT-HD and NEXT-HD BOLD

The ton-scale version of NEXT is called NEXT-HD. This will be a symmetric TPC with no need for a buffer region to step up the voltage to the cathode, using more of the xenon gas for the fiducial volume. This detector will have significantly less radiogenic backgrounds with the removal of PMTs. To reduce cosmogenic backgrounds two things will be implemented differently from the prototypes to date. One, the detector will be encased inside a water tank to stop gamma rays and neutrons coming from the mountain above it. Two, the detector will either be housed in a deeper lab than the LSC like the Laboratori Nazionali del Gran Sasso (LNGS), or Helium 3 doping should be implemented to collect any neutrons that will otherwise represent an important source of background in the energy region of interest at this detector scale. More details on the Helium 3 studies can be found in Chapter 5.

Figure 2.16 Left shows a simulation for the projected sensitivities of running a ton-scale NEXT-style experiment at LNGS[37]. In the case any of the electronics have more dark noise than is ideal for optimal energy measurements the detector can be cooled inside of a cryogenic chamber within the water tank. NEXT-HD BOLD is the final stage of the NEXT program, implementing barium tagging into NEXT-HD. To reach target sensitivities of $10^{28}$ years, improvements over the NEXT-100 background budget [38] will have to be made.

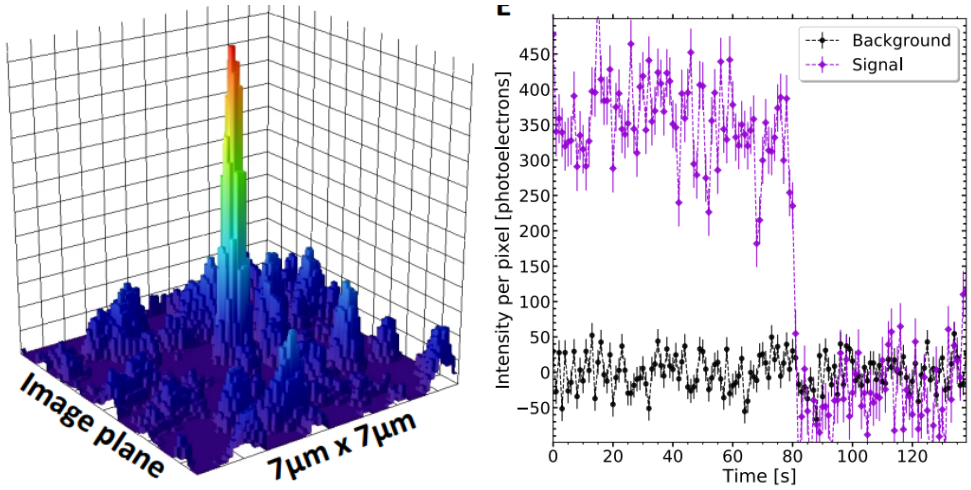


FIGURE 2.17: Plots from [40]. Left: A specific single, barium-chelated molecule. Right: Single-step photo-beaching from SMFI detection demonstrating that a barium had been captured.

**Barium Tagging**

To have entirely background free detection we absolutely must know when double beta decay has occurred in a way un-confusible with a background by directly detecting when the daughter nucleus of the decay, Ba++ has appeared in the system. For NEXT, using a system as described in Sec. 2.1.5 and having the cathode at ground allows for implementation of a barium tagging system. The Barium ions drift the opposite direction of the electrons and can be collected at the cathode. Once at the cathode an RF carpet is used to sweep the ions over to a window coated in a chemical that fluoresces when barium comes in contact with it and a CCD camera records the signal.

Currently under development and testing are Barium tagging and RF carpets in mini-CRAB tabletop experiments. There are two concepts being explored concurrently for tagging of the barium ion. One is a chemical coating at the cathode end of the detector that fluoresces when it comes in contact with barium[39]. While fluorescent tagging has been explored for many cations as a biochemistry technique, not much effort had been put in to tagging Ba ions, due to their low biological abundance. There have now been chemical dyes created specifically for this application and proven to work in dry environments[40].

Using super-resolution fluorescence microscopy, these tagged $Ba^{++}$ ions can be individually identified by their signature 'single-step' photobleaching process as shown in Fig. 2.17 right. The alternative approach to barium tagging uses a colorshifting two photon fluorphore, also tested and proven in a dry environment[41]. In this case their signature is a shift from green wavelength to blue and are kept fluorescing by a continuous sweep of a laser.

To accommodate the environment within a gaseous TPC, microscope objectives have been modified in-house to withstand up to 10 bar. Additionally, while these techniques normally rely on an oil coupled objective, the UTA group has developed a system (see Fig. 2.1.5) which can instead use air coupled objectives, maintaining gas purity.

Once $Ba^{++}$ reach the cathode they can be directed to the center using alternating ±180° phase-shifted RF signals to levitate them above the electrode plane and an additional RF field to

sweep them across[42]. Once at the center there will be a camera that continuously watches for the light up of the dyes.

In order to test the complete system and get an efficiency measurement, there needs to be a measurable barium ion source. The only realistic source of Ba++ is two neutrino decay from enriched xenon with a TPC being the only way to discern the decay has occurred. While barium tagging and tracking give the same function, the combination of having tracking, barium tagging, and energy resolution would provide absolute certainty that double beta decay occurred, giving a background free experiment.

nEXO is a liquid xenon TPC (described in Sec. 2.2.2) which is also exploring barium tagging. In this case rather than moving the barium ion over, a probe is put into the volume of xenon whenever a candidate event occurs which then cryogenically freezes and extracts that volume. This volume is then scanned with a laser and any barium atom within then flouresces for about 30 s before dropping off in a single step[43]. If able to be achieved for the 5 ton detector, the only background for nEXO would be $2\nu\beta\beta$ allowing the inner 2 ton volume to be used (rather than 1 ton) and a half-life sensitivity for $0\nu\beta\beta$ of $3.2\times10^{28}$ years would be achieved[44].

## 2.2 $0\nu\beta\beta$ with Other Isotopes and Phases

There are various other detector techniques being deployed world-wide in the search for $0\nu\beta\beta$ decay by various collaborations. This includes liquid phase TPCs, doped liquid scintillators, bolometric crystals, and many more. Figure 2.18 shows a variety of $0\nu\beta\beta$ decay detectors that are currently deployed.

### 2.2.1 EXO-200

EXO-200 was a 100 kg class $0\nu\beta\beta$ demonstrator [45] using a liquid xenon TPC. It collected charge via crossed-wire grids and light with large-area avalanche photodiodes. To determine a double beta decay event has occurred, a strict fiducial cut is is done, keeping only events contained within the active volume and if the signal was contained in a single spot of only 2-3 mm [46] or multiple. For maximizing the energy resolution, the amount of S1 light is compared to how much charge reaches the anode and utilizes signal anticorrelation, getting a background index of as low as $1.6 \pm 0.2x10^3$counts keV$^{-1}$kg$^{-1}$yr$^{-1}$[47] and setting a limit on the $0\nu\beta\beta$ half-life to $3.5 \times 10^{25}$ years[48].

### 2.2.2 nEXO

nEXO is the proposed ton-scale detector followup from EXO-200. To reduce backgrounds it will use the medium for self shielding meaning for a one-ton fiducial volume it will need five-tons of enriched xenon. The upgraded light collection system will be lower noise SiPMs with expected energy resolution of 2.4% FWHM[47].

### 2.2.3 KamLAND-Zen

KamLAND-Zen is a liquid scintillator detector that has been loaded with 320 kg of xenon that has been enriched for $^{136}$Xe and housed in a 3.08 m diameter transparent balloon[49] to reduce the backgrounds from $^{238}$U and $^{232}$Th decays. The balloon is inside a vessel filled with oil and surrounded by almost 1,900 PMTs for energy measurements. The liquid scintillator provides

around 10,000 photons/MeV of energy deposited[50]. KamLAND-Zen removes all events except those at the 1 m center of the volume and only keeping single site events [14] within the region of interest. KamLAND-Zen currently holds the world's leading experimental limit on $0\nu\beta\beta$ with a half-life greater than $1.07 \times 10^{26}$ yr[9].

### 2.2.4 SNO+

SNO+ is another liquid scintillator detector but this time is loaded with $^{130}$Te which is one of the highest natural abundance percents of the double beta decay isotopes. The goal of SNO+ for a ton-scale detector is 780 tons of liquid scintillator doped with 4 tons of natural, non-enriched tellurium [51], resulting in nearly 800 kg of $^{130}$Te. The detector structure is being reused from previous measurements of neutrino oscillations with Cherenkov light in heavy water[52], helping drastically reduce detector building costs. It is a 12 meter spherical vessel with 9300 PMTs viewing inwards for energy measurements and timing discrimination.[53].

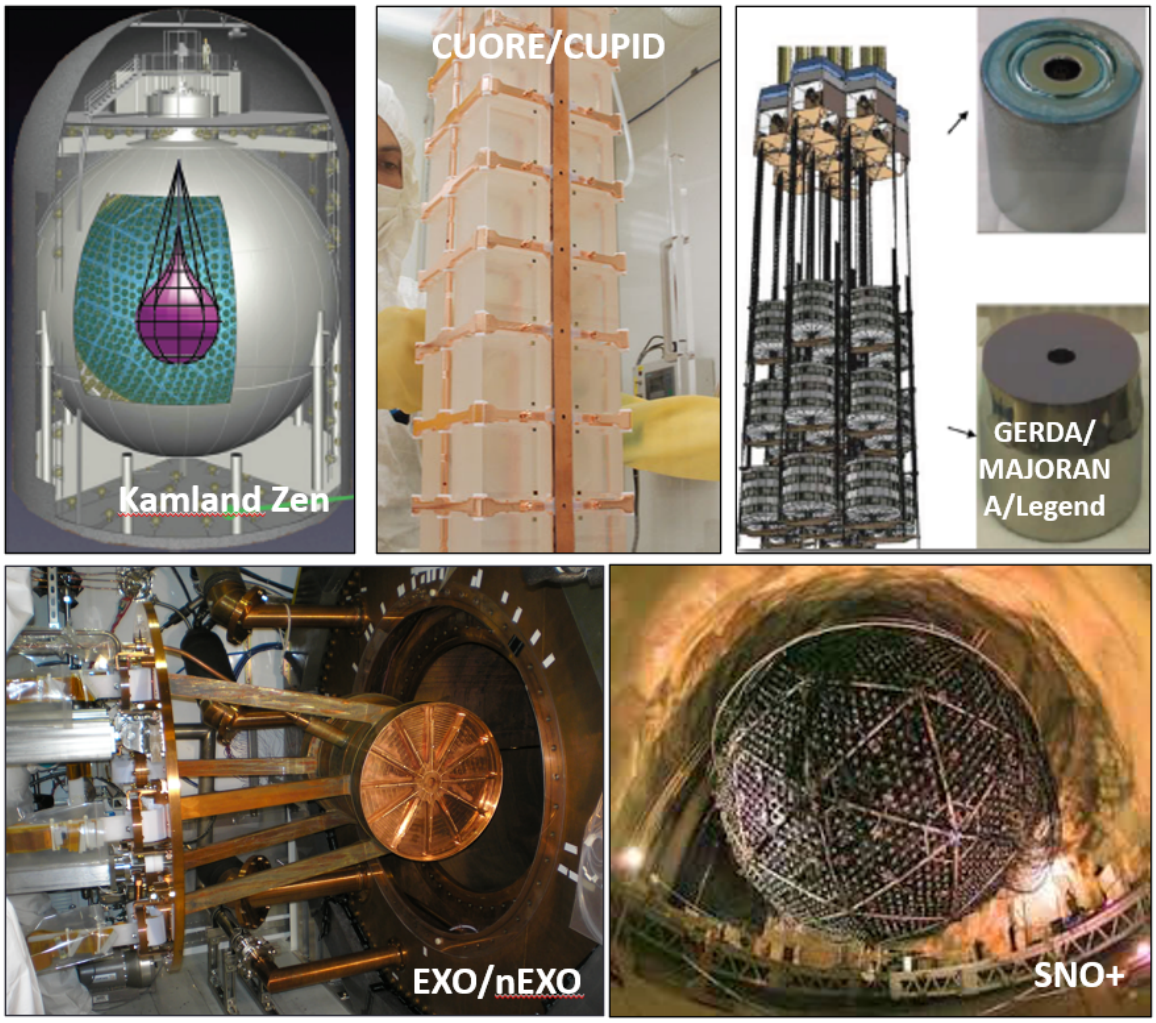


FIGURE 2.18: Experiments other than NEXT also searching for $0\nu\beta\beta$ .

SNO+ uses coincidence to remove backgrounds from $^{208}$Tl and $^{214}$Bi with great success, leaving solar neutrinos as the major background. The expected sensitivity after 5 years of data taking is greater than $1.9 \times 10^{26}$ years[54].

### 2.2.5 LEGEND/GERDA

LEGEND and GERDA are germanium crystal detectors which are deployed directly in a cryostat filled with liquid argon and surrounded by a water veto vessel to remove backgrounds from cosmogenic signals. To reduce cosmic muons the detector is also located deep underground in Laboratori Nazionali del Gran Sasso in Italy and on top of the clean room the detector is housed in are scintillator panels. There is essentially zero dark noise because of the low temperatures and the ionization signal is read out on charge-sensitive amplifiers. These experiments result in very low background signals with GERDA achieving a background index of $5 \times 10^4$ counts keV$^{-1}$ kg$^{-1}$ yr$^{-1}$ and a half-life of $1.8 \times 10^{26}$ years[55].

LEGEND is the follow up after GERDA proved the strengths of germanium crystal detectors. The first stage of LEGEND, LEGEND-200, has 200 kg of high purity germanium (HPGe) deployed in the existing GERDA infrastructure with the HPGe surfaces being covered to reduce background events. LEGEND has set the goal of reaching a half-life of $10^{28}$ years for $0\nu\beta\beta$ decay with 1000 kg of (HPGe) detectors[56].

### 2.2.6 CUORE/CUPID

CUORE is a calorimetric detector looking for phonons within $TeO_2$ crystals housed in cryogenic temperatures. It does not use enriched tellurium, instead relying on the high natural abundance. Each crystal has a germanium thermistor to record thermal pulses when a decay occurs.[57] This decay will be entirely housed in a single crystal and the heat created is converted to an energy measurement to determine if it is $0\nu\beta\beta$ or not. The background of CUORE is $0.014 \pm 0.002$ counts keV$^{-1}$ kg$^{-1}$ yr$^{-1}$[47] and plans to continue running and set limits on the $0\nu\beta\beta$ half life.

CUPID uses $Li_2^{100}$ Mo $O_4$ crystals also at cryogenic temperatures. However it uses a dual readout of temperature and light as an improvement from the design of CUORE for better background discrimination. It still measures energy with the temperature change readings, but uses scintillation to distinguish $\alpha$ events from signal.[58]

## 2.3 Summary

There are many different methods and isotopes being employed to look for $0\nu\beta\beta$ decay, with the need to develop low background ton-scale detectors becoming more and more apparent as stronger limits are being placed on the half life of the decay.

A high pressure gas xenon TPC with a ton or more of $^{136}$Xe has great discovery potential given the field's present understanding of neutrino masses. NEXT will use a $^{136}$Xe gas TPC to search for $0\nu\beta\beta$ , taking advantage of having a topological signature and good energy resolution. Future large scale versions of NEXT will implement barium tagging, reducing the backgrounds even further and increasing sensitivity.

# Chapter 3

# NEXT-100 EL and Cathode

A particular challenge in scaling detectors of the type described in Chapter 2 to ton-scale lies in creating EL regions which require a very high and well controlled reduced electric field on the order of 2-4 kV $cm^{-1}bar^{-1}$ for xenon [59]. This involves biasing large surfaces which must be transparent to 400 nm light, in order not to block the tracking or energy plane. The cathode side of the EL region also must be transparent to electrons, and so is commonly made with a thin wire mesh with high optical and electron transparency. At these large fields of around 30 kV/cm, the electrostatic force between the two electrodes may become sufficiently large as to cause significant deflection in a wire mesh at achievable tensions. Since an electric field is a function of voltage over distance between the two planes, deflection in the mesh causes the region to have a nonuniform field.

These challenges lead to EL design requirements as follows:

- There must be mechanical stability; a frame able to withstand the tension requirements to avoid deflection reducing the gap size no more than 10% under a 28 kV/cm field.
- The EL response must be smooth and better than 0.5% FWHM after calibration. The 0.5% FWHM is to make sure we can distinguish between $0\nu\beta\beta$ and and the photopeak from Bismuth-214 as discussed in Chapter 2 as well as $2\nu\beta\beta$ .
- There should be <1% peak-to-peak gain stability over time once charged. This is to insure Krypton calibration is possible and the energy extrapolations remain constant even after calibrations are complete.
- The stored energy within a large mesh will be high and can cause local heating if this energy discharges into the mesh.This must not lead to long-term damage.
- The photon transparency should be as high as possible, with 80% being the least we can accept.
- The materials used for the EL region must also be chosen for radiopurity resulting in radioactivity <20% of the tracking plane. Keeping backgrounds as low as possible is important to avoid falling into the energy region of interest.

The requirements for the cathode region are less strict but still equally important. The cathode must interface with a high voltage feed-through to hold high voltage without sparking in the buffer region and maintain a uniform electric field for as much of the fiducial volume as possible. The cathode must also be transparent to visible light and be mechanically sound with materials low in radioactivity.

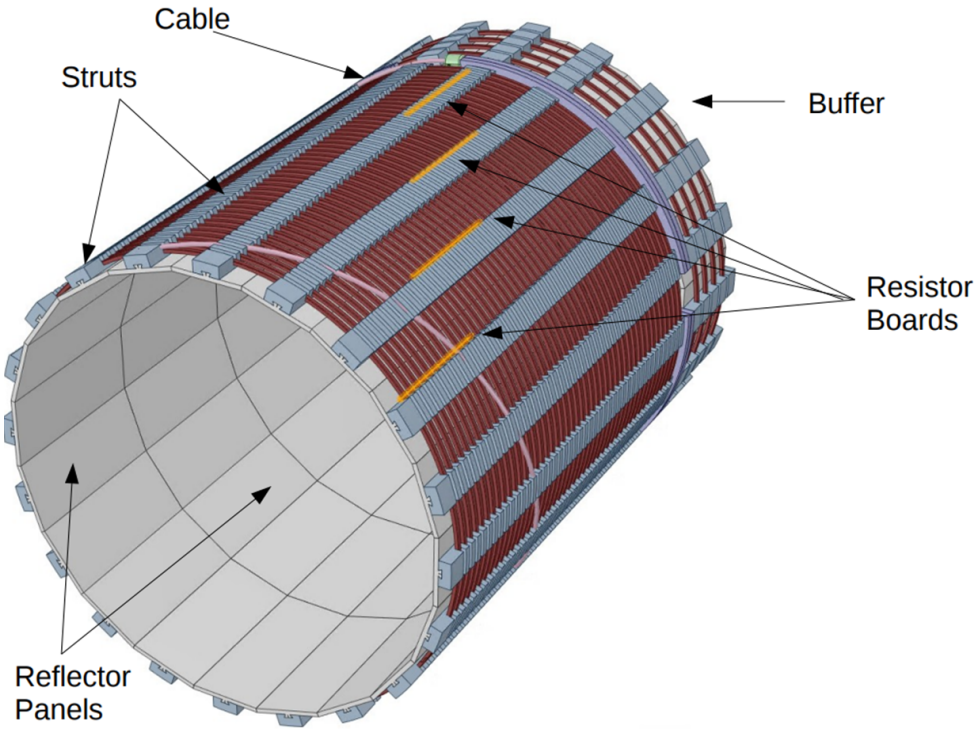


FIGURE 3.1: Field cage without insulator panel showing how everything assembles together.

This chapter outlines the design choices made for the NEXT-100 cathode and EL region. We begin with a broad overview of the design and assembly process, followed by a description of quantitative analyses performed to validate this design. Following an initial prototype with strung wires (details in Appendix E) we have decided to move instead to a photo-etched design for the cathode, gate, and anode. The reason for this change is the removal of many single-point failures associated with individually fixed wires, and the dramatically improved robustness of photo-etched hex vs single strung wires. Another prototype was built for the anode consisting of a resistive plane (details in Appendix F) but was moved away from for improved transparency, robustness under electrical discharges, and gas flow. Development and study of the NEXT-100 EL region was an important contribution of my PhD research.

## 3.1 NEXT-100 Design

The design for NEXT-100 was made with the requirement of being scalable so that NEXT-HD could be modeled after it. This was a collaborative effort among UTA, Harvard, Instituto de Física Corpuscular, and Argonne National Lab and took several years of R&D to come to the final design that is described here.

### 3.1.1 NEXT-100 TPC and Field Cage

NEXT-100 has three major sections, all defined axially. First is the buffer region which allows the cathode to be at a negative voltage of up to 100 kV without a high enough electric field between it and the electric ground that might cause sparking or additional electroluminescence. Second is

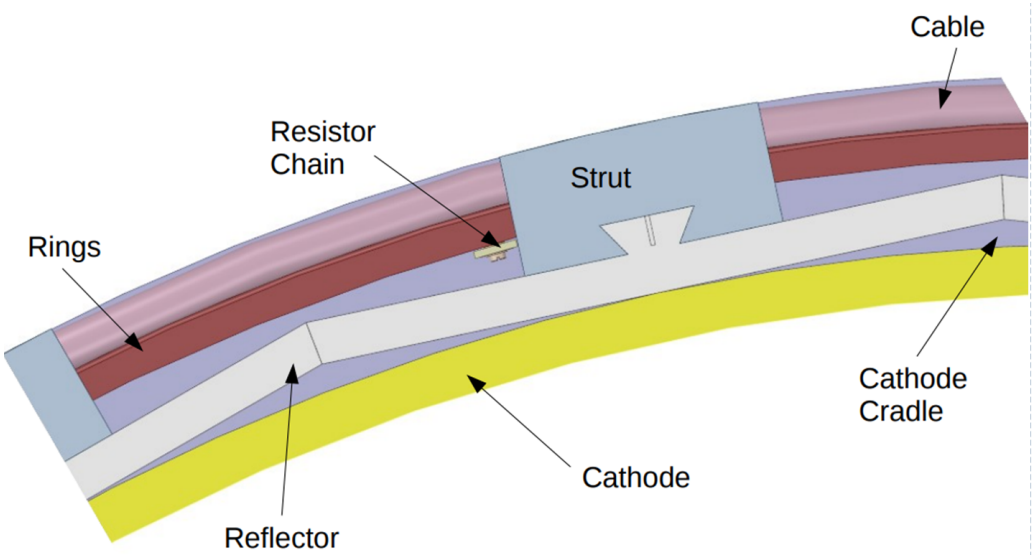


FIGURE 3.2: Section cut of NEXT-100 showing how the outer rim houses each component. Reflectors have easy insertion with dovetailing on the struts and minimize gas leakage with additional cutout in the dovetail.

the drift field where the electrons are moved in a well controlled electric field over to the third section. The third and final section is the electroluminescence plane which interfaces to the drift region but is mechanically attached to the endcap of the vessel rather than to the field cage which consists of the buffer and drift region.

An outer insulator made of teflon separates the field cage from the internal copper shielding within the vessel. The rest of the field cage can be assembled together and slid into place as one piece. Within the insulator are HDPE struts that run the full length of the field cage and provide structural support. Each strut has grooves which space copper rings uniformly and where the high voltage cable curves around the outside of the field cage the struts have additional ridges cut into the HDPE to minimize charge transport while providing room and a path for the cable to lay as it curves around to the cathode. For ease of machining the copper rings are built in three separate pieces and screwed together in house. To grade the potential along the drift field resistor chains are used and attached to the cathode and across the outside of the copper rings. The NEXT-100 field cage design is based on a prototype I initiated and I contributed to the full design alongside Argonne National Lab.

Attached to the struts with a dove tail connection are individual panels of TPB-coated PTFE reflectors. These reflectors create a light-tube that lines the active volume and enhances photon collection efficiency. To ensure maximum reflectivity[60] the panels are 0.5-cm thick . Where previous detectors had a solid light tube, these panels are done in sections to make coating with TPB easier and allow a similar design to be used for larger future detectors.

### 3.1.2 Frame Design and Assembly

Moving on from the field cage we are now talking about the electroluminescence region which is two steel meshes held on steel frames. I designed this and it was a major part of my PhD work. The frames will consist of three large parts; 1) the photo-etched mesh that is trapped on 2) the base frame and tensioned by 3) the tensioning ring. The mesh is held in the frame by

| | A (mBq/kg) |
|---|---|
| U-235 | < 1.3 |
| U-238/Pa-234m | < 120 |
| U-238/Pb-214 | < 1.6 |
| U-238/Bi-214 | < 1.4 |
| Th-232/Ac-228 | 3.9 ± 1.2 |
| Th-232/Pb-212 | 6.46 ± 0.83 |
| Th-232/Bi-212 | < 9.9 |
| Th-232/Tl-208 | 8.1 ± 1.0 |
| Th-232/Th-228 (combined) | 7.12 ± 0.64 |
| K-40 | < 4.9 |
| Cs-137 | < 0.44 |
| Co-60 | 13.8 ± 1.0 |
| Mn-54 | 1.84 ± 0.25 |

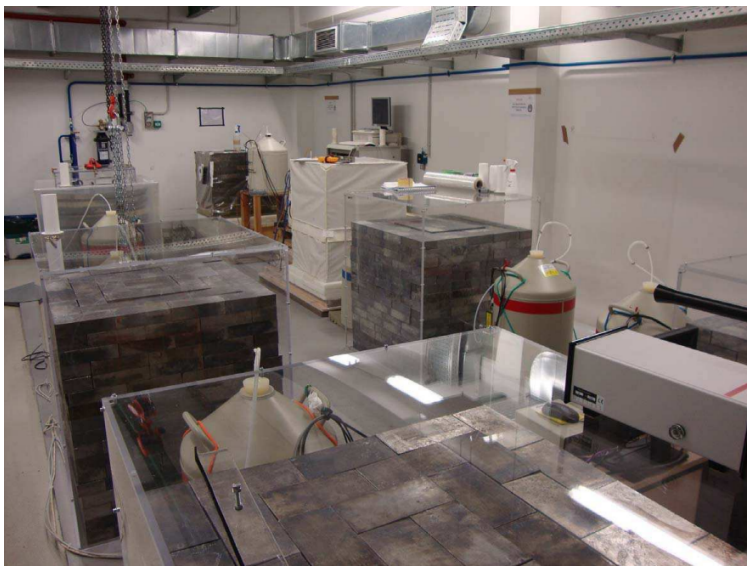

FIGURE 3.3: Left: Radioassay results from the original cathode we made whose manufacturers we are likely to go through again. Right: Laboratory at LSC with germanium detectors inside shielding[21] which performed the radiopurity screening shown left.

180×1/8" diameter, 1/4 inch length dowel pins that will hold the mesh in place, and tensioned by closing the two frame parts together. The frame will be made out of Stainless Steel 304, a change from the current cathode and gate frame in NEXT-White which uses Stainless Steel 316. SS304 is another material with the same range of radioactivity and the special type of SS304 called PRODEC is easier to machine, lowering production difficulty. Each EL frame will be 8.7 kg of steel with the rings, mesh, and hardware, and the cathode frame will be 8.5 kg. The original cathode prototype SS316 frame was radioassayed with a germanium spectrometer as described in [61] and shown in Fig. 3.3 right with results shown on left, and similar radioactivity budget is expected for these parts though investigation is ongoing to find a better supplier for clean stainless steel. The tracking plane is expected to have 35 mBq for both $^{208}$Tl and $^{214}$Bi [62]. Multiplying the corresponding radioassay results by 17.4 kg Fig. 3.3 gives 141mBq for $^{208}$Tl and 24 mBq for $^{214}$Bi. These numbers for radiopurity are marginal given our specifications and have been deemed acceptable by the collaboration while we continue to search for cleaner suppliers or use a different (and pricier) material for the NEXT-HD detector in the future.

| | Mtrl | Size | Qty |
|---|---|---|---|
| Pins | Brass | 1/8" dia x 1/4" len | 180 |
| Bolts | Silver Plated Stainless Steel | 6-32 x 1/2" len | 24 |
| Vented Bolts | Silver Plated Stainless Steel | 6-32 x 3/8" len | 72 |

TABLE 3.1: Hardware required for assembly. Longer bolts are used to start the tensioning of the mesh, but the shorter vented bolts are used for final closing.

The tension is applied to the mesh by closing the frame. The mesh starts by laying flat on the base frame as shown in Fig. 3.4 Left and held in position with pegs around the inside of the ring. Then the tensioning ring is placed on top and screwed down slowly using a 1/4 in length

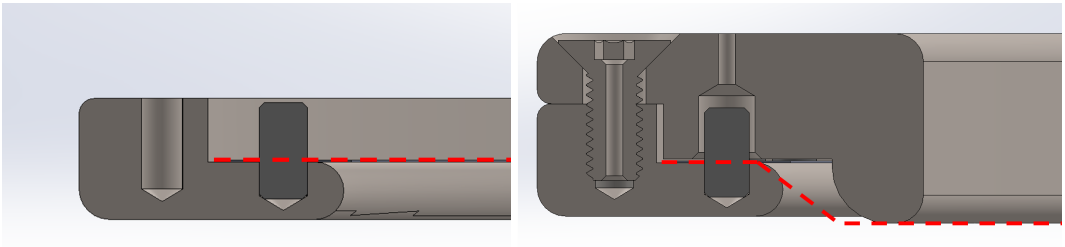

FIGURE 3.4: Visual of how the mesh will be assembled. Pegs fit securely into the base frame half and hold the mesh in place as the tensioning ring piece presses down and stretches the mesh.The mesh hole and the upper frame piece have oversized holes for the pins to go through for ease of assembly.

6-32 bolt. When those have bottomed out the vented bolts can be placed in the empty spots then replace the original bolts as well resulting in 72$\times$ 6-32$\times$3/8" bolts inset into the tensioning ring. This frame can apply a maximum of 2000Ñ of tension on the mesh (described in Sec. 3.2.3).

The pins will be brass and the bolts silver-plated stainless steel so as to prevent galling while avoiding standard lubricants which could compromise gas purity.

### 3.1.3 Photo-etched Mesh

Photo-etched meshes can be made with any two dimensional shape on almost any metal material (and some plastics) from 10 microns to 2 mm thick. The photo-etch process works by first laminating the material with a photo-resistive laminate then overlaying the laminate with the negative of what needs etched away. The laminate that is still exposed is hardened with UV light and the remaining laminate covering can be removed. The material is then washed with etching chemicals and everything that does not have the hardened ink gets etched away [63]. In almost all cases the ink will be put on both sides of the metal so that etching can be done from both directions to give a more uniform etch as the longer a material is in the etching fluid the more that will be removed and can end up with angles in the edges. To help reduce the sharp edges as much as possible we have opted to do a post-etch as well where after the ink is removed the part is rinsed in the etching fluid once more.

Using this photo-etched process hexagonal meshes become feasible and the tension of the mesh can be distributed around the frame along three axis, rather than just in x and y as normal wire meshes are done. This avoids "potato-chipping" instabilities that are commonly associated with a two-axis square mesh. We have investigated mesh designs with both 2.5 mm and 5 mm hexagonal holes. Small hexagons are advantageous in terms of field uniformity and mesh robustness so 2.5 mm meshes have been chosen for the EL region. However, larger holes are more preferable to maximize optical transparency and optimize light collection efficiency. 127 microns was the thinnest land that could be reliably etched into 75 micron stainless steel sheeting, and so we consider this as lower limit to the land width. Using simple geometry the direct transparency can be found with $\frac{(\text{Hex Radius})^2}{(\text{Hex Radius}+\text{LandWidth}/2)^2}$, resulting in 90 percent open area for 2.5 mm hexagons and 127 micron wire widths, and 95 percent open area for 5 mm hexagons and 127 micron wire widths. With two meshes back-to-back as the EL will be, this will make the transparency a minimum of 81%, which meets the 80% goal from the NEXT-100 specifications. Since our studies in Sec. 3.2.5 show that fringe fields become quickly vanishing within a few

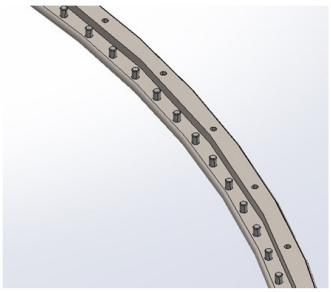

Step 1: Lay down base ring and insert dowel pins

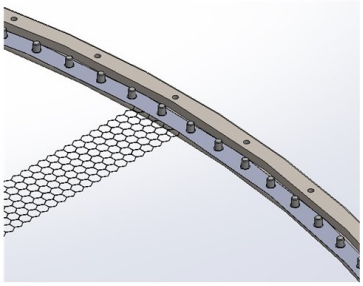

Step 2: Place Mesh over the dowel pins.

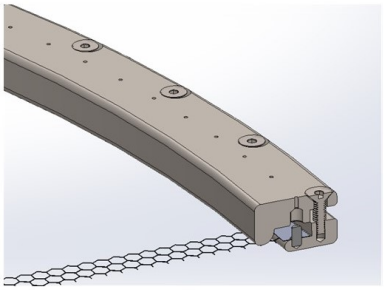

Step 3: Align the tension ring with the screw holes and insert the non-vented screws

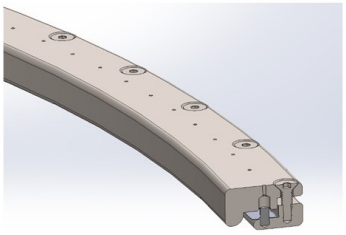

Step 4: Using a star pattern go around the ring tightening the bolts 1/4 turn at a time

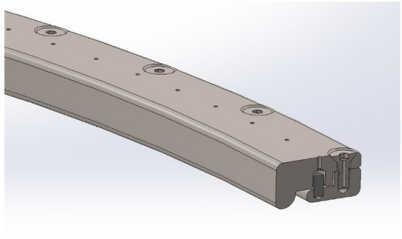

Step 5: Again in a star pattern go around the ring and replace the bolts one at a time with the vented bolts and tighten 1/4 turn at a time until fully closed

FIGURE 3.5: Steps for assembling the cathode and EL components. Only a small portion of the hexagons are modeled here due to computation limitations, however the real mesh will be fully filled in with.

centimeters of the cathode in all cases of interest, we have selected 5 mm hexagons and 127 micron wire width as the basis for further design for the cathode.

Photo-etching large enough for NEXT-100, and then an eventual NEXT-HD size mesh, is limited to only a small number of manufacturers. Before we had located a vendor with the appropriate capabilities we considered combining partial "pie slices" of meshes into a full circle and then tensioning it, as explained in Sec. 3.2.3. However, we found that the meshes were too thin for viably strong welding or soldering. Any additional frame components inside the readout area will certainly detract from the detector uniformity, light collection efficiency, and energy resolution, and thus we consider single full-sized photo-etched meshes as the only viable use case of the photo-etching technique for our application.

### 3.1.4 HV and Resistor Chain Interfaces

The cathode interfaces with the high voltage cable using a custom machined steel bracket. The high voltage cable wraps around the field cage and exits tangential to the cathode. There it will intersect with a bracket as shown in Fig. 3.6 which will take the HV cable into the center and hold the cable in place with a recessed set screw. This attachment will be made before inserting the field cage into the vessel, such that there is a robust mechanical and electrical connection between cable and cathode which will not be displaced during installation. The bracket will be held on the cathode with two additional inset set screws, again forming a robust mechanical and electrical connection.

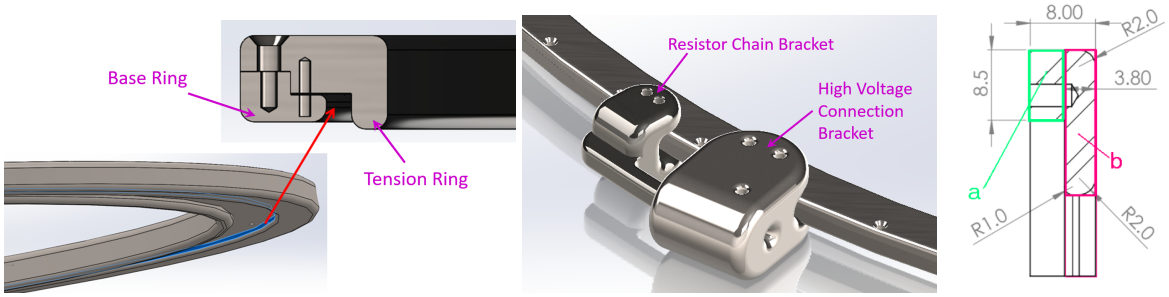


FIGURE 3.6: Left: Shape used for stress analysis within Solidworks. An inward pulling tension of 2000 N was placed around the ring on the face highlighted resulting in a maximum deformation of .91 mm. Middle: Shape used for moment of inertia calculations to check for buckling, resulting in a safety factor of 1.5. Right:Brackets for interfacing the cathode with high voltage cable (rightmost bracket) and resistor chain (leftmost bracket).

The resistor chain will interface with the field cage and cathode with a second bracket that has an offset bar with the same curvature and height as the copper rings in the field cage so it can connect with the same methods chosen for the other resistors. To minimize the potential for sparking, the end of the resistor chain bracket that juts out will be placed against the high voltage bracket. All edges are rounded to a radius of at least 3 mm.

For both cathode and HV cable interfaces we have opted to make connections using standalone brackets rather than machining these geometrical shapes into the cathode itself. This is because we recognize these regions to be high-field-stress areas, and thus potential failure points. The possibility of intervention in this area remains, if behaviour inside the detector is not as expected based on prototype tests and simulations (due to, for example, insulator charge-up effects, space charge, etc). Replacement with a differently designed bracket in response to any issues observed would be a straightforward operation, whereas replacing a full cathode would require a much more substantial field cage disassembly and rebuild. Maintaining flexibility in this critical region appears to be a prudent design choice.

### 3.1.5 Structural Interfacing

The cathode is held in place by the teflon staves from the field cage structure that are assembled around it as shown in Fig. 3.8 Left. However the EL frames will be held by 8 brackets made of HDPE with 6-32 HDPE bolts going through to connect in the countersunk side of the EL frames as shown in Fig. 3.7. These bracket positions have been chosen to avoid the SIPM boards used in the tracking plane. The ridges in the bracket are to help prevent sparking over the surface of the bracket as charges would have to travel over a longer distance this way. Additional sets of brackets will need to be made for differing spacings of the EL region to ensure uniform gaps around the entire circumference. To assemble the rings with NEXT-100, the rings will need to be connected to the bracket and then those be attached to the bulkhead of the vessel using 6-32 stainless steel 316 bolts.To ensure brackets align with the holes drilled in the copper the brackets will be slotted rather than just through holes to allow for some adjustments.

To assemble the EL region with the vessel, each ring plus mesh will be assembled as described in Sec 3.1.2. Then the top side (with reference to Fig. 3.7 right) of 4 brackets will be carefully secured within one semicircle of the first mesh using 6-32 HDPE bolts, making sure the mesh is

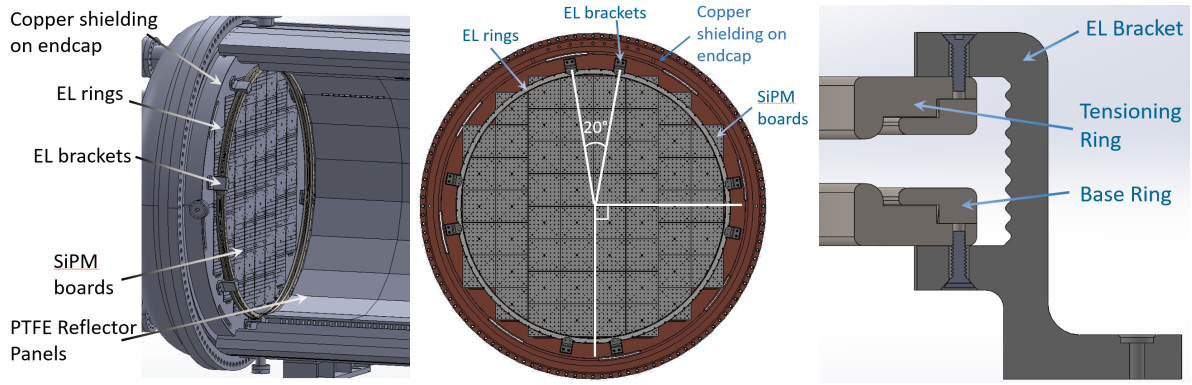


FIGURE 3.7: Left: EL rings attached to the copper shield on the endcap and closed into the field cage. Middle: Bracket spacing for NEXT-100 to avoid SIPM boards. Right: Section view showing how EL region is spaced.

facing inwards. Those brackets plus the mesh will then be placed upside-down and horizontal on a flat platform. Several spacers can be put around the edges of that ring to hold the second ring flat and stable once inserted with the mesh facing towards the other mesh. Once both rings are inside the brackets, the rest of the brackets will be put in position and secured to the second ring with HDPE bolts. Once those are done the assembly is flipped back over to bolt the last 4 brackets to the first ring. The assembly will then need to be turned vertical and bolted into the copper of the tracking plane.

### 3.1.6 Cleaning Procedure

Before assembling cleaning of the vented screws, dowel pins, mesh, and rings will be done with a soap cleaning solution bath using 1 ml Alconox Detergent soap per liter of deionized water in an ultrasonic bath for 30 minutes, followed by two ultrasonic baths for 30 minutes each in deionized water. The table it is assembled on will be cleaned using the same soap cleaning solution with lint free wipes by hand, followed by liberal rinsing with deionized water. This will be done inside a Class-10,000 clean room or better, preferably the same one it will be assembled in, but if not then during transfer all components need to be in clean anti-static plastic containers and wrapped in food grade shrink wrap. Standard clean room procedures, i.e. hair and beard nets, shoe covers, lab coats, and gloves will be followed by personnel at all times when handling the components once cleaning has begun.

### 3.1.7 Prevention of Virtual Leaks

With the assembly having so many individual components, virtual leaks become a serious concern. To prevent air from getting trapped and slowly leaking into the vessel continuously we added multiple holes for the air to vent from. Each tightening bolt will be vented and each of the one hundred and eighty dowel pins has a small hole drilled through the frame directly to it. Fig. 3.8 right shows how as long as the mesh is less than 10 mil thick there will be a gap between the rings and the mesh, preventing any gas from getting trapped. Thus so everywhere there is a gap there is also direct access to the outside environment. We also chose all materials carefully, optimizing for vacuum compatibility and a prototype system was made which evacuated to $10^{-}7$ Torr.

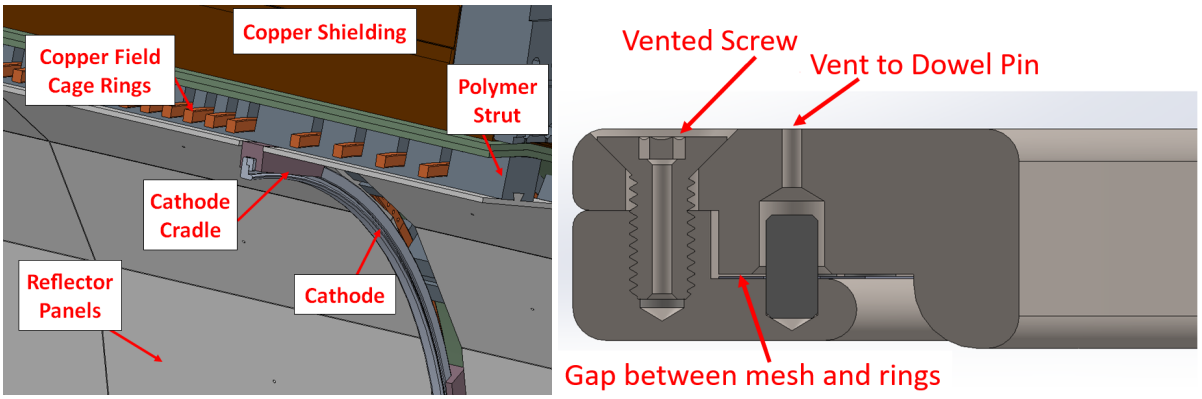


FIGURE 3.8: Left: Cathode held in the field cage. Right: Venting locations for connecting pieces within the frame to prevent trapped gases.

## 3.2 Quantitative Analyses

### 3.2.1 Stress and Deformation Analysis

A stress analysis was performed within the modeling program Solidworks which resulted in 0.91 mm deflection of the frame under 2000 N of tension with the geometry shown in Fig. 3.6 Left. This is within specifications for frame deformation, given the maximum applicable tension. To ensure the frame would not suddenly buckle while tensioning the mesh we also went through theoretical buckling calculations. Until the rings are fully tightened the base ring carries all the mesh tension. To compute the section area moment of inertia we treated the rings as two individual rectangular areas as shown in 3.6 Middle. Using these shapes and formulas from [64] to calculate the composite moment of inertia about the neutral axis and then compare with calculations for the base ring only, we were able to find the that the ring will not buckle with the meshes chosen for a safety factor of 1.5.

### 3.2.2 Mesh Deformation Under Electric Fields

In the EL region, the need to maintain flatness under strong applied E fields is a design driver. Thus we have designed around the requirement of flatness under the fields in the EL region, for this frame geometry. With no supports, if a mesh is tensioned with 2000 N then applying an Electric field of 28 kV/cm would result in 1.26 mm of maximum deflection as shown in Fig. 3.9 left. Given two meshes then the amount of non-uniformity would be twice this number, in the center. We consider this to be beyond the limit of our specifications for mesh deflection in the EL region. To combat deflection in the EL region we will use radius-edged support posts made of HDPE. More information for the studies of the supports and their materials can be found in Chapter 4.

The support posts will create places where an event track going over it will have some blind spots. To check first order how many events will be lost, monte carlo $0\nu\beta\beta$ tracks generated in the NEXUS Geant-4 code, and straight line tracks (for illustration only) were simulated occurring randomly throughout the detector volume at 15 bar with 7 posts equally spread out between the EL rings. If any part of the track crossed one or more of the post's effective area it is counted as a lost event. Effective area in this case is not just the diameter of the support post, but also any distortion of light collection around it. The results are shown in Fig. 3.9 right. We expect that the

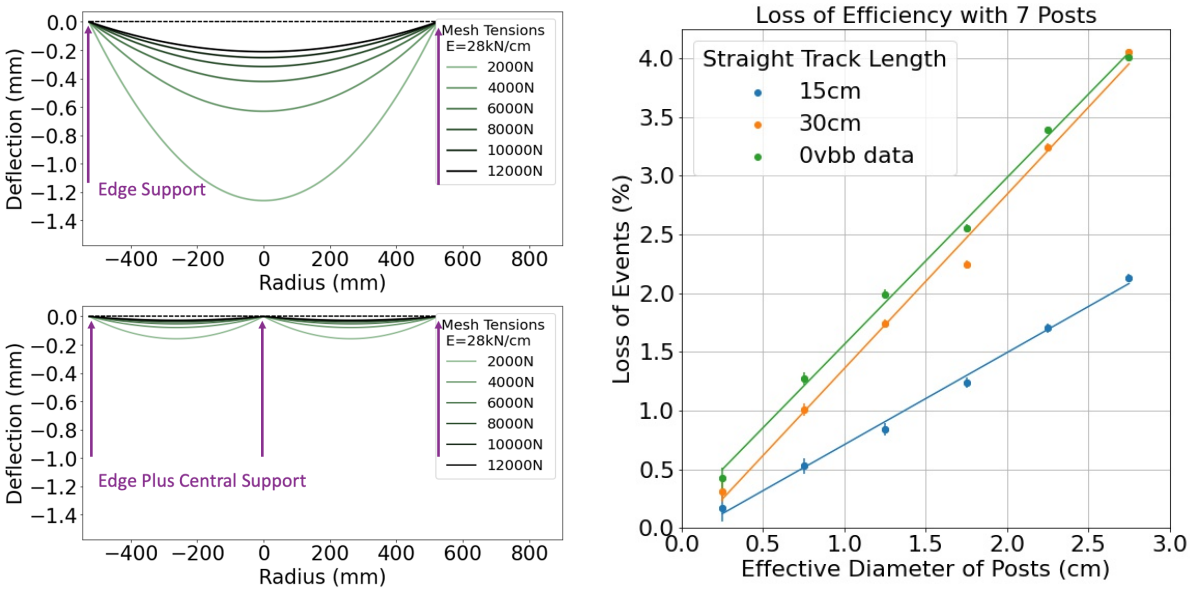


FIGURE 3.9: Left: Deflection of mesh under EL forces with varying tensions. Support post drastically decreases amount of tension needed. Calculations for these plots can be found in Appendix A. We are designing the gate to have 2000 N on it with 1 support in the middle. In reality we expect to use 7 supports and not tension fully so as to have additional safety factor. Right: Loss of double beta decay events if all events crossing a support post are discarded.

effective diameter will be at the lower end of this plot with no more than 1.5% of event lost which we deem acceptable. Most likely calibration will help recover much of the lost information.

At the cathode, fields are much smaller and very little deflection is expected. Since the cathode diameter is smaller than the EL and will need a different frame manufactured, it is designed for 1 kN tension instead of 2 kN to reduce the amount of material used within the detector.

### 3.2.3 Yield Tests

We tested the breaking yield for small scale meshes, as well as half-meshes joined with various bonding techniques that were considered in earlier designs. Spot welding showed some promise for connecting opposing hexagon faces, but because the weld was localized, tension was not distributed across the mesh area and failure was observed at rather low tensions. Soldering was more robust, with silver-based solders appearing the strongest. While solder-joined meshes could withstand a reasonable amount of tension at first, we observed creep over time due to the softness of the solder, followed by tearing within a few days.

To test the breaking yield we spread bonded or unbonded meshes over a 3 inch ring as shown in Fig. 3.10 left. Placing the tensioning ring on top of the mesh until the mesh was pressed lightly flat, the distance between the two rings, $L_0$ was measured. We then continued to close the 2 rings together until the mesh or bonded joint ripped and recorded the new distance, $\Delta L$ between the rings at the moment before ripping. Using the Youngs modulus of steel, $Y$, and Eq 3.1 where $A$ is the cross sectional area of one of the hexagon wires, we were able to estimate the breaking tension per wire. This is shown in Fig. 3.11 Left.

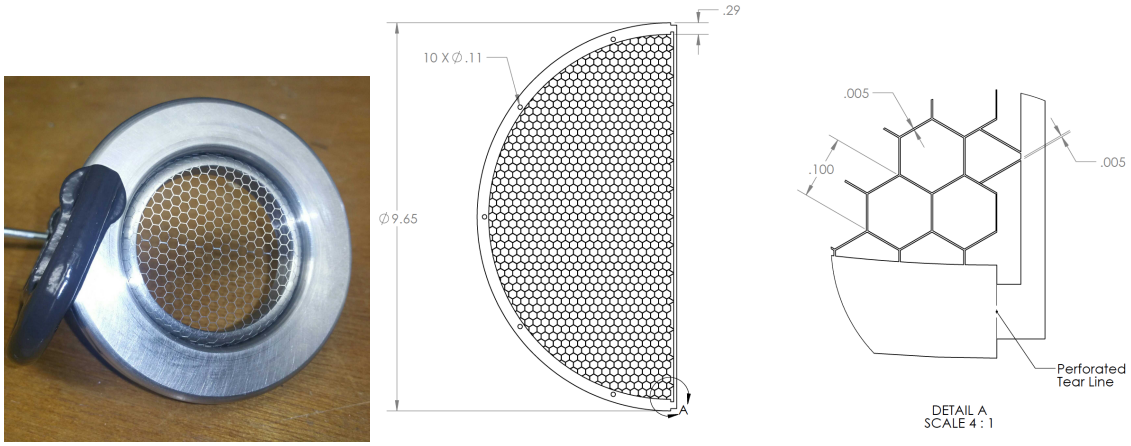


FIGURE 3.10: Left: Setup for stretching and measuring the change in length of the mesh. Right: Drawing for one of the halves for a DEMO++ prototype of the 5 mm hexagon meshes where the tear line and attached links were removed before soldering.

Then using Eq. 3.1 we convert Fig. 3.11, Left into the tension over the entire mesh by determining $N$, the number of wires equivalent from the hexagons, resulting in Fig. 3.11, Right. Both plots are important since considerations of frame deformation depend on total distributed tension, whereas considerations about tearing strength are more strongly dependent on per-wire tension.

$$\begin{aligned}
\text{Single Wire Tension} &= \frac{\Delta L}{L_0} YA \\
\text{Mesh Tension} &= \frac{3}{2}\frac{\Delta L}{L_0} YAN \\
\text{Internal Stress} &= \frac{3}{2}\frac{\Delta L}{L_0} Y \\
N &= \frac{L_0}{\text{Hex Diameter} + \text{Land Width}} \\
Y &= \text{Young's Modulus (200 GPa for Stainless Steel 316)} \\
A &= \text{area of "wire"} = \text{Land Width} \times \text{ Mesh Thickness}
\end{aligned} \tag{3.1}$$

For the mesh tension, 3/2 comes from the fact the hexagons act as individual wires in 3 different directions, and the hexagons are only every other one so essentially half the total length of wire in each direction. $\Delta L$ is the distance of the mesh stretch, calculated by the original gap between the rings if the mesh is completely flat (16.75 mm) minus the distance measured before the mesh/join broke, $L_0$ is the original diameter of the mesh, and $N$ is the number of wires in one direction across the mesh.

Using the same set of equations, we show in Fig. 3.11 Left, how much tension is put on each wire for different diameter meshes with respect to the amount of stretch along the mesh. The grey dotted line indicates the point of breaking, showing that significantly more stretch is required before the mesh snaps for a larger diameter, 60 mm for the NEXT-100 size with 2.5 mm hexagons. Then extrapolating to mesh tension, we see that for 2.5 mm hexagons the mesh would be able to withstand 800 kN, significantly more than a reasonable sized frame would be able to

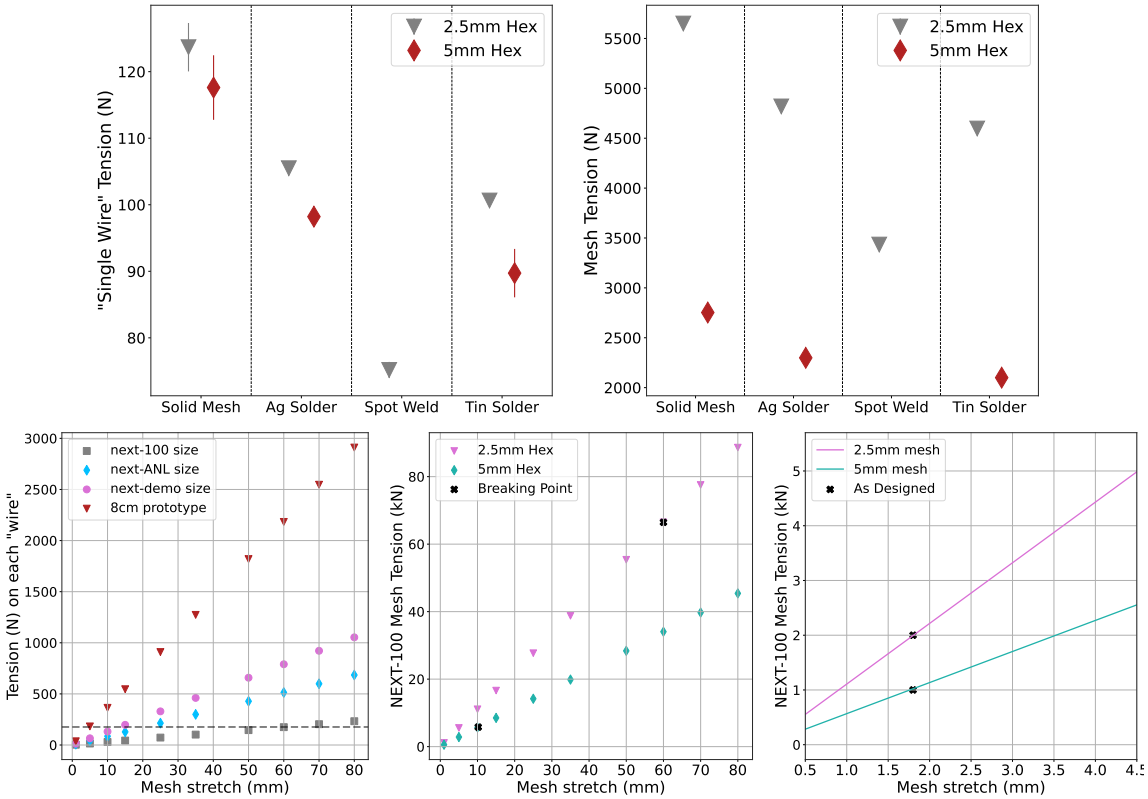


FIGURE 3.11: Upper Left: Amount of tension different connecting methods were at at the time of ripping as seen per each "wire". Upper Right: Tension on the mesh at the time of ripping. Lower Left: Tension on each "wire" as the mesh is stretched over rings of different diameters. The dashed line shows the breaking point for a solid mesh. Lower Middle: Mesh tension for NEXT-100 as it is stretched for the different hexagon diameters. The vertical dashed lines show the breaking point for 5 mm (left) and 2.5 mm (right). Lower Right: Next-100 mesh tension with the dashed line showing the design specs for the mesh with the frame design as shown in Fig. D.1.

withstand without buckling. To get 2000 N of tension across a 2.5 mm mesh of 1.05 m diameter requires 1.8 mm of stretching, or a frame that stretches .9 mm per side/section view. For the cathode to get 1000 N of tension across a 5 mm mesh of 1.02 m requires about the same amount of stretch at 1.76 mm so both frames have the same cross sectional dimensions.

To determine how many pins would be used around the mesh edge to hold it in place we had to determine the stress on each pin hole. Since the tension would be only on one half of the mesh hole, the area that the force is transmitted to is one half the circumference of the hole times the width of the mesh. The amount of tension transmitted to each hole is the tension over the entire mesh divided by the number of pins being used. Dividing the tension on each pin hole by the area the pin sits on results in Fig. 3.12 left. As long as the purple curve is beneath the yield strength line the holes will not start deforming or ripping. To account for the pins not sitting on exactly half of the hole we require a safety factor which is calculated by dividing the yield strength by the calculated stress on the pin hole. We chose to go with 180 pin holes for the NEXT-100 rings which was validated in the prototypes and results in a safety factor of 7.2.

In Fig. 3.12 right there is a minor amount of local damage around the pins. The damage

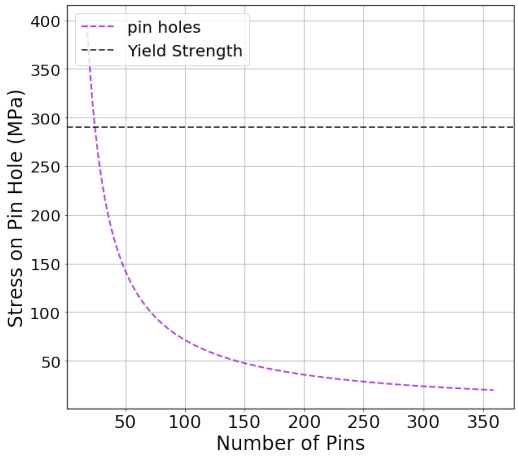


FIGURE 3.12: Left: Stress per pin hole versus number of pins when mesh is tensioned to 2 kN. Right: Picture of the ANL sized mesh after being tensioned to 2.76 kN then disassembled.

seems to be all around the circumference which is probably a result of the mesh rubbing up and down on the pin as it is being tightened. There is also some buckling around the the perimeter of the mesh, some upwards and some down which is a result of natural stress relief occurring. This did not compromise mesh quality or robustness in prototypes and is considered acceptable for the final design.

### 3.2.4 Robustness under Electrical Discharge

To see how the photoetched mesh would stand up to electrical discharges within the detector we set up a test of putting a tensioned mesh at voltage with a capacitor as shown in Fig. 3.13 and moved a metal wire held at ground towards the mesh until it discharged. A loud, bright, spark was observed. We repeated this test at both positive and negative polarities at voltages up to 20 kV, and capacitances of 1, 5, and 10 nF.

The capacitor was chosen to simulate the conditions of the electroluminescence region being a parallel plate capacitor. To calculate the capacitance of the EL region we used equation 3.2 where $\epsilon_r$ is the dielectric constant of Xenon gas, $\sim 1$, $A$ is the area of the mesh, and $L$ is the gap between the gate and anode. Assuming 1 cm between the EL plates, and 1m diameter, the capacitance of the EL region would be 1.4 nF, with 0.52 Joule of energy at the 28 kV design voltage. Notably, NEXT-White successfully operates the EL region substantially below this voltage [34], with an implied stored energy in NEXT-100 of 0.25 Joules at 20 kV.

$$\begin{aligned} C &= \epsilon_0 \epsilon_r \frac{A}{L} \\ E &= \frac{1}{2} C V^2 \end{aligned} \tag{3.2}$$

No substantial damage was found at any energy. At the highest energy discharged (2 Joules), we discharged around 10 sparks. A few barely visible marks were observed on the mesh - identified as regions of extra shine where some surface metal had ablated, as shown in Fig 3.13 though no structural damage was found. The highest energy tested was around four times the default NEXT-100 design energy for the EL gap and around eight times the energy stored if runs

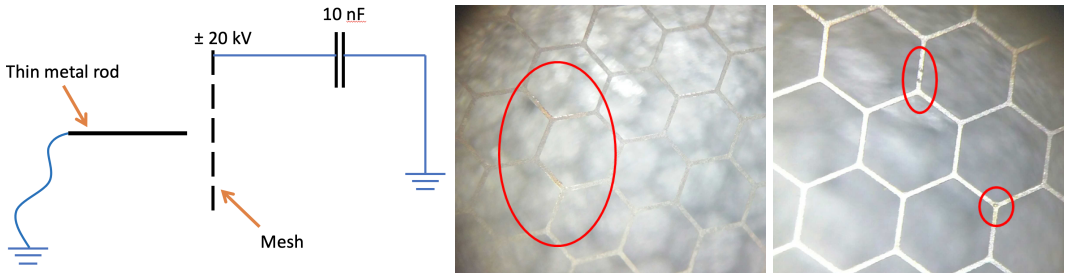


FIGURE 3.13: Left: Test set up for high energy sparks to photoetched mesh. Middle: With 10 nF and $-20kV$ some shiny areas could be seen but no breaks or pockmarks. Right: With 10 nF and $+20kV$ very small pockmarks were visible under the microscope but no breaks or holes through the mesh were found.

in NEXT-White-like EL conditions. The photo-etched meshes thus appear highly robust against possible discharge conditions unlike thin single wires or ITO coated quartz design which have been observed to experience breakage or pock-marks under similar conditions.

### 3.2.5 Fringe Field Simulations

The issue of fringe fields penetrating the cathode from the buffer was raised and has been investigated with COMSOL simulations. Because the buffer field is strong relative to the drift field and the cathode is not a solid plane, lines of electric field are expected to penetrate some distance into the fiducial volume. Some charges inside the drift volume near the cathode, therefore, will travel back to the buffer region and not forward to the EL plane. For any given geometry and ratio of buffer region electric field to drift region electric field, there is some maximal distance into the drift volume from where all charge will travel to the anode rather than the cathode - the maximal penetration distance of the buffer-originating field lines. This distance was established for various combinations of wire thickness and pitch by finding the maximal distance into the drift direction where the electric field switched direction (ie tended to carry charge back toward the buffer region rather than forward to the anode), scanned across the cathode plane. The results show that for all reasonable hex pitches and wire widths, fringe fields that could remove charge from the active volume penetrate at most a few mm into the drift region. A sample field map can be seen in Fig. 3.14 top where the field originates in the center on the wire, reaches into the drift region, then bends back to touch the adjacent wires. The results of a systematic scan of mesh parameters are shown in Fig. 3.14 bottom.

## 3.3 Electrostatic Simulations

Electrostatic simulations with the COMSOL package established the maximal electric field near the wires. Our design criterion is to maximize transparency while 1) avoiding the onset of dielectric breakdown near the wires, which occurs around 60 kV/cm in pure xenon; and 2) maintaining a uniform electric field for as much of the fiducial volume as possible.

For this purpose, wire planes with various pitches and wire thickness were simulated using a meshed finite element analysis, and the maximal field in each geometry was calculated. The field configuration is assumed to be 2 kV/cm in the buffer region, and 400 V/cm in the TPC region. Fig 3.15, left shows these max field strengths. Even with very thin wires of 0.2 mm diameter we remain below the onset of breakdown near the wires. For the thinnest wires we do see fields

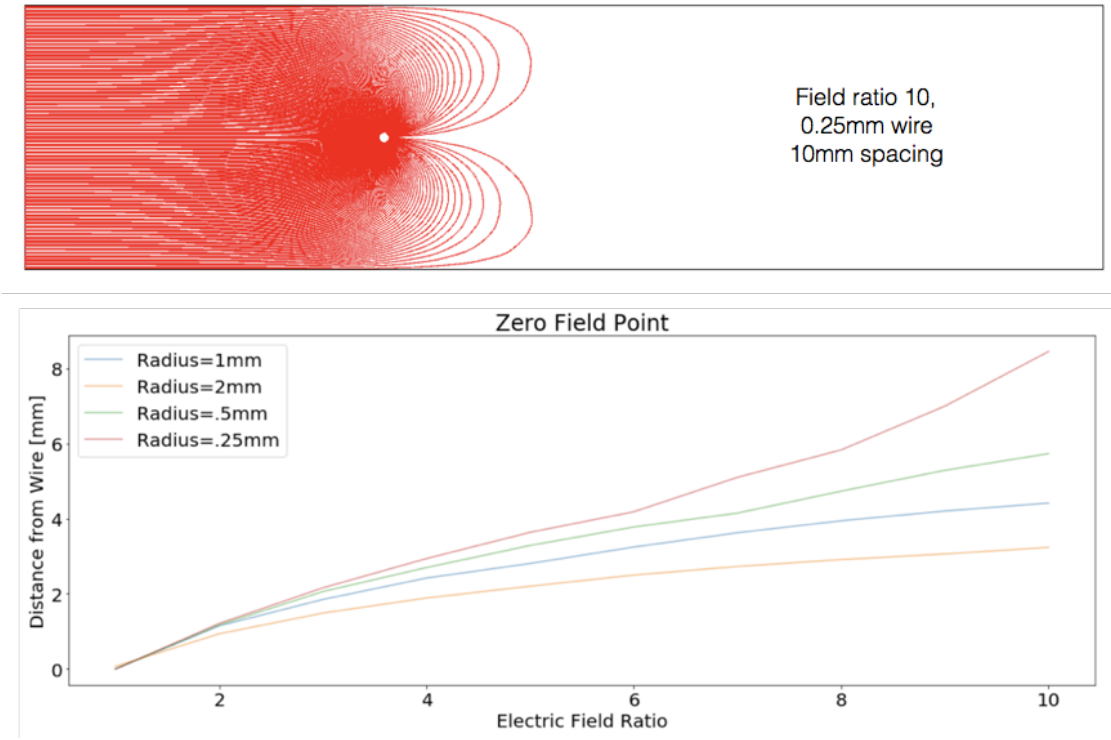


FIGURE 3.14: Top: Sample fringe field calculation showing field lines from the buffer penetrating partially into the active volume. Bottom: systematic study showing maximal penetration distance for various geometries. The maximal distance for charge to return to the buffer rather than the anode is only a few mm, in all cases.

above the EL threshold near the wire, and so electrons in this region may electroluminesce. However, electrons are repelled from the cathode, and therefore only particles emitted near the wire will exhibit the behaviour. The only significant source of electroluminescence near the cathode, then, are from radioactive decays of elements plated on the cathode itself, for example, from radon progeny that drifted there after an in-volume decay. The bright electroluminescence light that immediately accompanies S1 may indeed serve as a useful background rejection tool for these events. We do not anticipate problems from some degree of EL around the cathode wires from rare cathode-born events, so long as we remain far below the threshold for spark formation.

To maximize optical transparency, the wires would be as distantly separated as possible, or in the case of hexagons as large of a hexagon opening as possible. The opposing constraint is that they must still maintain a uniform field in the most of the fiducial volume, though of course, some non-uniformity near the wires is unavoidable. Fig 3.15, right shows the distance into the fiducial volume where the electric field has returned to within 10% of its nominal value for the various geometries. We see that for 1 cm spacing of 0.2 mm wires, uniformity is restored within 3.5 mm from the cathode plane, which is a sufficiently short distance for our purposes.

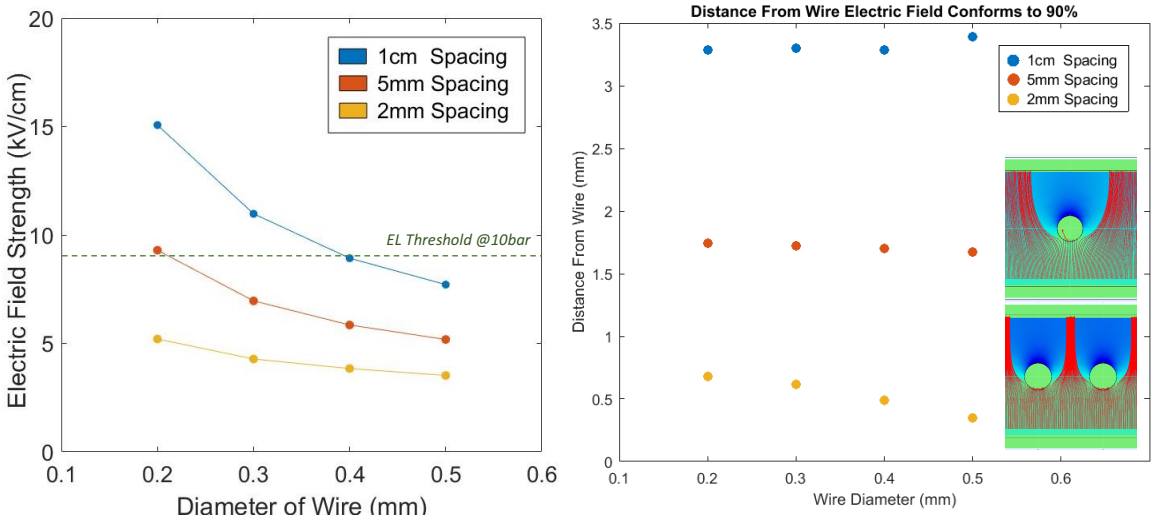


FIGURE 3.15: Wire field simulations from the COMSOL package. Left: Maximal field near the wire for various thicknesses and diameters; Right: distance from wire where field conforms to uniformity within 90%. Insets show simulated field lines for two example configurations.

## 3.4 Mini-CRAB Prototype

NEXT-CRAB (camera readout with barium tagging) is a prototype series that works towards implementing a fast optical camera for topological reconstruction rather than SiPMs as well as finding a way to tag barium ions within the vessel. One of the prototypes built at UTA included an EL region with meshes like what will be used in NEXT-100. One of the differences in the set up of this type of detector is that the cathode must be at ground and a camera read out directly behind it for the barium ions to be swept over to the window and be sensed once in contact with a fluorescing chemical (more details about barium tagging efforts and the CRAB line of detectors can be found in Chapter 2. This results in a buffer region behind the EL so that it can be at positive voltage rather than negative. Once the components shown in Fig. 3.16 are inserted into the vessel an image intensifier is used outside the vessel against the window to amplify the signal so that a CCD camera can be used to capture images. On the end behind the buffer region is a PMT which is used for energy read out.

The EL response of the mini meshes used within the mini-CRAB was demonstrated briefly by bringing a gamma source towards the vessel and observing the response. There was increased activity on the camera as well as increased light collected by the PMT. Proper function of CRAB at applied reduced electroluminescence fields validated the photo-etched mesh design for NEXT-100.

## 3.5 Large Scale Electroluminescence Test Vessel

At UTA we have a specially designed high pressure test facility built for testing components on the scale of NEXT-100 and NEXT-HD diameters. Specific dimensions and machine drawings can be found in Appendix B. This vessel can hold a cubic meter of gas up to 15 bar and will be used to quantify the energy resolution and gain of the electroluminescence in argon gas. There

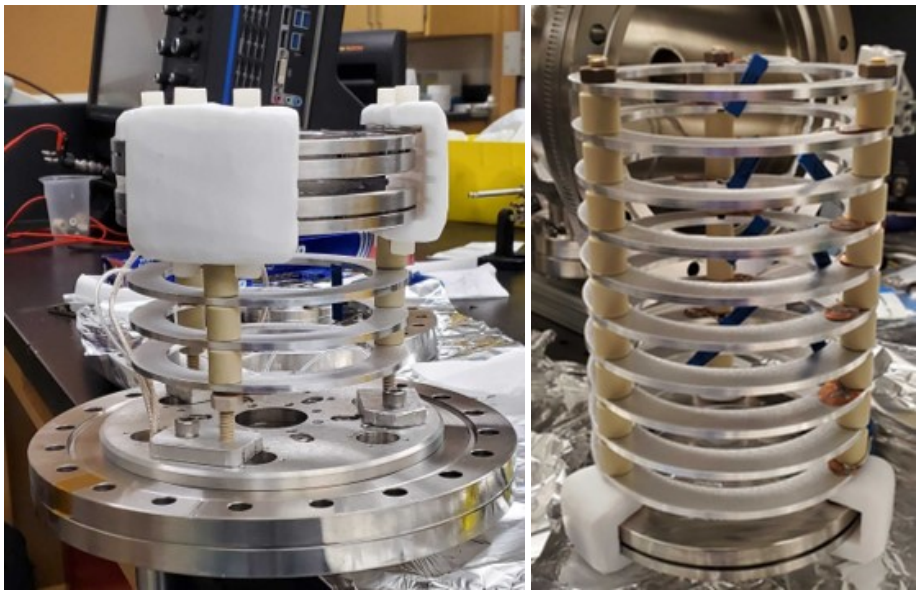

FIGURE 3.16: Mini-CRAB assembly that resides at UTA and has been used to test the NEXT-100 style EL meshes. Left is the buffer region plus two meshes for the EL planes. Right is the field cage for the drift region.

are 6 view-ports around the outside with cameras attached to be able to watch for and diagnose sparking in order to test the electro-mechanical stability of large electroluminescence regions

Included on the top of the vessel is one 4-1/2 inch CV feed through for putting a PMT or additional camera. The vessel was designed with three 8 inch feedthroughs, one radially and the other two on the bottom of the vessel so that high voltage connections could be tested with whichever connections are used in the real detectors. Centered on both halves of the vessel are CF 12 inch flanges that can be adapted to whichever size adaptors are needed. There are 6 CF 2-3/4 inch plus 1 CF 4-1/2" feedthroughs on the 12 inch adaptor plate which allows a plethora of instruments to be inserted and swapped out simultaneously.

To measure the energy resolution across the entire EL region a robot was designed and built

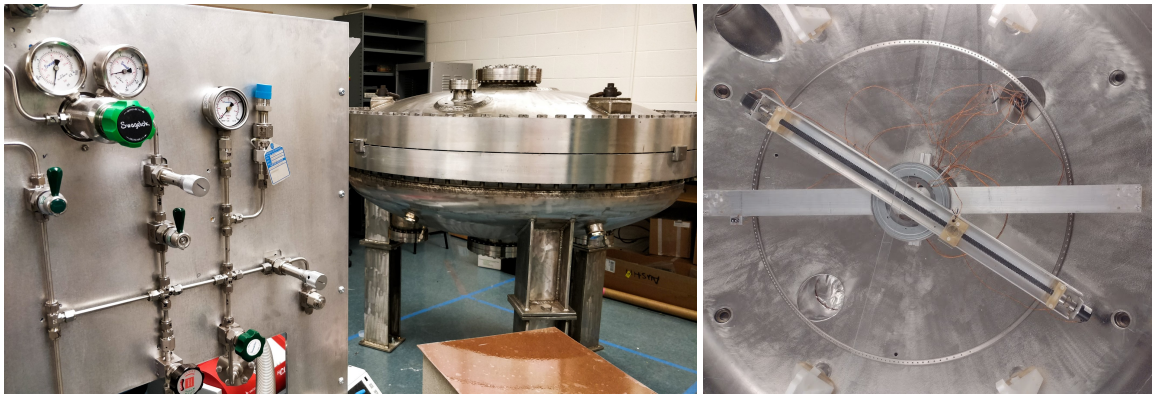

FIGURE 3.17: Left: Gas re-circulation panel and large scale testing vessel at the University of Texas at Arlington. Right: bottom half of the robot that can move a radiation source or light detector to different radii and angles.

that sits on the bottom of the vessel and can move a radiation source across all radii and angles. A mirror of this robot is attached to the lid of the vessel and can move a light sensor in parallel with the radiation source.

As explained earlier in Sec. 2.1.2 electroluminescence cannot occur with impurities in the gas so attached to the vessel is a gas re-circulation panel which uses a diaphragm pump to circulate the gas through both a hot getter and a cold getter to remove impurities like oxygen and water that can be released over time from outgassing.

Tests in this system, which I designed and built, are now underway with the NEXT-100 EL design and will be completed in the months following my graduation.

# Chapter 4

# High Voltage Insulation and Gas Absorption of Polymers in High Pressure Argon and Xenon Gases

When exploring design of the electroluminescent region for NEXT-100 as described in Chapter 3, the need for a discrete support post became apparent. This post would need to impact the transparency as little as possible in order to maximize energy resolution as topological reconstruction as well as need to be able to withstand a high electric field without experiencing breakdowns.

While investigating various materials that could potentially be used for the posts we took the opportunity to characterize the materials more fully to better understand how they would react within the detector. This included seeing how the materials changed density or size after prolonged exposure to noble gases commonly used within particle detectors.

Gas being absorbed into the plastics has several repercussions. Re-evacuating a detector after the components have become saturated with xenon gas can give a sense of a leak in the vessel as the xenon will keep outgassing for a long period of time. This also results in a loss of xenon with standard recapturing methods as the xenon in the plastics will not be recovered and will be lost during the subsequent evacuation process. The other thing the absorption showed is that the dimensions of certain plastic components will enlarge and may need to be taken into consideration during designs so that nothing ends up pressing into each other and resulting in buckling.

The following paper was published in the Journal of Instrumentation as [26] describing the absorption of argon and xenon in various plastics and how these plastics hold up to high electric fields. Based off the results found, the support posts used in NEXT-100 will be made from high density polyethylene.

Jinst

Published by IOP Publishing for Sissa Medialab

Received: *July 10, 2018*
Accepted: *September 19, 2018*
Published: *October 1, 2018*

# High voltage insulation and gas absorption of polymers in high pressure argon and xenon gases

2018 JINST 13 P10002

## The NEXT collaboration

**L. Rogers,**[c,1] **R.A. Clark,**[c] **B.J.P. Jones,**[c] **A.D. McDonald,**[c] **D.R. Nygren,**[c,2] **F. Psihas,**[c] **C. Adams,**[j] **V. Álvarez,**[q] **L. Arazi,**[f] **C.D.R Azevedo,**[d] **K. Bailey,**[b] **F. Ballester,**[s] **J.M. Benlloch-Rodríguez,**[q] **F.I.G.M. Borges,**[l] **A. Botas,**[q] **S. Cárcel,**[q] **J.V. Carrión,**[q] **S. Cebrián,**[t] **C.A.N. Conde,**[l] **J. Díaz,**[q] **M. Diesburg,**[e] **J. Escada,**[l] **R. Esteve,**[s] **R. Felkai,**[q] **A.F.M. Fernandes,**[k] **L.M.P. Fernandes,**[k] **P. Ferrario,**[n,h,q] **A.L. Ferreira,**[d] **E.D.C. Freitas,**[k] **J. Generowicz,**[n] **A. Goldschmidt,**[g] **J.J. Gómez-Cadenas,**[n,h,q,3] **D. González-Díaz,**[r] **R. Guenette,**[j] **R.M. Gutiérrez,**[i] **K. Hafidi,**[b] **J. Hauptman,**[a] **C.A.O. Henriques,**[k] **A.I. Hernandez,**[i] **J.A. Hernando Morata,**[r] **V. Herrero,**[s] **S. Johnston,**[b] **M. Kekic,**[q] **L. Labarga,**[p] **A. Laing,**[q] **P. Lebrun,**[e] **N. López-March,**[q] **M. Losada,**[i] **R.D.P. Mano,**[k] **J. Martín-Albo,**[j] **A. Martínez,**[q] **G. Martínez-Lema,**[q,r] **F. Monrabal,**[c,n] **C.M.B. Monteiro,**[k] **F.J. Mora,**[s] **J. Muñoz Vidal,**[q] **M. Musti,**[q] **M. Nebot-Guinot,**[q] **P. Novella,**[q] **B. Palmeiro,**[q] **A. Para,**[e] **J. Pérez,**[q,4] **M. Querol,**[q] **J. Renner,**[q] **J. Repond,**[b] **S. Riordan,**[b] **L. Ripoll,**[o] **J. Rodríguez,**[q] **C. Romo-Luque,**[q] **F.P. Santos,**[l] **J.M.F. dos Santos,**[k] **A. Simón,**[q,f] **C. Sofka,**[m,5] **M. Sorel,**[q] **T. Stiegler,**[m] **J.F. Toledo,**[s] **J. Torrent,**[q] **J.F.C.A. Veloso,**[d] **R. Webb,**[m] **J.T. White,**[m,6] **N. Yahlali**[q]

[a] *Department of Physics and Astronomy, Iowa State University, 12 Physics Hall, Ames, IA 50011-3160, U.S.A.*

[b] *Argonne National Laboratory, Argonne, IL 60439, U.S.A.*

[c] *Department of Physics, University of Texas at Arlington, Arlington, TX 76019, U.S.A.*

[d] *Institute of Nanostructures, Nanomodelling and Nanofabrication (i3N), Universidade de Aveiro, Campus de Santiago, Aveiro, 3810-193, Portugal*

[e] *Fermi National Accelerator Laboratory, Batavia, IL 60510, U.S.A.*

[f] *Nuclear Engineering Unit, Faculty of Engineering Sciences, Ben-Gurion University of the Negev, P.O.B. 653, Beer-Sheva, 8410501, Israel*

[1] Corresponding author.
[2] NEXT Co-spokesperson.
[3] NEXT Co-spokesperson.
[4] Now at Laboratorio Subterráneo de Canfranc, Spain.
[5] Now at University of Texas at Austin, U.S.A.
[6] Deceased.



https://doi.org/10.1088/1748-0221/13/10/P10002

[g] *Lawrence Berkeley National Laboratory (LBNL), 1 Cyclotron Road, Berkeley, CA 94720, U.S.A.*
[h] *Ikerbasque, Basque Foundation for Science, Bilbao, E-48013, Spain*
[i] *Centro de Investigación en Ciencias Básicas y Aplicadas, Universidad Antonio Nariño, Sede Circunvalar, Carretera 3 Este No. 47 A-15, Bogotá, Colombia*
[j] *Department of Physics, Harvard University, Cambridge, MA 02138, U.S.A.*
[k] *LIBPhys, Physics Department, University of Coimbra, Rua Larga, Coimbra, 3004-516, Portugal*
[l] *LIP, Department of Physics, University of Coimbra, Coimbra, 3004-516, Portugal*
[m] *Department of Physics and Astronomy, Texas A&M University, College Station, TX 77843-4242, U.S.A.*
[n] *Donostia International Physics Center (DIPC), Paseo Manuel Lardizabal, 4, Donostia-San Sebastian, E-20018, Spain*
[o] *Escola Politècnica Superior, Universitat de Girona, Av. Montilivi, s/n, Girona, E-17071, Spain*
[p] *Departamento de Física Teórica, Universidad Autónoma de Madrid, Campus de Cantoblanco, Madrid, E-28049, Spain*
[q] *Instituto de Física Corpuscular (IFIC), CSIC & Universitat de València, Calle Catedrático José Beltrán, 2, Paterna, E-46980, Spain*
[r] *Instituto Gallego de Física de Altas Energías, Univ. de Santiago de Compostela, Campus sur, Rúa Xosé María Suárez Núñez, s/n, Santiago de Compostela, E-15782, Spain*
[s] *Instituto de Instrumentación para Imagen Molecular (I3M), Centro Mixto CSIC - Universitat Politècnica de València, Camino de Vera s/n, Valencia, E-46022, Spain*
[t] *Laboratorio de Física Nuclear y Astropartículas, Universidad de Zaragoza, Calle Pedro Cerbuna, 12, Zaragoza, E-50009, Spain*

*E-mail:* leslie.rogers@mavs.uta.edu

Abstract: High pressure gas time projection chambers (HPGTPCs) are made with a variety of materials, many of which still await proper characterization in high pressure noble gas environments. As HPGTPCs increase in size toward ton-scale detectors, assemblies become larger and more complex, creating a need for detailed understanding of how structural supports and high voltage insulators behave. This includes identification of materials with predictable mechanical properties and without surface charge accumulation that may lead to field deformation or sparking. This paper explores the mechanical and electrical effects of high pressure gas environments on insulating polymers PTFE, HDPE, PEEK, POM and UHMW in argon and xenon, including studying gas absorption, swelling and high voltage insulation strength.

Keywords: Gaseous detectors; Scintillators, scintillation and light emission processes (solid, gas and liquid scintillators)

ArXiv ePrint: 1804.04116

2018 JINST 13 P10002

## Contents



2018 JINST 13 P10002

## 1 High pressure gas time projection chambers

High pressure gas time projection chambers (HPGTPC) are powerful detectors used in searches for neutrinoless double beta decay [1–3] and neutrino oscillation measurements [4, 5]. Advantages of HPGTPCs include precise energy and spatial resolution that enables event topology discrimination. This combination of energy measurements and event topology allows for particle identification resulting in strong background rejections [6, 7]. HPGTPCs use a drift region with a typical electric field strength of 200–500 V/cm to induce electron transport to the anode plane. Electrons reach the anode after a finite drift time, with this time serving as a proxy for $z$ position. The 2D location of charge in the electroluminescent (EL) plane provides the $x$ and $y$ components. Taking these together provides a 3D reconstruction of the initial event. This is the basis for the time projection chamber concept [8].

Several technical variations of HPGTPCs exist. Due to its high price, xenon is generally only used when it has a very specific benefit, such as searching for lepton number violation. Xenon 136 is a candidate double beta decay isotope, because energy conservation allows for the double beta decay into Barium, while disallowing single beta decay into Cesium [9].

The NEXT program [10–14] is a sequence of high pressure xenon gas TPCs. The existing detector designs use an asymmetrical configuration as shown in figure 1, running at 10-15 bar. When ionization electrons reach the end of the drift region, they enter an EL region which has a high electric field that sufficiently accelerates charges to excite the noble gas atoms, but not ionize them. With appropriate tuning of this field strength, near-fluctationless gain can be achieved by collecting the copious photons that are produced as the excited atoms return to the ground

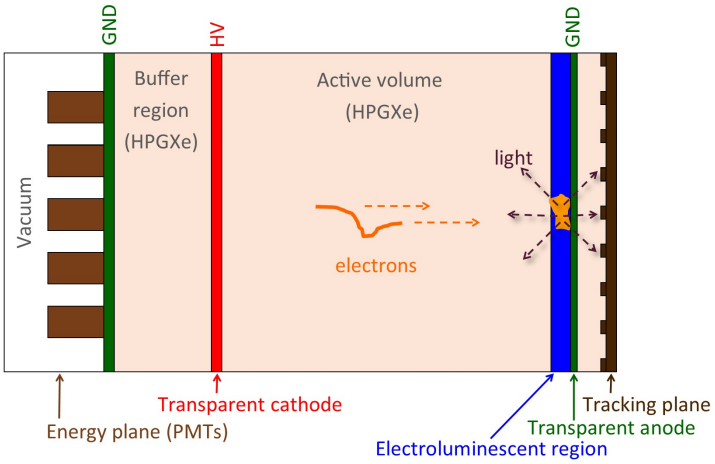


**Figure 1**. Schematic of an asymmetrical NEXT detector with PMTs on the left which collect light for an energy reading. A buffer region is used for stepping voltage up to the strength needed at the cathode and the drift region then steps voltage across to the EL region. Behind the EL region is an array of SiPMs to collect light for topological reconstruction.

state. Photomultiplier tubes (PMTs) and/or silicon photomultipliers (SiPMs) are used to collect the photons, following a wavelength shift by TPB [15] coating the outside walls of the active volume. The initial photons created from the scintillation (S1) are used as a trigger for the event, whereas the photons from the excitations in the EL region (S2) are collected for a precise energy reading and topological event characterization.

A particular challenge in scaling detectors of this type to ton-scale lies in creating EL regions which require a very high and well controlled reduced electric field on the order of 2–4 kv $cm^{-1}$ $bar^{-1}$ for argon and xenon [16]. This involves biasing large surfaces which must be transparent to 400 nm light, in order not to block the tracking or energy plane. The cathode side of the EL region also must be transparent to electrons, and so is commonly made with a thin wire mesh with high optical and electron transparency. At these large fields of around 30 kV/cm, the electrostatic force between the two electrodes may become sufficiently large as to cause significant deflection in a wire mesh at achievable tensions. Since an electric field is a function of voltage over distance between the two planes, deflection in the mesh causes the region to have a nonuniform field. Calculated deflections at 28 kV/cm for different mesh tensions in a NEXT-100 sized mesh are shown in figure 2, top.

To avoid such deflections, support materials may be introduced sporadically between the gate and anode figure 2, bottom. This material introduces non-conducting surfaces into the EL region, and there is a risk that this may encourage sparks between the electrodes. This must be avoided, since as mesh size grows, the stored electrostatic energy increases as the square of the radius. In the event of a spark, this energy is discharged through a single point, which for larger meshes may cause damage through localized heating. These sparks may be nucleated by the accumulation of charges on insulating surfaces. The ideal material is thus dielectrically strong but somewhat resistive, in order to maintain a uniform axial field in the EL gap and avoid charge-up effects. Such discharges may be quenched by other means, for example, by replacing the anode with a resistive material.



2018 JINST 13 P10002

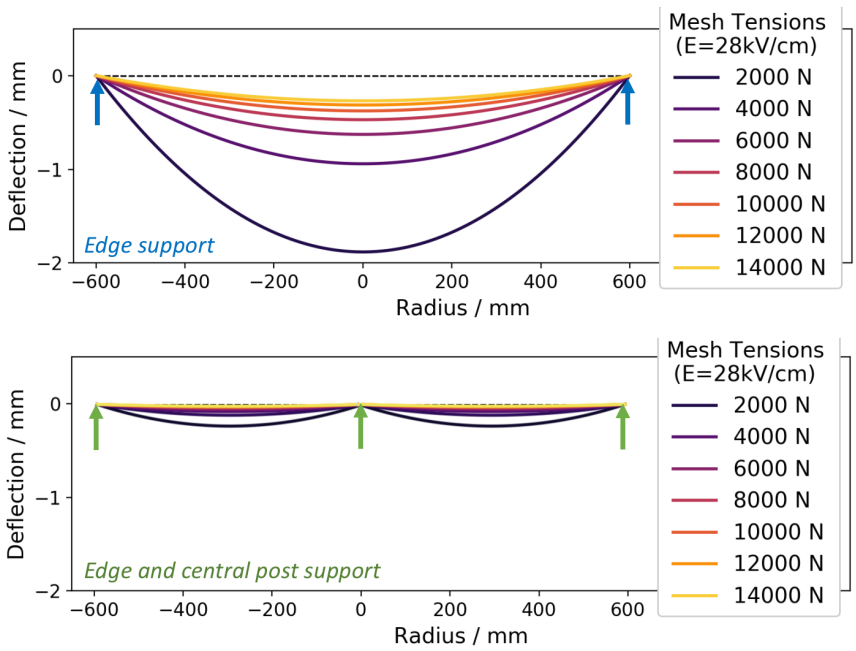


**Figure 2**. Simulated EL mesh deflection due to electrostatic forces with only edge support (top) or with edge support plus a single central support post (bottom). Dramatic deflection reductions are observed with only a small number of support posts, thus maintaining EL field and gain uniformity.

As well as NEXT, other examples of HPGTPC experiments include: Gotthard [3], a pioneering predecessor for HPGXe neutrinoless double beta decay experiments. Gotthard was an asymmetrical xenon TPC with 4% $CH_4$ at 5 bar that read charges out via a multi-wire proportional chamber rather than SiPMs or PMTs and used the same plane for both energy and tracking; AXEL [17], which is similar to NEXT with 10 bar xenon, asymmetrical and with an EL region; and, PANDAX-III [2], a proposed 10 bar xenon TPC which is symmetrical with the cathode in the middle and drift towards both ends of the detector and charge readout via Micromegas, with TMA added as a quench gas.

When a large active volume is needed for viewing interactions, argon is a more cost effective medium. A proposed high-pressure argon near detector for the DUNE experiment [4] would be used to characterize the neutrino beam at short baseline in order to facilitate a precise neutrino oscillation search. This would be classified as an asymmetrical HPGTPC with a large drift region.

A persistent challenge for noble TPC detectors is the capability to stably apply high voltages to produce constant drift fields over long distances. The difficulty of creating this field naturally increases as experiments grow in size and the maximal high voltage increases. Unfortunately, the importance of reaching the design field also increases, as drift distances become longer and finite free electron lifetime due to attachment on impurities becomes a limiting factor. Many major TPC experiments in both liquid and gas phase have failed to achieve their design field strengths, and so better understanding of insulating materials and their electrical breakdown properties is of much interest.

EL TPCs must, in addition to the drift field, apply an EL amplification field. While the EL field strength does not change between different detector scales, for larger detectors the maintenance of

2018 JINST 13 P10002

EL region planarity without deflection also becomes an electro-mechanical challenge. The work in this paper is motivated by the need to satisfy the material requirements of EL support structures in NEXT-100 and NEXT-ton scale detectors, and may also inform HV design of drift regions where insulating materials are used. We investigate the behaviour of various insulating materials in high pressure argon and xenon gases, under large applied voltages at ~ cm length scales. Previously uncharacterized swelling behaviour through xenon gas absorption is studied, and dielectric strength measurements transverse to the insulating surfaces are made.

This paper is organized as follows. Section 2 describes the materials under consideration and some previously used gases in noble TPC experiments. Section 3 reports on swelling through absorption of argon or xenon gases in high pressure environments; section 4 reports on measurements of surface strength under applied transverse high voltage. Finally, in section 5 we discuss our findings and their implications for HPGTPC experiments, and specifically as support material for the NEXT-100 and NEXT-ton scale EL regions.

## 2 Polymers as HV insulators in TPCs

A variety of polymers are used in HPGTPCs as both structural components and as insulation from the high voltages required to produce high electric fields. These materials are required to have a low outgassing rate to avoid contaminating the noble gas as well as generally needing to satisfy strict radiopurity requirements. The ideal materials for HV applications are insulators with sufficient leakage current to avoid charge up effects that can distort electric fields or cause sparking. For other applications, properties such as reflectivity and structural strength may also be design drivers. This paper characterizes the behavior of some commonly used structural polymers that may find application in HPGTPCs, with a particular focus on candidates for EL support material in NEXT-100. In this section we describe the materials under consideration and review some past use cases.

**High Density Polyethylene (HDPE)** is a commonly used thermoplastic which has found past application as a structural field cage material in the NEXT-NEW [18] experiment. It has also been used as an insulating material in high voltage feedthroughs for use in liquid argon R&D towards DUNE [19], as cable insulation in the liquid xenon LZ experiment [20] and as a shield material for XENON10 [21].

**Polytetrafluoroethylene (PTFE)**, widely known under trade name Teflon, is a fluoropolymer which is often employed in xenon time projection chambers because of its properties as a strong diffuse reflector. It has been used for this purpose in the NEXT-NEW [18] HPGXeTPC and the LUX [22] and EXO-200 [23] liquid xenon detectors. Teflon has also been used in HV feedthrough applications in liquid xenon, forming a large part of the insulating material for the feedthroughs of the EXO-200 [23]. PTFE serves both structural and reflective purposes as the field cage frame in the XENON family of experiments [21] and LZ [20]. The properties of PTFE surface breakdowns in liquid argon were recently studied in [24].

**Ultra-high molecular weight polyethylene (UHMW)** is a higher density, softer polyethylene material than HDPE, which has found wide use in high voltage feedthrough applications in liquid argon detectors including the ICARUS T600 [25] and MicroBooNE [26] detectors. It is also used in structural field cage components of the LUX experiment [22]. The properties of UHMW surface breakdowns in liquid argon were recently studied in [24]. In addition to virgin UHMW we also tested



2018 JINST 13 P10002

**Figure 3**. Left: anti-static UHMW tested in air and failing through sparking and excessive heating at $\leq$ 10 kV; right: picture of PEEK post that had a destructive spark leave a track along the side.

**antistatic UHMW**, sometimes known by the trade name Tivar. This is formed by adding carbon powder to the UHMW resin to achieve surface resistivities of $10^9$ Ω/sq. It was anticipated that this surface resistivity would help avoid charge-up effects and sparking, although poor performance was obtained in preliminary tests. In a preliminary scan of material dielectric strength in air, antistatic UHMW exhibited surface breakdowns at low voltages yielding an electric current far in excess of those expected based on surface resistivity. This led to destructive heating under applied voltages of less than 10 kV, disqualifying antistatic UHMW from further tests (figure 3, left).

**Polyether ether ketone (PEEK)** is a high-performance engineering polymer commonly used for its robust mechanical properties and ultra high vacuum compatibility. It is extremely machinable and durable within a wide temperature range. PEEK has been used as a structural material in the WArP liquid argon dark matter search [27] and the PandaX [28] experiment, as well as an insulator in the feed-throughs of the liquid XENON10 detector [21]. PEEK has become relatively disfavored as a field cage material for ultra low background experiments, since radioactivity of recently tested samples has been quantified at higher levels than other candidate materials [29]. Notably, PEEK was also the only material which failed in a destructive way during our high pressure gas HV strength tests, as will be described later (figure 3, right).

**Polyoxymethylene (POM)**, often known as acetal or by trade names such as Delrin, is a machinable structural polymer. We are not aware of previous uses in TPC experiments, although its surface electrical strength was recently characterized in liquid argon [24]. Promising performance there motivated us to explore its potential for use in HPGTPC experiments.

## 3 Tests of mechanical effects of gas absorption

### 3.1 Methodology

To test the degree of swelling for polymers of interest, 6 cm length sections were cut on a band saw from rods of these materials that had been extruded at the manufacturer to a 0.64 cm diameter (figure 4, right). The rods edges were deburred and then cleaned for 15 minutes in ethyl-alcohol placed in a sonic bath. After taking the rods out and letting them dry, each was numbered with an identifying code. Each rod was measured in length 5 times with a pair of vernier calipers and



2018 JINST 13 P10002

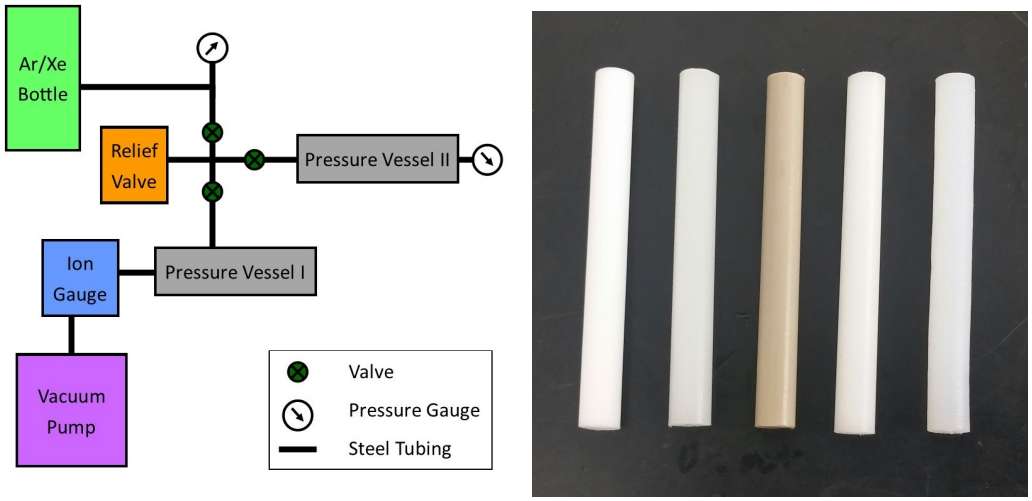


**Figure 4**. Left: schematic of the xenon absorption test set up. Pressure Vessel I was where the evacuation tests were performed and Pressure Vessel II was where the rods were soaked in noble gas. Pressure Vessel II could be closed off with its valve and removed from the system, allowing multiple vessels to run at the same time. Right: typical posts used for these tests. From left to right the materials are PTFE, HDPE, PEEK, POM, and UHMW.

3 times in mass with a digital analytical balance scale. Each rod's measured masses and lengths were averaged and their standard deviation calculated yielding an average precision of 0.004 cm in length and 2 mg in mass.

The pieces were put in a small, 0.15 liter pressure cylinder, evacuated overnight, weighed, and measured again, with no perceptible change in either quantity. The rods were placed back inside the cylinder, evacuated to $5 \times 10^{-8}$ bar, and then pressurized with noble gas and left sealed until ready to re-measure. This setup is shown schematically in figure 4, left. To test pressure dependence, rods were soaked under 5, 10, and 15 bar of xenon gas for 1 week each. Tests for time and noble gas dependence were performed by soaking rods in 10 bar of xenon and 10 bar of argon for 3.5, 7, 10, and 21 days. Significant swelling was observed in some cases, as will be described below.

To establish if the observed swelling was permanent, posts that had soaked for a week in 15 bar of xenon were evacuated. Every few days the lengths and masses were re-measured and compared with their initial values. The system vacuum was monitored and observed to improve over the 14 days of the study as the rods out-gassed the residual xenon and lost mass and length.

Each set of runs had control posts that were kept in a sealed container in atmospheric air and measured at the same times as the test pieces. All measurements were reported as the new mass (or length) divided by the original, so that no change would be equivalent to 1.0. The controls were used to correct for measurement device variations by dividing by the average control ratio.

Up to 5 posts were measured for each material, and the length and mass changes are reported as mean and standard deviation over these posts. The uncertainties on the ratios include a contribution from the control measurements, and so include some correlated uncertainty between points taken in the same run.



2018 JINST 13 P10002

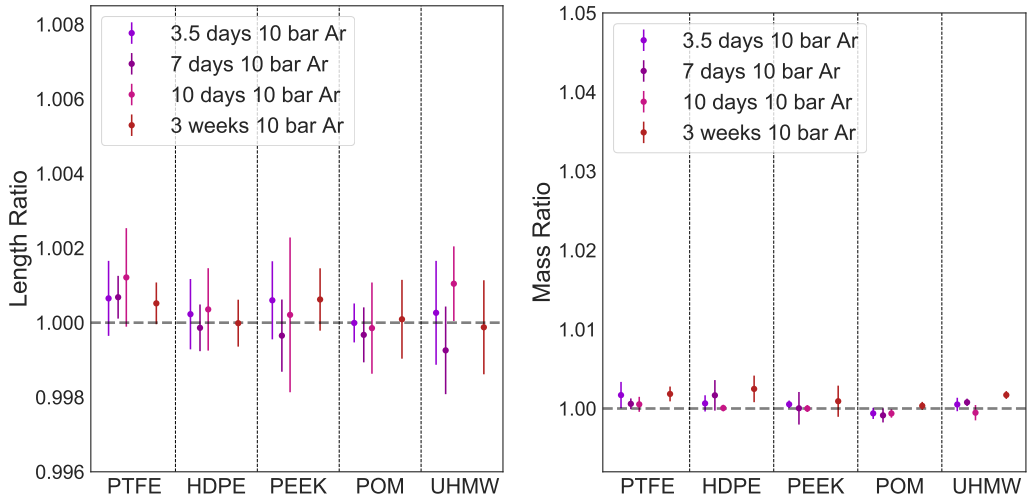


**Figure 5**. Left: ratios of lengths of posts after soaking for various lengths of time in argon at 10 bar divided by the original lengths of posts. Right: ratios of masses of posts after soaking for various lengths of time in argon at 10 bar divided by the original masses of posts.

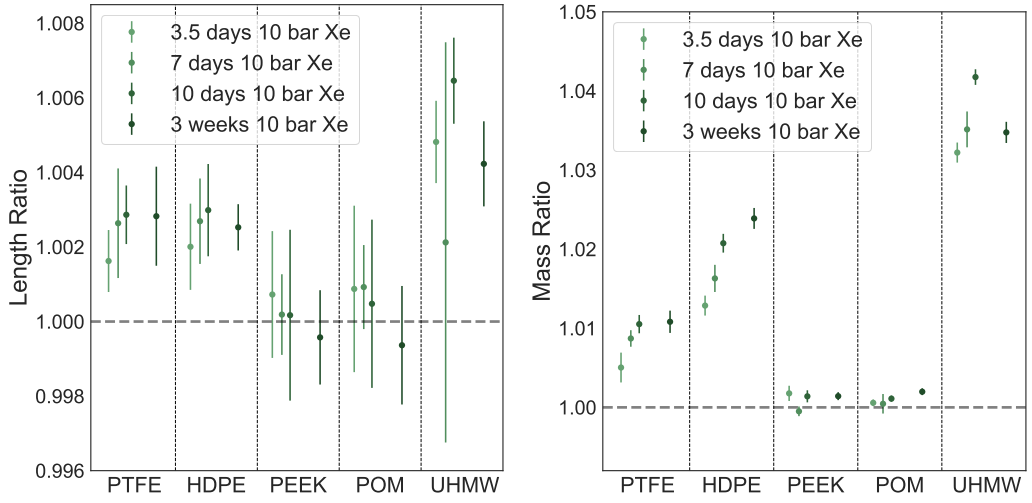


**Figure 6**. Left: ratios of lengths of posts after soaking for various lengths of time in xenon at 10 bar divided by the original lengths of posts. Right: ratios of masses of posts after soaking for various lengths of time in xenon at 10 bar divided by the original masses of posts.

### 3.2 Results

Figure 5 shows that no swelling was observed in argon for any material at the level of precision of this study with 0.2 percent and 0.5 percent being the threshold for confirming an increase in length and mass respectively.

Length and mass measurements in xenon are shown in figure 6. PEEK and POM were not observed to swell within the precision of this experiment, whereas PTFE, HDPE, and UHMW



2018 JINST 13 P10002

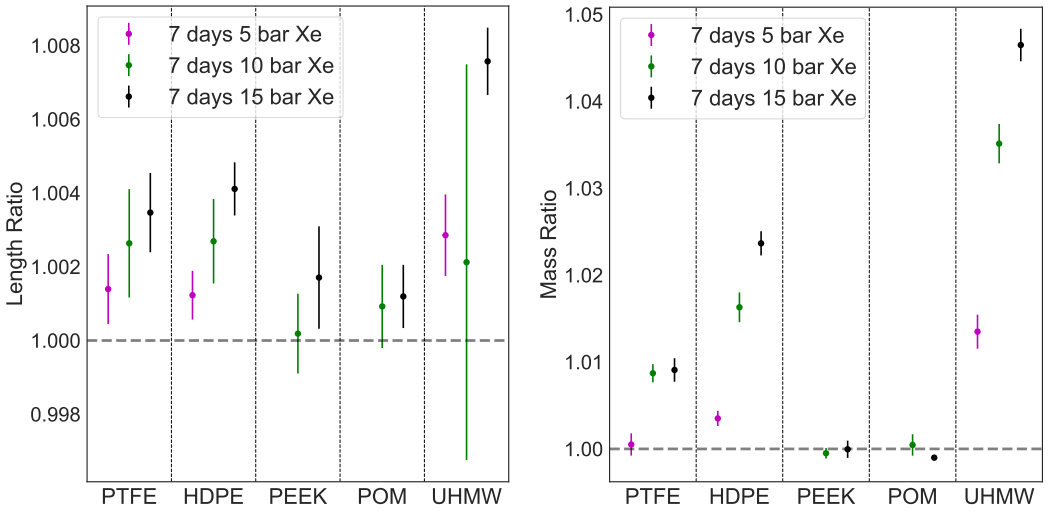


**Figure 7**. Left: ratios of lengths of posts after soaking for a week in xenon at various pressures divided by the original lengths of posts. Right: ratios of masses of posts after soaking for a week in various pressures of xenon divided by the original masses of posts.

showed an increase in both mass and length. UHMW had the largest mass and length increase with HDPE and PTFE less. All three materials showed a continuing upward trend in their mass increases up to ten days.

Higher pressure environments were observed to produce more absorption and swelling than the lower pressures within the same time period shown in figure 7. PEEK and POM did not have a perceptible change at any pressure. The large error on the length of UHMW reflects the difficulty of measuring the length accurately, given that the material is soft and flexible. This material experienced the largest gas absorption and length increase, absorbing almost 5% of its mass in xenon in 10 days at 10 bar, and swelling in length by nearly 1%.

Figure 8 shows the effects of vacuuming materials after soaking in xenon at 15 bar for 7 days. As expected, the masses and lengths shrink as the xenon is drawn out of the material. A ratio of 1.0 represents if the materials had no permanent swelling once they had absorbed and lost xenon — i.e. a return to the original pre-soak length. The lengths return to within 0.1% of their original values, and masses to within .3%, for all materials after two weeks of evacuation. After 25 days of evacuation all posts were consistent with their initial states.

## 4 Tests of electrical strength of surfaces under high voltage

### 4.1 Methodology

To test the breakdown voltage across the insulating materials, materials were cut on a band saw, sanded down to size and then deburred. The rods were inspected by eye for any surface defects then cleaned for 15 minutes in ethyl-alcohol placed in a sonic bath before being exposed to high voltage. As a preliminary test to help rule out poor HV materials, 1.0 cm length posts of 0.64 cm diameter were placed between two spherical electrodes and the voltage raised until sparking occurred between



2018 JINST 13 P10002

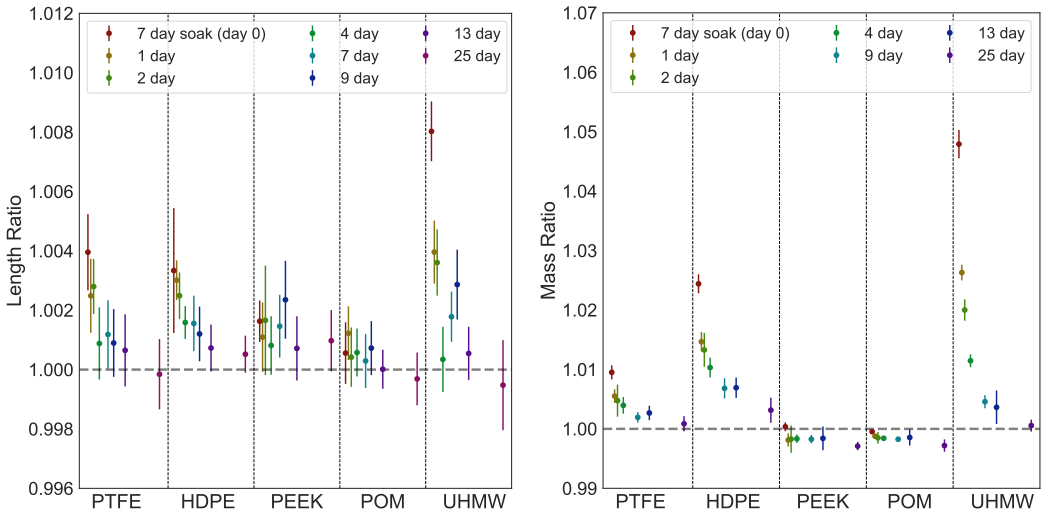


**Figure 8**. Left: ratios of lengths of posts after soaking for one week in xenon at 15 bar and then put under vacuum divided by the original length of posts. Right: ratios of masses of posts after soaking for one week in xenon at 15 bar and then put under vacuum divided by the original, pre-vacuum masses of posts.

the electrodes in air. All materials passed this preliminary scan except for antistatic UHMW, as described in section 2

The setup used to take these data can be seen in figure 9, where the right stainless steel ball bearing is connected to the chassis ground. The ground electrode is held with a threaded PEEK rod penetrating a G10 frame. The HV electrode ball is supported by a threaded PEEK rod penetrating two HDPE plates, separated with a ceramic spacer to lend extra structural strength. To secure an electrical connection, the ends of the electrical cables were fitted with panduit lugs, then attached

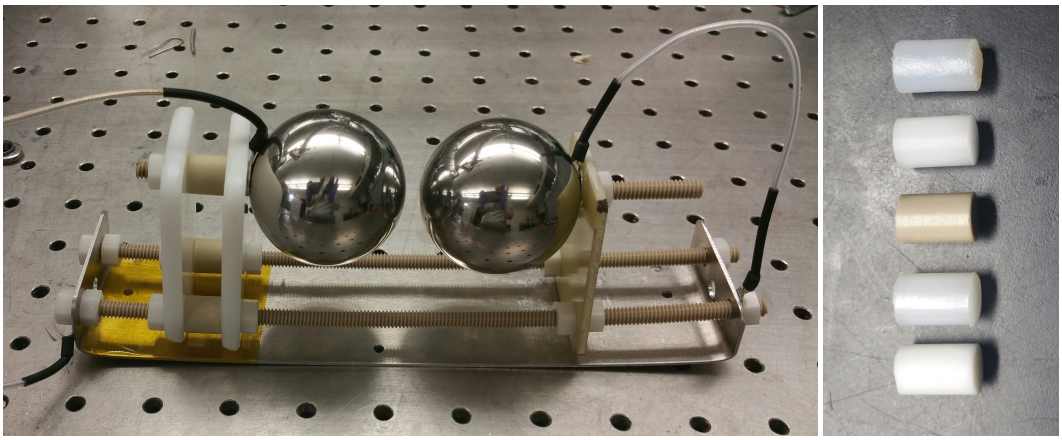

**Figure 9**. Left: setup for holding the insulating posts in a smooth electric field where the left sphere is the high voltage, right is ground. Right: typical posts used for these tests. From top to bottom the materials are UHMW, POM, PEEK, HDPE, and PTFE.



2018 JINST 13 P10002

to the PEEK rods between the electrodes and support plates. Nylon nuts were then threaded on and tightened to hold them in place. Both 5.1 cm ball bearings are tapped and drilled 1.2 cm deep for the PEEK rod to securely thread into and the opposite side ground down a slight amount to provide a flat spot for the insulating material posts to rest.

Several preliminary frames were tested to hold the ball bearings before settling on this design, which we denote A-C. Frame A used drilled acrylic blocks to hold the electrodes with PEEK rods, but the weight of the steel balls caused the acrylic to warp when heating the vessel during the vacuum stage, leading to misalignment of the spheres. The acrylic also outgassed profusely, leading to a high reading of water contaminants on the residual gas analyzer (RGA). Frame B was a high temperature 3D printable plastic, so that the spheres could be held without drilling into them, and Frame C was thin sheets of G10 with holes drilled through for the PEEK rods. Both Frame B and C gave sporadic values of breakdown voltage, oftentimes corresponding to milliamps of current being drawn and sometimes shorting of the system. The G10 showed visible carbon tracks along it, illustrating that the plates holding the high voltage sphere led to breakdowns when too insulative, likely due to charge pile-up effects causing a nonuniform electric field, leading to electrical breakdowns in places other than between the electrodes. These preliminary studies informed final design with HDPE on the high voltage side and G10 by the ground as shown in figure 9.

After preliminary tests in air we placed the setup inside a 6 liter, 14.6 cm ID pressure vessel large enough to avoid the electrodes sparking to the inside walls. HV was supplied via a Glassman KT100-R20 power supply via an epoxy-potted and pressure-rated feed-through. The feed-through was rated for 20 kV DC voltage, but a prototype was tested to 40 kV before this study. If breakdown had not occurred by 30 kV, the voltage was decreased again. For 0.5 cm posts, this is around three times the voltage specification required for the NEXT-100 EL region to obtain 2 kv $cm^{-1}$ $bar^{-1}$.

Once each post was between the electrodes and placed in the pressure vessel, the system was evacuated with a PFEIFFER HiCube 80 vacuum pump and baked at 85 degrees Celsius overnight. This temperature was high enough to bake most of the water out of the system as checked by an RGA, but not so high as to melt the HDPE support plates. After cooling to room temperature a digital ion gauge [30] was used to read a resulting vacuum between $5 \times 10^{-9}$ and $4 \times 10^{-8}$ bar. The vacuum line was then closed and the vessel filled with xenon gas. The voltage was then slowly increased between the spheres until there was a spark which could be recognized by an audible sound from within the vessel, and sometimes a current draw. The breakdown voltage varies with pressure, so each material was measured at varying pressures in 0.5 bar increments.

To ensure that the gas was not contaminated, an RGA scan was done at the beginning and end of every data run, obtaining results as shown in figure 10. The RGA plots show the atomic mass unit of the gases in the vessel. There were always peaks around 16 to 18, though these are consistent with the measured out-gassing from the vacuum lines alone. The left plot shows a reading from the end of an argon test, but with the vacuum scan seen as background and subtracted off. The double peaks for both gases is caused by the RGA double ionizing the atoms so that argon is shown at 40 and 20 AMU, and xenon is at 132 and 66 AMU. To check that this level of purity was adequate for reliable predictions of breakdown, the gas was circulated through a purifier (up to 10 bar), and tested again. The same breakdown voltage was achieved with the purified gas as with the gas directly from the bottle.

To test the repeatability of the system, a breakdown test was performed on three different 0.84 cm pieces of HDPE in argon. Each post was placed inside the setup within the pressure vessel



2018 JINST 13 P10002

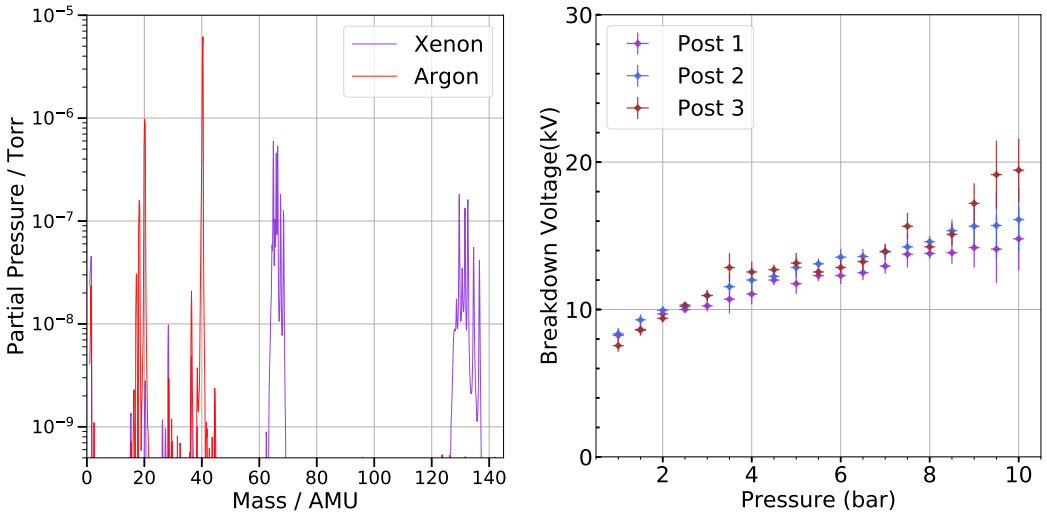


**Figure 10**. Left: reading from RGA at the end of a xenon and argon run with the vacuum subtracted resulting in peaks where we expect them for the two gases with very minor impurities. Right: three runs of different HDPE posts under identical conditions showing that the data is repeatable.

and evacuated overnight to $4 \times 10^{-8}$ bar, before closing off the vacuum and adding argon in half bar increments and checking for the break down voltage. The results of this test can be seen in figure 10. Above 8 bar, a small systematic difference between posts is observed, but this is sub-dominant to the variability within a single post, which is illustrated by the error bars on the points. The test was performed again using the same HDPE post twice and the results were consistent within error bars.

After taking the RGA measurements, the xenon was recaptured by cooling the recapture bottles in liquid Nitrogen to lower the temperature and therefore creating a pressure gradient to freeze the xenon into them. After this procedure, only a residual quantity of 300 millibar of xenon remained in the system, which was evacuated. The system was then filled with argon gas and the test repeated. After the data for argon were collected, the gas was vented out of the system down to 2 bar before closing off the gas panel and opening the vessel to switch out the post material. By running a test with a pre-mixed 3% xenon-argon mixture and comparing with pure argon, it was shown that a small amount of xenon does not affect the measurements taken in argon. This alleviates the possibility that residual xenon remaining after re-capture and evacuation influenced the argon measurements, which always followed with the same post shortly afterward. All the materials that passed the preliminary test in air were further tested using a 5 mm length post in both xenon and argon. To compare to the breakdown of pure gas, breakdowns between the spheres at the same lengths as the posts were also investigated.

### 4.2 Results

Figure 11 shows the breakdown voltages of 0.5 cm posts of each material as a function of pressure in pure xenon and argon gases. PEEK is not shown, due to its destructive failure at the relatively low voltage of 12 kV at 4 bar in xenon gas. This burned a 0.41 cm track into the material and reduced



2018 JINST 13 P10002

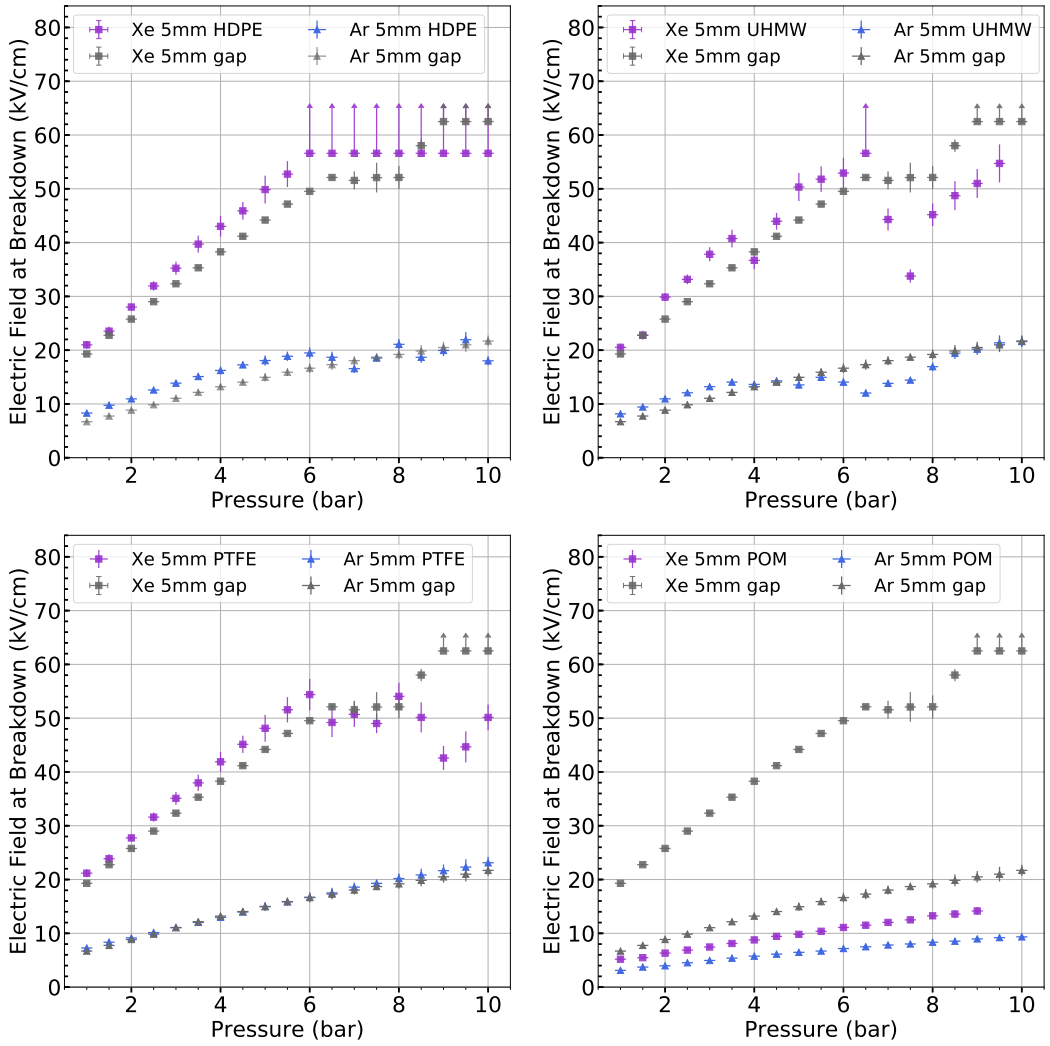


**Figure 11**. Breakdown point of various materials at different pressures in xenon and argon gases, with the grey points being the breakdown through the respective noble gas with no material between the electrodes. The high voltage feedthrough was only rated for 20 kV so we stopped taking data at 30 kV to reduce the risk of breakage. Upward arrows report that 30 kV was held without breakdown at this pressure.

its subsequent breakdown strength by almost 80 percent. This was the only catastrophic failure in any of the materials in these studies and is shown in figure 3.

At 1 bar the xenon and argon curves match within 20 percent of Paschen predictions for pure gas with explanations for the discrepancy given in [31]. All of HDPE, UHMW and PTFE appeared to increase the maximum voltage held versus a pure xenon gap at pressures below 6 bar, likely due to a reduction in total stressed area between the electrodes. At higher pressures, both UHMW and PTFE did not continue to show this effect at higher pressures / voltages, instead becoming stochastic in their breakdown point, which may be interpreted as these materials enabling surface discharges. HDPE maintained this strengthening effect even at the highest pressures.

2018 JINST 13 P10002

In argon gas, all of HDPE, UHMW and PTFE demonstrated a similar breakdown strength to a pure argon gap. Thus in this case it appears the spark is propagating across the argon itself, rather than via a surface mediated effect. In both gases, POM had breakdown values less than half of pure gas alone and should be avoided inside detectors.

## 5 Discussion

We have characterized the absorption of noble gases into polymers at high pressure, and the electrical strength of various materials in high pressure argon and xenon gases. While no swelling or mass increases are observed with argon gas, HDPE, PTFE and UHMW all exhibited substantial length and mass changes under exposure to xenon gas, with larger increases over longer times and at higher pressures. This suggests a qualitative difference in the absorption behaviour in argon and xenon environments.

The diffusion of noble and other gases through polymers has been studied in various contexts, because its of relevance for industries including the oil and gas industry and food packaging. References such as [32, 33] and [34] report on the seepage of gases through very thin polymer membranes. The effect on mechanical properties of the membrane, such as changes in shape or mass, are not reported.

Because they are heavier and thus move more slowly in thermal equilibrium, a naive expectation might be that more massive noble gases would diffuse through materials more slowly than less massive ones. This is observed in only some conditions. For example, in [35], xenon permeability through Kapton films is shown to be a factor ~10 times lower than krypton and ~100 times lower than argon at the same temperature. However, careful analysis of the time profiles and pressure dependencies of noble gas permeation as reported in ref. [33] illuminates more nuanced behaviour. There, two distinct absorption mechanisms are inferred in oriented polypropylene (OPP) from the two time constants in absorption and desorption curves. These are named the "normal pathway", or standard diffusion through the solid polymer matrix, and "cavity condensation", which occurs only for the heaviest gases and only at the highest pressures. Under this mechanism, small numbers of atoms may enter material voids, where interactions with the walls create potential wells that increase the local effective pressure. This causes condensation of the gas in these voids, enhancing the absorption rate. Related phenomena have been observed in porous carbon media, where enhanced production of nitrogen dimers is observed and effective pore pressures in excess of 1000 bar can be generated [36]. This process is postulated to also be active in the amorphous regions of polymer matrices, with measurements from [33] suggesting that it accounts for 8% of diffusion of xenon at 1 bar in OPP. The characteristic two-exponential behaviour is reported for Xe and Kr but not Ar, He or Ne, which have much lower boiling points.

At the pressures considered in this work, the cavity condensation mechanism is expected to be further enhanced relative to that reported at 1 bar in [33]. This may provide an explanation for the striking qualitative difference between xenon and argon absorption in bulk HDPE, UHMW and PTFE. The difference between these materials and POM and PEEK would then be understood to lie in the different density of microscopic voids in these materials that may enable the condensation mechanism.

2018 JINST 13 P10002

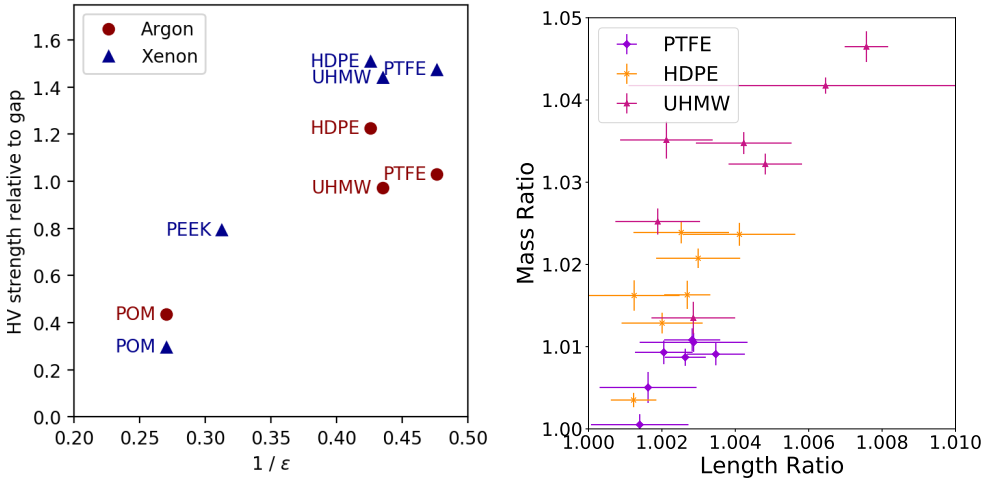


**Figure 12**. Left: comparison of breakdown strength at 5.5 bar with inverse dielectric constant (except PEEK, evaluated at 4 bar, before destructive failure). A correlation with dielectric constant is observed. Right: comparison of mass and length ratios of PTFE, HDPE, and UHMW soaked in xenon showing each material having a linear correlation between its mass and length.

Figure 12 (right) displays mass versus length for HDPE, UHMW, and PTFE soaked in xenon both with different pressures and different soaking times. There is a clear correlation between mass and length change ratio for each of the materials, with PTFE appearing to display a distinct slope compared to the other two.

In figure 12 (left) the dielectric strength of these materials show similar behaviours between high pressure argon and xenon gases. More scatter was observed between breakdown voltage points at different pressures in xenon. This may be because dielectric strength of xenon is simply higher, and thus the relevant surfaces carry more charge which may fluctuate to initiate a breakdown. This scatter is not observed for HDPE, which maintains a reliable and predictable breakdown strength until the pressure becomes sufficiently high that breakdown cannot be achieved in our system. In both cases, POM is the weakest material, apparently carrying surface breakdowns at low voltages in both cases.

We noted that under higher breakdown fields, some pitting occurred in the electrodes, and a dark residue was observed to accumulate on the HV cable insulation and posts, which we suspect may be the ejected material from the spark. This may potentially explain the more scattered behaviour in xenon gas, as this ejected material could introduce new but sporadic conductive paths. To ameliorate this effect on our key conclusions, we always started with the highest pressures first and then worked toward lower pressures by re-condensing xenon gas into the bottle. Thus the highest voltage points use the most pristine setup and are most reliable. A repeated run with HDPE, which did not show significant scatter or reduction in strength, suggests that there was no significant memory effect, producing an effectively identical set of data points. A repeated run with PTFE also did not show evidence for hysteresis, but it is more difficult to be conclusive due to the wider spread of points at high pressures.

Prior work with HV insulators in liquid argon [24] found that the threshold for surface breakdowns was inversely proportional to the material dielectric constant. This phenomenon has the

2018 JINST 13 P10002

intuitive explanation that materials with high permittivities induce larger electric fields near the interfaces which may initiate breakdowns. We observe approximately this trend in both high pressure argon and xenon gases (figure 12 left). In this plot, the strengths are shown relative to an empty gas gap at 5.5 bar, which is below the regime where large point scatter was observed. For PEEK, which failed destructively at 4 bar in xenon, the ratio is shown at this pressure.

## 6 Conclusions

In this paper, we show that argon gas does not cause swelling in PTFE, HDPE, PEEK, POM, or UHMW. However, in those same materials PTFE, HDPE, and UHMW do absorb Xenon, with over 4% mass increase in UHMW over 10 days and a more moderate 2.5% mass increase in HDPE after 3 weeks. We have also shown that a variety of polymers can raise the voltage required for sparking over a distance in gas. In both xenon and argon, HDPE appears to be the strongest and most stable option near high electric fields as it has a consistently higher breakdown voltage.

For structural supports within an EL region, the critical property is the ability to withstand a high electric field without sparking. In this work we have demonstrated that the materials such as HDPE and UHMW appear well suited for this purpose. Without further information, HDPE seems the optimal material as it consistently strengthened the gap's ability to hold high voltage relative to pure xenon, and had a consistent and predictable breakdown behaviour even at the highest pressures. Based on these data, HDPE has been preliminarily selected for the EL region support material to be used in the NEXT-100 and NEXT-ton detectors.

As expected, we find generally higher dielectric strengths in xenon than in argon. We conclude that the practice of testing components for HV strength in argon gas before installation in xenon detectors appears valid. Our measurements support the dependence of the insulator on inverse dielectric constant as has been shown in other works.

The length changes observed in PTFE, UHMW and HDPE under Xenon exposure have implications for the tolerances that can be achieved using these materials in Xenon gas detectors, with typically 1% length changes causing potentially important effects over meter-scale detectors. This swelling should be taken into consideration as part of the design of future experiments.

For structural elements, the effects of the gas absorption on mechanical strength may also be of interest. An interesting study in the future may be characterizing how the strength and durability of the materials changes with absorption, in order to inform stress analysis and mechanical deflection calculations.

Finally, we note that other materials are sometimes used in noble TPC experiments, including acrylic, G10 and Kapton. The significant swelling phenomena observed here, in addition to the non-trivial dependence of breakdown strength upon the gas environment, suggest that similar studies of these materials may be of value for future experiments.

## Acknowledgments

The NEXT Collaboration acknowledges support from the following agencies and institutions: the European Research Council (ERC) under the Advanced Grant 339787-NEXT; the European Union's Framework Programme for Research and Innovation Horizon 2020 (2014–2020) under the



2018 JINST 13 P10002

Marie Skłodowska-Curie Grant Agreements No. 674896, 690575 and 740055; the Ministerio de Economía y Competitividad of Spain under grants FIS2014-53371-C04, the Severo Ochoa Program SEV-2014-0398 and the María de Maetzu Program MDM-2016-0692; the GVA of Spain under grants PROMETEO/2016/120 and SEJI/2017/011; the Portuguese FCT and FEDER through the program COMPETE, projects PTDC/FIS-NUC/2525/2014 and UID/FIS/04559/2013; and the U.S. Department of Energy under contracts number DE-AC02-07CH11359 (Fermi National Accelerator Laboratory), DE-FG02-13ER42020 (Texas A&M), DE-SC0011686 (UTA) and DE-SC0017721 (UTA). F. Psihas is supported by a ConTex postdoctoral fellowship. We also warmly acknowledge the Laboratorio Nazionale di Gran Sasso (LNGS) and the Dark Side collaboration for their help with TPB coating of various parts of the NEXT-White TPC. Finally, we are grateful to the Laboratorio Subterráneo de Canfranc for hosting and supporting the NEXT experiment.

## References

[1] NEXT collaboration, J. Martín-Albo et al., *Sensitivity of NEXT-100 to Neutrinoless Double Beta Decay*, *JHEP* **05** (2016) 159 [arXiv:1511.09246].

[2] X. Chen et al., *PandaX-III: Searching for neutrinoless double beta decay with high pressure*$^{136}$*Xe gas time projection chambers*, *Sci. China Phys. Mech. Astron.* **60** (2017) 061011 [arXiv:1610.08883].

[3] R. Lüscher et al., *Search for beta beta decay in Xe-136: New results from the Gotthard experiment*, *Phys. Lett.* **B 434** (1998) 407.

[4] DUNE collaboration, J. Martin-Albo, *A pressurized argon gas TPC as DUNE near detector*, *J. Phys. Conf. Ser.* **888** (2017) 012154 [arXiv:1610.07803].

[5] P.A. Hamilton, *A Study of Neutrino Interactions in Argon Gas*, Ph.D. thesis, Imperial College, London (2015).

[6] NEXT collaboration, J. Renner et al., *Background rejection in NEXT using deep neural networks*, 2017 *JINST* **12** T01004 [arXiv:1609.06202].

[7] NEXT collaboration, P. Ferrario et al., *First proof of topological signature in the high pressure xenon gas TPC with electroluminescence amplification for the NEXT experiment*, *JHEP* **01** (2016) 104 [arXiv:1507.05902].

[8] D. Fancher et al., *Performance of a Time Projection Chamber*, *Nucl. Instrum. Meth.* **161** (1979) 383.

[9] F.T. Avignone, III, S.R. Elliott and J. Engel, *Double Beta Decay, Majorana Neutrinos and Neutrino Mass*, *Rev. Mod. Phys.* **80** (2008) 481 [arXiv:0708.1033].

[10] NEXT collaboration, V. Alvarez et al., *NEXT-100 Technical Design Report (TDR): Executive Summary*, 2012 *JINST* **7** T06001 [arXiv:1202.0721].

[11] NEXT collaboration, F. Granena et al., *NEXT, a HPGXe TPC for neutrinoless double beta decay searches*, arXiv:0907.4054.

[12] NEXT collaboration, J.J. Gomez-Cadenas et al., *Present status and future perspectives of the NEXT experiment*, *Adv. High Energy Phys.* **2014** (2014) 907067 [arXiv:1307.3914].

[13] NEXT collaboration, V. Alvarez et al., *Near-Intrinsic Energy Resolution for 30 to 662 keV Gamma Rays in a High Pressure Xenon Electroluminescent TPC*, *Nucl. Instrum. Meth.* **A 708** (2013) 101 [arXiv:1211.4474].

[14] NEXT collaboration, V. Alvarez et al., *Initial results of NEXT-DEMO, a large-scale prototype of the NEXT-100 experiment*, 2013 *JINST* **8** P04002 [arXiv:1211.4838].



2018 JINST 13 P10002

[15] V. Alvarez et al., *SiPMs coated with TPB: coating protocol and characterization for NEXT*, 2012 *JINST* **7** P02010 [arXiv:1201.2018].

[16] C.M.B. Monteiro, *Determination of argon and xenon absolute electroluminescence yields in Gas Proportional Scintillation Counters*, Ph.D. thesis, University of Coimbra (2011).

[17] S. Pan, *AXEL: High pressure xenon gas Time Projection Chamber for neutrinoless double beta decay search*, *J. Phys. Conf. Ser.* **718** (2016) 062047.

[18] NEXT collaboration, N. López March, *The NEXT high pressure xenon gas TPC for neutrinoless double beta decay searches*, 2018 *JINST* **13** C01048.

[19] C. Cantini et al., *First test of a high voltage feedthrough for liquid Argon TPCs connected to a 300 kV power supply*, 2017 *JINST* **12** P03021 [arXiv:1611.02085].

[20] B.J. Mount et al., *LUX-ZEPLIN (LZ) Technical Design Report*, arXiv:1703.09144.

[21] XENON collaboration, E. Aprile et al., *Design and Performance of the XENON10 Dark Matter Experiment*, *Astropart. Phys.* **34** (2011) 679 [arXiv:1001.2834].

[22] LUX collaboration, D.S. Akerib et al., *The Large Underground Xenon (LUX) Experiment*, *Nucl. Instrum. Meth.* **A 704** (2013) 111 [arXiv:1211.3788].

[23] M. Auger et al., *The EXO-200 detector, part I: Detector design and construction*, 2012 *JINST* **7** P05010 [arXiv:1202.2192].

[24] S. Lockwitz and H. Jostlein, *A Study of Dielectric Breakdown Along Insulators Surrounding Conductors in Liquid Argon*, 2016 *JINST* **11** P03026 [arXiv:1506.04185].

[25] ICARUS collaboration, S. Amerio et al., *Design, construction and tests of the ICARUS T600 detector*, *Nucl. Instrum. Meth.* **A 527** (2004) 329.

[26] MicroBooNE collaboration, R. Acciarri et al., *Design and Construction of the MicroBooNE Detector*, 2017 *JINST* **12** P02017 [arXiv:1612.05824].

[27] A. Zani, *The WArP experiment: A double-phase argon detector for dark matter searches*, *Adv. High Energy Phys.* **2014** (2014) 1.

[28] PandaX collaboration, X. Cao et al., *PandaX: A Liquid Xenon Dark Matter Experiment at CJPL*, *Sci. China Phys. Mech. Astron.* **57** (2014) 1476 [arXiv:1405.2882].

[29] V. Alvarez et al., *Radiopurity control in the NEXT-100 double beta decay experiment: procedures and initial measurements*, 2013 *JINST* **8** T01002 [arXiv:1211.3961].

[30] Kurt Lesker, *Kjlc 354 series ion gauge with integrated controller and display* https://www.lesker.com/newweb/gauges/ionization_kjlc_354.cfm.

[31] D. Gonzalez-Diaz, F. Monrabal and S. Murphy, *Gaseous and dual-phase time projection chambers for imaging rare processes*, *Nucl. Instrum. Meth.* **A 878** (2018) 200 [arXiv:1710.01018].

[32] B. Flaconneche, J. Martin and M. H. Klopffer, *Permeability, diffusion and solubility of gases in polyethylene, polyamide 11 and poly (vinylidene fluoride)*, *Oil Gas Sci. Technol.* **56** (2001) 261.

[33] H. Nörenberg, V. Burlakov, H.-J. Kosmella, G. Smith, G. Briggs, T. Miyamoto et al., *Pressure-dependent permeation of noble gases (he, ne, ar, kr, xe) through thin membranes of oriented polypropylene (OPP) studied by mass spectrometry.*, *Polymer* **42** (2001) 10021.

[34] B. Flaconneche, J. Martin and M. H. Klopffer, *Transport properties of gases in polymers: Experimental methods*, *Oil Gas Sci. Technol.* **56** (2001) 245.

[35] S.J. Schowalter, C.B. Connolly and J.M. Doyle, *Permeability of Noble Gases through Kapton, Butyl, Nylon and 'Silver Shield'*, *Nucl. Instrum. Meth.* **A 615** (2010) 267 [arXiv:0909.2610].

[36] K. Kaneko, *Molecular assembly formation in a solid nanospace*, *Colloid. Surface.* **A 109** (1996) 319.

2018 JINST 13 P10002

# Chapter 5

# Mitigation of Backgrounds from Cosmogenic $^{137}$Xe in Xenon Gas Experiments using $^{3}$He Neutron Capture

As discussed previously in Chapter 1, understanding and reducing backgrounds in 0vbb detectors is vital to realizing the discovery of 0vbb decay. While Chapter 6 focuses on identifying when a specific type of background particle passes through the detector; i.e. muons, this chapter focuses on reducing the effects of a different background particle; the neutron. Being able to suppress the backgrounds that fall in our region of interest is always desirable which is why so many detectors try to get deep underground.

The following paper was published in Journal of Physics G: Nuclear and Particle Physics as [65].

IOP Publishing Journal of Physics G: Nuclear and Particle Physics

J. Phys. G: Nucl. Part. Phys. **47** (2020) 075001 (17pp) https://doi.org/10.1088/1361-6471/ab8915

# Mitigation of backgrounds from cosmogenic $^{137}$Xe in xenon gas experiments using $^{3}$He neutron capture

**L Rogers[1,24], B J P Jones[1], A Laing[1], S Pingulkar[1], B Smithers[1], K Woodruff[1], C Adams[17], V Álvarez[7], L Arazi[4], I J Arnquist[5], C D R Azevedo[6], K Bailey[17], F Ballester[7], J M Benlloch-Rodríguez[12], F I G M Borges[9], N Byrnes[1], S Cárcel[8], J V Carrión[8], S Cebrián[10], E Church[5], C A N Conde[9], T Contreras[2], G Díaz[11], J Díaz[4], M Diesburg[13], R Dingler[1], J Escada[9], R Esteve[7], R Felkai[4,8], A F M Fernandes[14], L M P Fernandes[14], P Ferrario[12,15], A L Ferreira[6], E D C Freitas[14], J Generowicz[12], S Ghosh[2], A Goldschmidt[16], J J Gómez-Cadenas[12,15,25], D González-Díaz[11], R Guenette[2], R M Gutiérrez[3], J Haefner[2], K Hafidi[17], J Hauptman[18], C A O Henriques[14], J A Hernando Morata[11], P Herrero[12], V Herrero[7], Y Ifergan[4,19], S Johnston[17], M Kekic[8,11], L Labarga[20], P Lebrun[13], N López-March[8], M Losada[3], R D P Mano[14], J Martín-Albo[2,8], A Martínez[8], G Martínez-Lema[8,11,26], A D McDonald[1], F Monrabal[12,15], C M B Monteiro[14], F J Mora[7], J Muñoz Vidal[8], P Novella[8], D R Nygren[1,25], B Palmeiro[8], A Para[13], J Pérez[21], M Querol[8], A B Redwine[4], J Renner[11], J Repond[17], S Riordan[17], L Ripoll[22], Y Rodríguez García[3], J Rodríguez[7], B Romeo[12,21], C Romo-Luque[8], F P Santos[9], J M F dos Santos[14], A Simón[4], C Sofka[23,27], M Sorel[8], T Stiegler[23], J F Toledo[7], J Torrent[12], A Usón[8], J F C A Veloso[6], R Webb[23], R Weiss-Babai[4,28], J T White[23,29], N Yahlali[8] and The NEXT Collaboration**

[24] Author to whom any correspondence should be addressed.

[25] NEXT Co-spokesperson.

[26] Present address: Weizmann Institute of Science, Israel.

[27] Present address: University of Texas at Austin, USA.

[28] On leave from Soreq Nuclear Research Center, Yavneh, Israel.

[29] Deceased.

1361-6471/20/075001+17$33.00  

[1] Department of Physics, University of Texas at Arlington, Arlington, TX 76019, United States of America
[2] Department of Physics, Harvard University, Cambridge, MA 02138, United States of America
[3] Centro de Investigación en Ciencias Básicas y Aplicadas, Universidad Antonio Nariño, Sede Circunvalar, Carretera 3 Este No. 47 A-15, Bogotá, Colombia
[4] Nuclear Engineering Unit, Faculty of Engineering Sciences, Ben-Gurion University of the Negev, P.O.B. 653, Beer-Sheva, 8410501, Israel
[5] Pacific Northwest National Laboratory (PNNL), Richland, WA 99352, United States of America
[6] Institute of Nanostructures, Nanomodelling and Nanofabrication (i3N), Universidade de Aveiro, Campus de Santiago, Aveiro, 3810-193, Portugal
[7] Instituto de Instrumentación para Imagen Molecular (I3M), Centro Mixto CSIC - Universitat Politècnica de València, Camino de Vera s/n, Valencia, E-46022, Spain
[8] Instituto de Física Corpuscular (IFIC), CSIC & Universitat de València, Calle Catedrático José Beltrán, 2, Paterna, E-46980, Spain
[9] LIP, Department of Physics, University of Coimbra, Coimbra, 3004-516, Portugal
[10] Centro de Astropartículas y Física de Altas Energías (CAPA), Universidad de Zaragoza, Calle Pedro Cerbuna, 12, Zaragoza, E-50009, Spain
[11] Instituto Gallego de Física de Altas Energías, Univ. de Santiago de Compostela, Campus sur, Rúa Xosé María Suárez Núñez, s/n, Santiago de Compostela, E-15782, Spain
[12] Donostia International Physics Center (DIPC), Paseo Manuel Lardizabal, 4, Donostia-San Sebastian, E-20018, Spain
[13] Fermi National Accelerator Laboratory, Batavia, IL 60510, United States of America
[14] LIBPhys, Department of Physics University of Coimbra, Rua Larga, Coimbra, 3004-516, Portugal
[15] Ikerbasque, Basque Foundation for Science, Bilbao, E-48013, Spain
[16] Lawrence Berkeley National Laboratory (LBNL), 1 Cyclotron Road, Berkeley, CA 94720, United States of America
[17] Argonne National Laboratory, Argonne, IL 60439, United States of America
[18] Department of Physics and Astronomy, Iowa State University, 12 Physics Hall, Ames, IA 50011-3160, United States of America
[19] Nuclear Research Center Negev, Beer-Sheva, 84190, Israel
[20] Departamento de Física Teórica, Universidad Autónoma de Madrid, Campus de Cantoblanco, Madrid, E-28049, Spain
[21] Laboratorio Subterráneo de Canfranc, Paseo de los Ayerbe s/n, Canfranc Estación, E-22880, Spain
[22] Escola Politècnica Superior, Universitat de Girona, Av. Montilivi, s/n, Girona, E-17071, Spain
[23] Department of Physics and Astronomy, Texas A & M University, College Station, TX 77843-4242, United States of America

E-mail: leslie.rogers@mavs.uta.edu

Received 5 February 2020, revised 3 April 2020
Accepted for publication 14 April 2020
Published 25 May 2020

**Abstract**

$^{136}$Xe is used as the target medium for many experiments searching for $0\nu\beta\beta$. Despite underground operation, cosmic muons that reach the laboratory can produce spallation neutrons causing activation of detector materials. A potential background that is difficult to veto using muon tagging comes in the form of $^{137}$Xe created by the capture of neutrons on $^{136}$Xe. This isotope decays via beta decay with a half-life of 3.8 min and a $Q_\beta$ of ∼4.16 MeV. This work proposes and explores the concept of adding a small percentage of $^{3}$He to xenon as a means to capture thermal neutrons and reduce the number of activations in the detector volume. When using this technique we find the contamination from $^{137}$Xe activation can be reduced to negligible levels in tonne and multi-tonne scale high pressure gas xenon neutrinoless double beta decay experiments running at any depth in an underground laboratory.

Keywords: gaseous detectors, scintillators, scintillation and light emission processes, solid, gas and liquid scintillators

(Some figures may appear in colour only in the online journal)

## 1. The NEXT program of high pressure xenon gas TPCs

The NEXT program has developed the technology of high-pressure xenon gas time projection chambers (TPCs) with electroluminescent amplification (HPXeTPC) for neutrinoless double beta decay searches [1, 2]. The possibility to achieve sub-1% FWHM energy resolution and to topologically identify signal-like events was proven in small scale prototypes [3, 4] and has since been tested underground at demonstrator-scale with the NEXT-White (NEW) detector [5–8]. The subsequent stage of the project will deploy 100 kg of $^{136}$Xe as NEXT-100, currently under construction at Laboratorio Subterráneo de Canfranc (LSC), Spain, with the goal of setting a competitive limit on the $^{136}$Xe $0\nu\beta\beta$ half life with the world's lowest background index in xenon.

The future of $0\nu\beta\beta$ searches involves experiments using one to several metric tonnes of target mass running for tens of years deep underground. A HPXeTPC with a tonne or more of $^{136}$Xe has great discovery potential given the field's present understanding of neutrino masses. To reach target sensitivities of $10^{28}$ years, improvements over the NEXT-100 background budget [9] will have to be made. Selection of ever purer materials for the construction of detectors enables a considerable reduction in key backgrounds of a radiogenic nature, particularly those from the decays of $^{208}$Tl and $^{214}$Bi. As radiogenic backgrounds become sub-dominant, other sources of background become relevant, such as those of cosmogenic origin. These backgrounds cannot be reduced simply by selection of purer detector materials and must be mitigated by other means.

The location for the first module of the tonne-scale NEXT program, called NEXT-HD, has not yet been determined, but various underground labs worldwide are under consideration including SNOLab, LNGS, LSC, and SURF. The deeper the laboratory, the lower the muon flux, as shown in figure 2, left. A lower muon flux implies lower contamination of cosmogenic backgrounds, which has prompted most experimental neutrinoless double beta decay programs to favor the deepest available sites, with more than 5 km.w.e (kilometers water equivalent) of overburden.

Since the NEXT detectors operate using xenon gas, it is feasible to mix certain additives into the volume to improve detector properties. Any additive must meet a set of minimal criteria for

the experiment to succeed: it must not attach ionization electrons during their drift or interfere with the electroluminescence process, must not absorb scintillation light, and must not negatively affect energy resolution to a substantial degree. The additive must also be in gas phase at room temperature, be compatible with hot and cold getters in the purification system, and it must be possible to circulate it through the gas system. In addition, all considered additives should ideally be non-toxic.

The collaboration is investigating several possible additives which could improve the topological reconstruction when compared to operation with pure xenon, one of which is helium [10–14]. The predominant isotope of helium is $^4$He, which, if added in quantities between 10% and 15% has a substantial positive impact on transverse diffusion. The sub-dominant isotope of helium, $^3$He, is present in natural helium at the $2 \times 10^{-4}$ level. Unlike $^4$He, $^3$He has an extremely high capture cross section for neutrons. In this paper we consider the positive impacts of adding a small quantity of $^3$He to enriched xenon to dramatically reduce contamination from cosmogenic backgrounds in tonne or multi-tonne scale underground high pressure xenon gas detectors.

One can also consider the use of the technique presented here in liquid xenon experiments. With a boiling point of 3 K, however, $^3$He will tend to concentrate in the vapor of the ullage in a liquid xenon detector, rather than remaining in the liquid phase. A minority amount of helium will remain in the liquid, as implied by Henry's law, though the Henry coefficients for helium in xenon are not presently known. The LUX collaboration has shown that helium can be loaded into liquid xenon at the level of 0.003–0.009% by mass [15], but this level of doping is insufficient to affect a significant reduction in $^{137}$Xe contamination, based on the studies presented in this work.

## 2. Cosmogenic neutron backgrounds

As radiogenic background sources are reduced and target masses increase, cosmogenic backgrounds become more apparent. The most pernicious of these backgrounds derive from neutrons. This is because neutrons are very penetrating, and can capture on nuclei to create long-lived beta or gamma emitters, which can decay with a signal in the energy region of interest for double beta decay. While prompt backgrounds from nuclear cascades post-capture can be effectively vetoed using muon taggers of various types, longer lived isotopes pose a greater threat. In the case of $^{136}$Xe experiments, the only long lived isotope likely to be produced in laboratory conditions with a decay that can mimic the $0\nu\beta\beta$ signal is $^{137}$Xe. The beta-decay of this isotope with $Q_\beta$ of 4.162 MeV produces electrons with a continuum of energies that includes the $^{136}$Xe $Q$-value $Q_{\beta\beta} = 2.458$ MeV, and can constitute background to the search if not effectively filtered.

The decay of $^{137}$Xe has been identified as a significant contributor to the background expectations of several xenon-based double beta decay experiments. For example, 20 to 30 percent of EXO-200's background was from $^{137}$Xe [16, 17], prompting future liquid xenon TPCs to go very deep underground to escape it. Even at a depth of 6 km.w.e. at SNOLab, the proposed nEXO concept projects a non-trivial background from $^{137}$Xe [18]. KamLAND-Zen has also found a 7% dead-time from spallation products, the largest source being $^{137}$Xe with $(3.9 \pm 2.0) \times 10^{-3}$ tonne$^{-1}$ day$^{-1}$ produced [19]. Finally, it is notable that $^{137}$Xe activation provides a slow but non-zero source of non-double-beta-decay related barium production through the chain $^{137}\text{Xe} \rightarrow {}^{137}\text{Cs} \rightarrow {}^{137}\text{Ba}$, a potentially relevant consideration for barium tagging [20–25]. In the NEXT detectors these may be largely rejected by time-coincidence cuts with energy deposits of interest as the $Q_\beta$ for $^{137}\text{Cs} \rightarrow {}^{137}\text{Ba}$ is lower than the $Q_{\beta\beta}$ of interest.

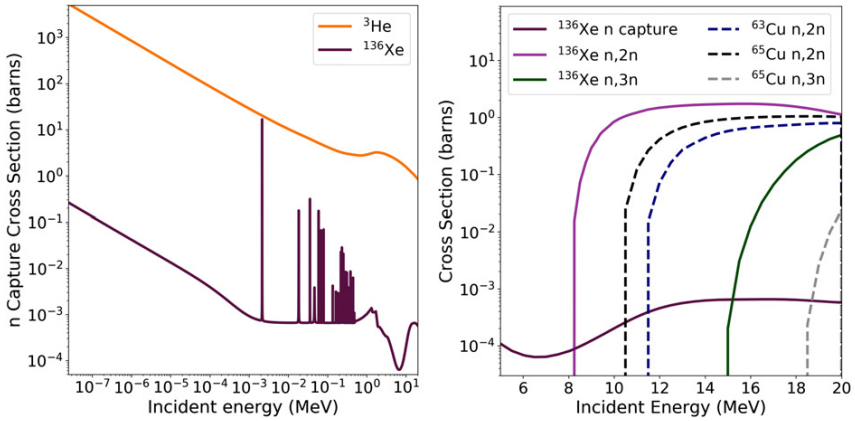


**Figure 1.** Left: cross sections for neutron capture on $^{136}$Xe and $^{3}$He. Right: cross sections for neutron capture and inelastic scattering on $^{136}$Xe and the most abundant copper isotopes. All cross sections are drawn from the ENDF database [26], which mirror those used in GEANT4 [27].

In this work we explore the impact of addition of a small fraction of $^{3}$He to pure xenon to mitigate $^{137}$Xe production and reduce cosmogenic backgrounds for neutrinoless double beta decay. $^{3}$He has a neutron capture cross-section that is four orders of magnitude greater than that of $^{136}$Xe, as shown in figure 1-left. The capture process produces hydrogen and tritium and an energy of 764 keV:

$$^{3}\mathrm{He} + n \rightarrow {}^{1}\mathrm{H} + {}^{3}\mathrm{H}. \tag{2.1}$$

This process is commonly used in $^{3}$He-based neutron detectors. The tritium later beta-decays to $^{3}$He with $Q_{\beta}$ of $\sim$18.6 keV with a half life of twelve years. Because their energies are all far below $Q_{\beta\beta}$, none of the products of neutron capture on $^{3}$He present potential background to the $0\nu\beta\beta$ search. Backgrounds from tritium contamination at high rates, either as a product of neutron captures or due to contamination of the raw gas (which is typically manufactured through tritium decay) could interfere with detector calibrations that use $^{83m}$Kr decay x-rays [28]. However, it has been demonstrated that tritium can be effectively removed by getters [29] and so purification both before filling and during detector operations are expected to mitigate this effect. Moreover, interference with krypton calibration would require pile up of various tritium decays and is, as such, likely to be a negligible contribution to the high statistics runs used for calibration. By absorbing a large quantity of thermal neutrons without introducing high energy backgrounds, the presence of $^{3}$He in the active volume is expected to significantly reduce the abundance of neutron captures on xenon. By effectively mitigating the background from $^{137}$Xe production, such an admixture could allow high pressure xenon gas detectors to operate at shallower depths, and also provide a tool for monitoring the neutron flux to better understand contributions from other neutron-induced signatures.

## 3. Simulations of $^{137}$Xe activation

A Monte Carlo study was carried out using the NEXT simulation framework to investigate the impact of $^{3}$He doping on cosmogenic background contamination. For this study we consider

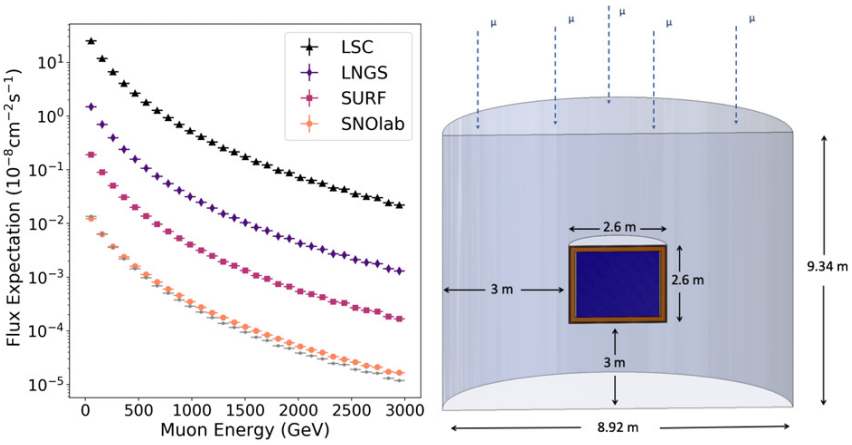


**Figure 2.** Left: expected cosmic muon energy spectrum in four different labs being considered for ton-scale detectors. Gray dots represent scaling LNGS muon distribution with SNOlab's muon flux while the orange are using the MUSIC muon simulation code for SNOlab. Right: geometry used in simulations.

an HPXeTPC with active volume diameter of 2.6 m and length of 2.6 m at 15 bar giving a total $^{136}$Xe target mass of ∼1109 kg for xenon enriched to 90.3% in $^{136}$Xe. The active volume is surrounded by a 1 cm thick plastic cylinder that represents the fieldcage and by 12 cm of copper on all sides. This closely mirrors the proposed geometry of the tonne-scale NEXT-HD, though using a simplified simulation volume. NEXT-HD will be submerged in an instrumented water tank as a means to mitigate interactions of rock neutrons and to tag cosmic muons. To this end we simulated a cylindrical water tank surrounding the TPC with diameter 9.34 m and a height of 8.92 m to give 3 m of water on all sides of the pressure vessel (see figure 2 right).

The effect of the addition of $^{3}$He on $^{137}$Xe activation was investigated in two ways: First, high statistics Monte Carlo sets with neutrons at low energies within the active volume were used to directly study activation (described in section 4.1). Two neutron injection energies were investigated: (a) 10 eV neutrons, which quickly thermalize ('thermal'); (b) 10 MeV neutrons which may experience harder scatters or inelastic processes before thermalizing ('fast'). Second, muons with energies between 1 GeV and 3 TeV, representing ∼99.5% of the expected energy range in most underground labs (see figure 2-left for flux expectations), were launched from above the water tank in order to study the expectations from this source both with and without $^{3}$He additive (section 4.2). The simulations were performed using `GEANT4` [30] version `10.5.p01`. In addition, further cross checks were performed using `GEANT4` version `10.6.p01` as well as `FLUKA` version `2011.2x-8` and found to be consistent. The cross checks are summarised in section 6.

The most important cross sections for this work are those relating to thermal neutron capture. The capture cross sections in this version of `GEANT4` are drawn from the `ENDF/B-VII.1` database [26]. The ENDF cross sections were derived originally from reference [31] and were recently tested experimentally, with the measured thermal neutron capture cross section on $^{136}$Xe validated at the $1\sigma$ (approx. 20%) level [32]. Scattering and capture of neutrons on $^{3}$He has been studied extensively (for example, references [31, 33–40]) and the ENDF database recommends a sub-percent uncertainty on the provided 3He(n,p)t cross section below 1 keV,

growing to 5% at 50 keV. Cross sections for neutron production through inelastic scattering are calculated within GEANT4 using the Bertini [41–43] intra-nuclear cascade model, which has been validated against data for inelastic neutron scattering in terms of both angular and energy distribution on a variety of nuclei [44], with agreement at the factor-few level [45]. The central result of this work, the expected improvement in $^{3}$He/$^{136}$Xe mixtures over pure $^{136}$Xe in terms of $^{137}$Xe production, depends primarily on the ratio of neutron capture cross sections of $^{3}$He and $^{136}$Xe. Based on the above considerations, this is expected to be accurate at the 20% level. The absolute $^{137}$Xe yield, however, depend on the details of neutron production in complex showers, and this carries a far larger uncertainty. This uncertainty provides a further motivation for the use of $^{3}$He in underground experiments using $^{136}$Xe, to monitor the total thermal neutron yield, itself proportional to the total rate of $^{137}$Xe activation in the detector.

## 4. Results

### *4.1. $^{137}$Xe production from internal neutrons*

The potential of $^{3}$He as a neutron-moderating additive in NEXT was first studied using neutrons simulated in the internal volumes of the detector. $10^{6}$ neutrons were simulated with energies $<$10 eV to check thermal neutron captures, and 10 MeV for fast neutrons, generated over 4 $\pi$ solid angle, starting in the field cage structure with xenon-helium gas mixtures at 15 bar and 300 K. The helium percentage-by-mass ranged between 0 to 5% and the number of $^{137}$Xe created were counted for each run. A control simulation set was generated using a mixture of the same enriched xenon with $^{4}$He. This helium isotope does not capture neutrons and, as such, its admixture is expected to have no effect on the number of $^{137}$Xe produced. This data set is used to validate that it is indeed the neutron-capturing properties of $^{3}$He that lead to any observed changes in $^{137}$Xe background, rather than dilution or the neutron-moderating impact associated with additional light target nuclei.

The number of activations is normalized to the total target mass, i.e, the number of kilograms of $^{136}$Xe in the active volume. With the largest helium fractions, dilution alone has some small impact on the $^{137}$Xe rate, which is not the effect we intend to study here. Using the mass of $^{136}$Xe as the denominator avoids this issue. The exact normalization used is

$$N'_{137} = \frac{N_{137}}{E_{136} \cdot P_{\mathrm{Xe}} \cdot m_{\mathrm{a}}}, \tag{4.1}$$

where $N_{137}$ is the number of $^{137}$Xe produced in the simulations, $E_{136}$ is the level of enrichment in the 136 isotope, $P_{\mathrm{Xe}}$ is the proportion of the gas mixture taken up by xenon, and $m_{\mathrm{a}}$ is the mass in the active volume of the detector.

Figure 3-left shows the results for mixtures with $^{4}$He and $^{3}$He. No statistically relevant change in the normalized number of activations for any proportion of $^{4}$He is found. This is not the case when we consider an addition of $^{3}$He to the gas. Figure 3-left clearly demonstrates the power of the $^{3}$He to absorb neutrons, and to remove contamination from $^{137}$Xe. Even at a fraction of a percent concentration, a clear reduction in $^{137}$Xe activation is seen. By 0.5% of $^{3}$He a reduction of two orders of magnitude is predicted from both thermal and fast neutrons.

Considering both a 0.1 and 1% $^{3}$He addition and varying the initial neutron energy, it can be seen that the number of activations continues to be significantly reduced across all energy

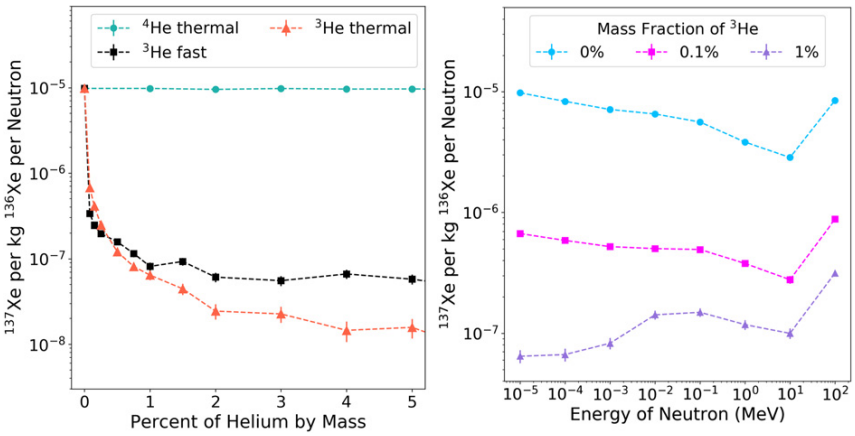


**Figure 3.** Left: number of $^{137}$Xe nuclei created by neutron capture with varying amounts of $^4$He and $^3$He. All thermal neutrons started at 0–10 eV and all fast neutrons started at 10 MeV. Right: comparison of helium plus enriched xenon and pure enriched xenon with varying neutron energies.

bins. Figure 3-right shows the dependency over several orders of magnitude in neutron energy. Such a reduction even at the 0.1% level appears sufficient to drive the $^{136}$Xe background in a ton-scale experiment to negligible levels, even at modest detector depths. We return to this point quantitatively in section 4.2.

There are notable features in the energy-dependencies of figure 3-right. The origins of these spectral effects were investigated by detailed examination of the Monte Carlo simulation predictions. The steady fall in activation as a function of energy between 10 eV and 1 MeV in pure xenon corresponds to the increasing probability that a neutron will leave the active volume without thermalizing as the energy increases. The neutron capture cross sections are also falling in this region, though the capture is predominantly effective for thermalized neutrons due to the very large number of scatters each neutron can undergo with its surroundings once thermal. The sharp increase in $^{137}$Xe production at around 10 MeV observed in all three curves corresponds to the sharp up-tick in rates of multi-neutron production processes at these energies. Both ($n$,2$n$) and ($n$,3$n$) cross sections on xenon and copper become large in this region, as can be seen in figure 1, right, reproduced from the ENDF database. Above 10 MeV, therefore, each primary neutron can be the parent of many more secondary neutrons, leading to enhanced production of $^{137}$Xe per injected parent neutron. The 'bump' in rate of capture at intermediate energies in the 1% $^3$He / $^{136}$Xe mix system is attributed to capture of fast neutrons by resonances in the $^{136}$Xe neutron capture cross section, shown in figure 1, left. In pure xenon and in the 0.1% $^3$He/$^{136}$Xe system, where the overwhelming majority of neutrons producing $^{137}$Xe are thermal, fast neutron captures are a negligible fraction of the population and no shape effect from these resonances is visible. In the 1% $^3$He/$^{136}$Xe system, with thermal neutrons effectively mitigated by $^3$He, fast neutron capture becomes a more substantial contribution. This transition explains the initially rapid drop breaking to a slower fall of figure 3, left. The addition of a small quantity of $^3$He quickly absorbs the majority of thermalized neutrons that have been slowed by repeated elastic collisions with $^{136}$Xe, for both initial injection energies. At higher concentrations the capture of fast neutrons becomes increasingly relevant, affecting the level at which the capture rate plateaus for high concentrations of $^3$He.

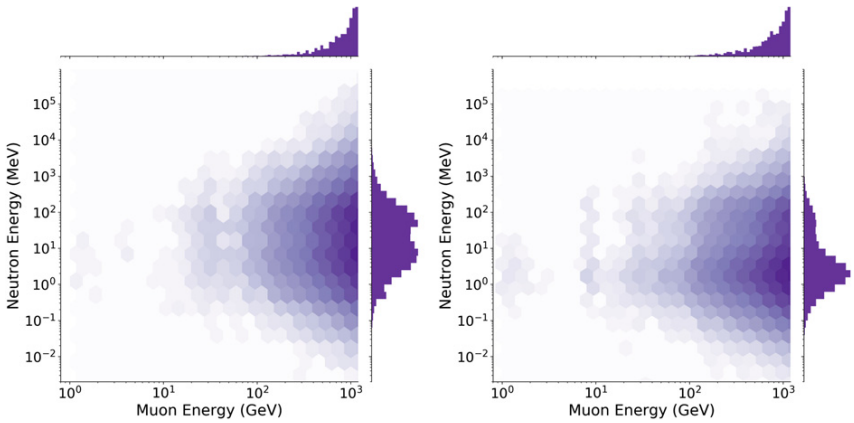


**Figure 4.** Left: correlation plot for neutron and muon energies for neutrons created within the water tank; right: correlation plot for neutrons created in detector materials.

### *4.2. $^{137}$Xe production from muons*

The source of neutrons most likely to reach the active volume of the detector comes in the form of spallation products created by muon-material interactions that thermalize in detector materials before being captured by the $^{136}$Xe. The showers created by muons are complicated systems, involving cascades of particles and a multitude of inelastic processes. Shown in figure 2-left is the expected cosmic muon energy spectrum in Laboratori Nazionali del Gran Sasso (LNGS) as calculated using the MUSIC muon simulation code [46]. To estimate the flux at different laboratories we have used the spectral shape for LNGS multiplied by the absolute normalization for different labs. While there is an expected hardening of the muon flux for deeper labs, our comparison of the SNOLab flux predicted by simply renormalizing LNGS flux with the measured flux from [47] shows that the effect is negligible within the precision of the present study.

To study the expected impact of the muon-material interactions, a high statistics simulation of muons uniformly distributed between 1 GeV and 3 TeV was performed. The neutron spectrum produced by muons interacting in the detector materials have energies in the range 0.01 MeV to 100 GeV (see figure 4). The distribution of neutron energies depends weakly on the muon energy, but the number of neutrons produced depends on it strongly. Figure 4 left gives the energy distribution of neutrons produced within the water tank, and figure 4 right gives the neutrons produced within the detector materials and xenon, but not the water tank. Additional contributions to the high energy peak in the water tank neutron energy distribution arise from capture processes including $\mu^- + p \rightarrow \nu + n$ and $\pi^- + p \rightarrow \gamma + n$. A sub-leading contribution from neutron, pion, and proton inelastic scattering populates the high energy peak in the detector volume.

The production of $^{137}$Xe per muon in the detector is the central result required to predict the contamination from $^{137}$Xe per unit time in an NEXT detector. Figure 5 shows the $^{137}$Xe production expectation per muon in bins of primary muon energy for pure xenon (left) and xenon with $^3$He admixtures (center). As suggested by the neutron production studies, there are more $^{137}$Xe produced at higher muon energies. Comparing the left and center plots from figure 5 (note the different vertical scales) it can be seen that there is significant magnitude reduction in $^{137}$Xe production with 0.1% $^3$He added across all muon energies. The right plot in

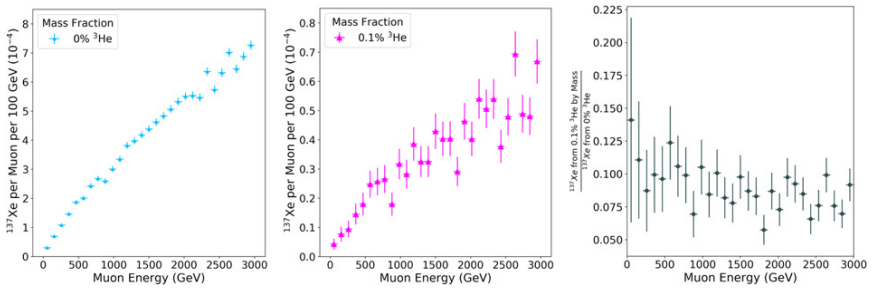


**Figure 5.** Production of $^{137}$Xe by various cosmic muons energies. Left: production per generated muon for pure enriched xenon; center: production with $^3$He doped gas. Note that the axes are scaled differently between both plots for easier comparison. Right: ratio of $^{137}$Xe produced in 0.1% helium gas mixture over the production in pure xenon.

figure 5 gives the ratio of the two, showing a cosmogenic background reduction of more than 10 times for 0.1% of $^3$He.

Additional contributions from neutrons produced by the muons in the rock surrounding the laboratory could be an additional contribution to the activations. Using the same simulation as described above and neutrons starting outside the water tank with energies over the range indicated by figure 4 we find a $^{137}$Xe production rate reduction in the presence of 0.1% $^3$He of the same order as that for muons.

We now consider an example experiment in Laboratori Nazionali del Gran Sasso (LNGS) where the cosmic muon energy spectrum is expected to be that shown in figure 2-left with an absolute flux normalization of $3.432 \times 10^{-8}$ cm$^{-2}$ s$^{-1}$ as measured by the Borexino experiment [48]. The impact on the background index of NEXT can be predicted using the spectrum shown in figure 2-left convolved with the activation expectations from figure 5. We predict the rate of activations per year shown in figure 6-left for the same experiment with and without 0.1% $^3$He.

Repeating this exercise for various laboratories (LSC, LNGS, SURF and SNOLab) we find the absolute counts of $^{137}$Xe yr$^{-1}$ shown in figure 6-right. Considering the full $^{137}$Xe decay spectrum without any filtering due to analysis, these numbers translate to the activation expectation indices shown in table 1. We note that while such absolute predictions carry a substantial uncertainty due to the physics of neutron production in high energy cascades, our primary results relating to the reduction of activation through $^3$He admixtures are expected to be robust at the twenty percent level.

To appreciate the impact of these activation rates on a given detector we must account for the acceptance factor for $^{137}$Xe decay electrons in the signal region of interest, after analysis cuts. Purely energy based arguments can already be used to reject most of these decays as the decay spectrum is broad and $0\nu\beta\beta$ experiments strive to achieve energy resolution at the few percent level. Most modern xenon gas experiments also have some power to reject single electron events in favor of the double electrons indicative of signal which further reduces this background. If we take into account the topological analysis and energy resolution of the NEXT experiment [6, 7], and a conservative, cut-based analysis, acceptance of $^{137}$Xe electrons into the signal sample is of order $1.65 \times 10^{-4}$ [49] for a symmetric ROI of width 22 keV at $Q_{\beta\beta}$. Table 1 also shows the background index that would be expected under these conditions.

A detailed evaluation of radiogenic backgrounds for the tonne-scale NEXT-HD detector, and how they relate to the initial $^{137}$Xe background contribution estimated in table 1 right, is

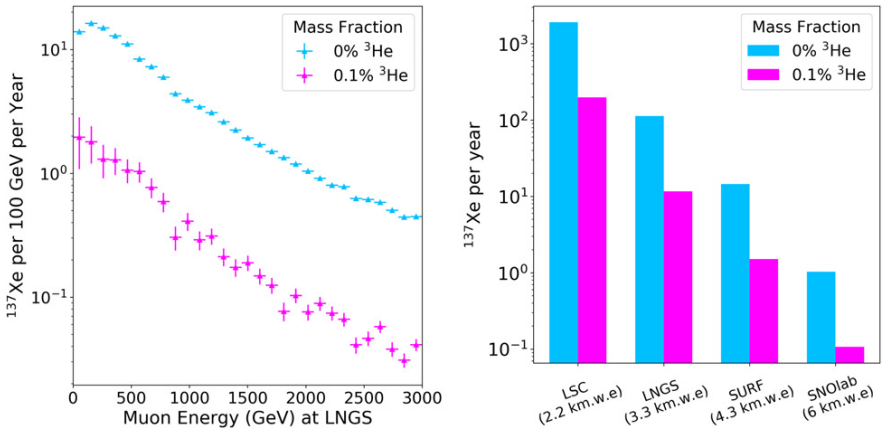


**Figure 6.** Left: rate of $^{137}$Xe activation expected as a result of the flux distribution of muon energies from LNGS. Right: $^{137}$Xe expected per year in four different underground laboratory locations and depths.

**Table 1.** $^{137}$Xe activation rate expectations with various percents of helium 3 by mass and example background indices given an analysis described in the text.

| | Activation rate | | Background index | |
|---|---|---|---|---|
| | 0% $^3$He ($kg^{-1}$ $year^{-1}$) | 0.1% $^3$He ($kg^{-1}$ $year^{-1}$) | 0% $^3$He ($keV^{-1}$ $kg^{-1}$ $year^{-1}$) | 0.1% $^3$He ($keV^{-1}$ $kg^{-1}$ $year^{-1}$) |
| LSC | $1.72 \times 10^{0}$ | $1.79 \times 10^{-1}$ | $1.29 \times 10^{-5}$ | $1.34 \times 10^{-6}$ |
| LNGS | $1.02 \times 10^{-1}$ | $1.06 \times 10^{-2}$ | $7.65 \times 10^{-7}$ | $7.91 \times 10^{-8}$ |
| SURF | $1.31 \times 10^{-2}$ | $1.36 \times 10^{-3}$ | $9.83 \times 10^{-8}$ | $1.02 \times 10^{-8}$ |
| SNOlab | $9.29 \times 10^{-4}$ | $9.65 \times 10^{-5}$ | $6.97 \times 10^{-9}$ | $7.24 \times 10^{-10}$ |

still underway. However, early estimates suggest that a successful experiment at a relatively shallow location such as LSC would benefit from the addition of $^3$He to the gas. At the multi-tonne scale, the background from $^{137}$Xe activation will become truly limiting, and its mitigation via this approach or others may become even more critical.

## 5. Economic viability

Two facts are widely known about $^3$He that should not be left unaddressed: (1) that is it is expensive, and (2) that the supply is limited. These factors influence discussions of the plausibility of, for example, practical nuclear fusion power based on $^3$He [50], which would speculatively consume tens of tonnes of raw $^3$He per year to meet the power needs of the United States. Such quantities do not exist worldwide at the present time, and have given rise to discussions of exotic acquisition strategies, such as mining the moon [51, 52], and more realistically in the near-term, breeding in nuclear reactors or extraction from oil and gas reservoirs [53].

Thankfully, far less $^3$He is required to mount a tonne or multi-tonne scale neutrinoless double beta decay program using a $^{136}$Xe/$^3$He mixture—on the order of 7500 l per tonne of $^{136}$Xe to achieve a 0.1% by mass concentration. The use of such quantities of $^3$He is precedented in

particle physics instrumentation. In the 1990s, for example, the SNO [54] experiment deployed an array of $^3$He counters to detect neutrons produced in neutrino interactions [55]. The quantity of $^3$He used was approximately 6000 l [29], similar to the quantity required for the presented application.

During the intervening decades since the existence-proof of the SNO+ $^3$He phase, the economics of $^3$He have changed in important ways. According to the 2010 Congressional Research Service report `The Helium-3 Shortage: Supply, Demand, and Options for Congress` [56], 'Helium-3 does not trade in the marketplace as many materials do. It is produced as a byproduct of nuclear weapons maintenance and, in the United States, is then accumulated in a stockpile from which supplies are either transferred directly to other agencies or sold publicly at auction.' US production in 2015 was estimated to generate approximately 8000 l of new $^3$He per year [53]. Until 2001 the price at auction was steady at $100 per liter, a little higher than the per-liter price of $^{136}$Xe. However, shortages instigated by the US need for neutron detectors for national security applications after the September 11 attacks of 2001, and the increased use of $^3$He in medical imaging [57] led to price spikes, reaching $2000/liter at times [58]. Even at the highest recent trading prices, however, the cost of the 0.1% component of $^3$He would be less than that of the 99.9% $^{136}$Xe component of the gas mixture. The stockpile and supply of US $^3$He is now directly controlled by the US Department of Energy, and not traded on an open market.

While this application would represent a significant fraction of one year's production, $^3$He can be efficiently extracted from $^{136}$Xe as needed, by liquefying or freezing the xenon and pumping to remove the helium component. This protocol is commonly employed in experimental studies with Xe/$^4$He mixtures (e.g. reference [13]). The separation process can be performed either completely or partially, as need arises, and so this application would represent storage and stewardship, rather than irreversible consumption. Furthermore, although $^3$He is a limited and expensive resource, it is notable that the majority isotope in this mixture is $^{136}$Xe, the world production and stockpile of which would both be zero, were it not for neutrinoless double beta decay experiments. Thus the difficulties associated with acquisition of the minority $^3$He component for temporary use in this manner should be assessed in relative terms. They do not appear prohibitive, based on the last traded market price, current levels of production, and precedented use cases in particle physics.

We may also consider alternative gases that have been explored to play a similar role to $^3$He in the face of limited supply. $BF_3$ enriched in $^{10}$B is one attractive possibility [59–63]. This gas has a high neutron capture cross section, can be mixed into xenon, and should not attach electrons. The challenge associated with $BF_3$ is that it is toxic, making operation of a detector in an underground laboratory challenging from a safety perspective. On the other hand, the $^{136}$Xe used in double beta decay experiments is sufficiently precious that they typically have elaborate systems to recapture the gas and to minimizes losses, even in small quantities, so perhaps $BF_3$ should not be immediately dismissed. Though this gas could offer the same function as a $^3$He additive without supply challenges, the R & D associated with circulating, purifying, achieving energy resolution in a Xe/$BF_3$ mix is likely more involved than with a Xe/He mix, which is why $^3$He has been our primary focus in this work.

## 6. Conclusions

The impact of the addition of small percentages of $^3$He to a tonne-scale underground high pressure xenon gas detector resembling NEXT-HD has been studied as a means to reduce backgrounds from the capture of thermal neutrons on $^{136}$Xe. Studies with injected neutrons show a reduction in the number of these activations of over 1 order of magnitude with as little

as 0.1% by mass of $^{3}$He doping. For higher energy neutrons, multi-neutron production from one initial parent is present, leading to larger production of $^{137}$Xe per primary neutron.

An example experiment with a fiducial mass of approximately 1 tonne surrounded with a water tank was used to study the impact on the background induced by the passage of cosmic muons. If the experiment took data at LNGS, an activation rate of $1.02 \times 10^{-1}$ kg$^{-1}$ year$^{-1}$ would be expected in the case of pure enriched xenon operation with a reduction to $1.24 \times 10^{-2}$ kg$^{-1}$ year$^{-1}$ expected with the addition of 0.1% $^{3}$He by mass. Similar predictions have been made for other underground sites. In addition to reducing background, the observed suppression of $^{137}$Xe can be used to relax requirements on the outer shielding, and potentially loosen analysis cuts designed to filter backgrounds from $^{137}$Xe for enhanced signal acceptance.

Given the background reduction power of high pressure xenon gas TPCs against beta decays from $^{137}$Xe, it is expected that any moderately deep underground laboratory, a $^{136}$Xe/$^{3}$He tonne or multi-tonne-scale experiment will be entirely free of background from cosmogenically activated $^{137}$Xe. As shown in figure 6, with $^{136}$Xe/$^{3}$He the number of $^{137}$Xe expected per year in LSC, the present home of NEXT-100 and the least deep laboratory considered, is lower than levels that would have a substantial effect on experimental sensitivity. This is true even when accounting for sizable uncertainties arising from cosmogenic shower modeling. We conclude that $^{136}$Xe/$^{3}$He mixtures may represent a promising technological component for future large high pressure xenon gas experiments.

## Acknowledgments

The work described was supported by the Department of Energy under Award numbers DE-SC0019054 and DE-SC0019223. The NEXT Collaboration acknowledges support from the following agencies and institutions: the European Research Council (ERC) under the Advanced Grant 339787-NEXT; the European Union's Framework Program for Research and Innovation Horizon 2020 (2014–2020) under the Marie Skłodowska-Curie Grant Agreements No. 674896, 690575 and 740055; the Ministerio de Economía y Competitividad of Spain under grants FIS2014-53371-C04, the Severo Ochoa Program SEV-2014-0398 and the María de Maetzu Program MDM-2016-0692; the GVA of Spain under grants PROMETEO/2016/120 and SEJI/2017/011; the Portuguese FCT under project PTDC/FIS-NUC/2525/2014, under project UID/FIS/04559/2013 to fund the activities of LIBPhys, and under grants PD/BD/105921/2014, SFRH/BPD/109180/2015 and SFRH/BPD/76842/2011. Finally, we are grateful to the Laboratorio Subterráneo de Canfranc for hosting and supporting the NEXT experiment.

## Appendix A

During the writing of this document a newer version of `GEANT4` was produced (`10.6.p01`) with some updates to the neutron production cross section. As a general cross check of the results additional data points were produced using this version of the simulation code.

Fast (10 MeV) and thermal (10 eV) neutrons were passed through the geometry as described in section 1 and the production rates for $^{137}$Xe can be seen in figure A1-left. We observed some systematic difference between `GEANT4` versions (`10.6.p01`) and (`10.5.p01`), with the largest discrepancy being for fast neutrons at 0.1% helium, where the ratio between simulated capture rates was $1.329 \pm 0.219$. This is within the envelope of systematic uncertainty ascribed to our results, and does not affect our primary conclusions.

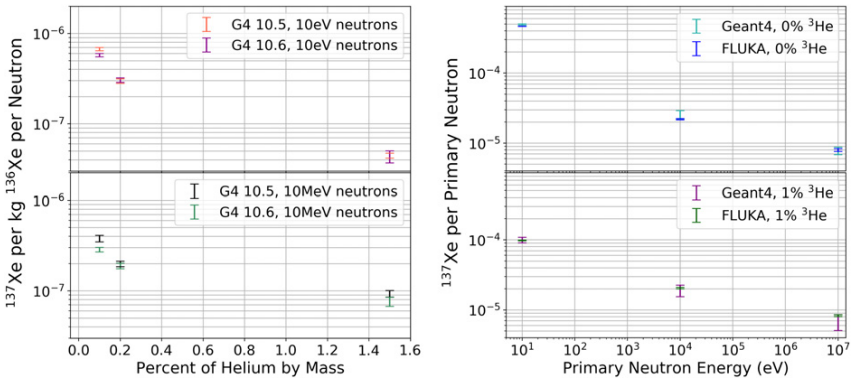


**Figure A1.** Left: rate of $^{137}$Xe activation expected as a result of thermal and fast neutrons with different GEANT4 versions. Right: $^{137}$Xe activation rates using FLUKA and GEANT4 10.5.p01.

As a further check of the validity of the results simulation of neutrons in GEANT4.10.5.p01 was compared to that in the 2011.2x-8 FLUKA Monte Carlo simulation package [64, 65]: a widely trusted tool for transport and interactions of low-energy neutrons. A simple 1 m by 1 m cylinder of enriched xenon gas and a mono-energetic beam of neutrons were simulated using both packages. Neutrons were injected uniformly along, and perpendicular to, one endcap of the cylinder. Figure A1-right shows a comparison of the rate of production of $^{137}$Xe in each simulation for a range of neutron energies. The results of GEANT4.10.5.p01 are compatible with 2011.2x-8 FLUKA within systematic uncertainties.

## ORCID iDs

L Rogers https://orcid.org/0000-0001-6505-1157
B Smithers https://orcid.org/0000-0003-1273-985X

## References

[1] Nygren D 2009 High-pressure xenon gas electroluminescent TPC for $0-\nu\,\beta\beta$-decay search *Nucl. Instrum. Methods Phys. Res.* A **603** 337–48
[2] Álvarez V *et al* NEXT Collaboration 2012 NEXT-100 Technical Design Report (TDR): Executive Summary *J. Instrum.* **7** T06001
[3] Alvarez V *et al* **NEXT** Collaboration 2013 Operation and first results of the NEXT-DEMO prototype using a silicon photomultiplier tracking array *J. Instrum.* **8** P09011
[4] Ferrario P *et al* **NEXT** Collaboration 2016 First proof of topological signature in the high pressure xenon gas TPC with electroluminescence amplification for the NEXT experiment *J. High Energy Phys.* JHEP01(2016)104
[5] Monrabal F *et al* NEXT Collaboration 2018 The Next White (NEW) Detector *J. Instrum.* **13** P12010
[6] Ferrario P *et al* NEXT Collaboration 2019 Demonstration of the event identification capabilities of the NEXT-White detector *J. High Energy Phys.* JHEP10(2019)052

[7] Renner J *et al* NEXT Collaboration 2019 Energy calibration of the NEXT-White detector with 1% resolution near $Q_{\beta\beta}$ of $^{136}$Xe *J. High Energy Phys.* JHEP10(2019)230
[8] Novella P *et al* NEXT Collaboration 2019 Radiogenic Backgrounds in the NEXT Double Beta Decay Experiment *J. High Energy Phys.* JHEP10(2019)051
[9] Martin-Albo J *et al* NEXT Collaboration 2016 Sensitivity of NEXT-100 to Neutrinoless Double Beta Decay *J. High Energy Phys.* JHEP05(2016)159
[10] Jones B J P 2016 XePA Project: Drift properties of helium added to xenon at 10 bar http://www-hep.uta.edu/ bjones/XePA/
[11] Felkai R *et al* 2018 Helium-Xenon mixtures to improve the topological signature in high pressure gas xenon TPCs *Nucl. Instrum. Methods Phys. Res.* **905** 82–90
[12] Henriques C A O *et al* NEXT Collaboration 2019 Electroluminescence TPCs at the thermal diffusion limit *J. High Energy Phys.* JHEP01(2019)027
[13] McDonald A D *et al* NEXT Collaboration 2019 Electron drift and longitudinal diffusion in high pressure xenon-helium gas mixtures *J. Instrum.* **14** P08009
[14] Fernandes A F M *et al* 2019 NEXT Collaboration electroluminescence yield in low-diffusion Xe-He gas mixtures (arXiv:1906.03984)
[15] Lippincott H, Alexander T and Hime A 2017 Increasing the sensitivity of LXe TPCs to dark matter by doping with helium or neon *PoS ICHEP2016* p 285
[16] Anton G *et al* EXO-200 Collaboration 2019 Search for Neutrinoless Double-Beta Decay with the Complete EXO-200 Dataset *Phys. Rev. Lett.* **123** 161802
[17] Albert J B *et al* EXO-200 Collaboration 2016 Cosmogenic Backgrounds to $0\nu\beta\beta$ in EXO-200 *J. Cosmol. Astropart. Phys.* JCAP04(2016)029
[18] Albert J B *et al* nEXO Collaboration 2018 Sensitivity and Discovery Potential of nEXO to Neutrinoless Double Beta Decay *Phys. Rev.* C **97** 065503
[19] Gando A, Gando Y, Hachiya T, Hayashi A, Hayashida S, Ikeda H, Inoue K, Ishidoshiro K, Karino Y, Koga M *et al* 2016 Search for Majorana neutrinos near the inverted mass hierarchy region with kamland-zen *Phys. Rev. Lett.* **117** 082503
[20] Jones B, McDonald A and Nygren D 2016 Single molecule fluorescence imaging as a technique for barium tagging in neutrinoless double beta decay *J. Instrum.* **11** P12011
[21] McDonald A, Jones B, Nygren D, Adams C, Álvarez V, Azevedo C, Benlloch-Rodríguez J, Borges F, Botas A, Cárcel S *et al* 2018 Demonstration of single-barium-ion sensitivity for neutrinoless double-beta decay using single-molecule fluorescence imaging *Phys. Rev. Lett.* **120** 132504
[22] Byrnes N, Denisenko A, Foss F Jr, Jones B, McDonald A, Nygren D, Thapa P and Woodruff K 2019 Barium tagging with selective, dry-functional, single molecule sensitive on-off fluorophores for the next experiment (arXiv:1909.04677)
[23] Thapa P, Arnquist I, Byrnes N, Denisenko A A, Foss F W, Jones B J P, Mcdonald A D, Nygren D R and Woodruff K 2019 Barium chemosensors with Dry-Phase fluorescence for neutrinoless double beta decay *Sci. Rep.* **9** 15097
[24] Rivilla I *et al* 2019 Towards a background-free neutrinoless double beta decay experiment based on a fluorescent bicolor sensor (arXiv:1909.02782)
[25] Woodruff K *et al* 2020 Radio Frequency and DC High Voltage Breakdown of High Pressure Helium, Argon, and Xenon (arXiv:1909.05860)
[26] Chadwick M, Herman M, Obložinskỳ P, Dunn M E, Danon Y, Kahler A, Smith D L, Pritychenko B, Arbanas G, Arcilla R *et al* 2011 ENDF/B-VII.1 nuclear data for science and technology: cross sections, covariances, fission product yields and decay data *Nucl. Data Sheets* **112** 2887–996
[27] Brown D A *et al* 2018 ENDF/B-VIII.0: The 8th Major Release of the Nuclear Reaction Data Library with CIELO-project Cross Sections, New Standards and Thermal Scattering Data *Nucl. Data Sheets* **148** 1–142
[28] Martinez-Lema G *et al* NEXT Collaboration 2018 Calibration of the NEXT-White detector using $^{83\,m}$Kr decays *J. Instrum.* **13** P10014
[29] Elliott S R, Heeger K M, Hime A, Robertson R G H, Smith M W E and Steiger T D 1999 Tritium contamination in ncds https://sno.phy.queensu.ca/sno/str/SNO-STR-99-006.ps.gz
[30] Agostinelli S *et al* GEANT4 Collaboration 2003 GEANT4: A Simulation toolkit *Nucl. Instrum. Methods Phys. Res.* A **506** 250–303
[31] Mughabghab S F 2006 *Atlas of Neutron Resonances: Resonance Parameters and Thermal Cross Sections. Z = 1–100* (Amsterdam: Elsevier)

[32] Albert J B, Daugherty S J, Johnson T N, O'Conner T, Kaufman L, Couture A, Ullmann J L and Krtička M 2016 Measurement of neutron capture on $^{136}$Xe *Phys. Rev.* C **94** 034617
[33] Batchelor R, Aves R and Skyrme T 1955 Helium-3 filled proportional counter for neutron spectroscopy *Rev. Sci. Instrum.* **26** 1037–47
[34] Manokhin V 1988 *Brond: USSR Recommended Evaluated Neutron Data Library, Tech. Rep.* (Vienna, Austria: International Atomic Energy Agency)
[35] Gibbons J and Macklin R 1959 Total neutron yields from light elements under proton and alpha bombardment *Phys. Rev.* **114** 571
[36] Haesner B, Heeringa W, Klages H, Dobiasch H, Schmalz G, Schwarz P, Wilczynski J, Zeitnitz B and Käppeler F 1983 Measurement of the $^{3}$He and $^{4}$He total neutron cross sections up to 40 MeV *Phys. Rev.* C **28** 995
[37] Antolković B, Paić G, Tomaš P and Rendić D 1967 Study of neutron-induced reactions on He$^{3}$ at $E_{\mathrm{n}} = 14.4$ MeV *Phys. Rev.* **159** 777
[38] Seagrave J, Cranberg L and Simmons J 1960 Elastic scattering of fast neutrons by tritium and He$^{3}$ *Phys. Rev.* **119** 1981
[39] Sayres A R, Jones K and Wu C 1961 Interaction of neutrons with He$^{3}$ *Phys. Rev.* **122** 1853
[40] Als-Nielsen J and Dietrich O 1964 Slow neutron cross sections for He$^{3}$, B, and Au *Phys. Rev.* **133** B925
[41] Bertini H W 1963 Low-Energy Intranuclear Cascade Calculation *Phys. Rev.* **131** 1801–21
[42] Barashenkov V S, Bertini H W, Chen K, Friedlander G, Harp G D, Iljinov A S, Miller J M and Toneev V D 1972 Medium energy intranuclear cascade calculations - a comparative study *Nucl. Phys.* A **187** 531–44
[43] Bertini H W 1969 Intranuclear-cascade calculation of the secondary nucleon spectra from nucleon-nucleus interactions in the energy range 340 to 2900 MeV and comparisons with experiment *Phys. Rev.* **188** 1711–30
[44] Heikkinen A, Stepanov N and Wellisch J P 2003 Bertini intra-nuclear cascade implementation in GEANT4 (arXiv:nucl-th/0306008)
[45] Wright D and Kelsey M 2015 The GEANT4 Bertini cascade *Nucl. Instrum. Methods Phys. Res.* A **804** 175–88
[46] Kudryavtsev V 2009 Muon simulation codes music and musun for underground physics *Comput. Phys. Commun.* **180** 339–46
[47] Aharmim B, Ahmed S N, Andersen T C, Anthony A E, Barros N, Beier E W, Bellerive A, Beltran B, Bergevin M, Biller S D *et al* 2009 Measurement of the cosmic ray and neutrino-induced muon flux at the Sudbury neutrino observatory *Phys. Rev.* D **80** 012001
[48] Agostini M *et al* Borexino Collaboration 2019 Modulations of the Cosmic Muon Signal in Ten Years of Borexino Data *J. Cosmol. Astropart. Phys.* JCAP02(2019)046
[49] Muñoz Vidal J 2017 The NEXT path to neutrino inverse hierarchy *PhD Thesis* Valencia U., IFIC
[50] Wittenberg L, Santarius J and Kulcinski G 1986 Lunar source of $^{3}$He for commercial fusion power *Fusion Technol.* **10** 167–78
[51] Bilder R B 2009 A legal regime for the mining of helium-3 on the moon: US policy options *Fordham Int'l LJ* **33** 243
[52] Taylor L A 1994 Helium-3 on the moon: model assumptions and abundances *Engineering, Construction, and Operations in Space IV* (*ASCE*) pp 678–86
[53] Slocum C A 2016 Defining the Helium-3 industry for private sector *Current and Projected Resources, Supply/demand, Processing and Transportation of the Critical Mineral Isotope 3-He* (Eastborough, KA: Arizona Oil and Gas Inc.)
[54] Ahmad Q R *et al* SNO Collaboration 2002 Direct evidence for neutrino flavor transformation from neutral current interactions in the Sudbury Neutrino Observatory *Phys. Rev. Lett.* **89** 011301
[55] Amsbaugh J F, Anaya J, Banar J, Bowles T, Browne M, Bullard T, Burritt T, Cox-Mobrand G, Dai X, Deng H *et al* 2007 An array of low-background $^{3}$He proportional counters for the Sudbury neutrino observatory *Nucl. Instrum. Methods Phys. Res.* A **579** 1054–80
[56] Shea D A and Morgan D L 2011 The helium-3 shortage: supply, demand, and options for Congress *Report* R41419 Congressional Research Service
[57] Tastevin G 2000 Optically polarized helium-3 for NMR imaging in medicine *Phys. Scr.* **2000** 46

[58] Fain S, Schiebler M L, McCormack D G and Parraga G 2010 Imaging of lung function using hyperpolarized helium-3 magnetic resonance imaging: review of current and emerging translational methods and applications *J. Magn. Reson. Imag.* **32** 1398–408

[59] Korff S and Danforth W 1939 Neutron measurements with boron-trifluoride counters *Phys. Rev.* **55** 980

[60] Lintereur A, Conlin K, Ely J, Erikson L, Kouzes R, Siciliano E, Stromswold D and Woodring M 2011 $^{3}$He and $BF_3$ neutron detector pressure effect and model comparison *Nucl. Instrum. Methods Phys. Res.* A **652** 347–50

[61] Goodings A and Leake J W 1972 Neutron counter filled with boron trifluoride gas *US Patent* 3702409

[62] Fowler I and Tunnicliffe P 1950 Boron trifluoride proportional counters *Rev. Sci. Instrum.* **21** 734–40

[63] Segrè E and Wiegand C 1947 Boron trifluoride neutron detector for low neutron intensities *Rev. Sci. Instrum.* **18** 86–9

[64] Böhlen T, Cerutti F, Chin M, Fassò A, Ferrari A, Ortega P, Mairani A, Sala P, Smirnov G and Vlachoudis V 2014 The FLUKA code: Developments and challenges for high energy and medical applications *Nucl. Data Sheets* **120** 211–4

[65] Ferrari A, Sala P R, Fassò A and Ranft J 2005 *FLUKA: A Multi-Particle Transport Code* (*Program version*)

# Chapter 6

# Measurement of Cosmogenic Backgrounds in NEXT-White

One source of backgrounds in almost all neutrinoless double beta decay experiments is muons which create spallation neutrons that are later captured producing prompt gammas and longer-lived nuclei which can decay at energies that produce a signal resembling $0\nu\beta\beta$ . As detectors get larger and the radiogenic backgrounds are decreased through purer material selections and larger fiducial volumes in relation to the detector materials, cosmogenic backgrounds will start to dominate. In NEXT specifically, the volume of enriched xenon provides the ideal environment for $Xe^{137}$ to be created through neutron capture on $Xe^{136}$, which decays with $Q_\beta$ of 4.2 MeV.

As discussed in chapter 5, one option to reducing these backgrounds is to use an additive that can absorb the neutrons that will later decay with a low enough energy to avoid the region of interest. The other options are to avoid muon interactions from occurring as much as possible by going deep underground to maximize shielding benefits of the overburden rock, or to trigger whenever a muon passes through and discard all events that occur directly after it. This work covers the steps taken to measure and classify the muon rate within NEXT-White as the spallation neutrons and therefore background rates are proportional to the muon flux at the detector site. This includes simulating from primary cosmic rays, through the atmosphere, and down to the detector for a well predicted muon flux to then be compared with the data.The results are also compared against an independent measurement in the same laboratory using a different detection technology.

Many experiments use a muon trigger such as a water tank lined with PMTs on the outside to count exactly how many muons pass and when. Neither NEXT-White nor NEXT-100 will have this option so the analysis in this chapter focuses on recognizing the muon characteristics within the detector volume. This work thus provides an important constraint on the rate of backgrounds produced from cosmological muon origins during Run Va,b, and c data taking of NEXT-White, covering a total of 271.6 days.

## 6.1 Track Finding

The most identifying characteristic of a muon passing through the detector is that it will pass straight through without stopping. As it goes through the NEXT detector it ionizes a stream of gas which can be recognized as a straight track. Though there can also be additional activity along with the track due to delta rays and other inelastic collisions, the straight line can be extracted for a muon identification parameterized by the zenith and azimuthal direction of the incoming muon. The initial energy of the muon cannot be extracted because muons in this

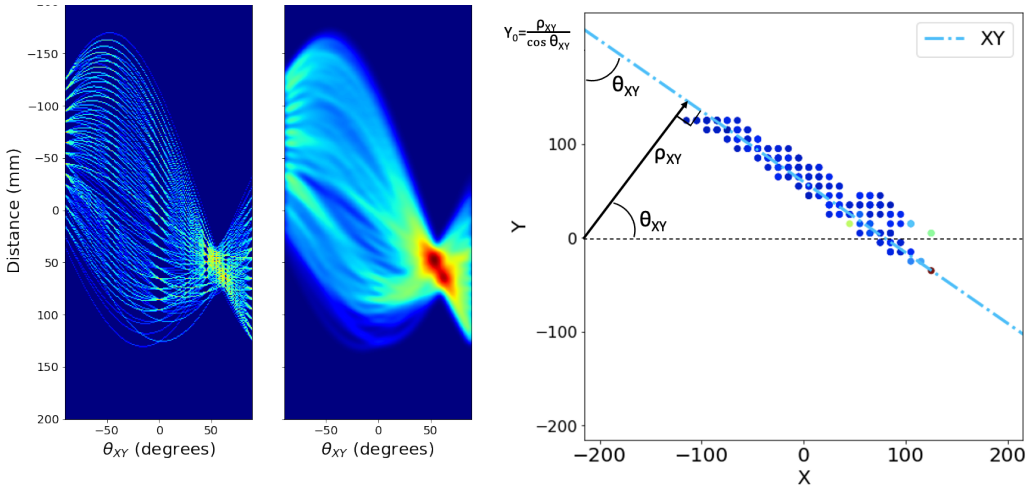


FIGURE 6.1: Left: Hough space for points from sipm data. Center: Hough space after convolving the accumulator matrix. Right: 2D representation of a rho and theta mapping to the main track line.

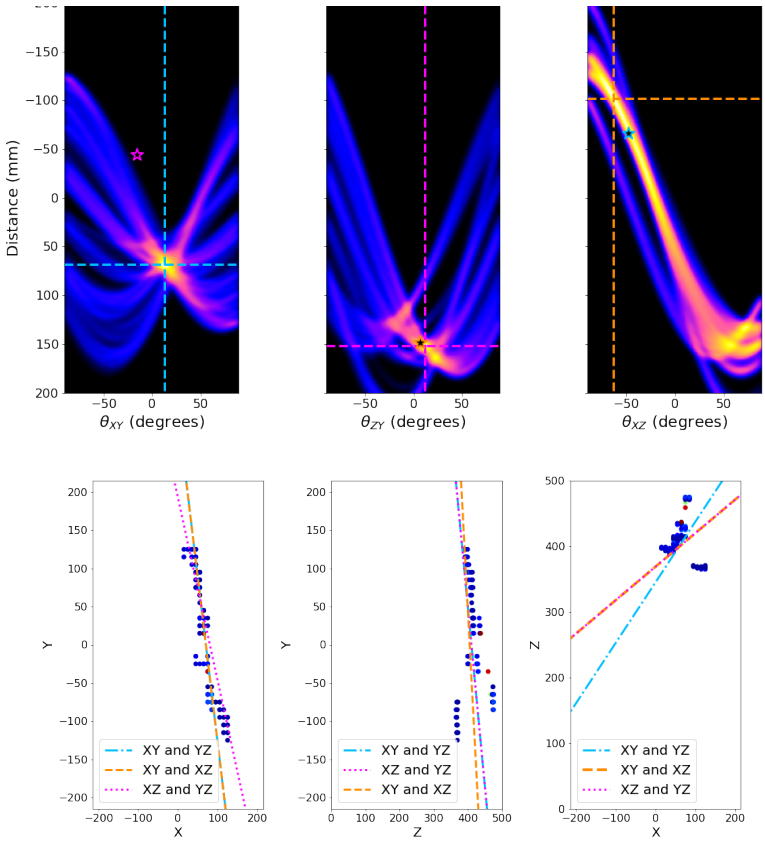


FIGURE 6.2: Top: Hough space for each plane where the dashed lines represent the selected point from the accumulator matrix and the stars represent the projection of the other two accumulator matrices. Bottom: Lines created from each pair of hough spaces.

energy range are approximately minimally ionizing. We validate the energy independence of the signature in our energy range of interest later with dedicated simulations.

To reconstruct the path of the muons we use the method of two dimensional Hough transformations. This works by converting every 2D data hit point into a set of parameters describing every line passing through that point in 2D space. Here we use parameters rho, the shortest distance between the line and the origin, and theta, the angle of the line from the negative vertical axis. Each of these theta and rho values is logged as a point in an accumulator matrix. The accumulator matrix is initially [2*diagonal length of the detector plane, number of angles] in size and filled with zeros. As each rho and corresponding theta value is found, 1 is added to that location in the matrix. Once each data point has been converted and saved, the max value location is extracted from the matrix for a rho and theta value correlating to the line describing the line in this projected plane to the main track as shown in Fig. 6.1 right.

Since the data is from a pixelated source, in this case SiPMs on a square array, the Hough transform space often has multiple faux max values as an artifact from the detector. To remove

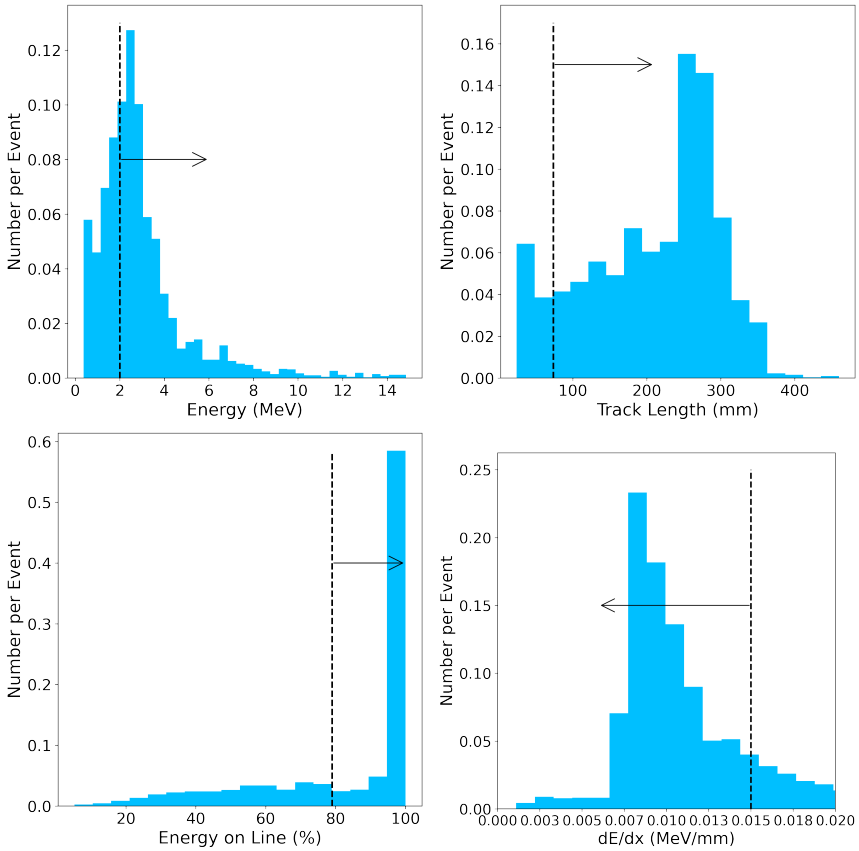


FIGURE 6.3: Upper Left: Energy distribution of all muons that passed through the fiducial volume. Upper Right: Length of the track within the detector for Monte Carlo muons. Everything right of the black dashed line would be kept in final analysis. Bottom Left: Percent of the total event energy that was within the chosen allowed distance from the line. Everything to the right of the black dashed line would be kept in final analysis. Bottom Right: The energy lost per mm traversed within the accepted distance from the track. Everything left of the black line is be kept for finding muons.

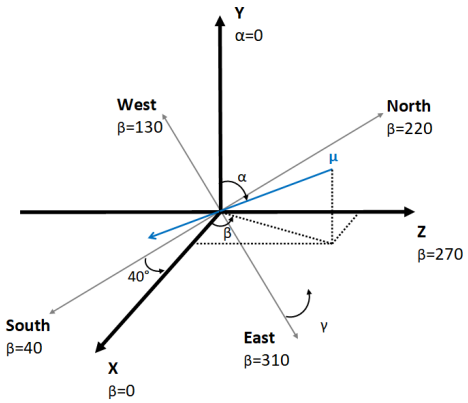


FIGURE 6.4: Right: How angles are defined with respect to detector coordinates.

these artifacts the accumulator matrices are convolved with $e^{-0.1t^2}$ resulting in a smoothing of the Hough space as shown in Fig. 6.1. Here the maximum value can be extracted resulting in a line tracing the path of the original muon that is consistent with the largest possible number of points in this plane.

NEXT-White collects data in three dimensions, therefore two accumulator matrices need to be calculated; one each for two separate planes in order to parametrize a line in three dimensions. The resulting rhos and thetas then are combined to find the polar coordinates of the track. To ensure the best fit, an accumulator matrix is determined in all three planes and each combination of two is projected into the third Hough space, represented by the stars in Fig. 6.2. Taking the value of the accumulator matrix in that location and multiplying by the location values of the original two gives the strength of the match with the largest product of the three plane hough spaces used to select which two planes to use. In the case shown here, using the ZY and XZ plane projects into an empty space in the XY accumulator matrix, being a less good fit than the other two combinations.

Fig. 6.4 shows how angles are defined within this text where X,Y, and Z are detector coordinates. The detector is 30°off North with the origin being at the center of the detector. When observing azimuth trends we define $\beta$ as the angle counter clockwise off X towards the Z plane. The zenith angle is defined off the y axis and is the same whether in detector or coordinate systems. Simulations were done with $cos\alpha > 0.4$ as we could not account for the undulations of the Pyrenees mountains at the shallowest angles. When working with global coordinate systems we choose to define $\gamma$ as the angle anticlockwise off East.

## 6.2 Muon Selections

Separating muons from all other backgrounds is necessary for measuring the cosmogenics background activity over a much more frequent radiogenic background rate. To ensure a true classification of muons we make selections based on muon characteristics. Because muons originate from outside the detector and traverse through, only events touching the edges of the fiducial volume with long track lengths need evaluation. For this we initially simulated several million monte carlo events and found the length of all events with energy greater than 2 MeV, seen in the histograms of Fig. 6.3. With muons passing straight through the detector, it is expected that most of the charge generated is within a few centimeters of the track. For this

we evaluate how much of the energy deposited was within 3.5 cm of the track line, shown in Fig. 6.3 bottom left. This histogram shows a very clear peak near 100 % of the event's energy being on the track. Muons are minimally ionizing particles and will have a dE/dx of around .007 MeV/mm in xenon, with the measurements found from muons through NEXT shown in Fig. 6.3 bottom right. We cut at dE/dx less than .015 MeV/mm and tracklengths greater than 73.5 mm in order to reject backgrounds.

Using Fig. 6.3 it was determined to use a combination of cuts including a track length longer than 73.5 mm, percent of the total energy deposited being within 35 mm greater than 79 %, and a dE/dx less than .015 MeV/mm. We also included an initial total energy deposit of 2 MeV to reduce computation time.

Placing these cuts on muons, background, and $2\nu\beta\beta$ Monte Carlo events results in Fig. 6.7. Demonstrated here is the strength of both the the track length cut and a dE/dx cut. These two cuts remove only a small fraction of muon candidate events while rejecting most other background events. These plots all include the fiducial cut in order to demonstrate more clearly the strength of the other cuts. Combining all the cuts, Fig. 6.5 shows the events remaining that would be positively identified as a muon. While the muons with the highest deposited energy are all lost, these happen so infrequently within the detector that this is not considered a concern. Note that this subsample of high deposited energy muons corresponds to those with much inelastic activity in the detector far from the track. We will show later that the dependence of our cuts on the true initial muon energy is not very large. After this series of cuts less than 0.009 % of $2\nu\beta\beta$ decay events are misidentified as muons and 0.125 % of the background are misidentified.

To check how close the reconstructed track directions are to the original muon tracks, we take the dot product of the reconstructed track to the Monte Carlo truth track, created from the start and end location of the muon. This gives the opening angle between the two tracks and provides a measure for the goodness of fit for the reconstructed tracks where the dot product equalling 1.0 represents perfect resolution for the incoming angles.

Starting with the entire set of Monte Carlo muon events and then taking different cuts for the features defined above results in Fig. 6.7. As expected, as cuts are applied to select better quality

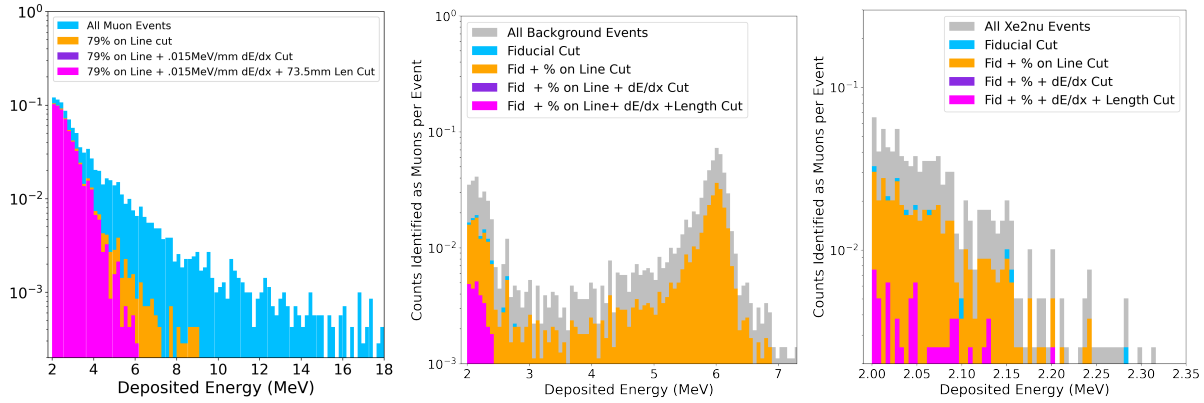


FIGURE 6.5: Left: Histogram of the different deposited energies within the detector volume from Monte Carlo muons. Each color represents the addition of another cut selecting out the muons. Middle: Monte Carlo background events of different deposited energies within the detector that pass each cut. Right: Monte Carlo two neutrino double beta decay events of different deposited energies within the detector that pass each cut.

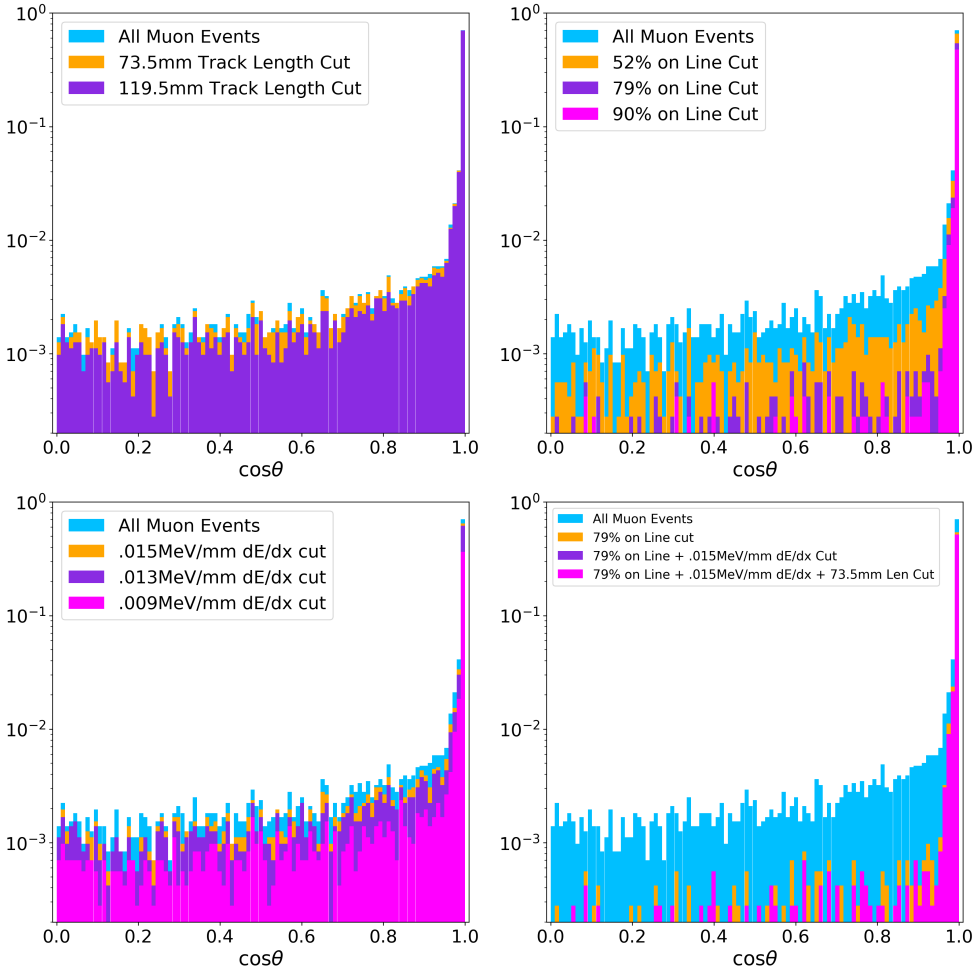


FIGURE 6.6: The dot product, i.e. $\cos\theta$ between the line found with a Hough transform and the Monte Carlo truth line where 1.0 is a perfect match. Each color represents a tighter cut selecting out the muons. Upper left: Cuts Selecting only events where the track length is at least 73.5 mm (orange) or 119.5 mm (purple) minimum. Upper Right: Cuts based off what percent of the total event energy deposited is within 35 mm of the reconstructed track line. Bottom left: Cuts based on the dE/dx values found from the energy near the track divided by the length. Bottom right: Histogram showing the muon events left with with each additional cut.

events, the angular resolution improves. The percent of the energy contained within 3.5 cm of the track is the strongest correlation to an accurate muon detection. Final cuts are chosen based off Figure 6.3 and once all three cuts are taken together as shown in Figure 6.6 right, there is a very sharp peak around 1.0, four orders of magnitude higher than the other events that remain after the three cuts are made. This peak proves the great accuracy in this method.

An additional cut that was required for the data analysis was a way to remove sparks. Discussed in Chapter 3, the electroluminescent region is under a high electric field which will occasionally result in break down as discussed in Chapter 4. While the collaboration tries to keep the voltage below the breakdown point, the charges will still build up over time on any imperfection within the EL region and jump across the gap. Whenever this occurs it creates a

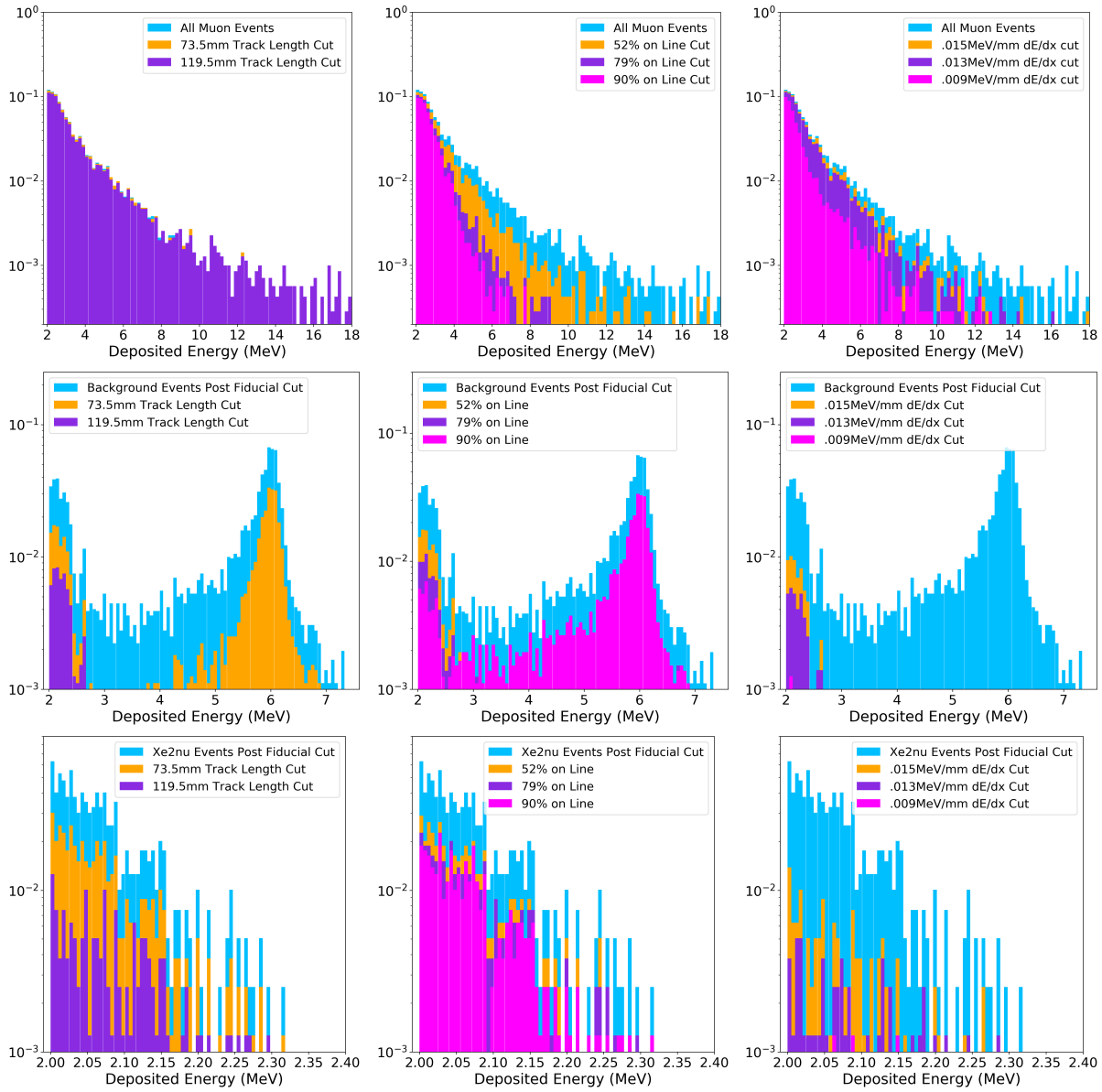


FIGURE 6.7: Top row: histograms of number of muon events found from Monte Carlo events with each amount of energy deposited within the detector. Second row: Histograms of number of false muon events found from Monte Carlo background events with each amount of energy deposited within the detector. Third row: Histograms of number of false muon events found from Monte Carlo two neutrino double beta decay events with each amount of energy deposited within the detector. Left Column: Selecting only events where the track length is at least 73.5 mm (orange) or 119.5 mm (purple) minimum. Middle Column: Cuts based off percent of the total event energy deposited within 35 mm of the reconstructed track line. Right Column: Cuts based on the dE/dx values found from the energy near the track divided by the length.

large flash of hits in X and Y in an instant in time as shown in Fig.6.8. This correlates to a $\theta_{XZ} = 0$ and a variance in $Z \approx 0$. To account for this we removed any events that had a variance in Z of less than 4 ms and a $\beta$-330°<4 value. This cut was performed on both Monte Carlo events and data events for the final analysis.

## 6.3 Predictions of Muon Flux

In order to predict the background rate created by cosmogenics the flux of muons through the detector has to first be known. To calculate the flux of muons that pass through the detector a three-stage simulation is made, to predict the rate from first principles, abstractly shown in

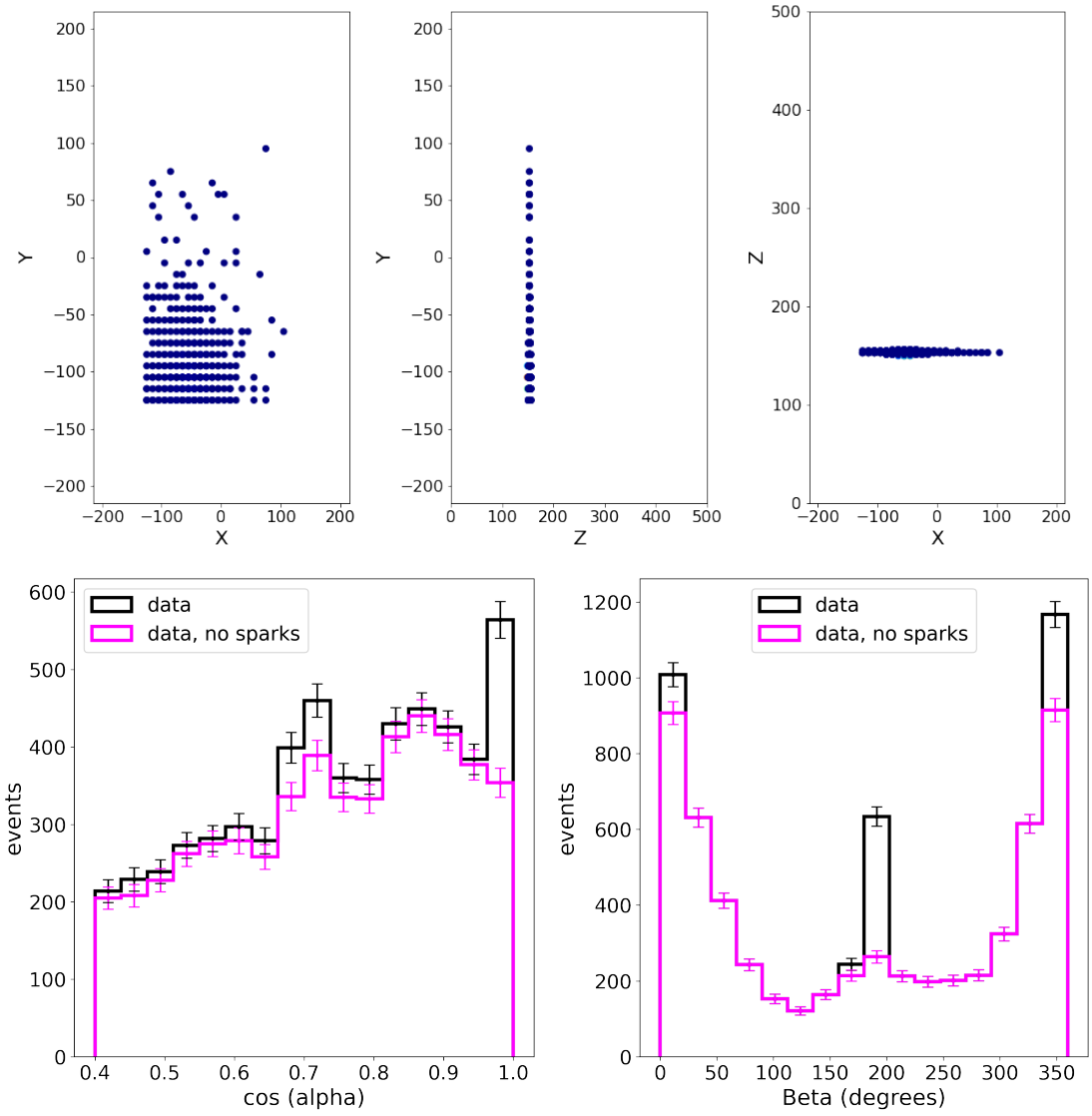


FIGURE 6.8: Top: Spark that occurred in one of the data run events where the events have a constant z because they happened instantaneously but x and y has a large spread of hits. Bottom left: cos $\alpha$ before and after spark cuts. Bottom right: $\beta$

Fig. 6.9. A primary cosmic ray model is simulated above the atmosphere then propagated down to the mountain under which NEXT-White is held. This cosmic ray propagation is done using Matrix Cascade Equations (MCeQ)[66] which simulates cosmic air showers through the atmosphere down to a given altitude from each angle input and is explained in more detail in Sec. 6.3.2. Section 6.3.3 then describes the propagation of muons through the rock of the mountain which is done with PROPOSAL. Section 6.3.4 covers how the outputs of MCeQ and PROPOSAL are combined in order to predict a muon flux through the laboratory. To then turn that flux into an expected signal rate Monte Carlo simulations of muons passing through the lead castle, the vessel, field cage, and finally through the active volume are done using Nexus as described in Sec. 6.3.5, the output of which is then passed through electronics and trigger simulations and then passed through our muon selection code to provide the efficiency of the detector. The final predicted rate is compared to the rate observed in data with the same cuts, and with an independent measurement using a different detection technology in the same laboratory.

### 6.3.1 Mt. Tobazo Profile

The flux of muons arriving from different azimuth and zenith combinations is dependent on how much atmosphere then mountain rock must be passed through before reaching the detector. For this analysis we took a 3d topographical map of the Pyrenees mountains above the Laboratorio Subterráneo de Canfranc (LSC) and inserted the location of the detector. Only one strip of the mountain was available so we extrapolated out on the edges where data was missing by linearly interpolating the height of the mountain for X,Y values. This does introduce some uncertainty on the flux predictions as they are dependent on whether the muons are transversing atmosphere

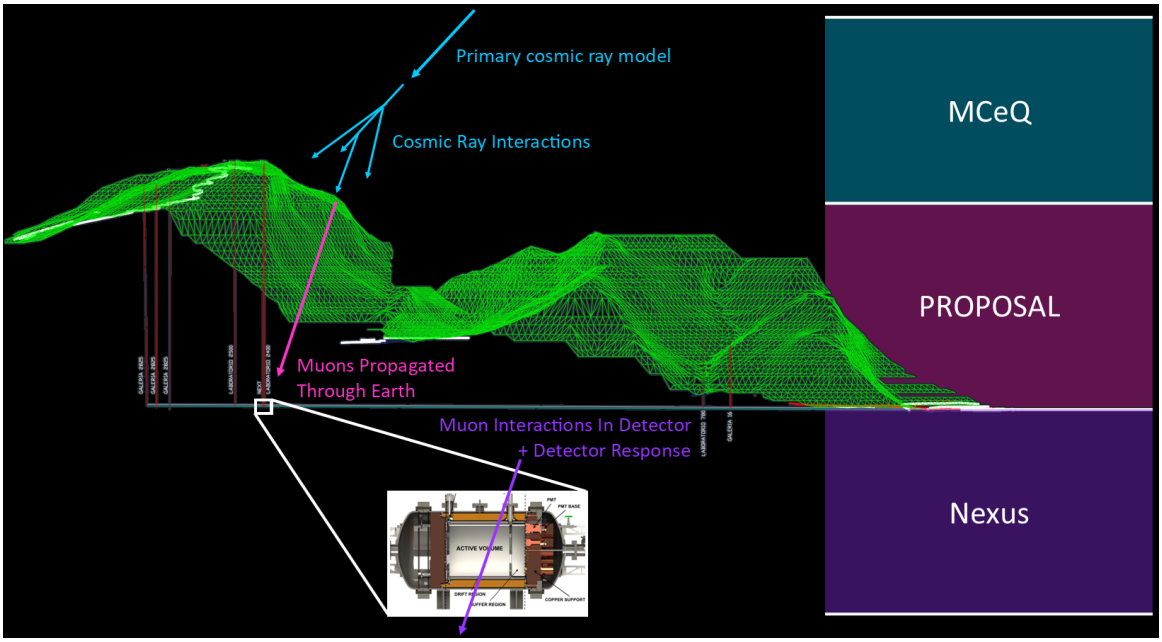


FIGURE 6.9: Steps of simulation taken to create a prediction of muons flux through the NEXT-White detector. Starting with a primary ray model and modeling the cosmic ray interactions in the atmosphere with MCeQ. Then propagating the muons through the mountain rock until they are dispersed or reach the detector where the detector's response is then modelled with Nexus.

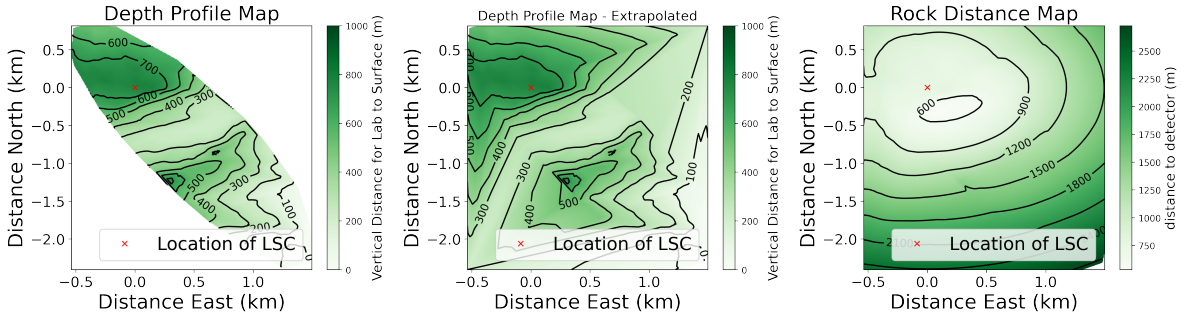


FIGURE 6.10: Left: Depth of mountain measured above the laboratory. Middle: Extrapolated depth of mountain above the laboratory for all X and Y values used in this analysis. Right: Distance of rock from each location to the detector. Note these plots are shown with North being in the positive Y direction and do not directly correspond to detector coordinates.

vs rock though in preliminary studies we found the uncertainty due to the extrapolation method to be subleading to the cosmic ray propagation uncertainties that will be described below. From this mountain profile the amount of rock a muon must past through to reach the detector coming from each X and Y location on the mountain in relation to North and East, (positive Y and positive X respectively) was calculated. The height of the mountain above the depth of the laboratory and corresponding distances of rock to detector can be seen in Fig. 6.10.

### 6.3.2 Matrix Cascade Equations

MCeQ simulates cosmic air showers that arrive from a given zenith direction at a given altitude so that we have a flux prediction all along the surface of the mountain. For this the heights of Fig. 6.10 Left were used with the addition of height above sea level as MCeQ needs the column depth of the atmosphere to simulate through as the rate and energy of muons is dependent on the height of the observation point within the evolving atmospheric cosmic ray air shower. To validate predictions were coming out of MCeQ as expected, we compared with [67] and found the muon flux matched at $\cos\theta = 1$ and $\cos\theta = .05$. For low angles and moderate energies [68] gives the following equation for muon flux:

$$\frac{dN_\mu}{dE_\mu d\Omega} \approx \frac{0.14 E_\mu^{-2.7}}{cm^2 \text{s sr GeV}} \times \left\{ \frac{1}{1 + \frac{1.1 E_\mu \cos\theta}{115 \text{GeV}}} + \frac{0.054}{1 + \frac{1.1 E_\mu \cos\theta}{850 \text{GeV}}} \right\} \tag{6.1}$$

which is plotted as a dashed line in Fig. 6.11 Left. This equation does not account for charge of the muon so the summation of both positive and negative muons simulated through MCeQ are shown here in red and grey. To account for systematic uncertainties two different cosmic ray flux models are used; Zatsepin Sokolskaya and Hillas Gaisser. Hillas Gaisser uses the fact that there are more $\mu^+$ than $\mu^-$ to calculate the excess of protons over neutrons[69] and to give an estimate of the energy spectra for each at the edge of the atmosphere. Zatsepin Sokolskaya takes a different approach by directly measuring the cosmic ray spectra above the atmosphere and with ground extensive air shower arrays[70] to model the initial flux and energies.

Currently both primary cosmic ray fluxes were run with the hadronic interaction model 'SIBYLL23C'. SIBYLL is tuned to accelerator data and models hadron-hadron interactions at high energies and hadron-nucleus interactions at the highest energies creating jet pairs[71]. SIBYLL

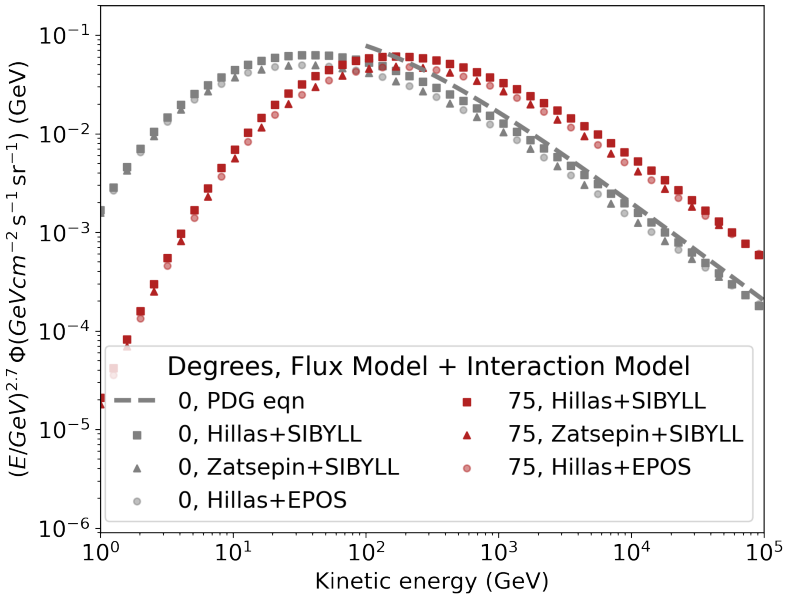


FIGURE 6.11: Left: Demonstration of MCeQ muon flux outputs of various energies using two different cosmic ray flux models matching the prediction of muon fluxes from the PDG which can also be directly compared with Fig. 3 right in [67].

takes the primary spectrum of the cosmic rays and uses a fragmentation process to give particle production rates from there as they cannot be calculated from first principles. This is done by assuming a uniform energy density between two partons which is split by quark-antiquark pair production and continues splitting until the energy remaining is just enough to form two hadrons[72].

For these interactions CORSIKA is used with SIBYLL to model the atmospheric density that SIBYLL requires to determine the probability of interaction or decay of high energy mesons[73], generating yields for the MCeQ solver. The density profile chosen was for Karlsruhe, Germany with no seasonal dependence which was the closest option available to Canfranc, Spain. When the detector gets to the ton scale seasonal dependence will likely become more applicable, but for the NEXT-White scale detector there are not enough muon interactions to have a measurable difference.

Figure 6.12 shows how the flux of muons varies over incoming angles and energies, at the point where air showers pointing towards the detector intersect the mountain surface. The spectrum falls rapidly with energy, with visible features due to the altitude and angular dependence of the flux on the surface. For mid range energies the mountain profile takes effect as the higher the mountain profile the more muons will arrive.

### 6.3.3 PROPOSAL

We use PROPOSAL[74] to determine what percentage of muons survive to the detector at each angle and energy. Using the mountain profile calculations of distance to the detector at different alpha and beta angles, we simulated muons of various starting energies through the mountain assuming standard rock with density 2.65 $g/cm^3$ [75]. Lower energy muons would lose all their energy before reaching the detector leading to 0 % survival whereas high energy results in 100 % of the muons reaching the detector. The plots in Fig. 6.13 demonstrate this by showing the

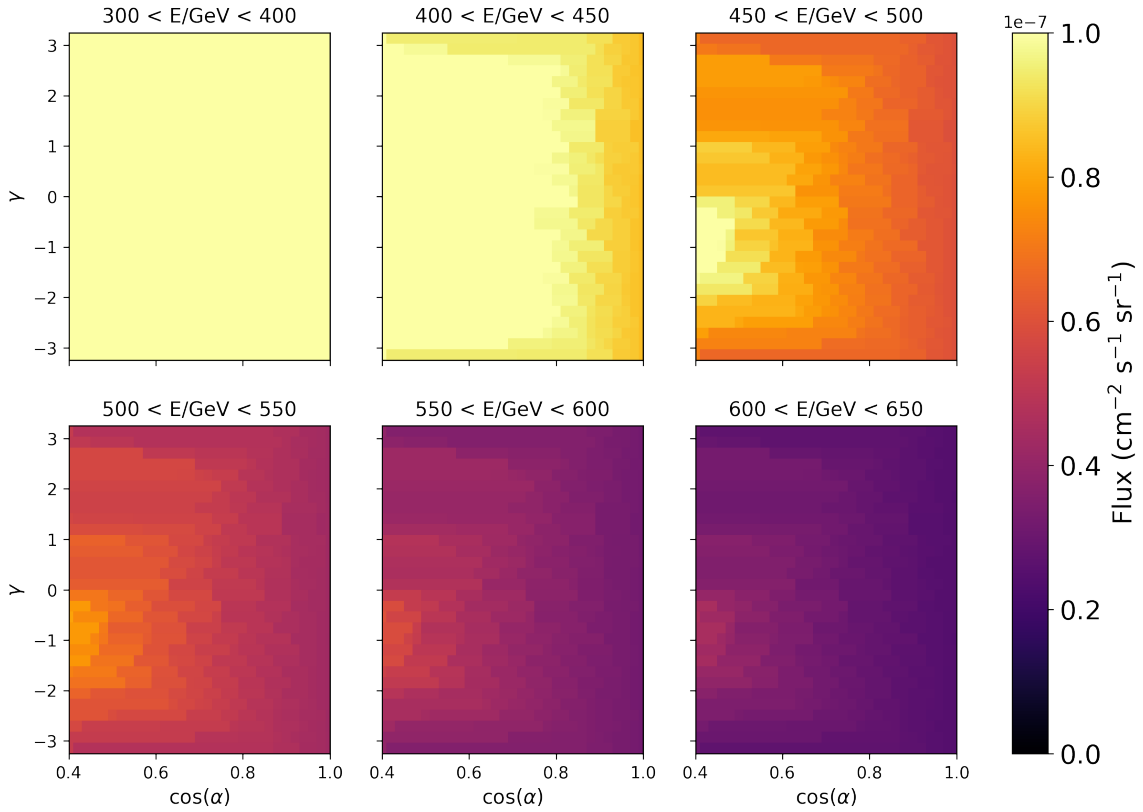


FIGURE 6.12: MCeQ predictions of flux of muons expected at each angle for various energies.

survival fraction of the muons to the detector for various energies. The plots also show how the mountain could in principle be mapped backwards from muon measurements as more muons come through the valley, and less from the more dense mountain topography. We note in passing that this method is how Alvarez et al discovered a hidden room in the great pyramids[76].

The Monte Carlo code PROPOSAL (PRopagator with Optimal Precision and Optimized Speed for All Leptons)[74] simulates leptons through transparent and opaque media. This code includes cross sections for all the ways a muon will interact with its surroundings and calculates energy loss. The muons will lose energy through a variety of processes until decay. At low energies the muons will lose energy through ionization and while the muon is heavier than the electron and loses less energy through bremsstrahlung than its lighter counterpart, it still encounters losses through elastic and inelastic bremsttraulung at these energiers[68]. PROPOSAL also takes into account losses through photonuclear interactions between the muons and atomic nuclei and electron pair production in the field of the nuclei.

### 6.3.4 Combining MCeQ and PROPOSAL

To obtain a full prediction of the muon flux arriving at the detector, the energies and flux of muons that reach the mountain are combined with the survival probability of the resulting muon through the mountain rock detector. To do this we interpolate across all energies and angles for

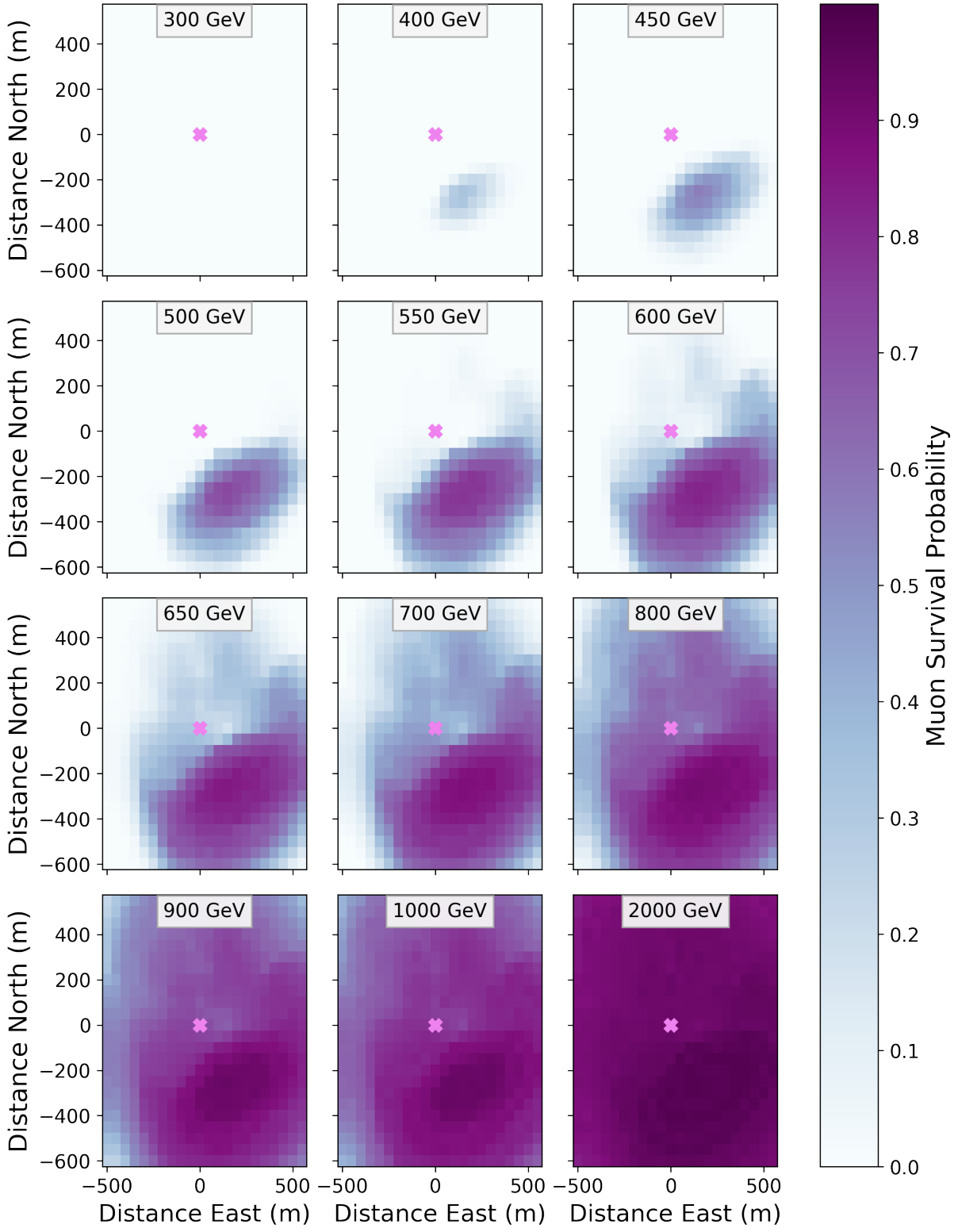


FIGURE 6.13: Percent of muons that make it to the detector at different energies coming from various locations of around the detector. The pink x shows the location of the detector in each plot.

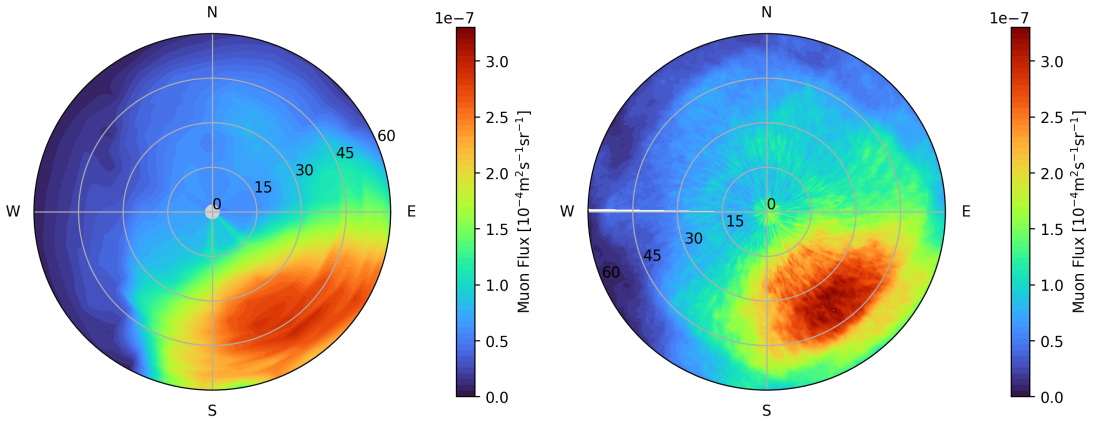


FIGURE 6.14: Left: Integrated flux of muons predicted to reach the lab from MCeQ and PROPOSAL from various directions. Right: Measured flux from [77].

the survival probability from PROPOSAL and initial fluxes from MCeQ, multiply the two and integrate across all energies. This results in a flux plot as shown in Fig. 6.14 Left.

We are able to compare this directly to muon measurements made in the same laboratory from [77], recreated here in Fig. 6.14 Right. These muon flux measurements were performed in the same hall but opposite end of Lab 2400 where NEXT-White resides, and were able to measure $cos\alpha > .2$ and all azimuth angles. This measurement was done with three layers of scintilator pixels stacked on top of each other which would scintilate as the muon passed through which could then be used to extrapolate the incident angle of the muons. This measurement resulted in an integrated flux of $(5.26 \pm 0.21) \times 10^3 m^2 s^{-1}$ in Lab 2400. Our predictions show pleasing agreement with these measurements both qualitatively and quantitatively, though notably we predict a slightly higher flux at low angles. The authors of [77] address the difficulty of the low angle measurement in their paper. Both our first principles prediction and the prior measurement will be used below in making comparisons to the muon flux measurement in NEXT.

### 6.3.5 Simulating Muons through NEXT

To understand the detector response to muons, Nexus, a Geant-4 based simulator, was used to simulate muons passing through the lead castle and detector containing 10.1 bar of enriched xenon. The preliminary Monte Carlo muons analyzed to determine cut values in Sec. 6.1 were all 200 GeV in energy and generated from a single point above the detector, covering only a portion of the zenith and azimuth angles. These were what were used for Figures 6.6 to 6.5. However the final muon flux predictions are evaluated with muons emitted uniformly around the detector on a 2 meter diameter sphere shell from all angles between $0 \leq \beta < 2\pi$ and $0.4 \leq \cos\alpha \leq 1$ with possibility to weight to the expected flux, as predicted in Fig. 6.14. Remaking Fig.6.6 with the new geometry and keeping all the events where a muon passed the fiducial volume results in Fig. 6.15. The same trends are observed as in Fig. 6.6.

The generation within Nexus simulates the true path of the muon through the walls and gas but does not simulate the electrons moving through the drift field or electroluminescent region. Further simulations must be done to simulate what happens in the gas before signal would be collected, and then the post processing that is done on the real run data.

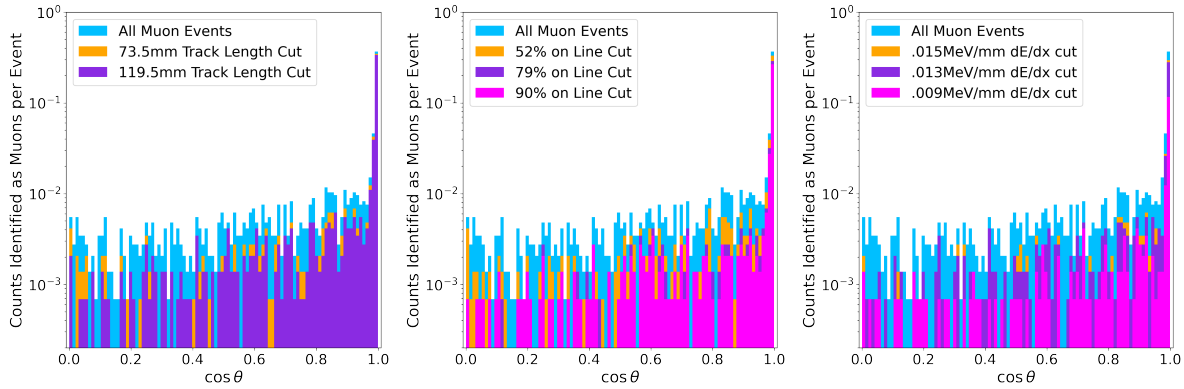


FIGURE 6.15: The dot product, i.e. $\cos\theta$ between the line found with a Hough transform and the Monte Carlo truth line where 1.0 is a perfect match. Each color represents a tighter cut selecting out the muons. Left: Cuts selecting only events where the track length is at least 73.5 mm (orange) or 119.5 mm (purple) minimum. Middle: Cuts based off what percent of the total event energy deposited is within 35 mm of the reconstructed track line. Right: Cuts based on the dE/dx values found from the energy near the track divided by the length.

The first step in turning the Nexus output into a realistic signature is used to make S1 and S2 waveforms for the PMTs and SiPMs. This step includes a light table to look up how much signal would be generated per photoelectron in each region. Here the initial ionization electrons within the active region are selected and a drift and EL field are applied. Within these fields transverse and longitudinal diffusion of the electrons is included as the electrons move through the gas.

The next step then simulates the electronics responses and puts in noise and gain fluctuations. This is where the true photoelectrons are converted into ADC counts and a trigger is implemented on the S2. At this point the output is in the same form as the data that comes from the NEXT

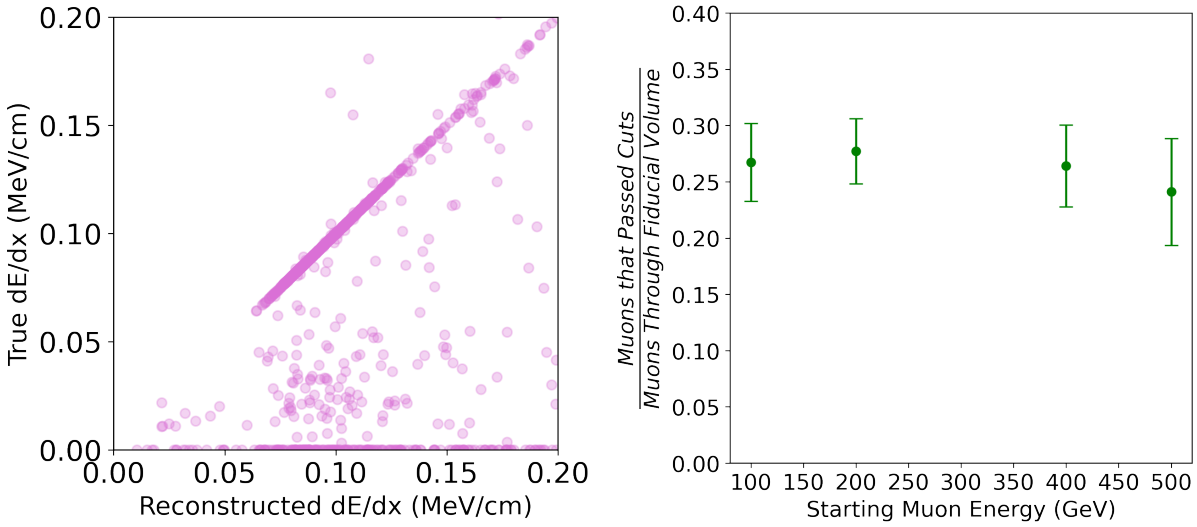


FIGURE 6.16: Left: True versus reconstructed dE/dx after applying an energy correction to the events that passed through the fiducial volume. Right: Rate of muons that pass cuts versus the muon starting energy.

detector and we apply the subsequent steps identically to simulations and data..

From here a calibration for both the PMTs and SiPMs is applied. The baseline is removed from the SiPM waveforms and the signal-derivative effect is removed from the PMT waveforms. A threshold is applied to the waveforms and the signal pulses are extracted. With this the time window of the PMTs and SiPMs are matched.

From these signals an S1 and S2 are selected and each hit is turned into X,Y,Z coordinates. The energy from the PMT maps are divided and distributed onto the SiPM hits according to how much charge each SiPM recorded so that each hit has an energy associated with it, summing to the total PMT measured event energy.

The final step separates the signals based on if they pass a high or low charge threshold constraint. This step uses a correction map created through calibration runs to determine charge thresholds across the SiPM plane. This step is important for data outputs as each SiPM will have a unique response based on natural variations and is necessary to account for edge effects where less light is collected. For this analysis the high threshold output was used for both the Monte Carlo simulations and the data.

A final energy correction factor was applied which resulted in Fig. 6.16, showing a clear trend between the true and reconstructed dE/dx. The true dE/dx values corresponding to 0 are from events whose reconstructed line did not match the true track and gave incorrect intersection points on the axis. This will be fixed by finding the true intersection points rather than using the reconstructed.

Due to the minimally ionizing nature of muons in this energy range, only a very modest energy dependence is expected in our selection efficiencies as explained earlier with the dE/dx remaining constant, we still checked to determine if there is energy dependence on the ability to detect muons. To do this we plotted the rate of muons that passed the cuts over the true muon paths that went through the fiducial volume, shown here in Fig. 6.16 for several independently simulated monoenergetic muon samples. Since there is no difference in the passing rate across various energies, we combine the statistics of all energies for the overall flux of muons to model the final passing rate.

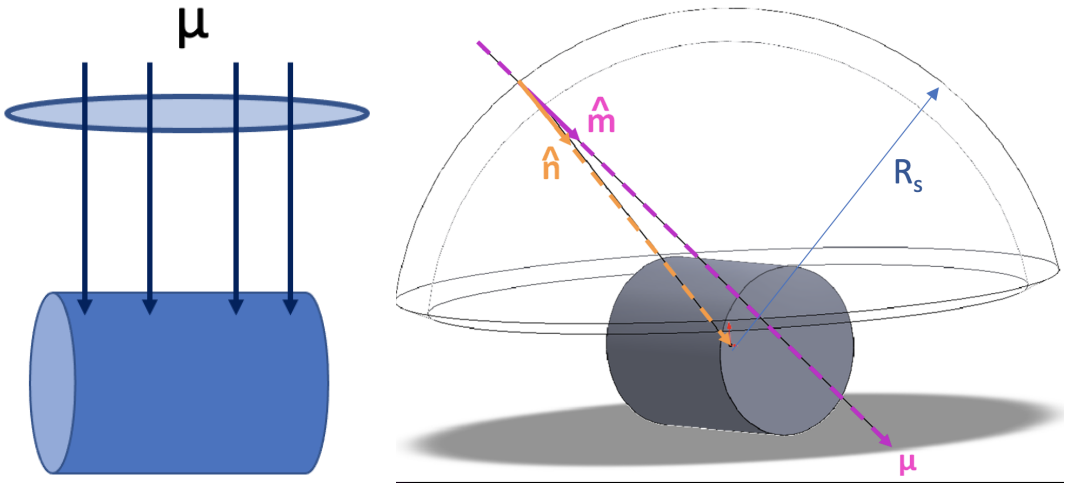


FIGURE 6.17: Left: Demonstration of a local flux of muons, each passing through the detector with the same probability. Right: Partial spherical shell used for GEANT4 distributions of muons around the detector.

## 6.4 Cosmogenic Background Rates

To compare predictions to data, each Monte Carlo muon that passed the cuts had to be weighted to take into account the flux simulated did not equally intersect the sphere. This is better understood by looking at Fig. 6.17 where the ideal situation has an equal flux of muons all intersecting the surface of the detector uniformly. However for the GEANT4 simulations the muons are being injected from a spherical shell uniformly so the likelihood of each muon to intersect the detector varies depending on the angles of incidence and position on the sphere it started from. This introduces a non-uniformity in the projected distribution of vertices into the injection plane which is proportional to $4\hat{n}\cdot\hat{m}$ where n is the direction from the insertion point of the muon on the sphere to the radius and m in the direction of the muon track. The flux of muons from each angle is also not uniform, as demonstrated in Fig. 6.14.The weighting is therefore given by:

$$W = F(\cos\alpha,\beta)\tau A(\frac{4\pi\ .6}{2})\frac{1}{N_L}W_a * 2 \tag{6.2}$$

where

$$\begin{gathered} F(\cos\alpha,\beta) = \text{Flux of Muons } (cm^{-2}s^{-1}sr^{-1}) \\ \tau = \text{exposure time of run V } (s) \\ N_L = \text{Number of MC muons launched through Nexus} \\ A = \text{Injection Area} = \pi * R_s^2(cm^2) \\ R_s = \text{injection sphere radius } (100cm) \\ W_a = \text{Weight of muons from direction of muon} = 4\hat{n}\cdot\hat{m} \\ \hat{n}\cdot\hat{m} = \text{dot product between muon direction and direction of } R_s \end{gathered} \tag{6.3}$$

.

The $\frac{4\pi\times0.6}{2}$ is the solid angle factor and accounts for how many muons were simulated through the full solid angle around the sphere. Since we only simulated above the undulations of the mountain, i.e. $\cos\alpha > 0.4$, only 60 % of top half of the sphere was covered. The muons were also simulated in all directions, both inwards and outwards from the detector, requiring an additional factor of 2 to take into account the half of muons that would never impact the detector.

The weighing was done with both fluxes in Fig. 6.14, and after normalizing and fitting the simulated and measured muon flux to the data, the histograms for $\alpha$ and $\beta$ are extracted as shown in Fig. 6.19. As can be seen the shapes of the histograms match showing that we can accurately predict the expected angles of incidence. These counts can then be turned into an integrated flux and compared with the measured fluxes from [77] and the flux that is currently used within NEXT to estimate the cosmogenic backgrounds.

### 6.4.1 Measured Muon Flux Rate

The Monte Carlo prediction of the muon flux to the detector could be determined either from the measured muon flux in the lab, or through simulations from air showers down through the mountain. Both were compared with similar results. The integrated fluxes through the detector shown in Fig. 6.18 show the simulated flux rate for various cosmic ray models and interaction models, the rate as measured in [77], and the flux rate measured from Run-V data through this analysis. Taking into account the systematic uncertainties from the three simulations options

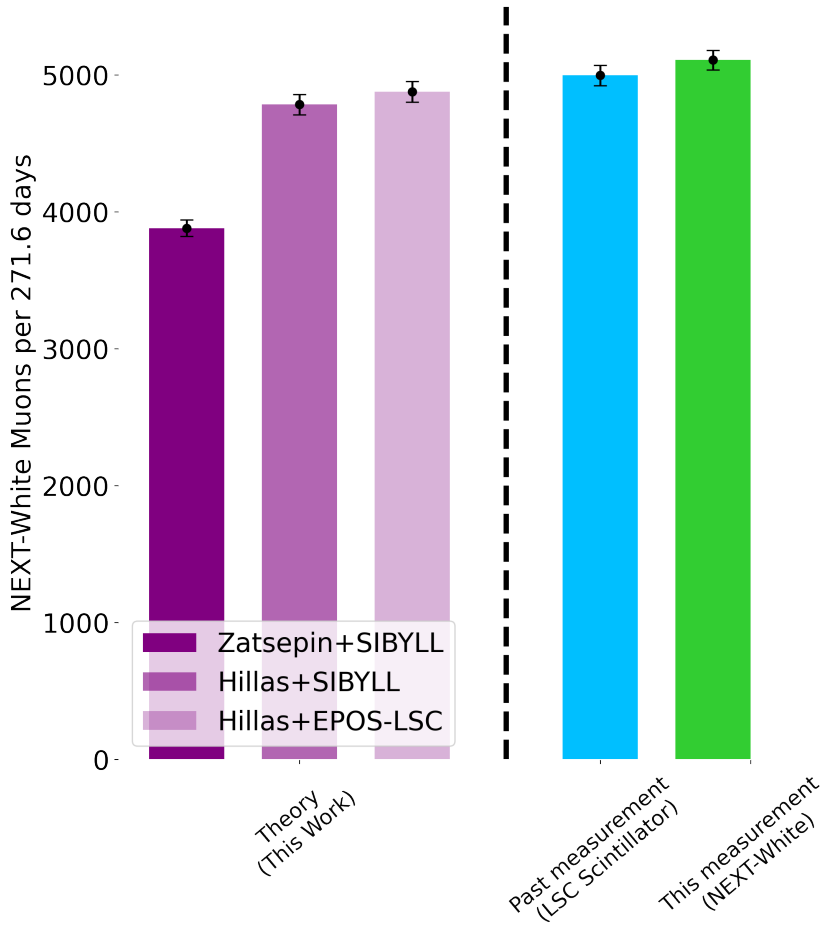


FIGURE 6.18: Integrated fluxes from [77], the current flux used withing NEXT, and measured from the data through this work

used in MCeQ we simulated a total rate of muons through NEXT-White during Run-V to be 4512.1 $\pm$ 449.4 muons. The measured muon flux gave a rate of 4995.2 $\pm$ 70.7 muons and from the data itself we measured 5108.0 $\pm$ 71.5 muons.

The shapes of the histograms in Fig. 6.19 match indicating good agreement between predicted and measured muon rates from all directions. This demonstrates that we have a good model for the mountain and accurate cuts to select muons out of data.

From these muon rates we can get the total muon flux that will pass through the detector. Using this muon flux to weight the pdfs we will be able to calculate background rates expected from the data. The backgrounds from the neutron captures of the most common isotopes, are prompt gammas and the beta decay from $^{137}$Xe. After weighting the pdfs in the energy range above most of the radiogenic backgrounds, the background rate taken from the pdfs can be added to the radiogenic rates. This provides a total expected background rate in the $2\nu\beta\beta$ region of interest and can be extrapolated into larger volume detectors.

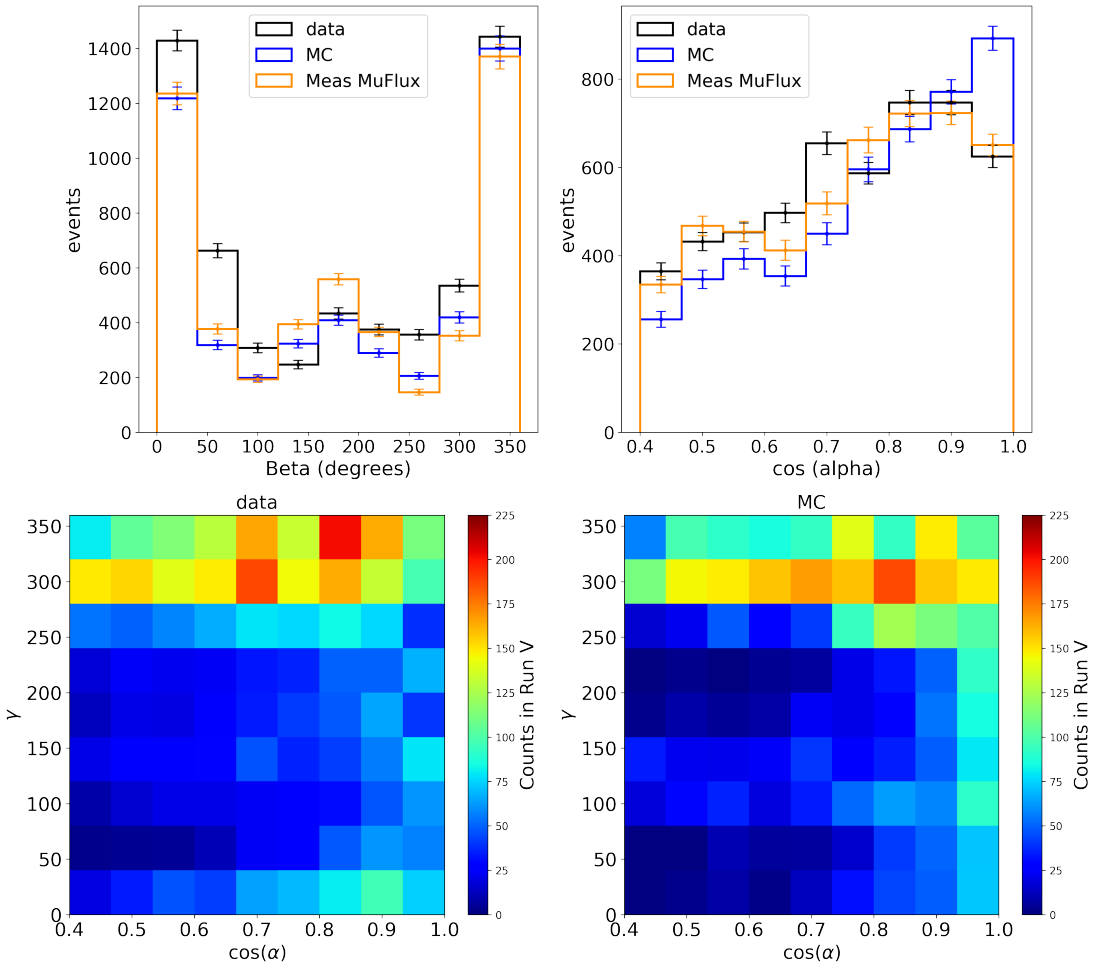


FIGURE 6.19: Top row: Counts of muons for run V in NEXT-White over beta and cos $\alpha$ comparing data with predicted counts using simulated and measured muon fluxes. Bottom Left: Counts of Muons found in Run V data. Bottom Right: Counts of Muons expected during Run V

.

# Chapter 7

# Closing Remarks

The field of particle physics is becoming dependent on larger and larger detectors to reach sensitivity levels where new physics resides. With this comes many technical challenges to create background free detectors with clear signals. These challenges include material selection requirements of low radioactivity, or high voltage compatibility as new supports have to be introduced at larger scales. These selections require vigorous testing before implementation, some of which are covered in Chapter 4.

Neutrinoless double beta decay is a physics process of interest which would give us insight into the Majorana nature of neutrinos. Positively demonstrating that neutrinos are their own antiparticles gives merit to Leptogenesis, explaining the origin of matter in the universe.

There are a variety of detection methods and isotopes used to search for $0\nu\beta\beta$ decay as discussed in Chapter 2 with different limits on the sensitivities capable of being reached. Each method is currently in the prototype stage with 10s of kilograms to 100s of kilograms of candidate isotope being deployed with plans for ton-scale capabilities. One such detector is NEXT, described in great detail in Chapter 2 and 3. NEXT has great event selection capabilities with tracking through topological signatures and strong energy resolutions through well controlled electroluminescence regions.

On top of being able to detect a $0\nu\beta\beta$ event should it occur, backgrounds must be suppressed in order not to interfere with the signal. This can be done manually by adding additives such as Helium-3 to the detector volume which capture neutrons with a higher cross section than Xenon-136 and decays with an energy well below the $Q_{\beta\beta}$ value as described in Chapter 5. Another option is using selection cuts to recognize when a background event has occurred. This is done in numerous ways for the numerous different backgrounds that occur. One way is topological selection, removing anything with number of blobs other than two or tracks that are not continuous. There are also energy cuts, only keeping events in the region of interest.

Quantifying all backgrounds which cannot be suppressed through cleaner materials and deeper detector sites is vital to confidently claiming a signal of $0\nu\beta\beta$ . One of the origins of backgrounds all detectors must contend with are cosmogenics. Chapter 6 covers how NEXT-White gets their cosmogenics measurements, the method of which will be used for NEXT-100.

While the path towards the discovery of neutrinoless double beta decay shows many challenges, the reward will be a revolution to the scientific community and may be one of the major scientific breakthroughs of our time. Definitive measurements or exclusion lies in scaleable, background-free experiments which are driving the invention of new technologies and techniques.

# Appendix A

# Mesh Deflection Calculations

The following calculations are adapted from [78].

## A.1 Notation:

- $Y$: Young modulus of wire material
- $g$: Gap spacing at zero field
- $V$: Applied voltage
- $A$: Wire cross section
- $\epsilon$: Dielectric permittivity of medium
- $T$: Wire tension with no applied field
- $z(x, y)$: Mesh position as a function of 2D position
- $\sigma$: stress
- $s$: strain
- $R$: Radius of Mesh

## A.2 Calculation

The stored energy in each mesh segment has contributions from both elastic energy in the wires and from the electrostatic energy from the capacitance between planes. The equilibrium shape is determined by functionally minimizing the sum of these contributions using the Euler Lagrange equation.

### A.2.1 Stress Energy:

A wire segment of length $\delta l_0$ pre-tensioned to $T$ stores elastic energy at zero field:

$$E^0_{elastic} = \frac{1}{2}\frac{(A\delta l_0)}{E}\sigma^2 \tag{A.1}$$

Or in terms of tension, $T$ where ($\sigma = T/A$):

$$E^0_{elastic} = \frac{1}{2}\frac{\delta l_0}{EA}T^2 \tag{A.2}$$

The length of the pre-tensioned segment at zero field will be:

$$\delta l_{pt} = \delta l_0 \left(1 + \frac{T}{AE}\right) \tag{A.3}$$

With voltage applied, this segment gets stretched further. If this wire runs in the $x$ direction and has local deformation gradient $\partial z/\partial x$, the deformed length can be related to the un-deformed length by:

$$\delta l_{deformed} = \delta l_{pt} \left[\sqrt{1 + \left(\frac{dz}{dx}\right)^2}\right]. \tag{A.4}$$

We will always be considering situations where the total curvature is small - that is, mesh displacement much smaller than the radius of the EL assembly. In such cases, $dz/dx \ll 1$ and so we can expand to first order:

$$\delta l_{deformed} = \delta l_{pt} \left[1 + \frac{1}{2}\left(\frac{dz}{dx}\right)^2\right]. \tag{A.5}$$

The total stored energy is given by:

$$E_{elastic} = \frac{1}{2}\left(A\delta l_0\right)E_s^2 = \frac{AE\delta l_0}{2}\left(\frac{\delta l_{deformed} - \delta l_0}{\delta l_0}\right)^2 \tag{A.6}$$

$$= \frac{AE\delta l_0}{2}\left(\left(1 + \frac{T}{AE}\right)\left[1 + \frac{1}{2}\left(\frac{dz}{dx}\right)^2\right] - 1\right)^2 \tag{A.7}$$

$$= \frac{AE\delta l_0}{2}\left(\frac{T}{AE} + \left(1 + \frac{T}{AE}\right)\left(\frac{dz}{dx}\right)^2\right)^2 \tag{A.8}$$

$$= \frac{T\delta l_0}{2}\left[\left(\frac{T}{AE}\right) + \left(1 + \frac{T}{AE}\right)\left(\frac{dz}{dx}\right)^2\right] + \mathcal{O}\left(\frac{dz}{dx}\right)^4 \tag{A.9}$$

Now we have to integrate over the wires. Recall the above is the expression for the energy stored in a length that was $\delta l$ when un-tensioned, but $\delta l_{pt}$ when pre-tensioned. An $x$-wire at position $y$ on the ring has a tensioned length that stretches from $-x_0 = -\sqrt{R^2 - y^2}$ to $x_0 = \sqrt{R^2 - y^2}$. Integrating along the pre-tensioned wire is equivalent to identifying the integratino measures $dx = dl_{pt}$,

$$E^{1wire}_{elastic} = \int_{-\sqrt{R^2-y^2}}^{\sqrt{R^2-y^2}} dx \frac{T}{2}\left[\left(\frac{T}{AE}\right)\left(1 + \frac{T}{AE}\right)^{-1} + \left(\frac{dz}{dx}\right)^2\right] \tag{A.10}$$

If there are $N_x$ wires per unit length in $Y$, we sum to find the contributions from all $X$ wires:

$$E_{elastic}^{x\ wires} = \sum_{j\sim -RN_x}^{j\sim RN_x} \int_{-R\sqrt{1-j^2}}^{R\sqrt{1-j^2}} dx \frac{T}{2} \left[ \left( \frac{T}{AE} \right) \left( 1 + \frac{T}{AE} \right)^{-1} + \left( \frac{dz}{dx} \right)^2 \right] \tag{A.11}$$

And if they are sufficiently densely packed, we can replace the sum with an integral:

$$\sum_{j\sim -RN_x}^{j\sim RN_x} \int_{-R\sqrt{1-j^2}}^{R\sqrt{1-j^2}} \to \int_{-RN_x}^{RN_x} dj \int_{-R\sqrt{1-j^2}}^{R\sqrt{1-j^2}} dx \tag{A.12}$$

writing $j/N_x = y$:

$$= N \int_{x-R}^{R} dy \int_{-\sqrt{R^2-y^2}}^{\sqrt{R^2-y^2}} dx = N_x \int_{\circ R} dxdy \tag{A.13}$$

Thus the total elastic contribution from the x wires is:

$$E_{elastic}^{x\ wires} = N_x \int_{\circ R} dxdy \frac{T}{2} \left[ \left( \frac{T}{AE} \right) \left( 1 + \frac{T}{AE} \right)^{-1} + \left( \frac{dz}{dx} \right)^2 \right] \tag{A.14}$$

$$= E_0^x + N_x \int_{\circ R} dxdy \frac{T}{2} \left( \frac{dz}{dx} \right)^2 \tag{A.15}$$

A notable observation about this formula is that if the wire were not pre-tensioned, the only restoring force would come from the $\mathcal{O}\left(\frac{dz}{dx}^4\right)$ term, which was neglected here. For our purposes, the mesh will always be pre-tensioned, so the second order term suffices.

### A.2.2 Electrostatic energy:

Next we have to asses the capacitive energy. We can think of each element of the surface as being a small parallel plate capacitor, all connected in parallel. Thus the total electric energy is:

$$E_{electrical} = \frac{2}{2} CV^2 = \sum_i \frac{1}{2} C_i V^2 = \sum_i \frac{1}{2} \epsilon \frac{\delta x \delta y}{g+z} V^2 \tag{A.16}$$

Taking the infinitessimal limit:

$$E_{electrical} \to \int_{\circ R} dxdy \frac{1}{2} \epsilon \frac{V^2}{g+z} \tag{A.17}$$

We will generally be able to consider small displacements of the mesh. Note that this is not quite as robust an approximation as the one above about its curvature. Nevertheless, it will provide considerable simplification:

$$E_{electrical} \sim \int_{\circ R} dxdy \frac{1}{2} \epsilon \frac{V^2}{g} \left( 1 - \frac{z}{g} \right) \tag{A.18}$$

### A.2.3 The equilibrium shape:

To find the equilibrium mesh shape $z(x,y)$, we need to minimize the energy functional:

$$E = E_0^x + E_0^y + \int d^2x_i \mathcal{E}\left[z\right] \tag{A.19}$$

$$\mathcal{E}\left[z\right] = \frac{T}{2}\left[N_x\left(\frac{dz}{dx}\right)^2 + N_y\left(\frac{dz}{dx}\right)^2\right] + \frac{1}{2}\epsilon\frac{V^2}{g}\left(1-\frac{z}{g}\right) \tag{A.20}$$

Which can be solved with the Euler Lagrange equation:

$$\sum_i \partial_i\left(\frac{\partial\mathcal{E}}{\partial\left[\partial_i z\right]}\right) = \frac{d\mathcal{E}}{dz} \tag{A.21}$$

Applying the ELG:

$$T\left(N_x\frac{\partial^2 z}{\partial x^2} + N_y\frac{\partial^2 z}{\partial y^2}\right) = -\frac{1}{2}\epsilon\frac{V^2}{g^2} \tag{A.22}$$

Life will be easier if we restrict ourselves to the symmetyric case, $N_x = N_y = N$, in which case this reduces to a cylindrically symmetric form:

$$\left(\partial_x^2 + \partial_y^2\right) z = -\kappa \qquad\qquad \kappa = \frac{\epsilon V^2}{2g^2 TN} \tag{A.23}$$

This is best attacked in cylindrical polars:

$$\frac{1}{\rho}\frac{\partial}{\partial\rho}\left(\rho\frac{\partial}{\partial\rho}\right) z = -\kappa \tag{A.24}$$

To find the general solution, we write $z$ as a power series in $\rho$:

$$z = \sum_n a_n\rho^n \tag{A.25}$$

Which, substituted into the above differential equation, gives:

$$\sum_n n^2 a_n\rho^{n-2} = -\kappa \tag{A.26}$$

Since there are no $\rho$ terms in the RIGHT, only the $n = 2$ and $n = 0$ terms contribute. The boundary condition $z(R) = 0$ fixes the relationship between $a_0$ and $a_2$, to yield, in the end

$$a_2 = -\frac{\kappa}{4} \qquad\qquad a_0 = \frac{\kappa}{4R^2} \qquad\qquad a_{others} = 0 \tag{A.27}$$

Giving the solution:

$$z = -\frac{\kappa}{4}\left(R^2 - \rho^2\right) \qquad\qquad \kappa = \frac{\epsilon V^2}{2g^2 TN} \tag{A.28}$$

The external distortion occurs at $\rho = 0$ and is:

$$z_{max} = \frac{\epsilon V^2 R^2}{8 g^2 T N} \tag{A.29}$$

The following points are notable:

- The Young modulus of the mesh material does not feature in this expression
- The total deflection depends only on the $E$ field, not on the gap size and voltage independently - which I guess is obvious, actually. We can express the terms of the EL field $E$ of $V$ and $g$:

$$z_{max} = \frac{\epsilon R^2 E^2}{8 T N} \tag{A.30}$$

- We can also express in terms of thetotal mesh tension $\tau = 2TNR$ rather than the tension per wire $T$, as:

$$z_{max} = \frac{\epsilon E^2 R^3}{4\tau} \tag{A.31}$$

## A.3 Putting in some real numbers

Lets put in some real units to be followed by some real numbers

$$z_{max} = 8.85 \times 10^{-12} * 10^{10} \frac{\left[^{-3}A^{-1}\right]^2 \left[^{3}\right] \left[^{-3-14}A^{2}\right]}{\left[^{-2}\right]} \frac{\left[E/(/)\right]^2 \left[R/\right]^3}{4\left[\tau/N\right]} \tag{A.32}$$

$$z_{max} = 22.22\text{mm} \frac{\left[E/(/)\right]^2 \left[R/\right]^3}{\left[\tau/N\right]} \tag{A.33}$$

For NEXT-100 dimensions, we fix plate radius at 1.2m. the nominal operating field is 2kV/cm/bar, which means 30kV/cm at 15 bar.

To maintain a deflection of less than 1mm for NEXT-100 with 1.2m diameter, a tension of around 400kg is required. 2mm can be achieved with 200kg. For NEXT-XXX, with 1.5m diameter, the required load increases to 600kg equivalent for 1mm, and 300kg ton for 2mm. Deflection at some various tensions are shown overleaf.

## A.4 Counteracting mesh deflection by deforming the back surface

By deforming the back plane to shape $b(\rho$ we change the capacitive stored energy term to:

$$E_{electrical} = \frac{1}{2} C V^2 = \sum_i \frac{1}{2} C_i V^2 = \sum_i \frac{1}{2} \epsilon \frac{\delta x \delta y}{g - b(\rho) + z} V^2 \tag{A.34}$$

If we assume $b(\rho) \ll g$ then:

$$= \int d^2x \frac{1}{2} \epsilon \frac{V^2}{g} \left(1 - \frac{z + b(\rho)}{g}\right) \tag{A.35}$$

Changing the total energy functional to:

$$\mathcal{E}[z] = T\left[N_x\left(\frac{dz}{dx}\right)^2 + N_y\left(\frac{dz}{dx}\right)^2\right] + \frac{1}{2}\epsilon\frac{V^2}{g}\left(1 - \frac{z - b(\rho)}{g}\right) \tag{A.36}$$

Notably the solution to the ELG equation is unaffected. The conclusion is that given small perturbations of the back surface, the first-order solution for the mesh curvature is unchanged. Thus for small perturbations relative to the gap size, adjusting the back surface to match the curvature at nominal field will achieve the desired effect. This can be understood as resulting from the fact that for small perturbations relative to gap size, the $E$ field as a function of $\rho$ remains approximately constant and so the distorted shape is not affected.

## A.5 What about larger perturbations?

By virtue of the geometry in question, we can safely assume the curvature is always small, $\frac{dz}{d\rho} \ll 1$. However, in some cases we are talking about distortions relative to the gap size that are not necessarily small, $z \lesssim g$. We modify the general energy function thus:

$$\mathcal{E}[z] = T\left[N_x\left(\frac{dz}{dx}\right)^2 + N_y\left(\frac{dz}{dx}\right)^2\right] + \frac{1}{2}\epsilon\frac{V^2}{g - b(\rho) + z} \tag{A.37}$$

The Euler Lagrange equation can be again solved, the only difference being in the RHS:

$$T\left(N_x\frac{\partial^2 z}{\partial x^2} + N_y\frac{\partial^2 z}{\partial y^2}\right) = -\frac{1}{2}\epsilon\frac{V^2}{(g - b(\rho) + z)^2} \tag{A.38}$$

A sanity check shows thatthis reduces to the previous form for $b + z \ll g$. Now, on to solve it. Again writing in cylindrical polars:

$$\frac{1}{\rho}\frac{\rho}{\partial\rho}\left(\rho\frac{\partial}{\partial\rho}\right)z = \frac{\epsilon V^2}{2TN}\frac{1}{(g - b(\rho) + z)^2} \tag{A.39}$$

It is helpful to change variables to $\eta(\rho) = g - b(\rho) + z(\rho)$, to yield:

$$\frac{1}{\rho}\frac{\rho}{\partial\rho}\left(\rho\frac{\partial}{\partial\rho}\right)[\eta(\rho) + b(\rho) - g] = \frac{\epsilon V^2}{2TN\eta(\rho)^2} \tag{A.40}$$

This is not completely trivial for arbitrary $b(\rho)$, so let us restrict to solutions we really want - a particular choice of back-plane shape where $\eta(\rho) = \eta_0$, some constant independent of radius. If such a solution exists, it would have $\eta = g$ and $\partial\eta/\partial\rho = 0$. The ELG would then reduce to:

$$\frac{1}{\rho}\frac{\rho}{\partial\rho}\left(\rho\frac{\partial b}{\partial\rho}\right) = \frac{\epsilon V^2}{2TNg^2} \tag{A.41}$$

The RHS is just a constant, so this is easy to solve exactly. Going step-by-step:

$$\frac{\rho}{\partial\rho}\left(\rho\frac{\partial b}{\partial\rho}\right) = \frac{\epsilon V^2}{2TNg^2}\rho \tag{A.42}$$

$$\frac{\partial b}{\partial\rho} = \frac{\epsilon V^2}{2TNg^2}\frac{\rho}{2} + \frac{C_1}{\rho} \tag{A.43}$$

$$b = \frac{\partial b}{\partial\rho} = \frac{\epsilon V^2}{2TNg^2}\frac{\rho^2}{4} + C_1\log\rho + C_2 \tag{A.44}$$

Where $C_1$ and $C_2$ are arbitrary constants. Because we must demand a solution regular at the origin, it must be the case that $C_1 = 0$. Thjis leaves $C_2$ to be determined by boundary conditions. We defined $z = 0$ atthe plate edges, so the appropriate condition is $b(R) = -g$:

$$b = \frac{\epsilon V^2 R^2}{8TNg^2} + C_2 = -g \tag{A.45}$$

$$b = \frac{\epsilon V^2}{8TNg^2}\left(\rho^2 - R^2\right) - g \qquad\qquad z = \frac{\epsilon V^2}{8TNg^2}\left(\rho^2 - R^2\right) \tag{A.46}$$

Notably, even though this was not the exact solution for the mesh stretched above a flate plane - it was only the first order term - this solution is exact given a parabolic anode plane behind the mesh, with the shape arranged such that the gap size is constant.

## Appendix B

# Mothership

SO-1340

| VESSEL DESIGN DATA | | |
|---|---|---|
| **Code** | Design Code | ASME Section VIII-1 2015 Ed. |
| | Inspection | OneCIS Insurance Company of Lynn, MA |
| | Code Stamp | U-Stamp |
| | National Board # | Yes, # TBD |
| **Design Condition** | MAWP - Int/Ext | 203/15 psi @ 100°F |
| | MDMT | -20 °F @ 203 psi |
| | Corrosion Allowance | 0" |
| | Insulation | N/A |
| **Examination** | Impact Test | N/A |
| | RT | Full |
| | PWHT | None |
| | Hydro Test | 203 x 1.3 = 264 psi |
| **Dimensions** | Total Volume | 37.7 cu.ft. ( 282 Gal) |
| | Volume w/o Ullage | N/A |
| | Weight - Empty | 3,510 lbs |
| | Weight - Operating | ? |
| | Paint-Surface Area | N/A |
| **Nameplate** | | per code |
| **Manufacturer Serial#** | | D962 |
| **Cust. Defined Service** | | Argon/Zenon |
| **Customer TAG #** | | TBD (Cust) |

## SCHEDULE OF OPENINGS

| Mark | Service | Size | Nozzle Type | Nozzle ID | Reinforcing | FITTING | Type | Class Rating | Projection in | Projection out | Radial from CL |
|---|---|---|---|---|---|---|---|---|---|---|---|
| N1 & N2 | Instruments | 12" | Pipe | 9.686" | 1/2" Plate | Zero Length Adapt. | 12" CF Flange | App2 | 0" | 2.88" | 0" |
| N3 | 30 kV HV | 6" | Pipe | 5.761" | 5/8" Plate | CF Blank | 8" CF Flange | App2 | 0" | 6.32" | 32.79" |
| N4 & N5 | 30 kV HV | 6" | Pipe | 5.761" | Integral | CF Blank | 6" CF Flange | App2 | 0" | 3.28" | 17.75" |
| N6 | PMT Insertion | 2 1/2" | Pipe | 2.328" | 1/2" Plate | CF Blank | 4 1/2" CF Flange | App2 | 0" | 3.00" | 20" |
| N7 - N12 | View Ports | 1 1/4" | Coupling | 1.380" | Integral | Plug w Glass | View Port | 6000 | 0" | 1.58" | 30.30" |
| N13 & N15 | VCR Gas Feedthru | 1/2" | Coupling | 0.40" | Integral | VCR Tube | VCR Tube F | 3000 | 0" | 1.375" | 39.38" |
| N16 | Leak Check | 1/2" | Tube | 0.40" | Integral | VCR Tube | VCR Tube F | N/A | 0" | 1.375" | 34.50" |

[NB]

CERTIFIED BY **Prentex**
ALLOY FABRICATORS INCORPORATED
DALLAS, TEXAS

| | | |
|---|---|---|
| MAXIMUM ALLOWABLE WORKING PRESSURE | 203 PSIG @ | 100 °F |
| MINIMUM DESIGN METAL TEMPERATURE | -20 °F @ | 203 PSIG |
| EXTERNAL PRESSURE | 15 PSIG @ | 100 °F |
| MANUFACTURER'S SERIAL NO. | D962 | |
| YEAR BUILT | 2017 | |

ASME

U

W

RT-1

POnum

## FAB NOTES

1. Welding: Welds shall be neat in appearance, free of slag, undercuts & all other defects. Remove ALL burrs & break ALL sharp edges. Where applicable: ¼" Weep Hole drilled in ALL Pads.
2. Flanges: The face of all flanges shall be perpendicular to the vessel major centerlines. Flange bolt holes shall stradle vessel major centerlines.
3. Cleaning: Clean ALL inner surfaces to PAF CP
4. Hydro-Test: Water used shall contain no more than 25PPM or Chloride for SST. Water shall also be treated w/Garrett Callahan Formula #159- Oxygen Scavenger (MFG Recommendation: 6oz per 1000 Gal.)
5. Ship Prep: Protect ALL machined surfaces & threaded connections. Plug ALL ports before shipping.

| WELD SPECIFICATIONS | | |
|---|---|---|
| 1 | GTAW | WPS 413-88 |
| 2 | GMAW/FCAW | SS 1005 94LT |
| 3 | GTSM | 00713 |
| 4 | GMAW | CSE71T1M |

| LEGEND | |
|---|---|
| (000) | Bill of Material ID |
| N1 | Opening ID |
| B | Revision |

| ZONE | REV. | DESCRIPTION | DATE | APPROVED |
|---|---|---|---|---|
| | 1 | Customer Approved | 08/24/2017 | 08/31/2017 |

REVISIONS

P.O.#:

**Prentex ALLOY FABRICATORS, INC.**
3108 SYLVAN AVENUE, DALLAS, TEXAS 75212
TEL: 214 748 7837 FAX: 214 748 7850
sales@prentex.com www.prentex.com

Cust.Approved



EL Test Stand Vessel

| DRAWN | CHECKED | DWG. NO. | REV | SHEET |
|---|---|---|---|---|
| TD 06/22/17 | BY 7/5/17 | SO-1340 | 1 8/31/17 | 1 OF 9 |

| BOM# | QTY. | Location | DESCRIPTION | MATERIAL | Weight | Rev. |
|---|---|---|---|---|---|---|
| 001 | 1 | Top Head | Plate - 3/4" Head Dished Only 74" ICR x 59" OD | SA-240 304/304L | 591.7 | - |
| 002 | 1 | Bottom Head | F&d Head - 5/8" Nom (0.59 Min.) x 59" ID, 2" SF, 60 1/4" ICR, 3 5/8" IKR, IS Bevel | SA-240 304/304L | 551.1 | - |
| 004 | 1 | Body Flange (Top) | Forged Ring - 4 3/8" x 3 1/4" x 59" ID | SA-182 F304/304L | 776.9 | - |
| 005 | 1 | Bottom Body Flange | Forging - 59" ID x 65 1/2" OD x 6" Tall | SA-182 F304/304L | 764.3 | - |
| 006 | 4 | Body Flange (Bottom Guides) | Plate - 1/2" x 2" x 2 7/8" | SA-240 304/304L | 3.1 | - |
| 007 | 6 | Upper Leg Flange | Plate - 1/2" x 6" x 13 1/2" | SA-240 304/304L | 70.3 | 3 |
| 008 | 3 | Upper Leg Web | Plate - 3/8" x 5 1/4" x 13 1/2" | SA-240 304/304L | 23.0 | 3 |
| 009 | 6 | Leg Flange | Plate - 1/2" x 6" x 22 1/2" | SA-240 304/304L | 117.1 | 3 |
| 010 | 3 | Leg Web | Plate - 3/8" x 5 1/4" x 22 1/2" | SA-240 304/304L | 38.4 | 3 |
| 011 | 9 | Leg Pads | Plate - 1/2" x 8" x 8" | SA-240 304/304L | 81.2 | - |
| 012 | 2 | N1 & N2 | Pipe - 10 Sch 100 (0.718" Wall) x 2 3/8" | SA-312 304/304L | 14.2 | - |
| 013 | 2 | N1 & N2 | CF Flange - 12" x 9.88" ID Lesker Part# F1200X1000N | SA-182 F304/304L | 18.5 | - |
| 014 | 2 | N1 & N2 | CF Flange - 12" Adapter (Blank) Lesker Part# F1200x000N | SA-182 F304/304L | 52.8 | - |
| 015 | 2 | N1 & N2 | CF Flange Gasket - 12" Lesker Part# ga-1200 | Copper | 0.6 | - |
| 016 | 3 | N1, N2 & N6 Blind | CF Flange - 4.5" x Blank Lesker Part# F0450x000N | SA-182 F304/304L | 8.5 | - |
| 017 | 3 | N1, N2 & N6 | CF Flange Gasket 4.5" Lesker Part # ga-0450 | Copper | 0.3 | - |
| 018 | 12 | N1 - N2 | CF Flange - 2.75" Blank Lesker Part # F0275x000N | SA-182 F304/304L | 9.0 | - |
| 019 | 12 | N1 - N2 | CF Flange Gasket - 2.75" Lesker Part# ga-0275 | Copper | 0.4 | - |
| 020 | 4 | N13 - N16 | Fitting - VCR Part# SS-8-VCR-1050506 & 6lv-8-VCR-3-8tb7050506 Swagelok | SA-182 F316/316L | 1.1 | - |
| 021 | 1 | N1 Repad | Plate - 1/2" x 9 9/16" ID x 16 9/16" OD | SA-240 304/304L | 20.8 | 2 |
| 022 | 1 | N3 | Pipe - 6 Sch120 (.562) x 11 1/2" | SA-312 304/304L | 16.2 | - |
| 023 | 1 | N3 Pad | Plate - 5/8" x 10" x 16" | SA-240 304/304L | 9.7 | - |
| 024 | 3 | N3, N4 & N5 | CF Flange - 8" OD x 5.92" ID Lesker Part# F0800x | SA-182 F304/304L | 15.1 | - |
| 025 | 3 | N3, N4 & N5 | CF Flange - 8" OD, Blank, Lesker Part# F0900x000 | SA-182 F304/304L | 35.3 | - |
| 026 | 3 | N3, N4 & N5 | CF Flange Gasket - 8" Lesker Part# ga-0800 | Copper | 0.6 | - |
| 027 | 1 | N6 Neck | Pipe - 2 1/2 Sch80 (0.276 wall) x 3" | SA-312 304/304L | 1.7 | - |
| 028 | 1 | N6 Flange | CF Flange - 4.5" x 2.44" ID Lesker Part# F0450x250N | SA-182 F304/304L | 2.0 | - |
| 029 | 1 | N6 Repad | Plate - 1/2" x 20" ID x 16 9/16 | SA-240 304/304L | 4.5 | - |
| 030 | 2 | N5 & N6 | Pipe - 6 Sch120 (.562) x 4 1/2" | SA-312 304/304L | 15.2 | - |
| 031 | 6 | N7 - N12 (View Port) | Coupling - 1 1/4" Class 6000 | SA-182 F304/304L | 7.6 | 1 |
| 032 | 6 | N7 - N12 | Rayotek - 1 1/4" NPT Sight Glass 101006C | SA-240 304/304L | 2.8 | - |
| 033 | 1 | Body Flange | O-Ring - 1/2 Nom x 60.813 ID | Buna-N | 1.8 | - |
| 034 | 1 | Body Flange (Bottom) | Helicoflex - 1/2" Aluminum Jacket Helicoflex HN10 | Aluminum & ? | 1.1 | - |
| 035 | 72 | N1 & N2 Bolt Set | Bolt Set - 2.75" CF Flange - Lesker Part# hbk25028088 (bolt & washer) | SA-193 B8 1 | 1.4 | - |
| 036 | 16 | N1, N2 Bolt Set | Bolt Set - 4.5" CF Flange Lesker Part # HHBU3124-12554 (bolt & washer) | SA-193 B8 1 | 0.0 | - |
| 037 | 8 | N6 Bolt Set | CF Flange Bolt Set 5/16"-28 x 2" with washer & Nut Lesker Part# hbs31224200 | SA-193 B8 1 | 0.6 | - |
| 038 | 60 | N3, N4 & N5 | Bolt Set - 8" CF Flange Lesker Part# hbs31224225 | SA-193 B8 1 | 4.2 | - |
| 039 | 64 | N1 & N2 Bolt Set | Bolt Set - 12" CF Flange Lesker Part # hbt31224250 (bolt, nut & washer) | SA-193 B8 1 | 5.1 | - |
| 040 | 82 | Body Flanges | Heavy Hex Bolt - 3/4-16 x 9 9/16" | SA-193 B8 1 | 113.4 | - |
| 041 | 82 | Body Flange | Hex Nut - 3/4"-16 | SA-194 Gr8 | 11.3 | - |
| 042 | 6 | Leg Bolt | Heavy Hex Bolt - 7/8" x 2" | SA-193 B8 1 | 4.0 | - |
| 043 | 6 | Leg Nut | Heavy Hex Nut - 7/8" | SA-194 Gr8 | 2.0 | - |
| 044 | 1 | Nameplate | Plate - 1/4" x 5" x 5 3/4" | SA-240 304/304L | 2.1 | - |
| 045 | 1 | Nameplate | 18" GA x 4" x 4-1/2" Prentex | 304 Bright | 0.3 | - |
| 046 | 3 | Lift Swivel Support | Plate - 3/4" x 4" x 4" | SA-240 304/304L | 10.0 | - |
| 047 | 12 | Lift Swivel Support | Plate - 1/4" x 2 1/2" x 4" | SA-240 304/304L | 8.6 | - |
| 048 | 3 | Lift Swivel Support | Lift Swivel w Ring - 1" Bolt | SA-182 F304/304L | 10.9 | - |
| 049 | 3 | N13 - N15 | Half Coupling - 1/2" Socket Weld | SA-182 F304/304L | 0.6 | - |
| 050 | 12 | Internal Supports | Round Bar - 1 1/2" x 1 1/2" | SA-479 304 | 6.8 | - |

drw.#: SO-1340

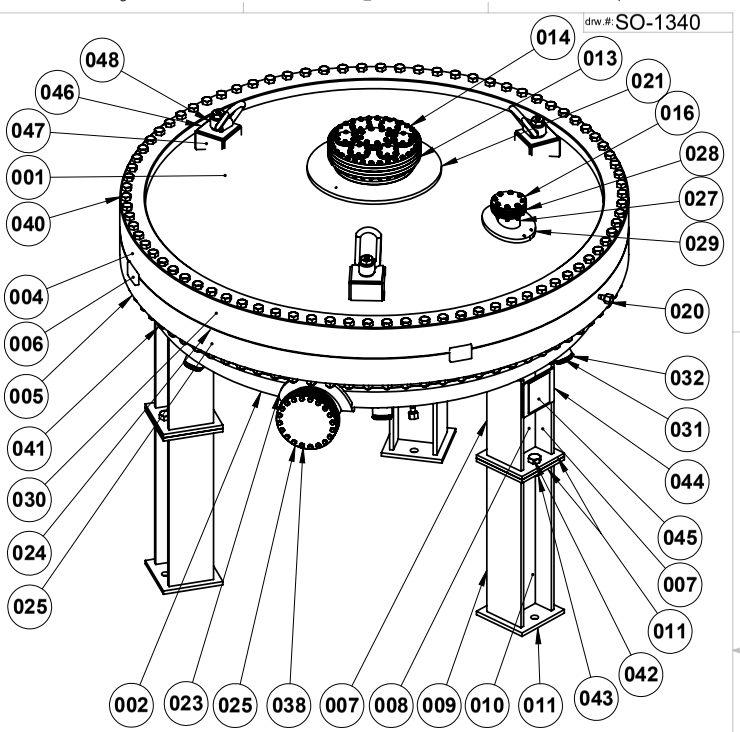


**Prentex ALLOY FABRICATORS, INC.**
3108 SYLVAN AVENUE, DALLAS, TEXAS 75212
TEL: 214 748 7837 FAX: 214 748 7850
sales@prentex.com www.prentex.com

**Cust.Approved**



# EL Test Stand Vessel
## BILL OF MATERIALS

| DRAWN | CHECKED | DWG. NO. | REV | SHEET |
|---|---|---|---|---|
| TD 06/22/17 | BY 7/5/17 | SO-1340 | 1 8/31/17 | 2 OF 9 |

drw.#: SO-1340

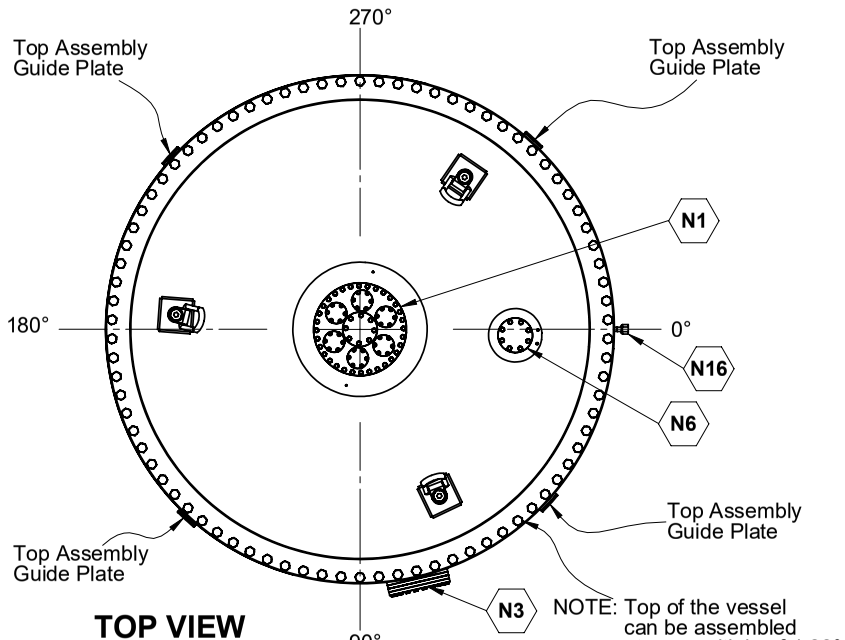


**TOP VIEW**

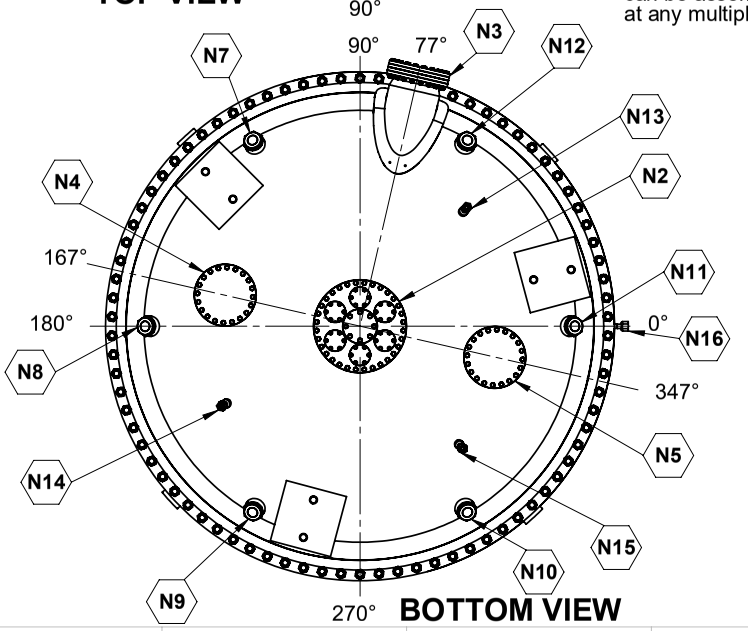


**BOTTOM VIEW**

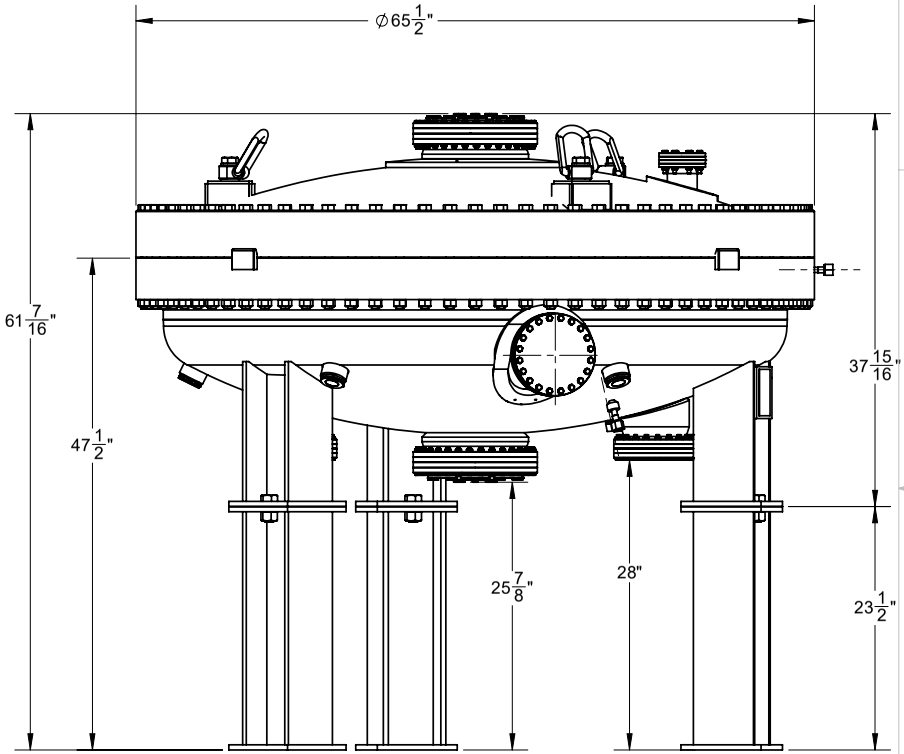


**ELEVATION**


**Prentex ALLOY FABRICATORS, INC.**
3108 SYLVAN AVENUE, DALLAS, TEXAS 75212
TEL: 214 748 7837 FAX: 214 748 7850
sales@prentex.com www.prentex.com


**Cust.Approved**



EL Test Stand Vessel
GENERAL VIEW

| DRAWN | CHECKED | DWG. NO. | REV | SHEET |
|---|---|---|---|---|
| TD 06/22/17 | BY 7/5/17 | SO-1340 | 1 8/31/17 | 3 OF 9 |

drw.#: SO-1340

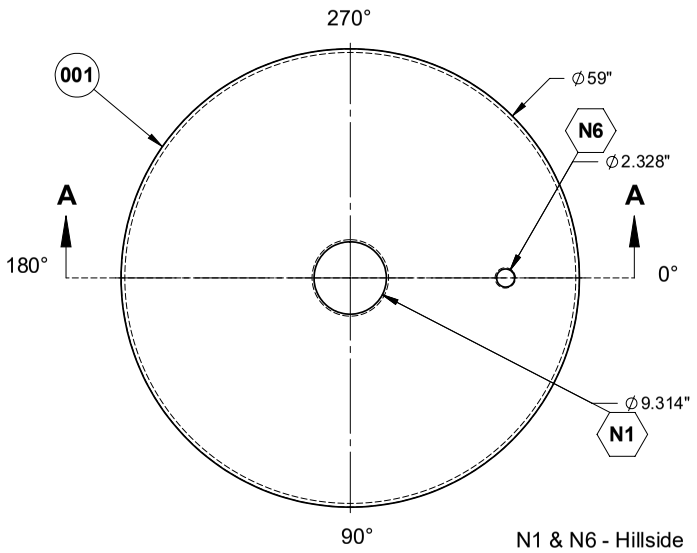


N1 & N6 - Hillside

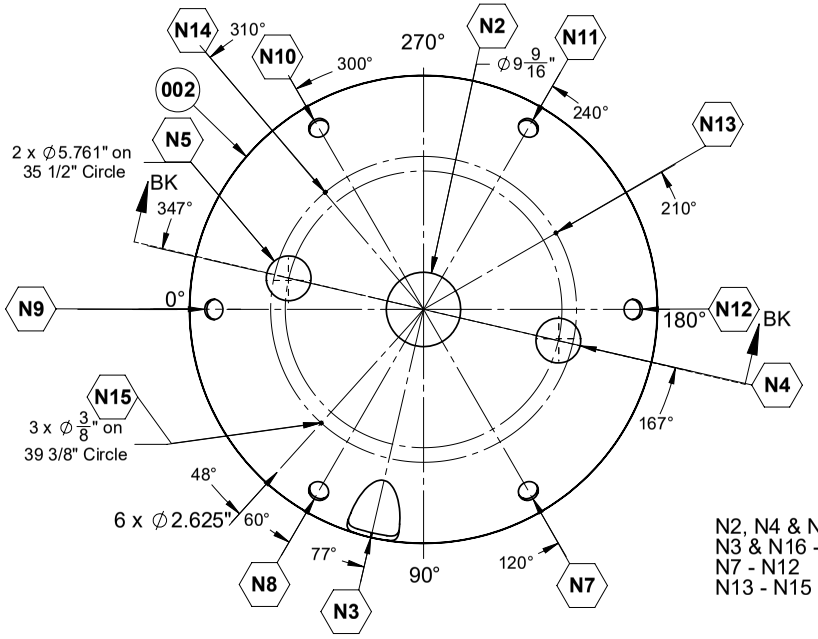


**BOTTOM HEAD**

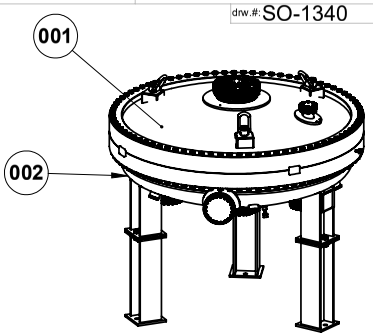


N2, N4 & N5 - Hillside
N3 & N16 - Horizontal
N7 - N12
N13 - N15 Radial

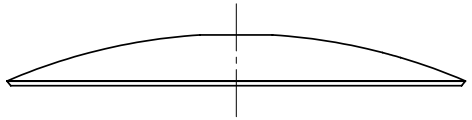

**TOP HEAD**

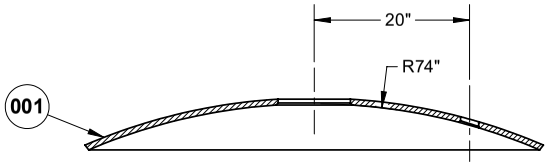


**SECTION A-A**

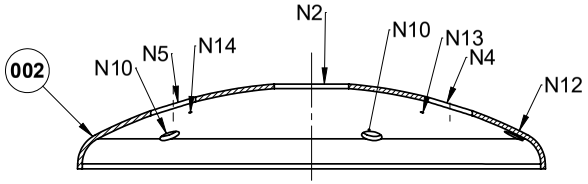


**SECTION BK-BK**


**Prentex ALLOY FABRICATORS, INC.**
3108 SYLVAN AVENUE, DALLAS, TEXAS 75212
TEL: 214 748 7837 FAX: 214 748 7850
sales@prentex.com www.prentex.com


**Cust.Approved**



EL Test Stand Vessel
HEAD DETAILS

| DRAWN | CHECKED | DWG. NO. | REV | SHEET |
|---|---|---|---|---|
| TD 06/22/17 | BY 7/5/17 | SO-1340 | 1 8/31/17 | 4 OF 9 |

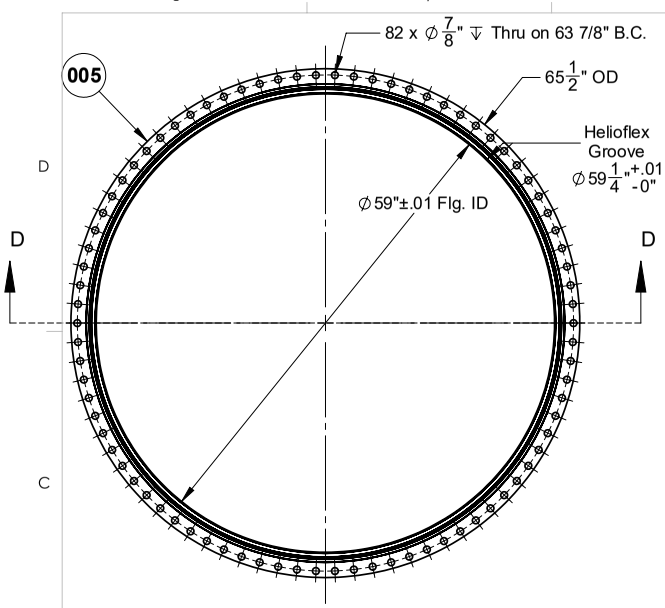


**BOTTOM BODY FLANGE**

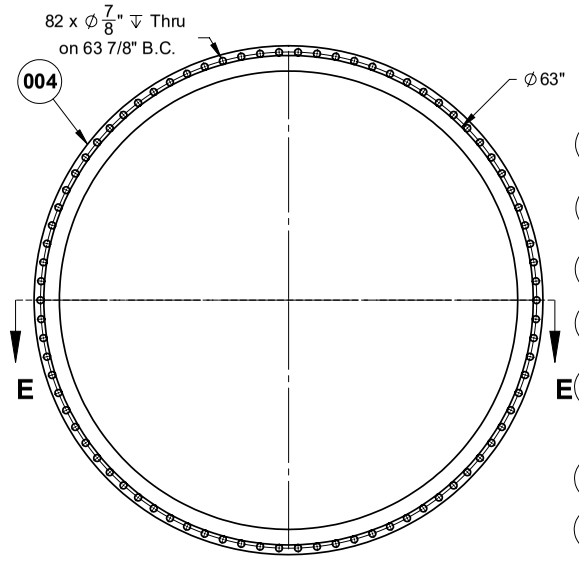


**TOP BODY FLANGE**

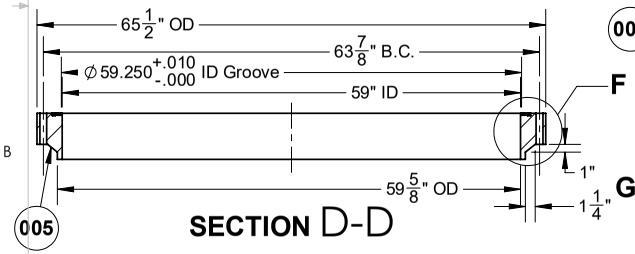


**SECTION D-D**

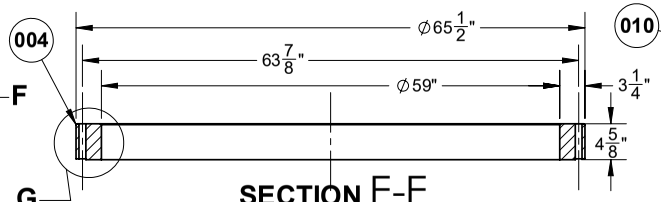


**SECTION E-E**

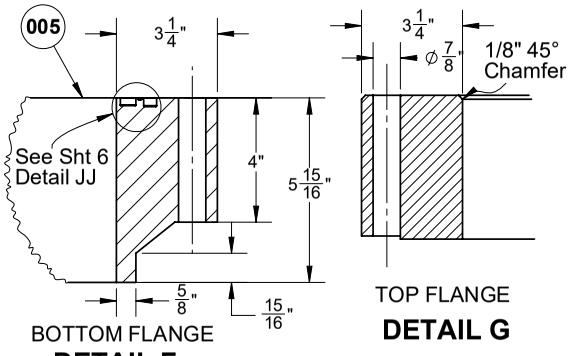


BOTTOM FLANGE
**DETAIL F**

TOP FLANGE
**DETAIL G**

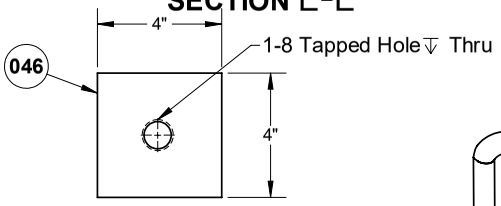


**LIFT SWIVEL SUPPORT PLATE**
4 REQ'D

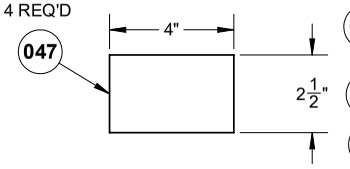


**LIFT SWIVEL SIDE PLATE**
16 REQ'D

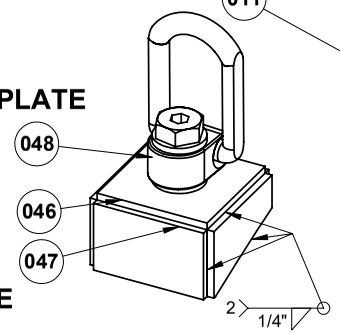


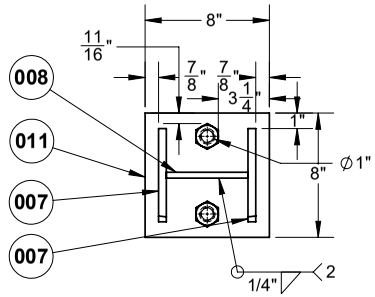


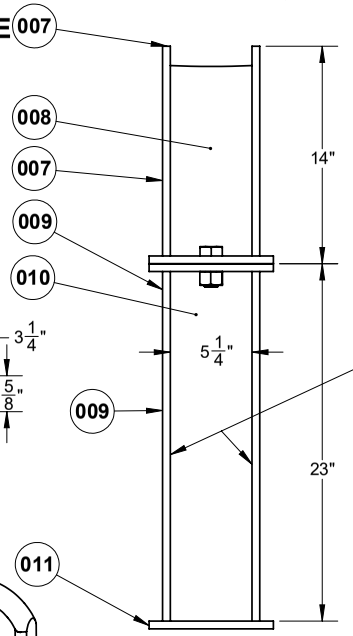


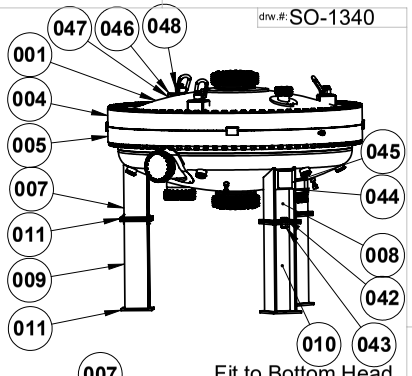


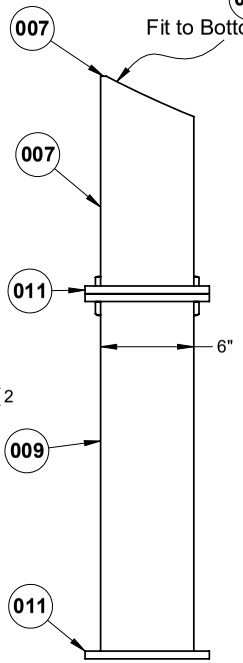


**LEGS**


**Prentex ALLOY FABRICATORS, INC.**
3108 SYLVAN AVENUE, DALLAS, TEXAS 75212
TEL: 214 748 7837 FAX: 214 748 7850
sales@prentex.com www.prentex.com


**Cust.Approved**



drw.#: SO-1340

EL Test Stand Vessel
BODY FLANGE & LEG DETAILS

| DRAWN | CHECKED | DWG. NO. | REV | SHEET |
|---|---|---|---|---|
| TD 06/22/17 | BY 7/5/17 | SO-1340 | 8/31/17 | 5 OF 9 |

drw.#: SO-1340

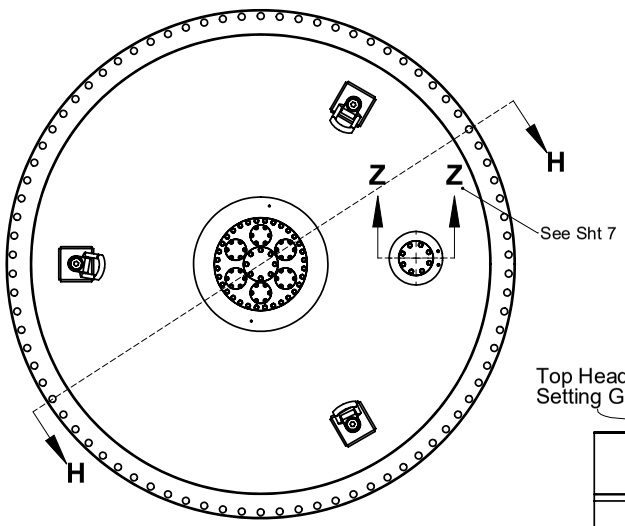


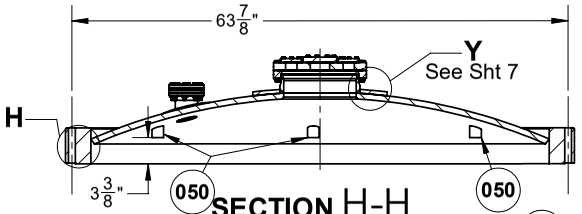


SECTION H-H

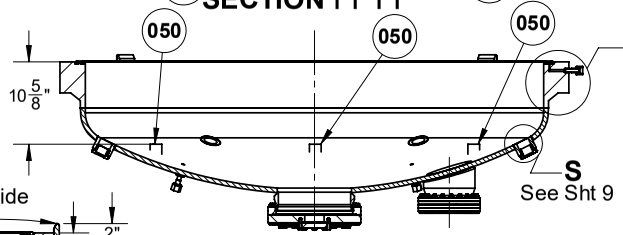


SECTION J-J

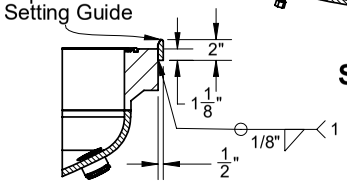


SECTION K-K

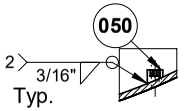


SECTION X-X

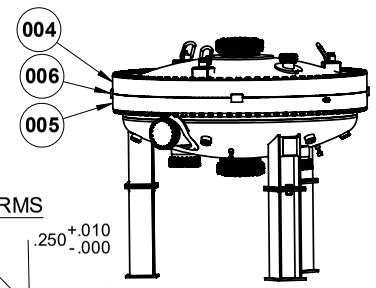


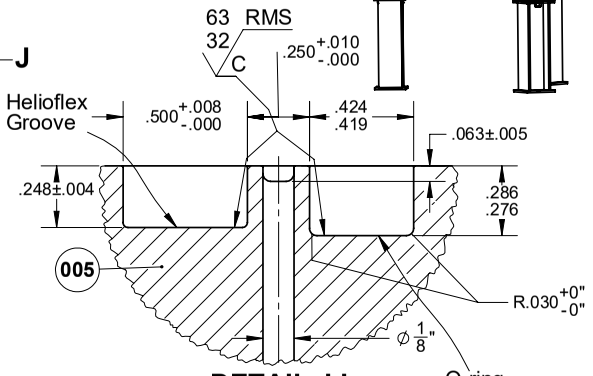


DETAIL JJ

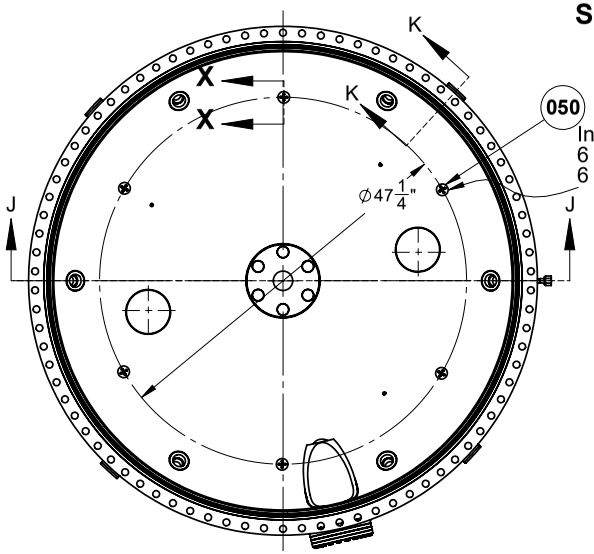


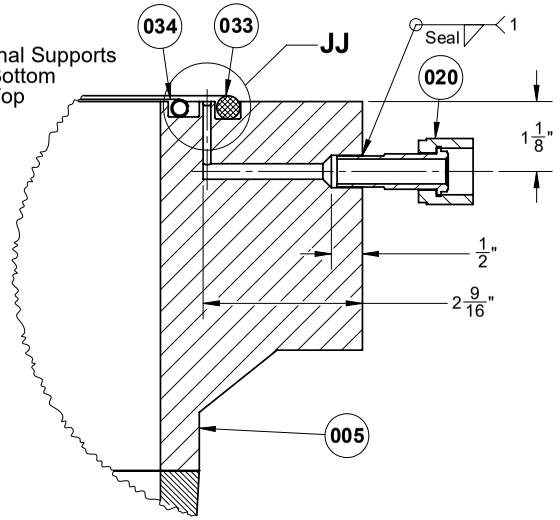


DETAIL J

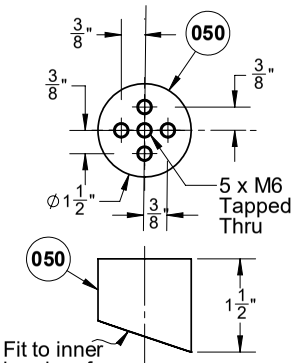


INTERNAL SUPPORTS

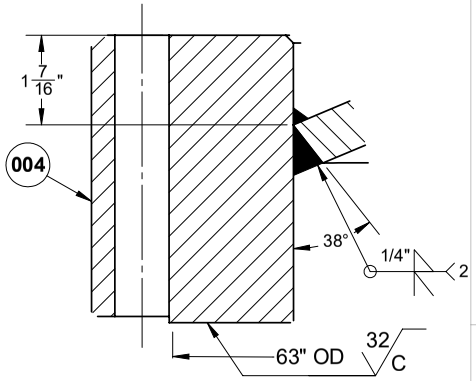


DETAIL H


Prentex ALLOY FABRICATORS, INC.
3108 SYLVAN AVENUE, DALLAS, TEXAS 75212
TEL: 214 748 7837 FAX: 214 748 7850
sales@prentex.com www.prentex.com


Cust.Approved



# EL Test Stand Vessel
## BODY FLANGE DETAILS

| DRAWN | CHECKED | DWG. NO. | REV | SHEET |
|---|---|---|---|---|
| TD 06/22/17 | BY 7/5/17 | SO-1340 | 1 8/31/17 | 6 OF 9 |

drw.#: SO-1340

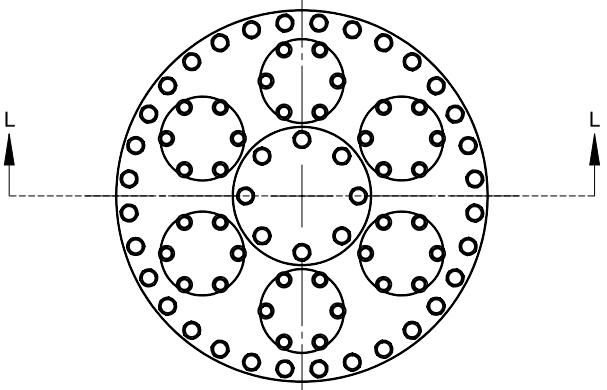


N1 & N2

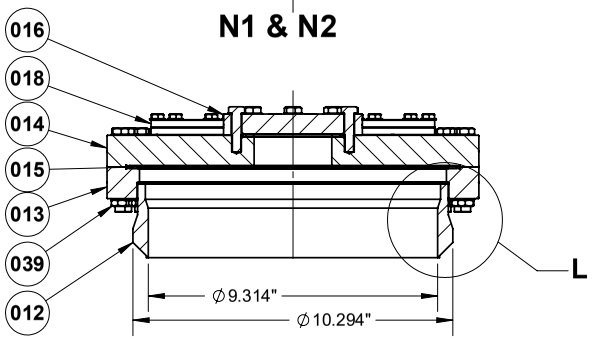


N1 & N2
SECTION L-L

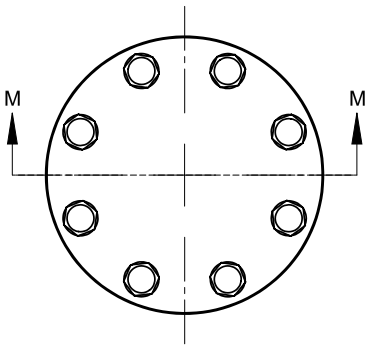


N6

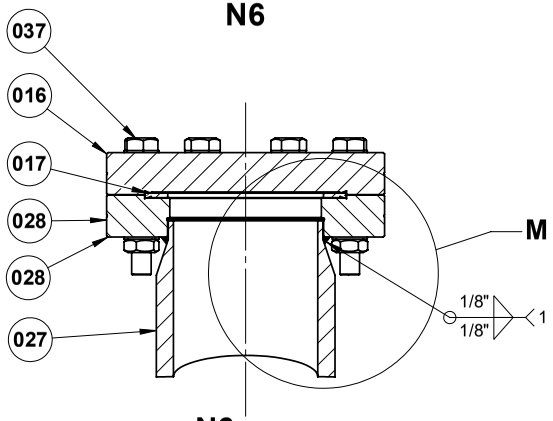


N6
SECTION M-M

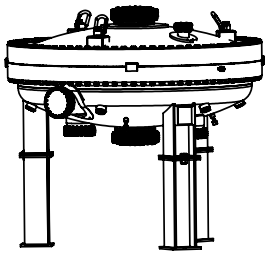

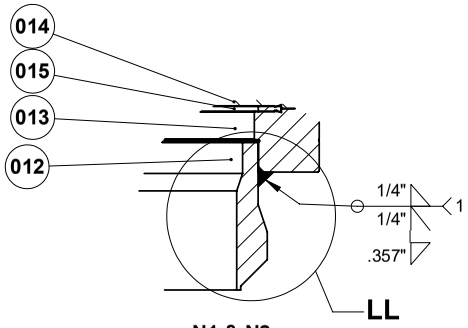


N1 & N2
DETAIL L

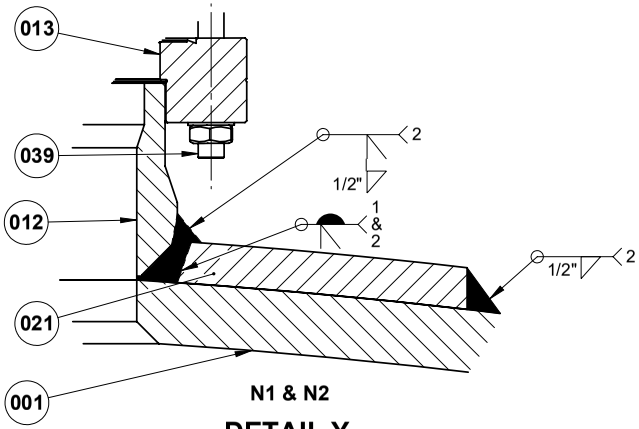


N1 & N2
DETAIL Y

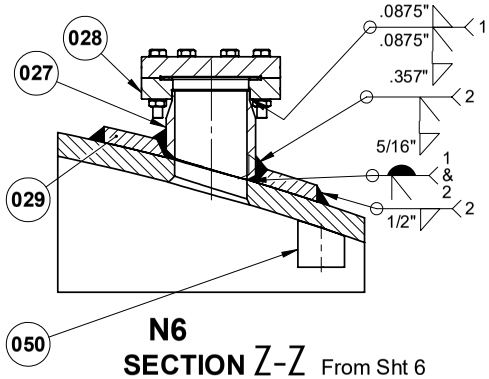


N6
SECTION Z-Z From Sht 6


**Prentex ALLOY FABRICATORS, INC.**
3108 SYLVAN AVENUE, DALLAS, TEXAS 75212
TEL: 214 748 7837 FAX: 214 748 7850
sales@prentex.com www.prentex.com


**Cust.Approved**



EL Test Stand Vessel
NOZZLE DETAILS - TOP HALF

| DRAWN | CHECKED | DWG. NO. | REV | SHEET |
|---|---|---|---|---|
| TD 06/22/17 | BY 7/5/17 | SO-1340 | 1 8/31/17 | 7 OF 9 |

drw.#: SO-1340

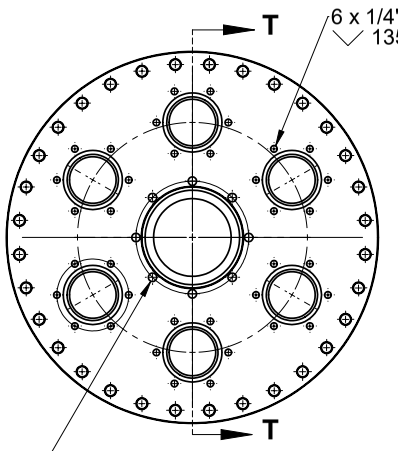


**12" CF FLANGE BLANK**

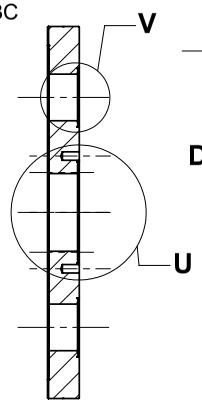


**SECTION T-T**

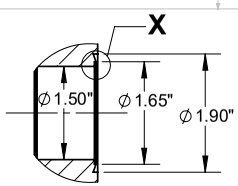


**DETAIL V**

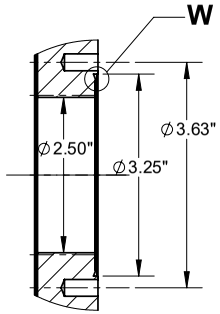


**DETAIL U**

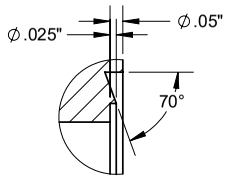


**DETAIL X**

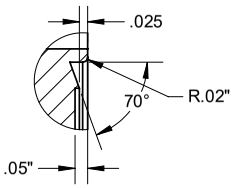


**DETAIL W**

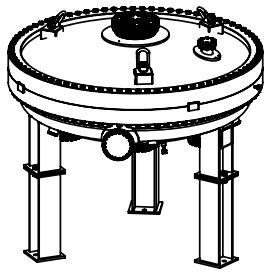

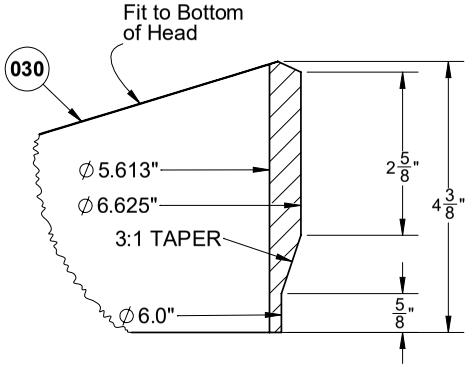


**N4 & N5**
6" NPS Sch120 Pipe
**DETAIL RRR**
**2 Req'd**

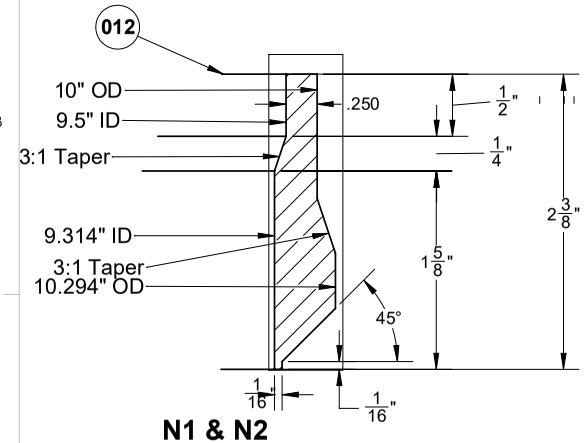


**N1 & N2**
10" Sch100 Pipe From Sheet 7
**DETAIL LL**
**2 Req'd**

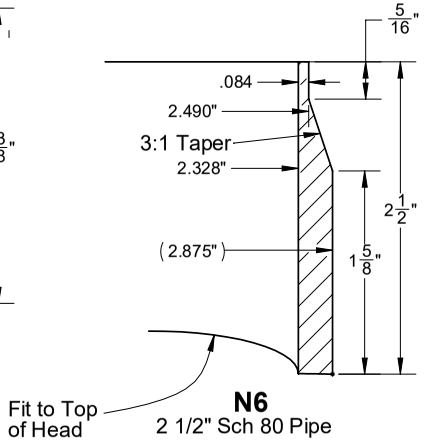


**N6**
2 1/2" Sch 80 Pipe
**DETAIL M** From Sheet 7
**1 Req'd**

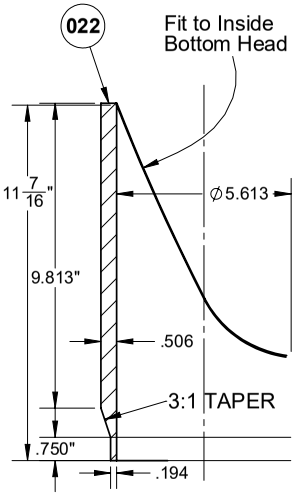


**N3**
6" NPS Sch120 Pipe
**DETAIL QQ**
**1 Req'd**


**Prentex ALLOY FABRICATORS, INC.**
3108 SYLVAN AVENUE, DALLAS, TEXAS 75212
TEL: 214 748 7837 FAX: 214 748 7850
sales@prentex.com www.prentex.com


**Cust.Approved**



EL Test Stand Vessel
MACHINING

| DRAWN | CHECKED | DWG. NO. | REV | SHEET |
|---|---|---|---|---|
| TD 06/22/17 | BY 7/5/17 | SO-1340 | 1 8/31/17 | 8 OF 9 |

drw.#: SO-1340

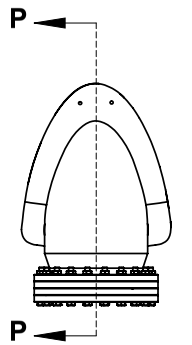


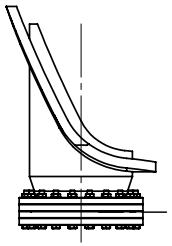

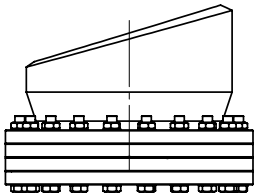

N4 & N5

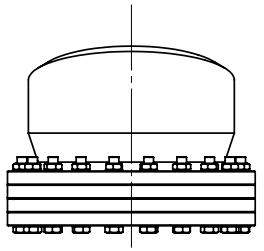

N4 & N5

See Sht 8 Detail RRR
for Pipe Machining

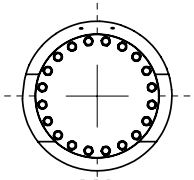

N3

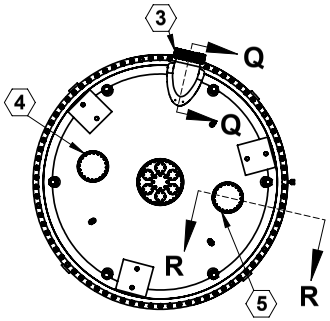


BOTTOM VIEW

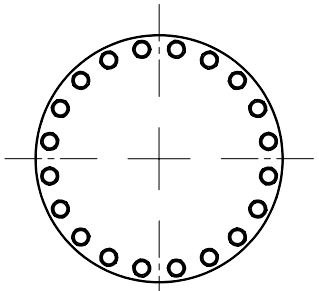

N4 & N5

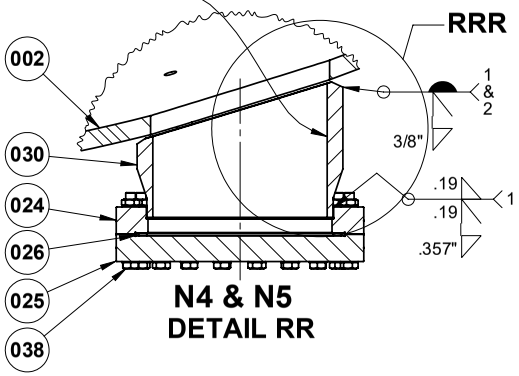


N4 & N5
DETAIL RR

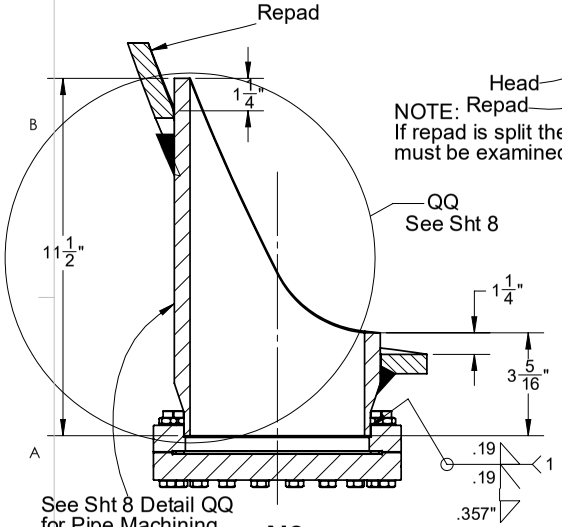


See Sht 8 Detail QQ
for Pipe Machining

N3
SECTION P-P

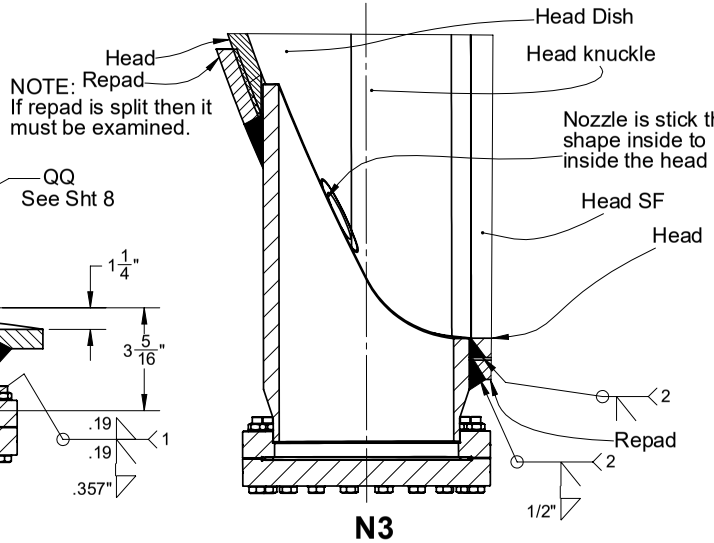


N3
SECTION Q-Q

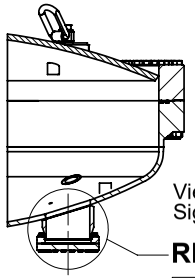


SECTION R-R

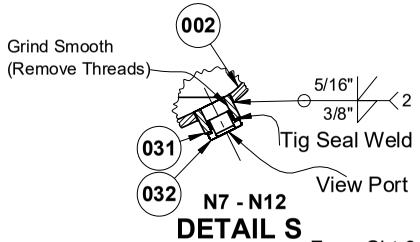


DETAIL S
From Sht 6

**Prentex ALLOY FABRICATORS, INC.**
3108 SYLVAN AVENUE, DALLAS, TEXAS 75212
TEL: 214 748 7837 FAX: 214 748 7850
sales@prentex.com www.prentex.com

**Cust.Approved**



EL Test Stand Vessel
NOZZLE DETAILS - BOTTOM HALF

| DRAWN | CHECKED | DWG. NO. | REV | SHEET |
|---|---|---|---|---|
| TD 06/22/17 | BY 7/5/17 | SO-1340 | 1 8/31/17 | 9 OF 9 |

# Appendix C

# NEXT-100 EL and Cathode Drawings

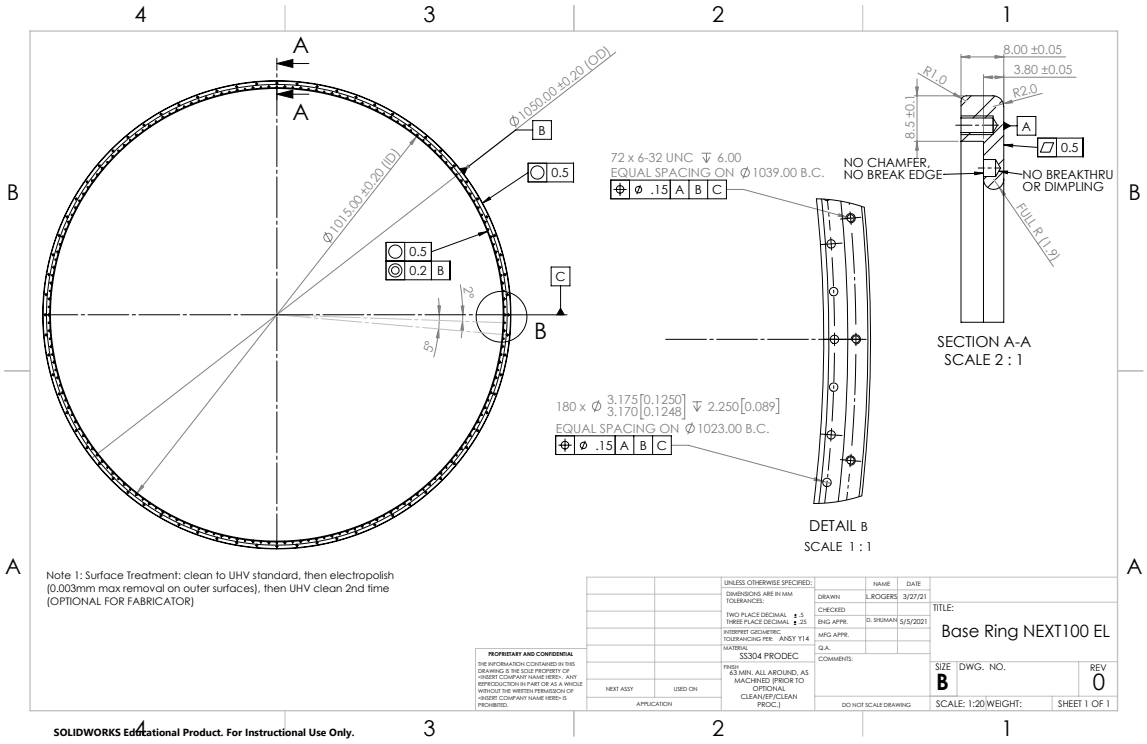


FIGURE C.1: Machine drawing for manufacturing the EL Base rings.

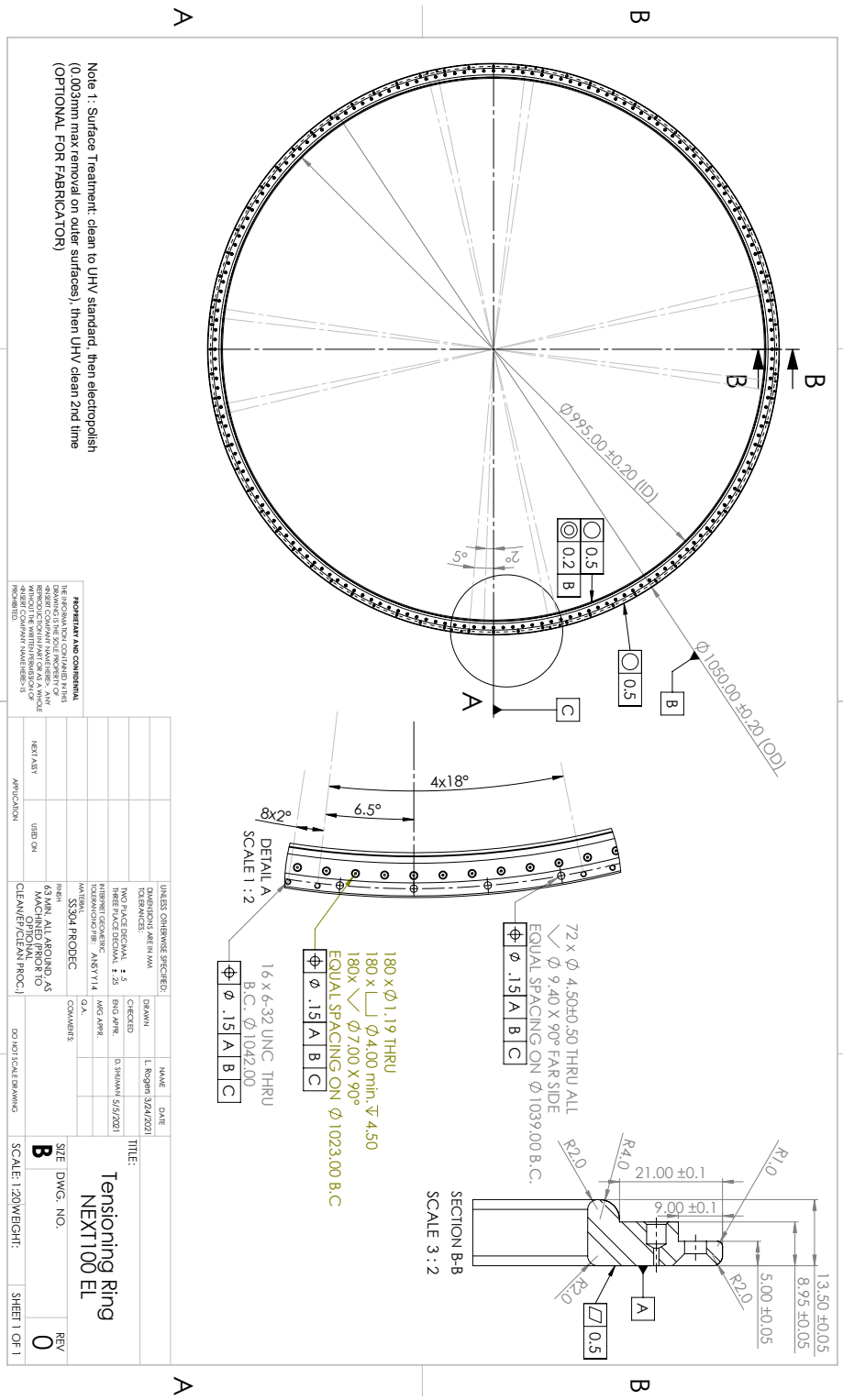


FIGURE C.2: Machine drawings for manufacturing the EL Tension rings.

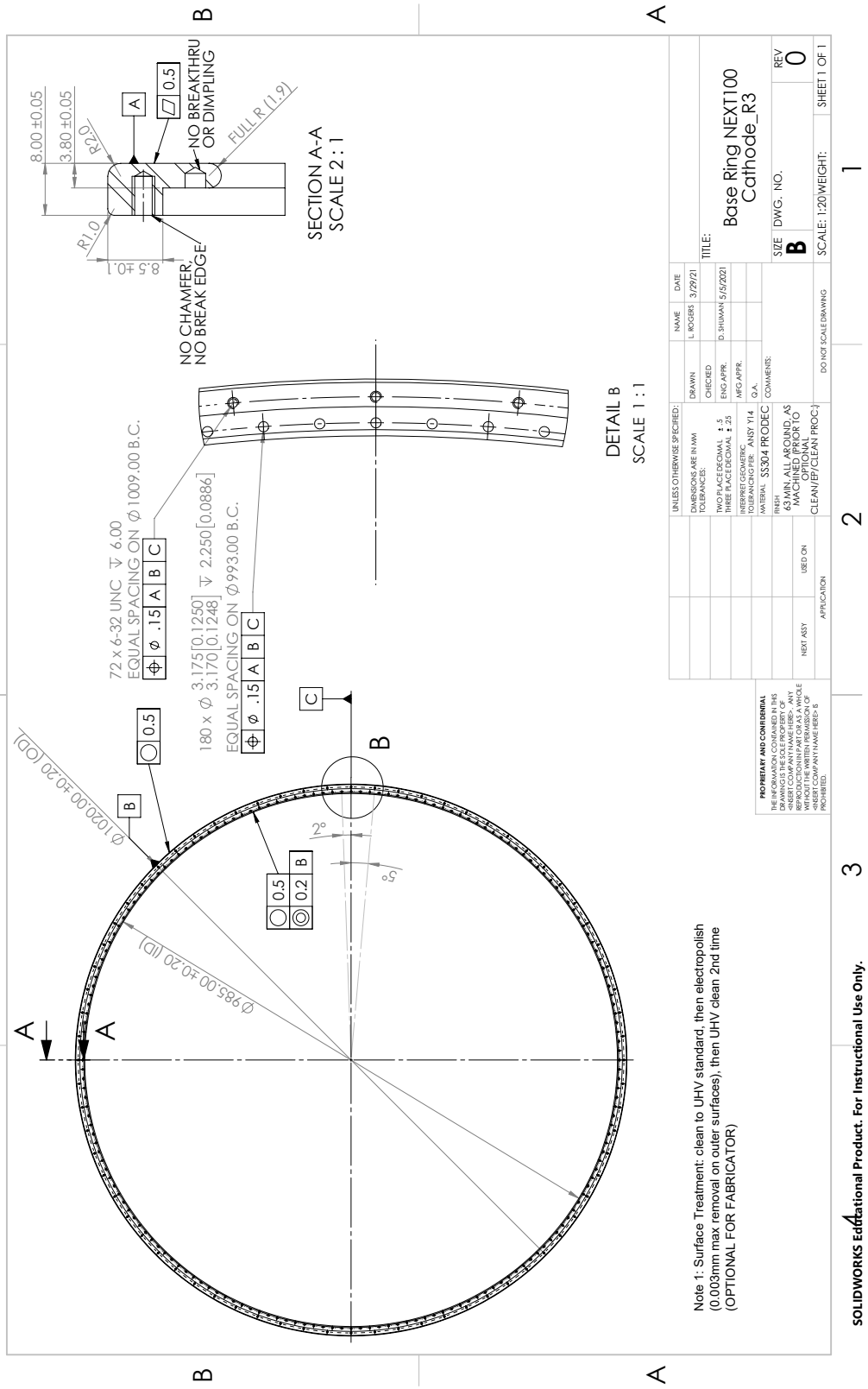


FIGURE C.3: Machine drawings for manufacturing the Cathode Base ring.

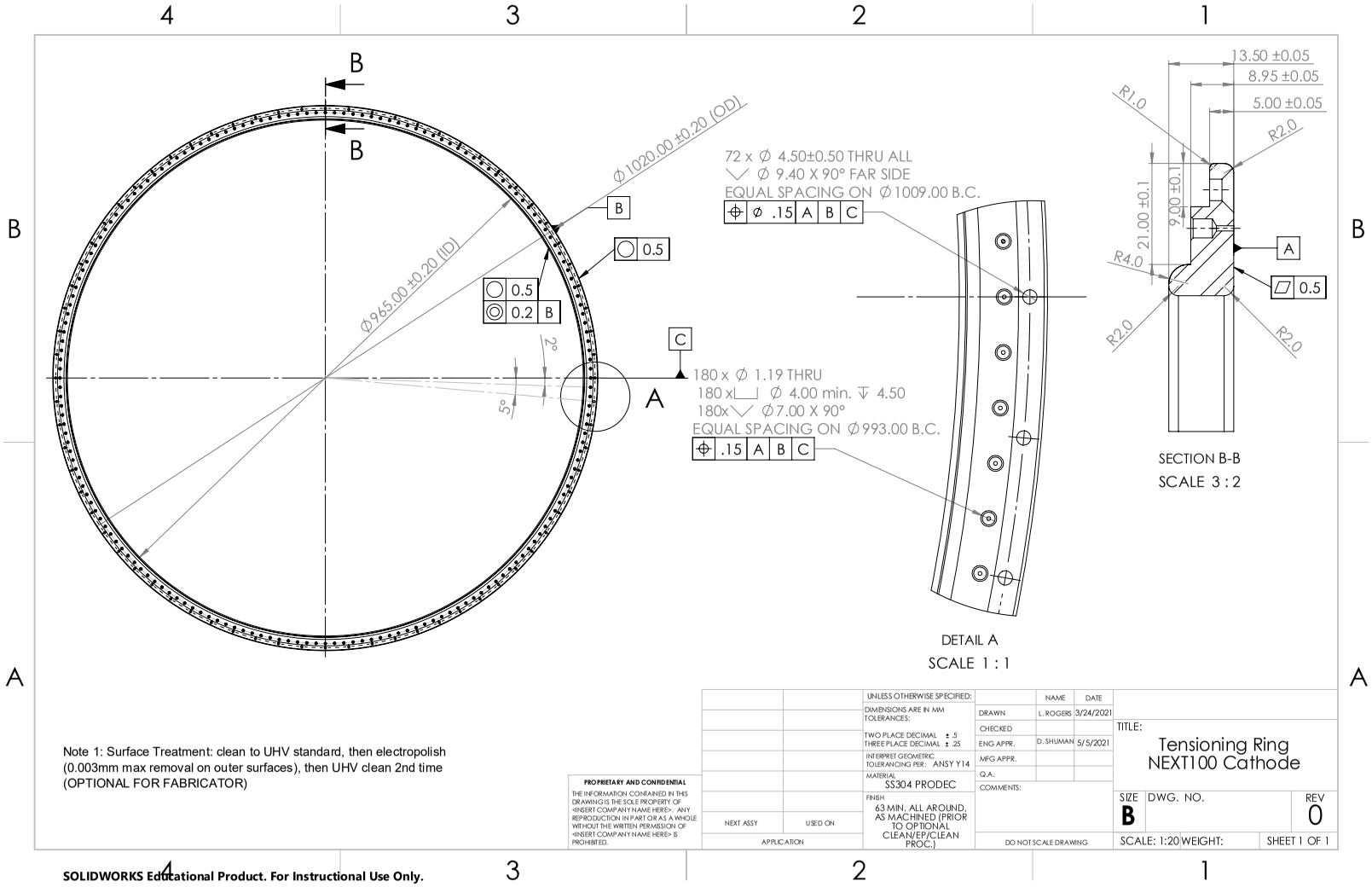


FIGURE C.4: Machine drawings for manufacturing the Cathode Tension ring.

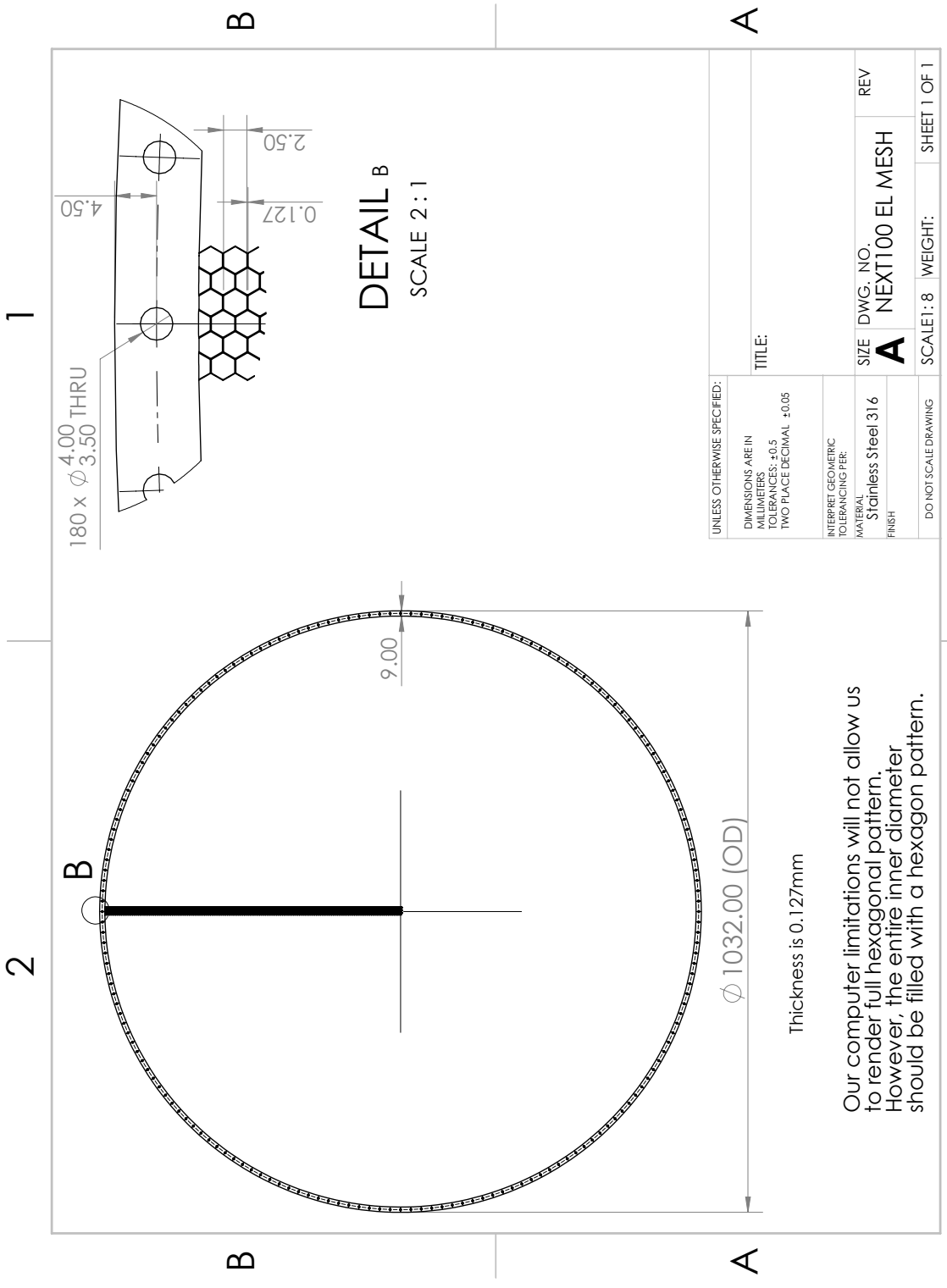


FIGURE C.5: Machine drawings for manufacturing the standard photoeteched meshes for the EL region.

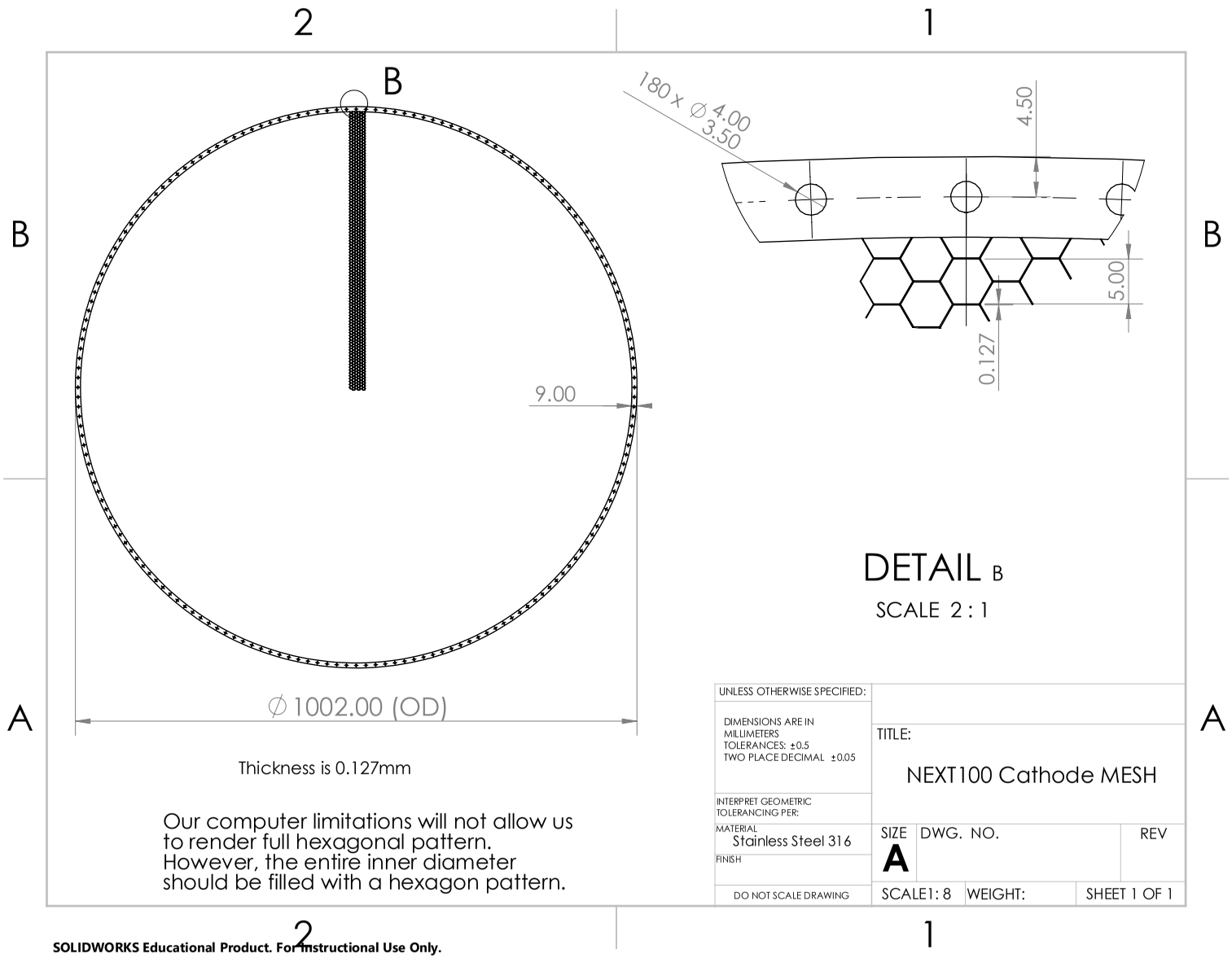


FIGURE C.6: Machine drawings for manufacturing the standard photoeteched mesh for the Cathode region.

# Appendix D

# NEXT-CRAB EL and Cathode Drawings for ANL's vessel

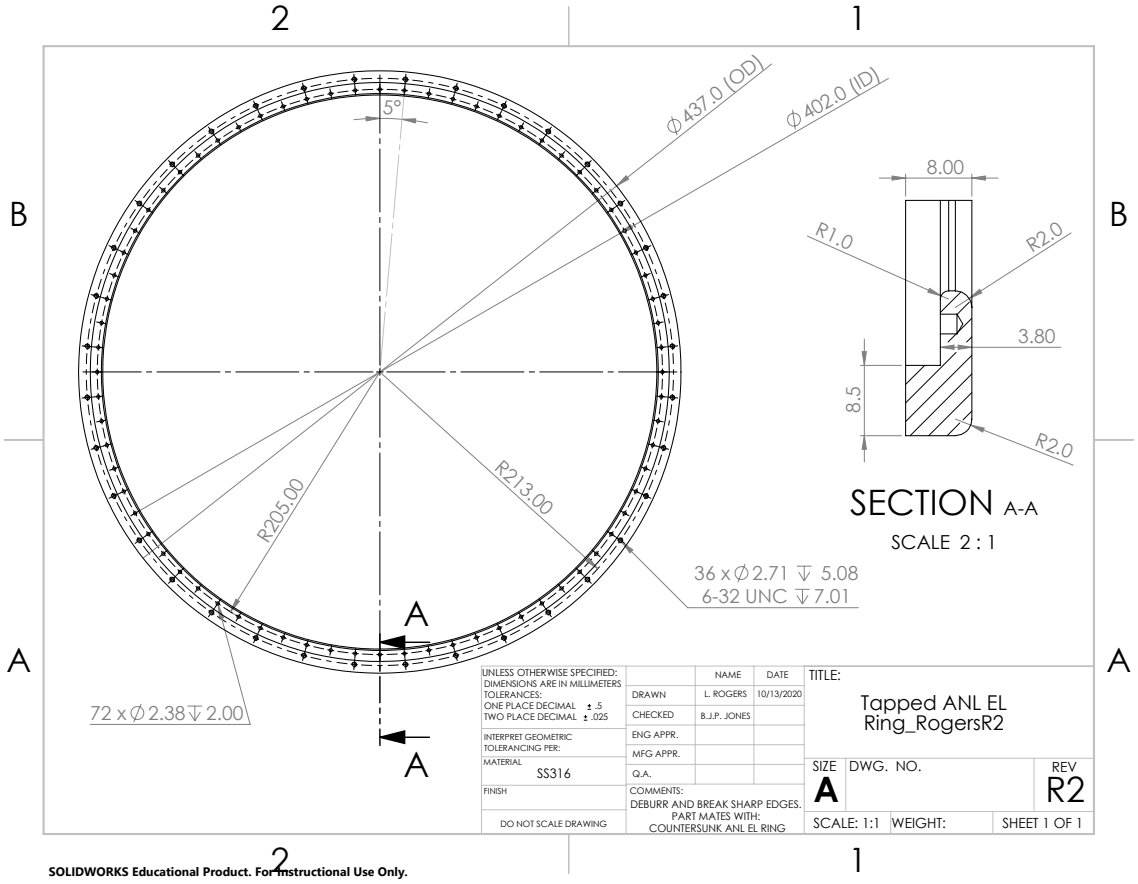


FIGURE D.1: Machine drawing for manufacturing the EL Base rings.

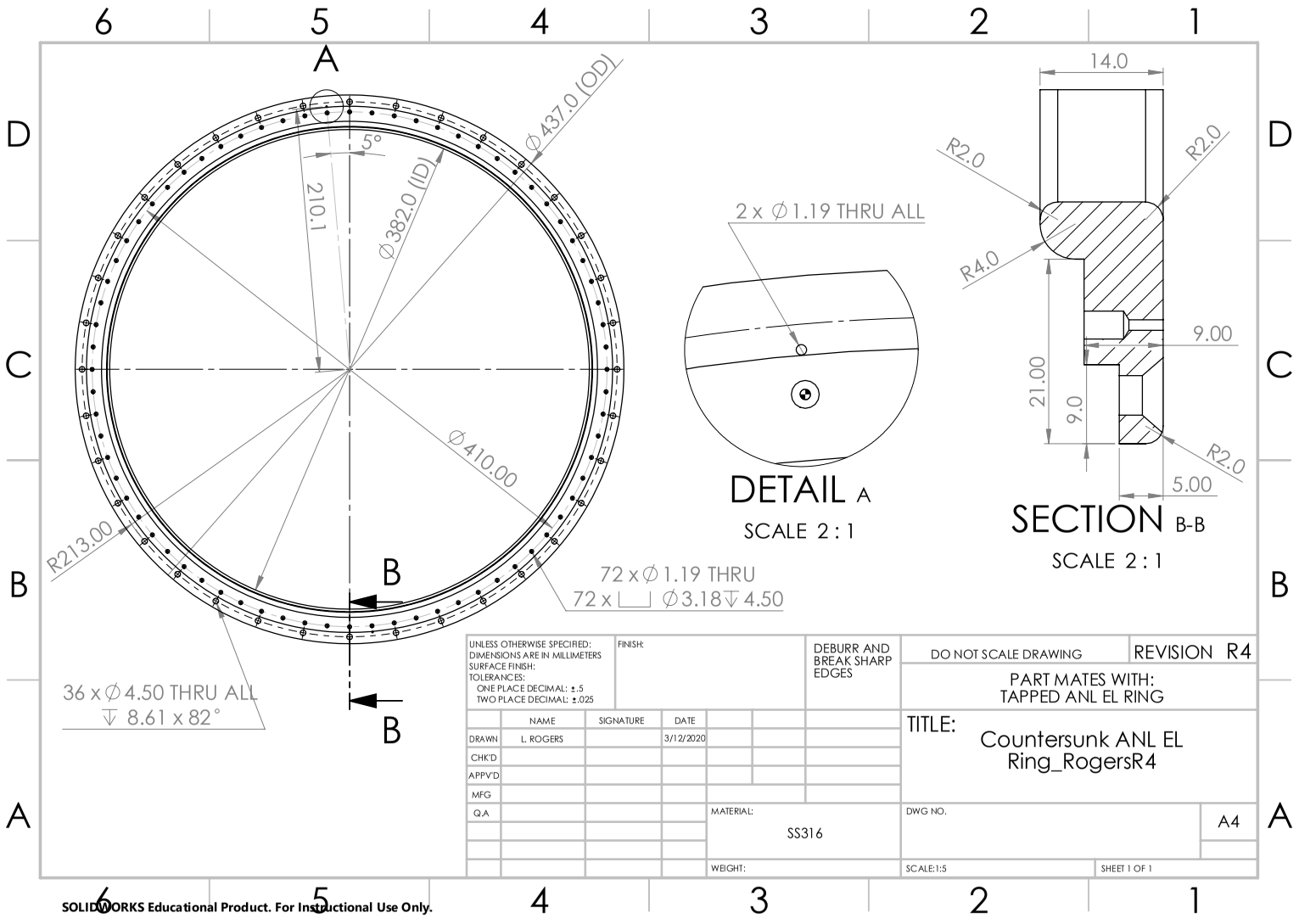


FIGURE D.2: Machine drawings for manufacturing the EL Tension rings.

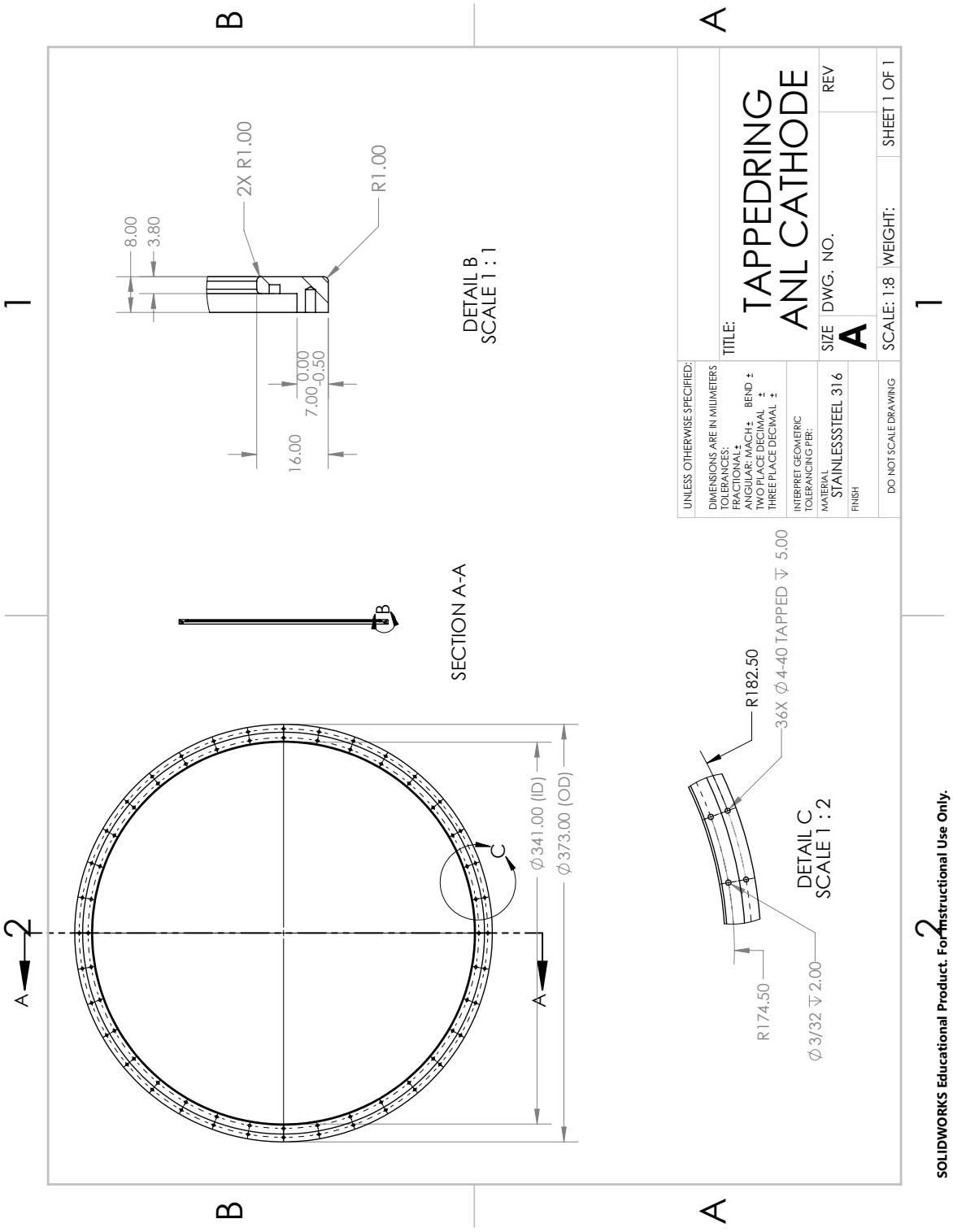


FIGURE D.3: Machine drawings for manufacturing the Cathode Base rings.

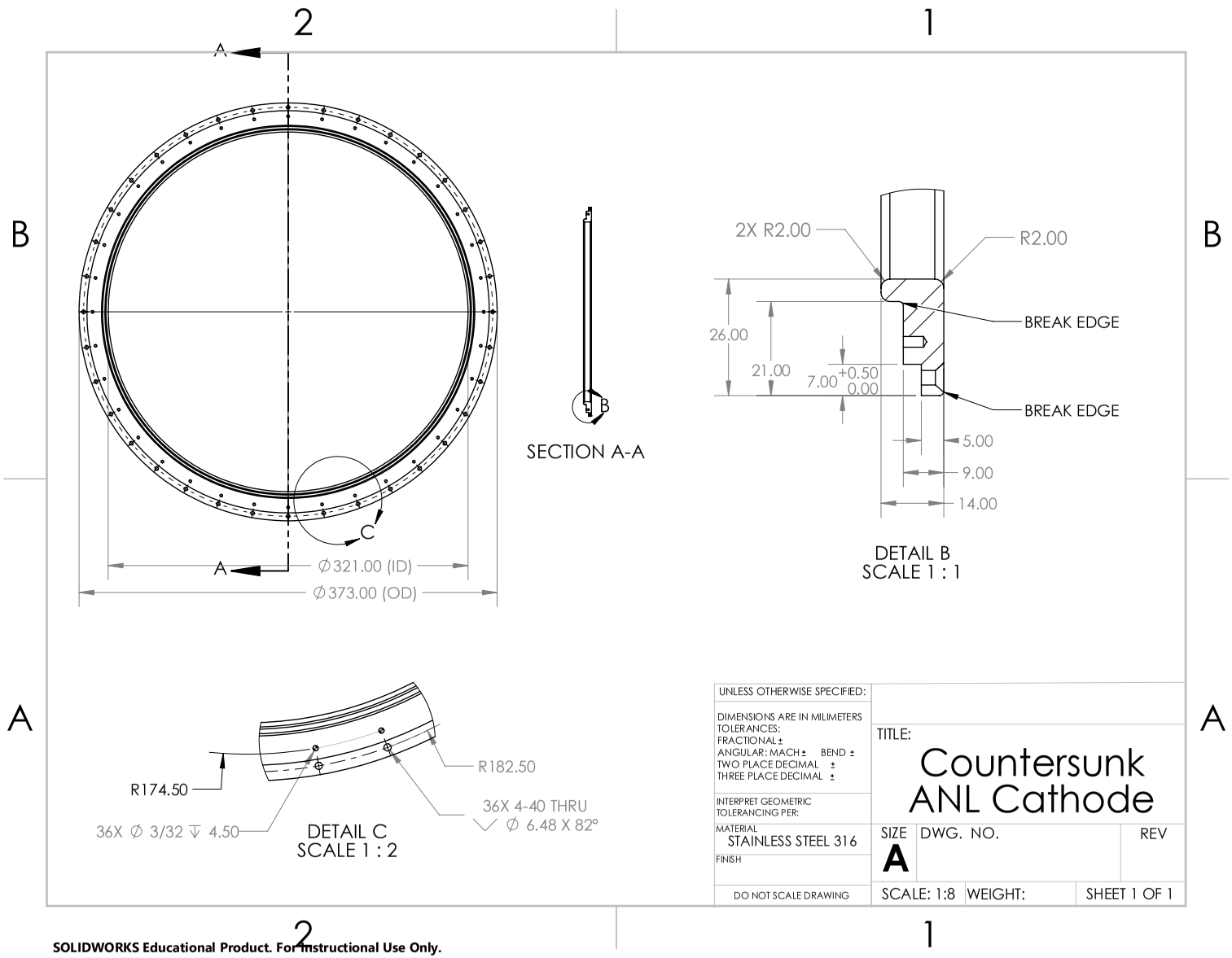


FIGURE D.4: Machine drawings for manufacturing the Cathode Tension rings.

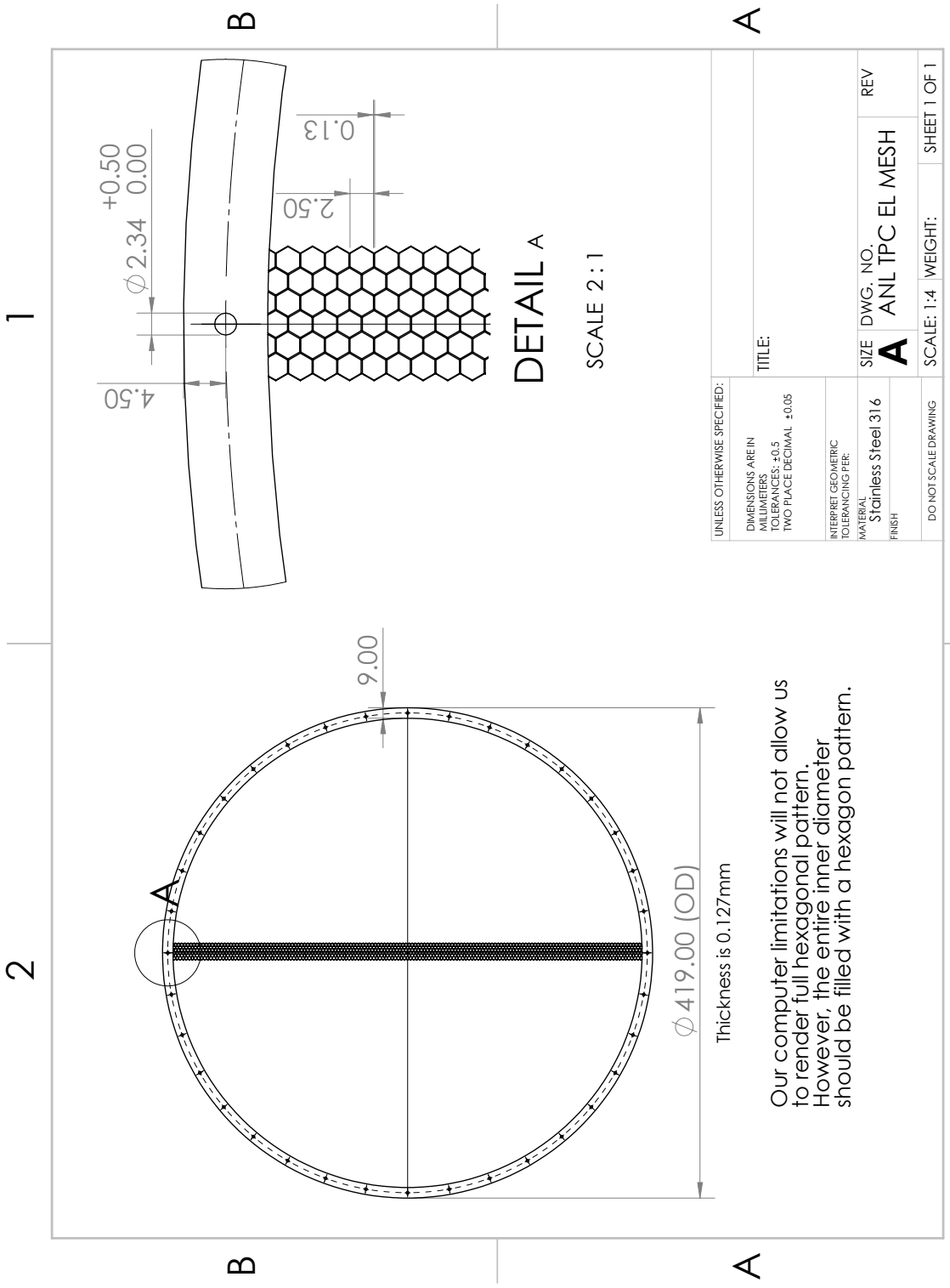


FIGURE D.5: Machine drawings for manufacturing the EL mesh.

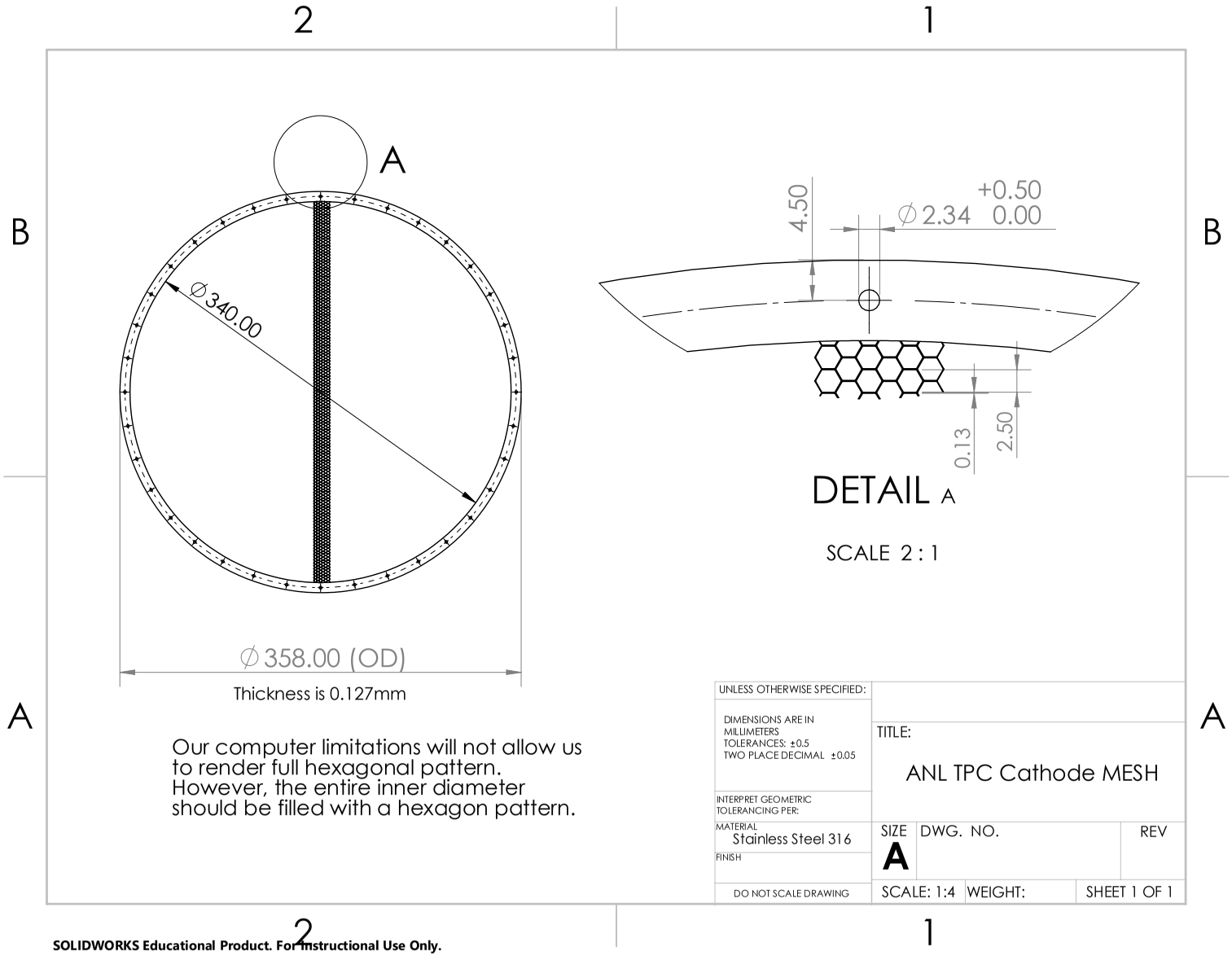


FIGURE D.6: Machine drawings for manufacturing the Cathode mesh.

# Appendix E

# Cathode Separate Wires Prototype

## E.1 Overview of Separate Wire Design

The first version of the cathode for NEXT-100 was machined, strung and made ready for installation. The final part can be see in Fig. E.1. This design was based on a ring of 316 stainless steel, strung with 0.2 mm diameter wires with a spacing of 1 per centimeter. This design was selected to optimize for gas flow and optical transparency (98%). A drawing of the cathode frame is shown in Fig. E.2, Left.

The wire used in the cathode is Stainless Steel 302 (Material #: 100-191), stress relieved, spooled, round wire with Ultra Finish from California Fine Wire. It is fed through bevelled through-holes on both sides of the frame and affixed into place on both sides of the cathode by a vented cup set screw and a small ball bearing. Details of the wire fixture are shown in Fig. E.2

## E.2 Assembly

Cleaning of the set screws, ball bearings, hooks, and weights were done with a soap cleaning solution bath using 1 ml Alconox Detergent soap per liter of deionized water in an ultrasound bath for 30 minutes, followed by two ultrasound baths for 30 minutes each in deionized water.

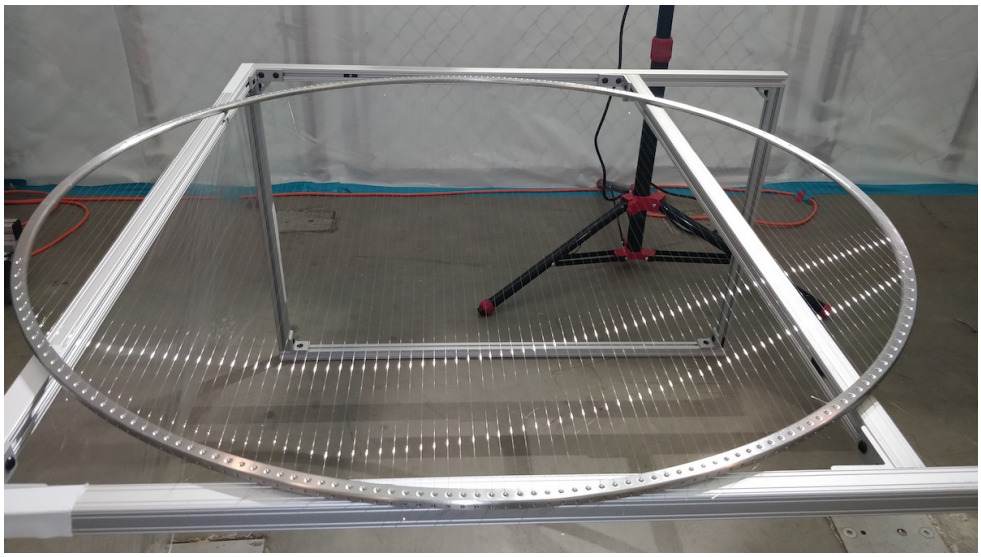

FIGURE E.1: Photograph of the completed strung-style NEXT-100 cathode.

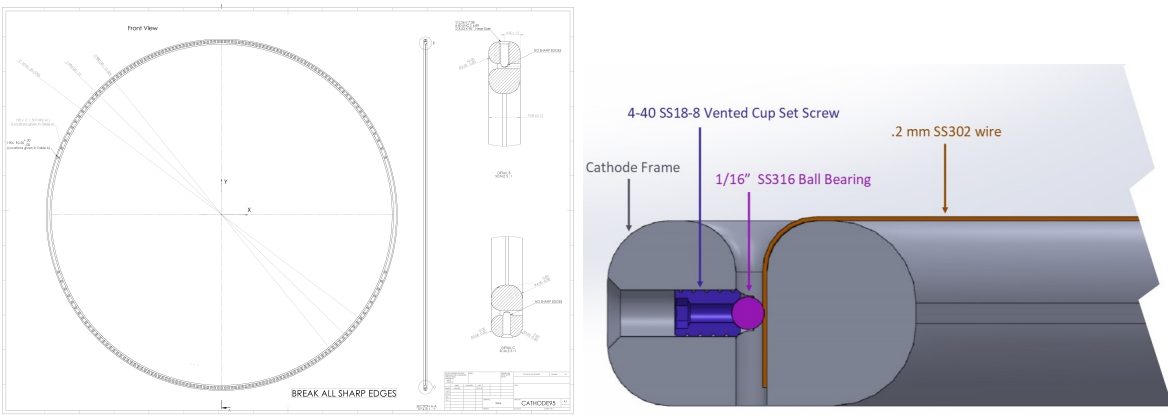


FIGURE E.2: Left: Drawing of the NEXT-100 cathode design; Right: Detail of the wire fixture using set screw and ball bearing.

The cathode frame and the table it was strung on was cleaned using the same soap cleaning solution but using a syringe and kimwipes by hand, followed by liberal rinsing with deionized water. This was done once outside the clean room, and then again inside.

Assembly of the cathode was done inside a Class-10,000 clean room at UTA. Hair and beard nets, shoe covers, lab coats, and gloves were worn by personnel inside the clean room at all times. The Cathode hung from a table made out of aluminum t-slot framing with 4 S-hooks while stringing. The wire spool also stayed on an aluminum plate while stringing and the end clipped to a banana clip between each strand so the spool never unwound which helped avoid kinks and scratches on the wires.

With the Cathode hanging level from the table, a 1/16" Stainless Steel 316 ball bearing was put in each side hole followed by a 18-8 Stainless Steel vented 4-40 thread cup-point set screw 1/8" long, tightened until flush with the frame edge. The cup-point of the set screw insured a solid grip on the ball bearing and minimizes chances of rolling and allowing the wire to slip. Because the ball bearing is sitting flush in the set screw, vented screws are used to avoid a virtual vacuum leak. The ball bearing was used in place of oval head set screws because of

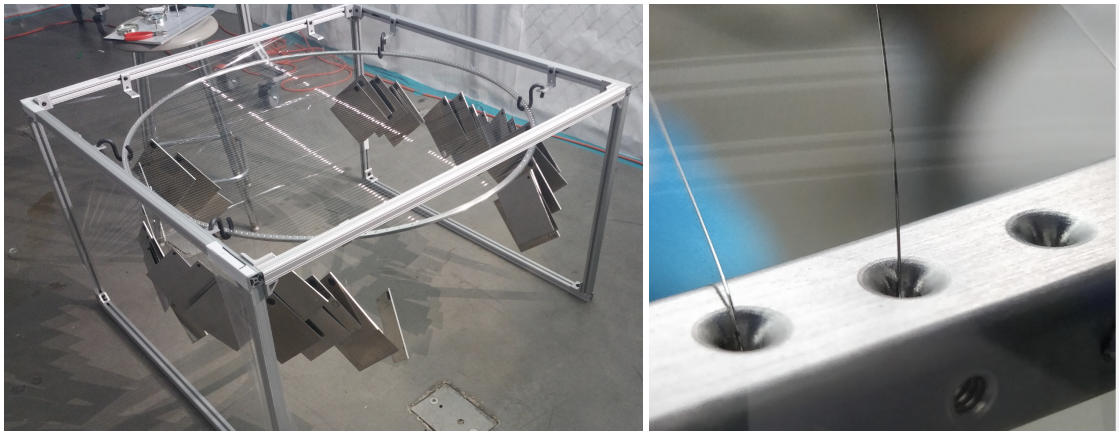

FIGURE E.3: Left: Cathode sitting in S-hooks from aluminum table with weights hanging from wires while they stretch. Right: piece of debris found on one of the wires during inspection which then got replaced.

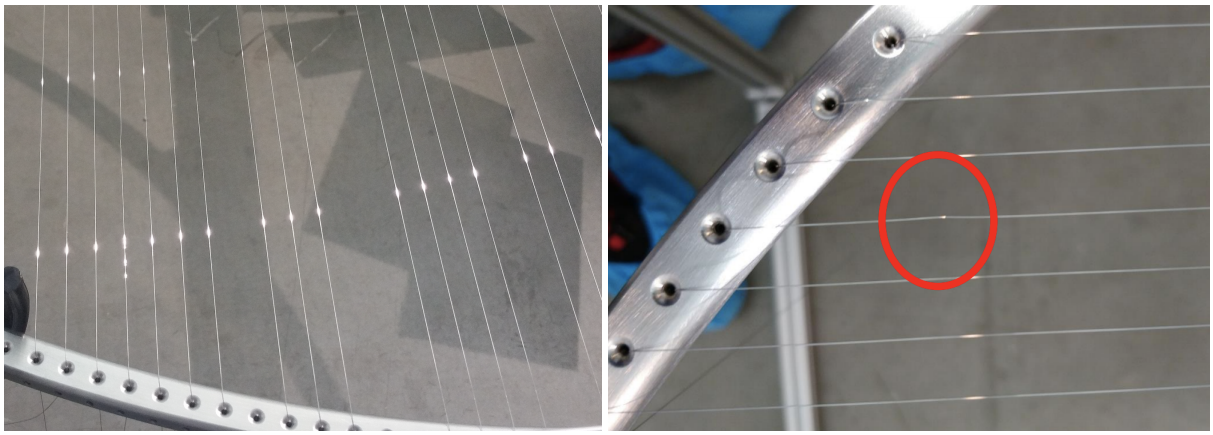

FIGURE E.4: Left: Fourth wire from the left reflected light differently than the surrounding wires indicating a crimp in the wire and was therefore replaced. Right: Kink found in wire during inspection which was then replaced.

manufacturing tolerances on the blind tapped hole. To get the threads deep enough for the set screw to push against the wire, the tap itself would be required to go into the part a little which would create a sharp point for the wire to rest against.

To string the Cathode we used a magnifying glass to check for defects/debris on first 20cm of wire then put wire through one end of the cathode and secured with a set screw. Then enough wire was fed out to reach fully across the Cathode plus 20 cm and clamped wire to wire stand. The wire was cut on proper side of banana clip so wire spool does not unravel and use magnifying glass to check for defects/dirt on entirety of wire length. The wire was then taken across to hole on opposite side of the frame, fed through the hole then tied to .45lb weight through rubber grommet. The weights were made from aluminum stock plates with a hole drilled in the corner and rubber grommets inserted for the wire to go through so that it wouldn't crimp against a rough metal edge. Weights alternate on which side of the frame they are hanging from so that load is distributed all around the frame, as shown in E.3 left.

A final by-eye check of light reflections along the wires checks for kinks or deformations, shown in E.4. The weights are then hung for a week to allow for early wire creep, and then the set screws were secured and the weights cut off to yield the finished cathode.

Unfortunately with so many individual wires there were an abundance of options for single point failures. While many of the wires held their tension after the weights were removed, not all of them did so we opted to go for the more robust option as described in Chapter 3. Where the tension was not held fully, it appeared the ball bearing was not pressed into the wire hard enough which would probably require a deeper tap into each hole so the set screw could be tightened further. The taps are so tiny though that every time we re-tapped a hole we had a possibility of breaking a tap in the hole, which when removed had a high probability of leaving the hole deformed.

# Appendix F

# Anode Resistive Planes Prototype

Initially we considered making an anode more similar to the current design of NEXT-White where there would be a solid plate of resistive transparent material behind the gate coated in tetraphenyl butadiene (TPB) for shifting photons into the visible spectrum.The advantages to this would be extra protection of the SiPMs whenever there is a spark and there would be half as much deflection in the EL region as the plate would remain flat compared to the mesh gate which would be deformed. The downside of a solid plate is difficulty getting good gas circulation. A quartz plate however would not be able to be made large enough for NEXT-100 or NEXT-HD so we explored other material options. The design parameters we were designing for was that one, it needed to be robust under high voltage discharges; i.e. sparks, two, transparent to visible light, three, resistive to help quench any sparks that occurred and be able to hold equipotential along the entire surface, and four, have minimal deflection under high electrostatic forces.

There were two transparent, resistive anode configurations considered, each which involved a base of acrylic. One was static dissipative acrylic (SDA) which is acrylic that "has a polymeric, crosslinked coating which exhibits excellent clarity, chemical resistance, and mar resistance" [79]. The other option was Poly(3,4-ethylenedioxythiophene) (PEDOT) coating on acrylic. At the time of these studies PEDOT coating was known to be radiopure whereas the purity of SDA was unknown. The con to PEDOT was that at the time manufacturing at a large scale would be awkward and potentially non-uniform as it required us to do it in house. However I note that there are manufacturing companies now that advertise being able to produce PEDOT covered acrylic of all shapes and sizes. The benefit to SDA was that it is easy to manufacture at all scales

| A (mBq/kg) | SD Acrylic | PMMA (Evonik) |
|---|---|---|
| U-235 | **< 0.36** | < 1.1 |
| U-238/Pa-234m | **< 67** | < 208 |
| U-238/Pb-214 | **< 0.76** | < 2.5 |
| U-238/Bi-214 | **< 0.69** | < 2.2 |
| Th-232/Ac-228 | **< 1.6** | < 3.9 |
| Th-232/Pb-212 | **< 0.55** | < 1.5 |
| Th-232/Bi-212 | **< 4.2** | < 12 |
| Th-232/Tl-208 | **< 1.4** | < 3.4 |
| K-40 | **38.6±4.2** | < 8.1 |
| Cs-137 | **< 0.18** | < 0.6 |
| Co-60 | **< 0.21** | < 0.4 |

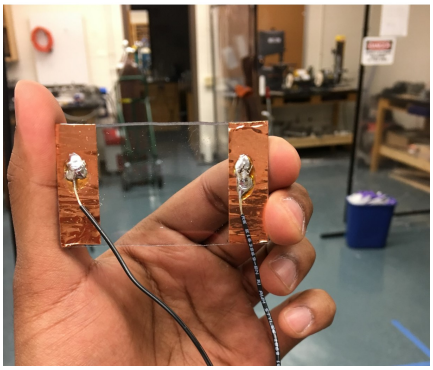

FIGURE F.1: Left: Radioassay results of SDA and Plexiglass (PMMA). Right: PEDOT coated acrylic, spin coated onto a large disk and cut into rectangles before placing electrodes on either side.

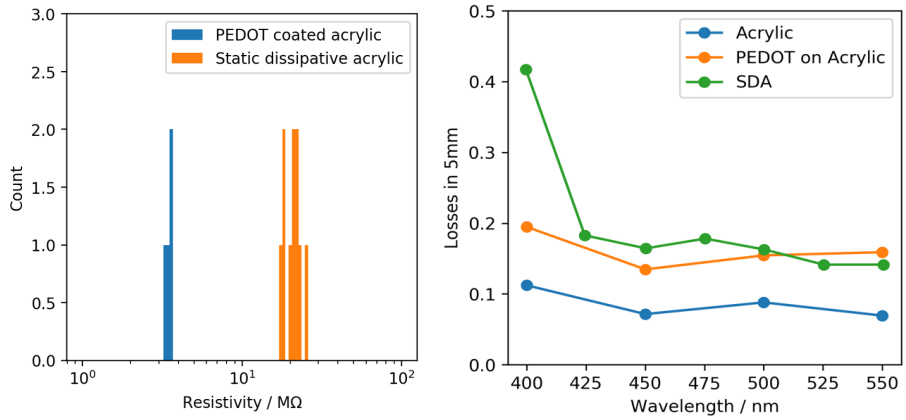


FIGURE F.2: Left: Resistivity uniformity of PEDOT and SDA. Right: Optical transparency of both samples over different wavelengths.

and is guaranteed to be uniform. SDA was found to be within acceptable range of radioactivity with the radioassay results shown in Fig. F.1.

Two of our undergraduates Ryan Clark and Fahad Karim worked to characterize the two options for a solid plate anode.To test the resistivity of the SDA and PEDOT coated acrylic, several pieces of identically sized rectangles were cut out as shown in Figure F.1 right and copper tape put across the edge. Placing an ohmmeter across the copper tapes provided the resistivity measurements shown in Figure F.2 left.

Figure F.2 right shows the percent of transparency lost in the wavelengths of interest for a 5mm thick piece of material. From 400 to 500nm, the wavelengths after photons are shifted due to TPB [80], the SDA was found to be about 78% transparent and the PEDOT coated acrylic was about 83% transparent.

Another design criteria mentioned in Chapter 4 was that there had to be voltage stability in the EL region once the gate and anode are charged. To check this voltage was placed across the plates and the current measured over time. For reasons not understood the PEDOT exhibited a hysteresis whether on normal acrylic or SDA whereas the SDA stayed steady overtime.

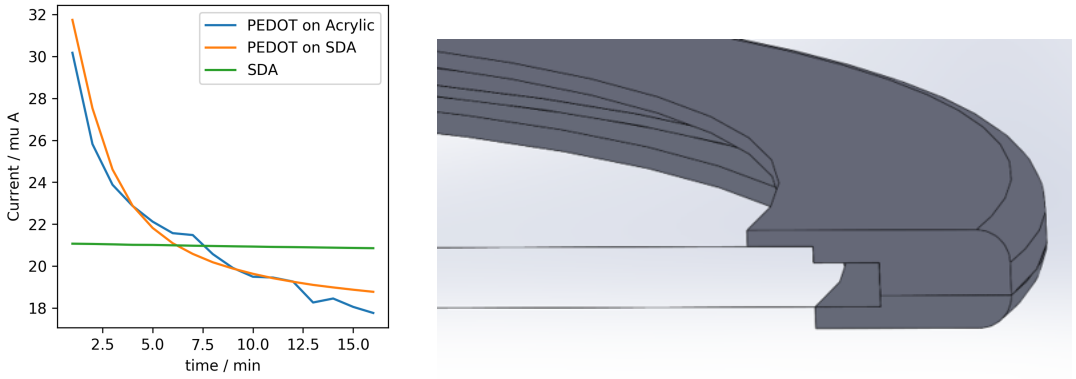


FIGURE F.3: Left: Anode materials charge up. Center: Section view of metal frame used for a solid uniform voltage along the resistive surface of the SDA.

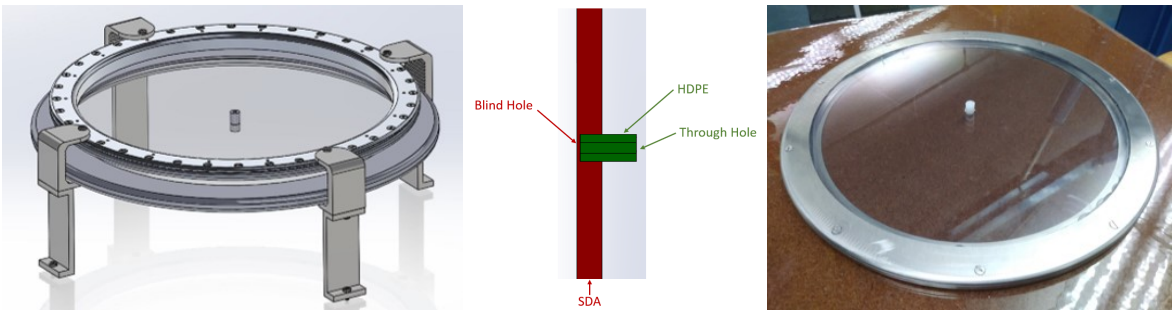


FIGURE F.4: Left: assembled DEMO++ compatible assembly. Center: Connection of SDA with vented support post. Right: Fully assembled NEXT-DEMO sized SDA prototype anode with support post inserted.

All the points up to here led to the decision of working with SDA rather than PEDOT coated acrylic. Because the polymers that make SDA resistive are on the surface, a frame had to be designed to give a solid electrical connection all along the face of the plate without protruding towards the gate frame enough to cause an increased electric field to the point of sparks. This was accomplished as shown in Fig. F.3 right. The frame was composed of two parts to tightly clamp down around the edge of the SDA with a thin lip all around the surface. The frame was stainless steel so that ground could be established anywhere around the edge the same way NEXT-White and NEXT-DEMO were done. To avoid edge effects the anode had a larger diameter than the gate as shown in Fig. F.4 left.

To place the support post into the Anode a blind hole the exact size of the post was drilled into the SDA and the post cryofit in using liquid nitrogen. To avoid outgassing a through hole was put through the HDPE post so that gas would not get trapped at the base of the post as shown in Fig. F.3. The downside of this type of assembly was that the posts could not be interchanged without drilling them out so changing the gap size of the EL region would require a new anode each time. However compared to most detector components the SDA and HDPE posts are relatively cheap to manufacture so making a few lengths of posts would not be a large undertaking and the entire plastic assembly could be swapped into the metal frames as needed.

## Appendix G

# NEXT-DEMO Static Dissipative Acrylic Anode Frame Drawings

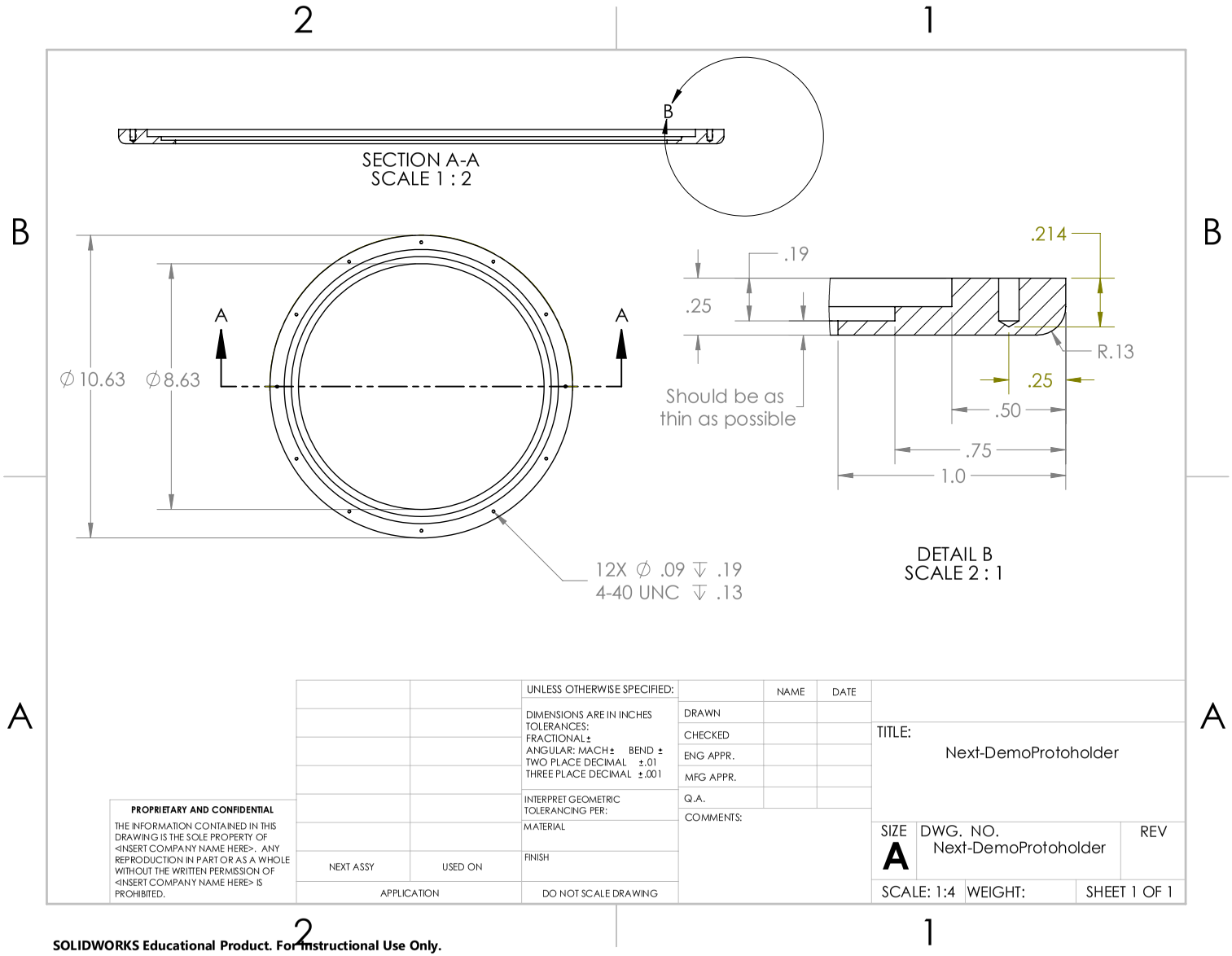


FIGURE G.1: Machine drawing for manufacturing the Anode Electrical connection ring for DEMo++.

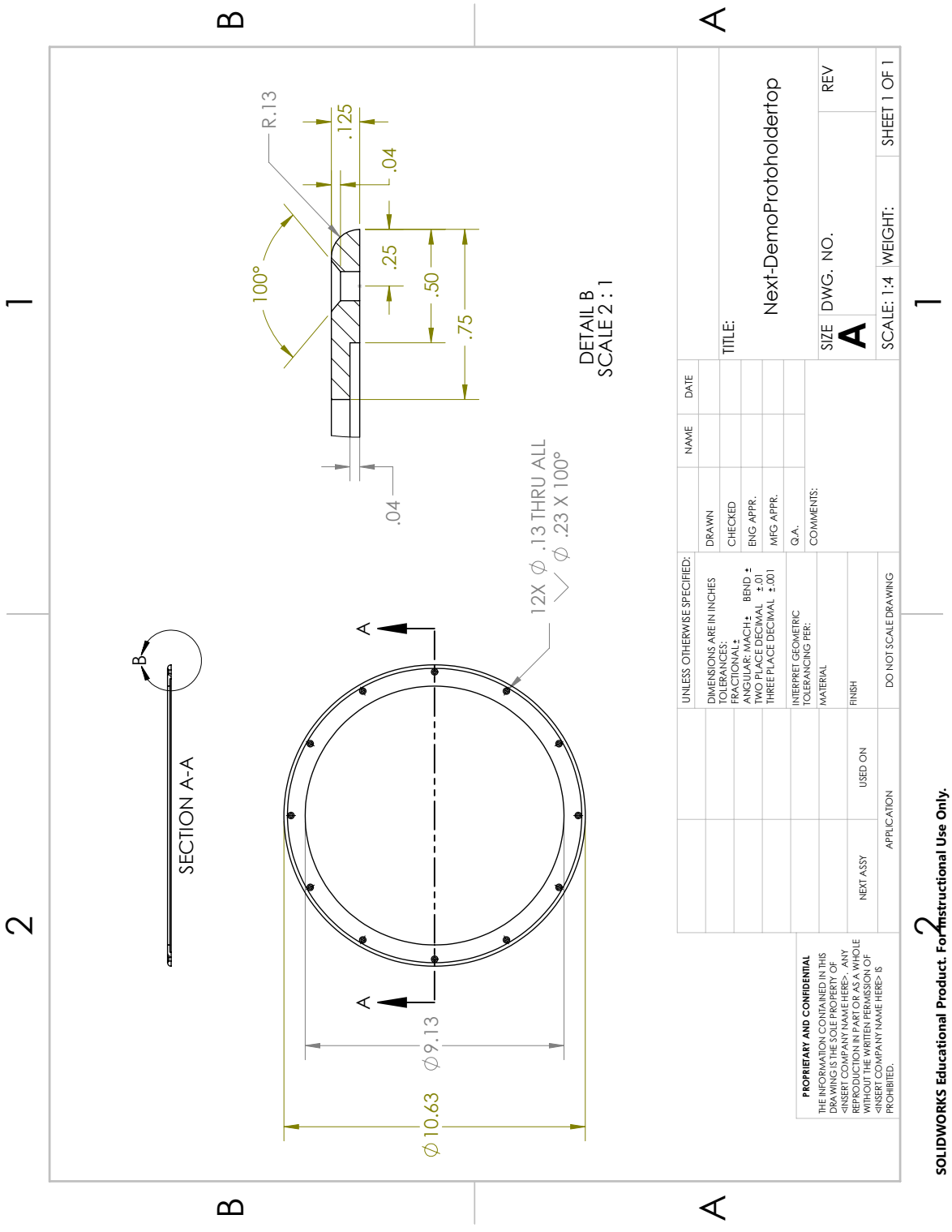


FIGURE G.2: Machine drawing for manufacturing the Anode base ring for DEMo++.

# Bibliography


[1] Kaori Fuyuto. *Electroweak Baryogenesis and Its Phenomenology*. PhD thesis, 2018.

[2] Sacha Davidson, Enrico Nardi, and Yosef Nir. Leptogenesis. *Physics Reports*, 466(4-5):105–177, Sep 2008.

[3] Mark Thomson. *Modern Particle Physics*. Cambridge University Press, 2013.

[4] X. Qian and P. Vogel. Neutrino mass hierarchy. *Progress in Particle and Nuclear Physics*, 83:1–30, Jul 2015.

[5] Robert-Jan Hagebout. Beyond the standard model with neutrino physics. 2014.

[6] Steven R. Elliott and Petr Vogel. Double beta decay. *Annual Review of Nuclear and Particle Science*, 52(1):115–151, 2002.

[7] M. Goeppert-Mayer. Double beta-disintegration. *Phys. Rev.*, 48:512–516, Sep 1935.

[8] Jonathan Engel and Javier Menéndez. Status and future of nuclear matrix elements for neutrinoless double-beta decay: a review. *Reports on Progress in Physics*, 80(4):046301, Mar 2017.

[9] A. Gando, Y. Gando, T. Hachiya, A. Hayashi, S. Hayashida, H. Ikeda, K. Inoue, K. Ishidoshiro, Y. Karino, M. Koga, and et al. Search for majorana neutrinos near the inverted mass hierarchy region with kamland-zen. *Physical Review Letters*, 117(8), Aug 2016.

[10] J. Kotila and F. Iachello. Phase-space factors for double-decay. *Physical Review C*, 85(3), Mar 2012.

[11] B. J. P. Jones. The physics of neutrinoless double beta decay: A primer, 2021.

[12] J. Schechter and J. W. F. Valle. Neutrinoless double-$\beta$ decay in su(2)×u(1) theories. *Phys. Rev. D*, 25:2951–2954, Jun 1982.

[13] J. B. Albert et al. Cosmogenic Backgrounds to $0\nu\beta\beta$ in EXO-200. *JCAP*, 1604(04):029, 2016.

[14] A. Gando, Y. Gando, H. Hanakago, H. Ikeda, K. Inoue, R. Kato, M. Koga, S. Matsuda, T. Mitsui, T. Nakada, and et al. Measurement of the double-decay half-life of136xe with the kamland-zen experiment. *Physical Review C*, 85(4), Apr 2012.

[15] P. Ferrario et al. First proof of topological signature in the high pressure xenon gas TPC with electroluminescence amplification for the NEXT experiment. *JHEP*, 01:104, 2016.

[16] D. R. Nygren. The Time Projection Chamber: A New 4 pi Detector for Charged Particles. *eConf*, C740805:58, 1974.

[17] Vitaly A. Kudryavtsev. Recent results from lux and prospects for dark matter searches with lz. *Universe*, 5(3), 2019.

[18] T2K ND280 TPC collaboration. Time projection chambers for the t2k near detectors, 2010.

[19] Cristina Monteiro. *Determination of argon and xenon absolute electroluminescence yields in Gas Proportional Scintillation Counters*. PhD thesis, 02 2011.

[20] E. mez, R.M. rrez, M. Losada, Giovanna Navarro, Antonio Ferreira, C.A.B. Oliveira, Joao Veloso, D. Chan, A. Goldschmidt, D. Hogan, Tom Miller, D. Nygren, J. Renner, D. Shuman, Helmuth Spieler, T. Weber, F.I.G.M. Borges, Carlos Conde, T.H.V.T. Dias, and Julia Villar. Conceptual design report: The next-100 experiment for 0 searches at lsc. *Journal of Instrumentation*, 7, 06 2012.

[21] V Álvarez, I Bandac, A Bettini, F I G M Borges, S Cárcel, J Castel, S Cebrián, A Cervera, C A N Conde, T Dafni, and et al. Radiopurity control in the next-100 double beta decay experiment: procedures and initial measurements. *Journal of Instrumentation*, 8(01):T01002–T01002, Jan 2013.

[22] Aleksey Bolotnikov and Brian Ramsey. The spectroscopic properties of high-pressure xenon. *Nuclear Instruments and Methods in Physics Research Section A: Accelerators, Spectrometers, Detectors and Associated Equipment*, 396(3):360–370, 1997.

[23] C A B Oliveira, M Sorel, J Martin-Albo, J J Gomez-Cadenas, A L Ferreira, and J F C A Veloso. Energy resolution studies for NEXT. *Journal of Instrumentation*, 6(05):P05007–P05007, may 2011.

[24] D. G. Simons and P. A. J. de Korte. *Soft X-ray energy resolution and background rejection in a driftless Gas Scintillation Proportional Counter*. Nuclear Instruments and Methods, 1989.

[25] A. Simon et al. Boosting background suppression in the next experiment through richardson-lucy deconvolution. *Journal of High Energy Physics (Online)*, 2021(10), 7 2021.

[26] L. Rogers et al. High voltage insulation and gas absorption of polymers in high pressure argon and xenon gases. *Journal of Instrumentation*, 13(10):P10002–P10002, oct 2018.

[27] V. Alvarez et al. Near-Intrinsic Energy Resolution for 30 to 662 keV Gamma Rays in a High Pressure Xenon Electroluminescent TPC. *Nucl. Instrum. Meth.*, A708:101–114, 2013.

[28] Vicente Alvarez et al. Next-100 technical design report (tdr). executive summary. *Journal of Instrumentation*, 7, 06 2012.

[29] C A B Oliveira and. Results from the NEXT prototypes. *Journal of Physics: Conference Series*, 460:012011, oct 2013.

[30] P. Ferrario et al. Demonstration of the event identification capabilities of the NEXT-White detector. *JHEP*, 10:052, 2019.

[31] M. Kekic, C. Adams, K. Woodruff, J. Renner, E. Church, M. Del Tutto, J. A. Hernando Morata, J. J. Gómez-Cadenas, V. Álvarez, and et al. Demonstration of background rejection using deep convolutional neural networks in the next experiment. *Journal of High Energy Physics*, 2021(1), Jan 2021.

[32] P. Novella et al. Radiogenic Backgrounds in the NEXT Double Beta Decay Experiment. *JHEP*, 10:051, 2019.

[33] G. Martinez-Lema et al. Calibration of the NEXT-White detector using $^{83m}$Kr decays. *JINST*, 13(10):P10014, 2018.

[34] J. Renner et al. Energy calibration of the next-white detector with 1q of 136xe. *Journal of High Energy Physics (Online)*, 2019(10), 10 2019.

[35] N. López-March and. Sensitivity of the NEXT-100 detector to neutrinoless double beta decay. *Journal of Physics: Conference Series*, 888:012243, sep 2017.

[36] V. Álvarez, V. Herrero-Bosch, R. Esteve, A. Laing, J. Rodríguez, M. Querol, F. Monrabal, J.F. Toledo, and J.J. Gómez-Cadenas. The electronics of the energy plane of the next-white detector. *Nuclear Instruments and Methods in Physics Research Section A: Accelerators, Spectrometers, Detectors and Associated Equipment*, 917:68–76, Feb 2019.

[37] NEXT Collaboration, C. Adams, et al. Sensitivity of a tonne-scale next detector for neutrinoless double beta decay searches, 2021.

[38] J. Martin-Albo et al. Sensitivity of NEXT-100 to Neutrinoless Double Beta Decay. *JHEP*, 05:159, 2016.

[39] AD McDonald, BJP Jones, DR Nygren, C Adams, V Álvarez, CDR Azevedo, JM Benlloch-Rodríguez, FIGM Borges, A Botas, S Cárcel, et al. Demonstration of single-barium-ion sensitivity for neutrinoless double-beta decay using single-molecule fluorescence imaging. *Physical review letters*, 120(13):132504, 2018.

[40] P. Thapa, N. K. Byrnes, A. A. Denisenko, Jr. au2 F. W. Foss, B. J. P. Jones, J. X. Mao, K. Nam, C. A. Newhouse, D. R. Nygren, A. D. McDonald, T. T. Vuong, and K. Woodruff. Barium selective chemosensing by diazacrown ether naphthalimide turn-on fluorophores for single ion barium tagging, 2020.

[41] Aparicio B. Bueno J.M Rivilla, I. and et al. Fluorescent bicolour sensor for low-background neutrinoless double  decay experiments. *Nature*, 583:48–54, 2020.

[42] NEXT Collaboration, B. J. P. Jones, et al. The dynamics of ions on phased radio-frequency carpets in high pressure gases and application for barium tagging in xenon gas time projection chambers, 2021.

[43] C. Chambers et al. Imaging individual barium atoms in solid xenon for barium tagging in nexo, 2018.

[44] K. Twelker and S. Kravitz. Barium tagging from nexo using resonance ionization spectroscopy. *Physics Procedia*, 61:278–282, 2015. 13th International Conference on Topics in Astroparticle and Underground Physics, TAUP 2013.

[45] J. B. Albert et al. Sensitivity and Discovery Potential of nEXO to Neutrinoless Double Beta Decay. *Phys. Rev.*, C97(6):065503, 2018.

[46] J. B. Albert, M. Auger, D. J. Auty, P. S. Barbeau, E. Beauchamp, D. Beck, V. Belov, C. Benitez-Medina, J. Bonatt, M. Breidenbach, and et al. Improved measurement of the2half-life of136xe with the exo-200 detector. *Physical Review C*, 89(1), Jan 2014.

[47] Michelle J. Dolinski, Alan W.P. Poon, and Werner Rodejohann. Neutrinoless double-beta decay: Status and prospects. *Annual Review of Nuclear and Particle Science*, 69(1):219–251, Oct 2019.

[48] G. Anton, I. Badhrees, P.S. Barbeau, D. Beck, V. Belov, T. Bhatta, M. Breidenbach, T. Brunner, G.F. Cao, W.R. Cen, and et al. Search for neutrinoless double- decay with the complete exo-200 dataset. *Physical Review Letters*, 123(16), Oct 2019.

[49] Y. Gando, A. Gando, T. Hachiya, S. Hayashida, K. Hosokawa, H. Ikeda, T. Mitsui, T. Nakada, S. Obara, H. Ozaki, and et al. The nylon balloon for xenon loaded liquid scintillator in kamland-zen 800 neutrinoless double-beta decay search experiment. *Journal of Instrumentation*, 16(08):P08023, Aug 2021.

[50] Itaru Shimizu and Mark Chen. Double beta decay experiments with loaded liquid scintillator. *Frontiers in Physics*, 7:33, 2019.

[51] V. Lozza. The sno+ experiment for neutrinoless double-beta decay. *Nuclear and Particle Physics Proceedings*, 273-275:1836–1841, 2016. 37th International Conference on High Energy Physics (ICHEP).

[52] A. Bellerive, J.R. Klein, A.B. McDonald, A.J. Noble, and A.W.P. Poon. The sudbury neutrino observatory. *Nuclear Physics B*, 908:30–51, 2016. Neutrino Oscillations: Celebrating the Nobel Prize in Physics 2015.

[53] S. Andringa, E. Arushanova, S. Asahi, M. Askins, D. J. Auty, A. R. Back, Z. Barnard, N. Barros, E. W. Beier, A. Bialek, and et al. Current status and future prospects of the sno+ experiment. *Advances in High Energy Physics*, 2016:1–21, 2016.

[54] Josephine Paton. Neutrinoless double beta decay in the sno+ experiment, 2019.

[55] M. Agostini, G.R. Araujo, A.M. Bakalyarov, M. Balata, I. Barabanov, L. Baudis, C. Bauer, E. Bellotti, S. Belogurov, A. Bettini, and et al. Final results of gerda on the search for neutrinoless double- decay. *Physical Review Letters*, 125(25), Dec 2020.

[56] J. M. López-Castaño and I. Guinn. Current status of legend: Searching for neutrinoless double-beta decay in 76ge: Part ii, 2019.

[57] D. Q. Adams et al. High sensitivity neutrinoless double-beta decay search with one tonne-year of cuore data, 2021.

[58] E. Armengaud, C. Augier, A.S. Barabash, F. Bellini, G. Benato, A. Benoît, M. Beretta, L. Bergé, J. Billard, Yu.A. Borovlev, and et al. New limit for neutrinoless double-beta decay of mo100 from the cupid-mo experiment. *Physical Review Letters*, 126(18), May 2021.

[59] Cristina Maria Bernardes Monteiro. *Determination of argon and xenon absolute electroluminescence yields in Gas Proportional Scintillation Counters*. PhD thesis, 2011.

[60] Martin Janecek. Reflectivity spectra for commonly used reflectors. *IEEE Transactions on Nuclear Science*, 59:490–497, 2012.

[61] L Baudis, A D Ferella, A Askin, J Angle, E Aprile, T Bruch, A Kish, M Laubenstein, A Manalaysay, T Marrodán Undagoitia, and M Schumann. Gator: a low-background counting facility at the gran sasso underground laboratory. *Journal of Instrumentation*, 6(08):P08010–P08010, aug 2011.

[62] S. Cebrián et al. Radiopurity assessment of the tracking readout for the NEXT double beta decay experiment. *Journal of Instrumentation*, 10(05):P05006–P05006, may 2015.

[63] Overcoming the limitations of traditional sheet metal machining technologies. Technical report, Birmingham, United Kingdom.

[64] Shigley's mechanical engineering design, 1977.

[65] L Rogers et al. Mitigation of backgrounds from cosmogenic 137 xe in xenon gas experiments using 3 he neutron capture. *Journal of Physics G: Nuclear and Particle Physics*, 47(7):075001, may 2020.

[66] Anatoli Fedynitch et al. Calculation of conventional and prompt lepton fluxes at very high energy, 2015.

[67] Thomas K. Gaisser, Dennis Soldin, Andrew Crossman, and Anatoli Fedynitch. Precision of analytical approximations in calculations of atmospheric leptons, 2019.

[68] P.A. Zyla et al. Review of Particle Physics. *PTEP*, 2020(8), 2020.

[69] Thomas K. Gaisser. Spectrum of cosmic-ray nucleons, kaon production, and the atmospheric muon charge ratio. *Astroparticle Physics*, 35(12):801–806, Jul 2012.

[70] N. V. Sokolskaya V. I. Zatsepin. Three component model of cosmic ray spectra from 10 gev to 100 pev. *Astronomy and Astrophysics Physics*, (458), 2006.

[71] R. S. Fletcher, T. K. Gaisser, Paolo Lipari, and Todor Stanev. sibyll: An event generator for simulation of high energy cosmic ray cascades. *Phys. Rev. D*, 50:5710–5731, Nov 1994.

[72] A. Fedynitch T.K. Gaisser T. Stanev F. Riehn, R. Engel. Charm production in sibyll. *EPJ Web of Conferences*, 99, 2015.

[73] D. Heck and T. Pierog. Extensive air shower simulation with corsika: A user's guide, May 2021.

[74] M. Schmitz T. Fuchs W. Rhode D. Chirkin J. Becker Tjus J.-H. Koehne, K. Frantzen. Proposal: A tool for propagation of charged leptons. *Computer Physics Communications*, 184:2070–2090, 2013.

[75] L. N. Bogdanova, M. G. Gavrilov, V. N. Kornoukhov, and A. S. Starostin. Cosmic muon flux at shallow depths underground. *Physics of Atomic Nuclei*, 69(8):1293–1298, Aug 2006.

[76] J. Marchant. Cosmic-ray particles reveal secret chamber in Egypt's Great Pyramid. *Nature*, 2017.

[77] Cosmic-ray muon flux at canfranc underground laboratory. *Eur. Phys. J. C*, 2019.

[78] B.J.P. Jones. Mesh deformation. https://github.com/UTA-REST/ELWiki.wiki.git, 2018.

[79] Fabrication of c-300™ coated plastics. Technical report, Amarillo, TX.

[80] V.M. Gehman, S.R. Seibert, K. Rielage, A. Hime, Y. Sun, D.-M. Mei, J. Maassen, and D. Moore. Fluorescence efficiency and visible re-emission spectrum of tetraphenyl butadiene films at extreme ultraviolet wavelengths. *Nuclear Instruments and Methods in Physics Research Section A: Accelerators, Spectrometers, Detectors and Associated Equipment*, 654(1):116–121, 2011.